Reduction of Conductivity Uncertainty Propagations in the Inverse Problem of EEG Source Analysis

Reductie van de propagatie van de geleidbaarheidsonzekerheden in het inverse probleem van EEG-bronlokalisatie

Bertrand Russel Yitembe

Promotoren: prof. dr. ir. L. Dupré, dr. ir. G. Crevecoeur
Proefschrift ingediend tot het behalen van de graad van
Doctor in de Ingenieurswetenschappen: Wiskundige Ingenieurstechnieken

Vakgroep Elektrische Energie, Systemen en Automatisering
Voorzitter: prof. dr. ir. J. Melkebeek
Faculteit Ingenieurswetenschappen en Architectuur
Academiejaar 2011 - 2012

UNIVERSITEIT GENT

ISBN 978-90-8578-447-0
NUR 918
Wettelijk depot: D/2011/10.500/51

Reduction of Conductivity Uncertainty Propagations in the Inverse Problem of EEG Source Analysis

Bertrand Russel Yitembe

Dissertation submitted to obtain the academic degree of
PhD in Mathematical Engineering

Publicly defended at Ghent University on September 28, 2011

Research in cooperation with research group Numerical Analysis and Mathematical Modelling
coordinated by Prof. R. Van Keer from the Department of Mathematical Analysis, Ghent University

Supervisor:

prof. dr. ir. L. Dupré, dr. ir. G. Crevecoeur
Electrical Energy Laboratory
Department of Electrical Energy, Systems and Automation
Faculty of Engineering and Architecture
Ghent University
St.-Pietersnieuwstraat 41
B-9000 Ghent, Belgium
http://www.eesa.ugent.be

Members of the examining board:

prof. dr. ir. R. Van de Walle (chairman)	Ghent University, Belgium
prof. dr. R. Van Keer (secretary)	Ghent University, Belgium
prof. dr. ir. L. Dupré (supervisor)	Ghent University, Belgium
dr. ir. G. Crevecoeur (supervisor)	Ghent University, Belgium
prof. dr. ir. W.H.A. Schilders	Technische Universiteit Eindhoven, Netherlands
prof. dr. ir. S. Clénet	Université de Lille 1, France
prof. dr. ir. C. Geuzaine	University of Liége, Belgium
prof. dr. ir. T. Dhaene	Ghent University, Belgium
dr. ir. H. Hallez	Catholic University College of Bruges-Ostend, Belgium

Acknowledgement

A PhD is a long journey which started for me about four years ago and is presently moving towards the end. Coming in Ghent has been very positive on the issue of my life. Along the road, I have met many valuable persons without who this enriching experience would have never been possible.

My stay in Ghent was a challenge in my academic life and today I could see that many things have been accomplished. First of all, I thank Prof. Roger Van Keer for inviting me to join in 2007 for 4 years the research group Numerical Analysis and Mathematical Modelling (NaM^2) for preparing a PhD in the frame of the Inverse Problems and Optimization in Low Frequency Electromagnetism (IPOLFE) project in the frame of the Interuniversity Attraction Poles (IAP) Programme Phase VI of the European Commssion and the Belgian Science Policy (BELSPO). I also would like to thank Prof. Roger Van Keer for constantly motivating and encouraging me especially in difficult times, and also for his invaluable advice during the course of my doctoral studies.

I am highly grateful to Prof. Luc Dupré and Dr. Guillaume Crevecoeur for accepting the challenge in 2008 of having a student with a purely background in mathematics within their research group in the Department of Electrical Energy, Systems and Automation (EESA) and for reorienting my research activities towards the application of uncertainties in EEG source analysis. During the last 3 years, at every stage of the research, they were constantly watching on me, giving me advices and useful guidance in order to succeed in this challenging field of inverse problems and EEG source analysis.

In addition, I would like to thank Dr. Guillaume Crevecoeur who provided timely and instructive comments and evaluation at every stage of the thesis process, allowing me to complete this project. His constant effort and determination in the numerics in order to reach the final objective has certainly led to the completion of this thesis. The patience and motivation of these three persons from the very beginning, pushed me beyond limits and with perseverance the present thesis is now a reality.

Next, I also would like to thank the members of the EELAB group with a special note to the PhD students Damien, Nele, Setareh, and in particular to

Ahmed for his willingness to help me in numerics. They provided insights that guided and challenged my thinking, and this has substantially improved the quality of the thesis.

I am also very grateful to Samuel Perez the former secretary of the Department of Mathematical Analysis for all the administrative support during my thesis. He was a good link between the administration of the university and me. His help in my earlier days in Ghent with the filling of papers related to my house and stay in Belgium was indeed very important since I could not read all the documents in Dutch. I will not forget Dr. Benny Malengier who also encouraged me at the beginning of the thesis. The discussion with the other PhD colleagues from the Department of Mathematical Analysis has also been very useful for this research.

Besides the technical and administrative assistance above, I received equally important assistance from friends in the Netherlands. I wish to thank them for their constant and continuous support since I arrived in Belgium for my studies. Being with them in the Netherlands for a weekend for a visit was very pleasant and refreshing for the moral.

The financial support for this work was partially used to support two of my sisters in their studies in the field of medicine. The first one is in Milan and the second one is in Brussel. This will have a high value in the near future.

My deep gratitude goes to my wife and children for inspiring and supporting me toward this doctoral degree. They were not physically in Ghent with me, but they are very close to me in my heart. The success of this thesis is before all, their own success.

I am grateful to God for his grace which allowed me to continue my studies in the Netherlands at a point in life where the situation was desperate, and for all the favors I have obtained in Belgium and in other countries that I visited during this PhD.

As a mathematician, I learned a lot from real life problems. I have particularly appreciated engineering skills and in particular delivering high quality results. Even at the end of the thesis, I think I still have things to learn to improve in my life as a scientist since I am at the intersection of Mathematics and Engineering.

Yitembe Bertrand
September 2011, Ghent

Contents

Samenvatting

De respons van een systeem hangt af van de waarden van de inputparameters en kan bepaald worden aan de hand van computersimulaties. Een zogenaamd voorwaarts model kan opgelost worden voor gegeven inputparameterwaarden en dient de output van het systeem zo goed als mogelijk te benaderen. Het is mogelijk om parameterwaarden te gaan identificeren door een zogenaamd invers probleem op te lossen startende van welbepaalde metingen. Deze parameteridentificatie is in die mate dat de output van het systeem de metingen zo goed mogelijk benadert. Indien dit een niet lineair invers probleem betreft dienen niet lineaire minimalisatietechnieken gebruikt te worden waarbij het voorwaartse model iteratief geëvalueerd wordt voor verschillende inputparameterwaarden.

De nauwkeurigheid van de oplossingen van inverse problemen wordt echter verkleind doordat de metingen ruis bevatten en de voorwaartse modellering onzekerheden inhoudt. Onzekerheden zijn modelparameters waarvan de waarden niet exact gekend zijn, parameters die in de tijd kunnen veranderen of die afhangen van de omgeving. Afhankelijk van de gegeven inputparameterwaarden, hebben deze onzekerheden een invloed op de voorwaartse oplossingen. Deze voorwaartse onzekerheidspropagatie geeft aanleiding tot fouten in de inverse oplossingen omdat het voorwaartse model iteratief geëvalueerd dient te worden voor de reconstructie van de inverse oplossingen. Tot nog toe werd aangenomen dat deze reconstructiefouten niet gereduceerd konden worden. Onzekerheden dienden ofwel juister gekwantificeerd te worden of moesten in de inverse oplossing aanwezig zijn door de regio in de parameterruimte aan te geven waarin de gereconstrueerde parameterwaarden liggen.

Het doel van dit doctoraal proefschrift is numerieke technieken voor het reduceren van inverse reconstructiefouten te ontwikkelingen opdat het inverse probleem opgelost wordt op een zo robuust en zo nauwkeurig mogelijk manier. Methodologieën werden specifiek ontwikkeld voor elektro-

encefalografie (EEG) bronanalyse. EEG is een niet invasieve techniek dat de elektrische potentialen ten gevolge van elektrische activiteit in de hersenen meet op de hoofdhuid. EEG heeft vele toepassingen in de biomedische ingenieurswetenschappen en is belangrijk voor het stellen van diagnosen. Zo kan EEG gebruikt worden om hersenregio's te bepalen die in extreme mate actief zijn bij epilepsiepatiënten en kan aangewend worden voordat een chirurgische operatie uitgevoerd wordt. Het EEG voorwaartse model kan de metingen gaan nabootsen voor gegeven bronparameters waarbij de Maxwell vergelijkingen in de quasi-statische benadering opgelost dienen te worden. De hoofdmodellen gebruikt tijdens het doctoraat zijn sferische hoofdmodellen met meerdere lagen. De neurale bronnen worden geparametriseerd als elektrische dipolen met welbepaalde plaats en oriëntatie. Het inverse probleem in deze thesis is goed geconditioneerd omdat we gebruik maken van een beperkt aantal elektrische dipolen die kleiner zijn dan het aantal sensoren. De plaats en oriëntatie van de elektrische dipoolbronnen worden gereconstrueerd door het EEG inverse probleem op te lossen startende van EEG data. De nauwkeurigheid van de gereconstrueerde dipoolbronnen is verminderd door de ruis in de EEG metingen en door onzekerheden in het voorwaartse model. Vooral de geleidbaarheidswaarden van hoofdhuid, schedel en hersenen zijn niet goed gekend aangezien deze moeilijk te meten zijn. Deze onzekerheden kunnen ook veranderen van persoon tot persoon, etc. Nieuwe numerieke technieken werden ontwikkeld tijdens dit doctoraat opdat de spatiale nauwkeurigheid van EEG bronanalyse verhoogd wordt door rekening te houden met de modelonzekerheden.

Opdat de nauwkeurigheid van de oplossingen van de inverse problemen zou verbeterd worden, voeren we nieuwe concepten in bij de formulering van de kostenfunctionaal en incorporeren we nieuwe technieken in het iteratief schema van de inverse reconstructie. Het doctoraal werk omvat drie belangrijke fases. In een eerste fase, hebben we robuuste methodologieën uitgewerkt voor de reductie van reconstructiefouten van één elektrische dipool met één enkele onzekerheid. Deze onzekerheid is de verhouding van de elektrische geleidbaarheid van schedel ten opzichte van de geleidbaarheid van het zachte weefsel. Deze verhouding is moeilijk te bepalen en kan van persoon tot persoon veranderen. Het voorwaartse model dat wij gebruiken is een drie sferisch hoofdmodel waarbij de potentialen, berekend via het voorwaartse model, afhangen van de geleidbaarheidsverhouding. We introduceren een nieuwe formulering van het voorwaartse model door gebruik te maken van een Taylor expansie rond de werkelijke geleidbaarheidsverhouding. Op die manier bestaat er een verband tussen de werkelijke potentialen en de potentialen met aangenomen geleidbaarheidsverhouding.

We stellen in dit doctoraal proefschrift de "Reduced Conductivity Dependence (RCD) methode" voor waarbij de traditionele kostenfunctie geherformuleerd wordt en waarbij we veranderingen invoeren ten aanzien van het iteratief schema van het inverse probleem. Meer bepaald, we nemen in iedere iteratie een interne fittingprocedure op alsook een selectie van sensoren. De fittingprocedure maakt het mogelijk om een zo nauwkeurig mogelijk voorwaarts model te hebben, terwijl de selectieprocedure ervoor zorgt dat in iedere iteratie sensoren die de hoogste sensitiviteit hebben naar de onzekere geleidbaarheidsverhouding geëlimineerd worden. Aan de hand van numerieke experimenten hebben we aangetoond dat de reconstructiefouten van de elektrische dipolen gereduceerd konden worden met behulp van de RCD methode voor zowel het geval de metingen geen ruis of ruis bevatten. We hebben een grondige studie gemaakt van de selectieprocedure van elektroden en de invloed bekeken van het gebruik van de RCD methode voor verschillende EEG elektrodeconfiguraties. Wanneer er gebruik gemaakt wordt van de traditionele reconstructiemethode heeft het aantal elektroden een kleine invloed op de gereconstrueerde dipolen terwijl we hier aantonen dat indien er gebruik gemaakt wordt van de RCD methode dat dit wel het geval is: de nauwkeurigheid wordt verhoogd indien het aantal sensoren verhoogt. Dit omwille van de selectieprocedure in de RCD methode.

In een tweede fase hebben we een RCD methode ingevoerd die toegepast kan worden voor de reconstructie van een beperkt aantal dipolen in het geval van een enkelvoudige onzekerheid. Hierbij werd het "Recursively Applied and Projected Multiple Signal Classification" (RAP-MUSIC) algoritme aangepast. Het drie sferisch hoofdmodel werd gebruikt als voorwaarts model waarbij de conductiviteitsverhouding van schedel ten opzichte van zacht weefsel als onzekerheid werd beschouwd. Aan de hand van numerieke experimenten hebben we aangetoond dat de spatiale nauwkeurigheid van elke gereconstrueerde dipool verhoogd werd en dat het gebruik van de RCD gebaseerde subspace gecorreleerde kostenfunctie tot een hoge efficiëntie leidt zelfs voor metingen met veel ruis.

Tenslotte hebben we een RCD methodologie ontworpen voor de reductie van reconstructiefouten in het geval het voorwaartse model meerdere onzekerheden bevat. We hebben een vijf sferisch hoofdmodel gebruikt waarbij de geleidbaarheidsverhouding ten aanzien van schedel, cerebrospinaal vocht, en witte materie, als onzeker beschouwd werden. We hebben zowel de kostenfunctionaal als de fitting- en selectieprocedure van de RCD methode uitgebreid. De resultaten tonen dat er reductie van reconstructiefouten optreedt in vergelijking met de traditionele methode en de RCD methode die ontworpen werd om fouten van een enkelvoudige onzekerheid te reduceren.

Summary

In computer simulations, the response of a system under study depends on the input parameters. Each of these parameters can be assigned a fixed value or a range of values within the input parameter space for system performance evaluations. Starting from values of the input parameters and a certain given model, the so-called forward problem can be solved that needs to approximate the output of the system. Starting from measurements related to the output of the system model it is possible to determine the state of the system by solving the so-called inverse problem. In the case of a non-linear inverse problem, non-linear minimization techniques need to be used where the forward model is iteratively evaluated for different input parameters.

The accuracy of the solution in the inverse problem is however decreased due to the noise available in the measurements and due to uncertainties in the system model. Uncertainties are parameters for which their values are not exactly known and/or that can vary in time and/or depend on the environment. These uncertainties have, for given input parameter values, an influence on the forward problem solution. This forward uncertainty propagation leads then to errors in the inverse solutions because the forward model is iteratively evaluated for recovering the inverse solutions. Until now, it was assumed that the recovery errors could not be reduced. The only option was to either quantify the uncertain parameter values as accurate as possible or to reflect the uncertainty in the inverse solutions, i.e. determination of the region in parameter space wherein the inverse solution is likely to be situated.

The overall aim of this thesis was to develop reduction techniques of inverse reconstruction errors so that the inverse problem is solved in a more robust and thus accurate way. Methodologies were specifically developed for electroencephalography (EEG) source analysis. EEG is a non-invasive technique that measures on the scalp of the head, the electric potentials induced by the neuronal activity. EEG has several applications in biomedical engineering and is an important diagnostic tool in clinical neurophysiology. In epilepsy, EEG

is used to map brain areas and to receive source localization information that can be used prior to surgical operation. Starting from Maxwell's equations in their quasi-static formulation and from a physical model of the head, the forward problem predicts the measurements that would be obtained for a given configuration of current sources. The used head models in this thesis are multi-layered spherical head models. The neural sources are parameterized by the location and orientation of electrical dipoles. In this thesis, a set of limited number of dipole sources is used as source model leading to a well-posed inverse problem. The inverse problem starts from measured EEG data and recovers the locations and orientations of the electrical dipole sources. A loss in accuracy of the recovered neural sources occurs because of noise in the EEG measurements and uncertainties in the forward model. Especially the conductivity values of scalp, skull and brain are not well known since these values are difficult to measure. Moreover, these uncertainties can vary from person to person, in time, etc. In this thesis, novel numerical methods are developed so to provide new approaches in the improvement of spatial accuracy in EEG source analysis, taking into account model uncertainties.

Nowadays, the localization of the electrical activity in the brain is still a current and challenging research topic due to the many difficulties arising e.g. in the process of modeling the head and dealing with the not well known conductivity values of its different tissues. Due to uncertainty in the conductivity value of the head tissues, high values of errors are introduced when solving the EEG inverse problem. In order to improve the accuracy of the solution of the inverse problem taking into account the uncertainty of the conductivity values, a new mathematical approach in the definition of the cost function is introduced and new techniques in the iterative scheme of the inverse reconstruction are proposed.

The work in this thesis concerns three important phases. In a first stage, we developed a robust methodology for the reduction of errors when reconstructing a single electrical dipole in the case of a single uncertainty. This uncertainty concerns the skull to soft tissue conductivity ratio which is an important parameter in the forward model. This conductivity ratio is difficult to quantify and depends from person to person. The forward model that we employed is a three shell spherical head model where the forward potentials depend on the conductivity ratio. We reformulated the solution of the forward problem by using a Taylor expansion around an actual value of the conductivity ratio which led to a linear model of the solution for the simulated potentials. The introduction of this expanded forward model, led to a sensitivity analysis which provided relevant information for the reconstruction of the sources in EEG source analysis. In order to develop

a technique for reducing the errors in inverse solutions, some challenging mathematical questions and computational problems needed to be tackled.

We proposed in this thesis the Reduced Conductivity Dependence (RCD) method where we reformulate the traditional cost function and where we incorporated some changes with respect to the iterative scheme. More specifically, in each iteration we include an internal fitting procedure and we propose selection of sensors. The fitting procedure makes it possible to have an as accurate as possible forward model while the selection procedure eliminates the sensors which have the highest sensitivity to the uncertain skull to brain conductivity ratio. Using numerical experiments we showed that errors in reconstructed electrical dipoles are reduced using the RCD methodology in the case of no noise in measurements and in the case of noise in measurements. Moreover, the procedure for the selection of electrodes was thoroughly investigated as well as the influence of the use of different EEG caps (with different number of electrodes). When using traditional reconstruction methods, the number of electrodes has not a high influence on the spatial accuracy of the reconstructed single electrical dipole. However, we showed that when using the RCD methodology the spatial accuracy can be even more increased. This because of the selection procedure that is included within the RCD methodology.

In a second stage, we proposed a RCD method that can be applied for the reconstruction of a limited number of dipoles in the case of a single uncertainty. The same ideas were applied onto the Recursively Applied and Projected Multiple Signal Classification (RAP-MUSIC) algorithm. The three shell spherical head model was employed with the skull to brain conductivity ratio as single uncertainty. We showed using numerical experiments that the spatial accuracy of each reconstructed dipole is increased, i.e. reduction of the conductivity dependence of the inverse solutions. Moreover, we illustrated that the use of the RCD-based subspace correlation cost function leads to a high efficiency even for high noise levels.

Finally, in a third stage, we developed a RCD methodology for the reduction of errors in the case of multiple uncertainties. We used a five shell spherical head model where conductivity ratios with respect to skull, cerebrospinal fluid, and white matter were uncertain. The cost function as well as the fitting and selection procedure of the RCD method were extended. The numerical experiments showed reductions in the reconstructed electrical dipoles in comparison with the traditional methodology and also compared to the RCD methodology developed for dealing with a single uncertainty.

List of Abbreviations

2D	Two dimensional
3D	Three dimensional
EEG	Electroencephalography
IEEG	Intracranial Electroencephalography
MEG	Magnetoencephalography
ECG	Electrocardiography
PET	Positron Emission Tomography
EIT	Electrical Impedance Tomography
CT	Computed Tomography
CPI	Cortical Potential Imaging
fMRI	Functional Magnetic Resonance Imaging
ICM	Information Criterion method
MRI	Magnetic Resonance Imaging
DT-MRI	Diffusion Tensor Magnetic Resonance Imaging
ICA	Independent Component Analysis
PCA	Principal Component Analysis
ECD	Equivalent Current Dipoles
RDM	Relative Difference Measure
DPE	Dipole Position Error
RRE	Relative Residual Energy
RCD	Reduced Conductivity Dependence
SNR	Signal to Noise Ratio
SVD	Singular Value Decomposition
FDM	Finite Difference Method
FVM	Finite Volume Method
FEM	Finite Element Method
BEM	Boundary Element Method
iFDM	Finite Difference method in isotropic media
aFDM	Finite Difference Method in Anisotropic Media
CSF	Cerebro-Spinal Fluid

List of Symbols

Scalars, Vectors, Volumes and matrices

x_i	i-th element of vector $\mathbf{x}$
X_{ij}	ij-th element of matrix $\mathbf{X}$
$\mathbf{X}^T$	Transpose of Matrix $\mathbf{X}$
$\mathbf{X}^{-1}$	Inverse of Matrix $\mathbf{X}$
$\mathbf{X}^{\dagger}$	Moore-Penrose Pseudo-Inverse of matrix $\mathbf{X}$

Mathematical symbols

L_2	By definition, $\mathrm{f} \in \mathrm{L}_2(\Omega)$ if $\left(\int_\Omega \lvert\mathrm{f}\rvert^2 \mathrm{dx} \right)^{1/2} < \infty$
L_∞	Infinity Norm: $\lVert f \rVert_\infty = \mathrm{Inf}\{C \geq 0 : \lvert f(x) \rvert \leq C \quad \text{for almost every x}\}$
$\cdot$	Dot product
$\times$	Cross product
∇	Gradient
$\nabla\cdot$	Divergence
$\nabla\times$	Curl
$\delta(\mathbf{r})$	Spatial Dirac distribution
$\delta_{a,b}$	Kronecker delta: $\delta_{a,b} = 1$ if $a = b$, otherwise $\delta_{a,b} = 0$
$\mathbf{I}_n$	n-dimensional identity matrix
Ω	Volume conductor
$\partial\Omega$	Boundary of the volume conductor
P_n	Legendre polynomial of n^{th} Order
P_n^m	Associated Legendre polynomial of n^{th} order and m^{th} degree
$\mathbf{n}$	Unit normal vector on boundary
$\mathbf{e}_x$	Unit vector along the x-axis
$\mathbf{e}_y$	Unit vector along the y-axis
$\lVert \cdot \rVert$	L_2-norm or the Euclidean norm
ϕ	Test function in the variational formulation

Symbols

$\mathbf{r}_d$	Dipole location with components $[r_x, r_y, r_z]$
$\mathbf{d}$	Dipole orientation with components $[d_x, d_y, d_z]$
$\mathbf{L}$	Lead field matrix
p	Number of electrical dipoles
N	Number of electrodes
N_s	Selected number of electrodes in RCD method
$\mathbf{d}_{\text{opt}}$	Optimal orientation in the least-squares sense
$\widetilde{\mathbf{X}}$	Actual conductivity ratio
$\widehat{\mathbf{X}}$	Assumed conductivity ratio
$\widetilde{\mathbf{r}_d}$	Actual dipole location
$\mathbf{r}_d^*$	Reconstructed dipole position using $\widehat{\mathbf{X}}$
$\mathbf{V}_m$	Simulated EEG data vector or matrix
$\mathbf{V}_{\text{meas}}$	Measured EEG data vector or matrix
V_{RMS}	Root mean square value of the electrical potential $\mathbf{V}$
nl	Noise level
Σ	Standard deviation
ϵ	Stopping criteria used for algorithms of traditional and RCD method
k	Iteration number
γ	Threshold for the derivatives in the selection procedure of the RCD method
α	Taylor coefficient
Φ_S	Signal subspace
Φ_N	Noise subspace
$\mathbf{E}$	Electric field
$\mathbf{H}$	Magnetic field
$\mathbf{D}$	Electric induction
$\mathbf{B}$	Magnetic induction
$\mathbf{J}$	Current density
$\mathbf{J}_p$	Primary current density
ρ	Charge density
ε_0	Permittivity of vacuüm
μ_0	Permeability of vacuüm
$\sigma(x,y,z)$	Conductivity of the medium

List of Publications

Articles in international SCI journals

1. B.R. Yitembe, G. Crevecoeur, L. Dupré, and R. Van Keer, "EEG inverse problem solution using a selection procedure on a high number of electrodes with minimal influence of conductivity," *IEEE Transactions on Magnetics*, may 2011, vol. 47, no 5, pp. 874-877

2. B.R. Yitembe, G. Crevecoeur, L. Dupré, and R. Van Keer, "Reduced Conductivity Dependence Method for increase of dipole localization accuracy in the EEG inverse problem," *IEEE Transcations on Biomedical Engineering*, may 2011, vol. 58, issue 5, pp. 1430-1440

Articles in conference proceedings

1. B.R. Yitembe, G. Crevecoeur, L. Dupré, and R. Van Keer, "EEG inverse problem solution with minimal influence of the conductivity, " *Proceedings of Computation of electromagnetic fields (Compumag 2009)*, in Florianopolis Brazil, CD-rom , from the 22nd to the 26th of November, 2009.

2. B.R. Yitembe, G. Crevecoeur, L. Dupré, and R. Van Keer, "EEG inverse problem solution using a selection procedure on a high number of electrodes with minimal influence of conductivity," *Proceedings 14th Biennial IEEE Conference on Electromagnetic Field Computation (CEFC 2010)*, in Chicago USA CD-rom, from the 9th-12th may, 2010.

Reduction of Conductivity Uncertainty Propagations in the Inverse Problem of EEG Source Analysis

CHAPTER 1

General Introduction

1.1. Situation

Since the beginning of the previous century, the human brain has always been an object of curiosity and study. The ability to monitor the activity of the human brain is of great importance to clinicians, medical doctors and to many researchers. Although a significant amount of knowledge has been collected, there are still more questions than answers. In order to deepen the knowledge of this research domain in medicine, many tools have been developed and are constantly under improvement for a better understanding of human brain activity.

Among the existing resources available such as functional magnetic resonance imaging, positron emission tomography, etc., electroencephalography (EEG) has become one of the main tools for the diagnosis and follow-up of epilepsy. Epilepsy is a highly prevalent neurological disease affecting 1% of the general population and is characterized by recurrent seizures that result from abnormal electrical discharges in the outer layers of the brain (i.e. brain cortex). About thirty percent of the patients suffer from uncontrolled seizures despite adequate treatment with anti-epileptic drugs (i.e. refractory epilepsy). For a substantial part of these patients, brain surgery is the treatment of choice to cure epilepsy. This requires localization of the brain region that is responsible for the seizures (i.e. the epileptogenic zone). To identify the epileptogenic zone, patients are included in a so-called presurgical evaluation protocol comprising several anatomic and functional investigations such as MRI and EEG. Indeed, the determination of the origin of specific EEG waveforms helps neurologists to pinpoint the origin of the epilepsy and to evaluate the patient for resective surgery. Especially for patients suffering from refractory epilepsy i.e epilepsy that cannot be treated with medication, the accurate specification of

the origin of seizure activity can be of a significant aid [1]. In many cases, the EEG of epileptic patients contains significant epileptic properties, both during the seizure (ictal EEG), and between succesive seizures ("spikes"-interictal EEG). The invasive EEG-registration can be considered as the "golden standard" for the localization of the epileptogenic zone [2]. The origin of these seizures and spikes can be determined by means of EEG source analysis.

More accurate localization of the epileptogenic zone should result in more patients being candidates for epilepsy surgery and in the end more refractory epilepsy patients being rendered seizure free with less sequelae caused by the brain surgery. Besides the huge impact of uncontrolled seizures on the patient's personal life and socio-economical conditions, psychosocial dysfunctioning and significant cognitive impairment, refractory epilepsy is associated with high direct and indirect costs for society [3]. As pointed out in [4], successful epilepsy surgery has a positive cost-benefit ratio for patients with previously uncontrolled seizures in terms of limiting hospital admissions and use of health care resources.
However, when coupling the non-invasive EEG measurements to a numerical method, inaccuracies in the neural source localization are introduced. The accuracy of EEG source analysis is mainly determined by the noise in the measurement and the accuracy of the head model.

It is known that, a simplified source modeling of the brain activity introduces an error. The head model on the other hand has a large impact on the accuracy of the solution of the EEG inverse problem where important errors are introduced by the uncertainties of the values of the electrical conductivity of the brain and the skull. As reported in [5, 6], the quantitative values of the electrical conductivity of the brain and the skull remain a very important parameter that attract a lot of debates in EEG source analysis. A great deal of research is still focused in this direction, coupled to efficient numerical methods for the reconstruction of the source in EEG source analysis which is of high importance for the treatment of patients in functional brain imaging. It becomes clear that qualitative and quantitative research methodologies are necessary in this domain, where many challenges and difficulties in the EEG source analysis still need to be solved.

The development of digital computers, together with the advances of signal processing methods contributed to transform EEG data analysis into a domain of research for engineers, physicists and mathematicians. However the functional localization of brain activity with a better accuracy is still a major challenge of EEG data analysis. To reach this goal, various computational and mathematical challenges need to be tackled, turning the study of the brain activities with EEG in a strongly multidisciplinary field of research at the

crossroads of neurophysiology, signal processing, electromagnetism, multivariate statistics, and scientific computing. EEG can benefit from advances in many disciplines, including signal analysis and mathematical modeling. Nowadays, the interpretations of EEG signals are done using numerical models. The acquisition of EEG signals from a human being is used for investigation of many clinical problems. As a consequence, developing and understanding advanced signal processing techniques for the analysis of EEG signals is crucial in the area of biomedical research. One of the major advantages of EEG source reconstruction over other brain imaging techniques such as positron emission tomography (PET) or functional magnetic resonance imaging (fMRI) is its high temporal resolution. The spatial resolution of these modalities are lower than for the EEG modality. EEG has a spatial resolution of about 8mm-15mm while magnetoencephalography (MEG) has a spatial resolution of 4-8mm. The function MRI, PET and Single Photon Emision Computed Tomography (SPECT) have a respectively a spatial resolution of 1.5-5mm, 5-7mm, and 8-10mm [7].

However, these numerical models contain uncertainties. In EEG, this mainly includes the head model used and the real conductivity values. In reality due to irregular behavior of the human head that varies from patient to patient, several approximations of the head are often used in computer simulations for interpreting the EEG signals. Different types of head models in combination with different types of conductivity models of the tissues can be used to predict the electrical activity in the brain based on mathematical models. These mathematical models need to be very accurate since, the solution of the forward problem is one of the input in the resolution of the inverse problem.
As often reported by many studies, one of the major factors that influences the accuracy of EEG source localization is the large uncertainty in the conductivity of most of the head tissues. It is reported in [8] that the spatial resolution is affected by blurring caused by volume conductor effects. For low conductivity values, the resolution is indeed not good and usually in that case, highest values of error are reported when solving the inverse problem. High spatial resolution is needed in presurgical evaluation, because a surgical procedure may follow. This dissertation mainly deals with the problem regarding error propagations in EEG inverse problems due to the uncertain conductivity values of head tissues.

1.2. Uncertainties

In general, uncertainties are parameters that are difficult to determine or to measure and for which the values are not reliable. Moreover, the parameter

values can change in time or can depend on the environment, etc. In scientific research, one is often confronted to uncertainty in the design of models. Uncertainty may result, e.g., from human mistakes and errors in the manufacture, from the use and maintenance of constructions, from expert evaluations, and from a lack of information. Small samples, changing reproduction conditions, and imprecise results of measurements are usual starting points for defining structural models and parameters [9]. These facts show that many engineering fields are significantly characterized by uncertainty. Uncertainty may also result from an incomplete knowledge, or a bad modeling, or imperfect theory in the physical domain or imprecise data. The description of systems typically involves the use of variables that describe measured or predicted quantities of the systems. Numerical methods are constantly under development in order to minimize the resulting propagation effects of uncertainty in the outputs.

1.2.1 Uncertainties in engineering

In many engineering fields, it is common to deal with a number of physical, biological, chemical, and other parameters whose uncertainties need to be addressed in order to solve the underlying mathematical equations. It is well known that uncertainty characterizes the accuracy of results obtained by measurement of physical quantities. It is common in biomedical engineering, to face uncertainties in clinical trials. Some rigorous scientific investigation is usually needed for the determination of parameters presenting a large variability and imprecision. In EEG source analysis, uncertainty of the head tissues conductivity value and inaccuracy in the head geometry are a specific set of parameters affecting the reconstruction of the source when solving the inverse problem. Uncertainties are also met in non-destructive evaluations like eddy current techniques. In general, uncertainty remains a challenge from a theoretical, physical and computational point of view. It is obvious that if the inputs of a given system contain one or several uncertainties, the output will reflect this situation both from a qualitative and quantitative perspective.

When incorporating uncertainty in the inputs, stochastic systems or random systems may be built in order to provide a better prediction and analysis of the outputs. The prediction of reliable or efficient outputs may use statistical and probability analysis. In electrical engineering, e.g. robust optimization procedures are needed in order to reduce the propagation of uncertainties in the design. There is a crucial need for appropriate methods for modeling and managing uncertainty for a better design of the product.

1.2.2 Uncertainties in EEG source analysis

For the presurgical evaluation of patients suffering from refractory epilepsy it is essential to have a correct localization of the epileptogenic zone, i.e. the brain region that is responsible for provoking seizures. Several modalities can be included in this clinical protocol: electroencephalogram (EEG), magnetoencephalogram (MEG), magnetic resonance imaging (MRI), Positron Emission Tomography (PET), neuropsychological assessments, etc. Especially the EEG is useful because of its high temporal resolution and by performing EEG source analysis, the epileptogenic zone can be estimated. The estimation of the neural source generators responsible for e.g. epileptic spikes is however subject to some sources of errors: noise in measurements and forward modeling errors.
A first class of model related errors are source modeling errors. A current dipole source is suitable because it represents an active pyramidal cell at the microscopic level ([10]) but is only valid if the activity itself is limited to a focal region and if it stays focal over a period of time. For patients suffering from epilepsy, focal brain activity is mostly the case. In order to reduce these source modeling errors, it is possible to use more complex source models. Distributed source models can represent an alternative where the inverse problem is highly underdetermined and regularization methods are required [11]. Another source modelling approach consists of limiting the parameters of the multidipolar sources to be less than the number of electrodes, e.g. the RAP-MUSIC algorithm [12]. The information criterion method is a possible means for determining the number of independent sources, as used in [13, 14]. A second class of model related errors is the inaccurate geometrical modeling of the head [15]. Since we can use patient-specific head models based on T1 segmented magnetic resonance images, it is possible to have an as accurate as possible geometrical modeling. A third type of forward modeling errors can be electrode misplacements [16]. However, by using correct EEG electrode placement techniques, it is possible to decrease that source of error [17], or by using more electrodes in the EEG source analysis problem [18]. In [16] one evaluated the influence of the electrode misplacement and concluded that the use of an incorrect skull conductivity leads to the most serious source of error.

A fourth type of modeling related errors is not to incorporate the anisotropic behavior of the conductivity. Using diffusion tensor magnetic resonance imaging (DT-MRI) it is possible to estimate the nerve bundle direction. In [19–21], the authors have shown that anisotropically conducting compartments should be incorporated in the volume conductor head models. Finally, large errors are introduced due to the use of inaccurate absolute conductivity values of several tissues in the volume conductor head model. The

large sensitivity of the EEG measurements to tissue conductivity have been reported e.g. in [22–25]. The uncertain conductivity values, more specifically the ratio of the skull conductivity to the conductivity values of the soft tissues have a large influence on the EEG dipole localization accuracy and are the most dominant source of error [16, 26–28]. Many values have already been suggested in literature for the scalp, skull, cerebrospinal fluid and brain: in [29], it is stated that the soft tissue to skull conductivity ratio was 80. In [30] it is 15, in [31] it is between 20-50, while in [32], the measured value lies in the interval 10-40 and in [33], it is 25. Moreover, the conductivity values may be patient and age dependent as pointed out in [34].

A probabilistic framework for incorporating the uncertain conductivity values in the reconstruction of neural sources is proposed in [27]. The authors concluded that the conductivity of the skull has to be either accurately measured by an independent technique, or that the uncertainties in the conductivity values should be reflected in the source localization estimates. In this dissertation, an alternative solution is proposed: a novel technique for limiting the propagation of the uncertain conductivity values towards the dipole source localization estimates.

1.3. Aims and objective

Although conventional EEG offers excellent temporal resolution in resolving rapidly changing patterns of brain electric activities, its spatial resolution is limited by the smoothing effect of the head volume conductor, especially due to the very low conductivity skull layer [35]. As a consequence, there is a need for the development of numerical techniques which can effectively and efficiently handle the issue of uncertainty of the brain-skull conductivity ratio for the inverse problem.

In this thesis, we present a novel numerical scheme, called Reduced Conductivity Dependence (RCD) method, that reduces the EEG source localization errors due to the use of a wrong conductivity value.

The purpose of our research is to make good use of sensitivity analysis in order to extract the best information needed to improve the reconstruction of neural sources when using spherical head models. An investigation on the influence of the material parameter on the reconstruction of the source in several regions of the brain when using the traditional method will be carried out and then we will develop a numerical method that will minimize the effect of the conductivity ratio and provide more accurate solutions of the EEG inverse problem. Such approach does not introduce new

modeling parameters but uses the best strategy in the existing ones to improve the accuracy of the inverse solutions.

1.4. Outline of the thesis

In the next chapter (**Chapter 2**) an introduction to electroencephalography (EEG) is given. Some EEG basics are presented. This is followed by an overview of the EEG forward problem. Here the physics of EEG are described mathematically. Understanding how a current generator located inside the head can produce a potential distribution on the scalp is called the forward problem.

Due to the low frequency of the signals measured with EEG, and the low electrical conductivity and magnetic permeability of the considered tissues, the electromagnetic phenomena can be described in a quasi-static way. In particular, the time derivatives in the Maxwell's equations can be neglected. In this approximation, the forward modeling implies that the signal measured on the sensors is the instantaneous sum of the signals produced by each current generator. Solutions for different head shape approximations are presented and an algebraic formulation of the forward problem is shown, introducing the so-called lead field matrix. The EEG forward model is a very important part for solving the inverse problem. Since brain functional imaging with EEG requires an efficient and accurate forward model, we review in this chapter the existing methods to solve the forward problem with different assumptions made on the human head model, and the conductivity model. The discussion so far on the forward model indicates the complexity and its importance in EEG source analysis. A sensitivity analysis using a large set of conductivity ratios for a three-shell spherical head model is presented at the end of the chapter.

Chapter 3 describes the main theory of inverse problems. Recovering electrical activity of the brain from EEG measurements at the surface of the head, is known as the EEG inverse problem. The inverse problem aims at estimating the positions and amplitudes of the sources responsible for the measurements of the electrical potentials at the surface of the head. In real EEG cases, these measurements often contain noise. Several approaches in solving EEG inverse problems exist: parametric methods also referred as dipole fitting, scanning techniques and image based methods with distributed source models. This chapter covers the methodological aspects of the multiple inverse solvers. It presents for each of them, the assumptions made and the eventual limitations when used with EEG data. These different formulations of the inverse problem take into account modeling assumptions of the head

and the conductivity specification. However, the EEG inverse problem is strongly ill-posed. The solution of such problem classically requires to impose constraints or priors on the solution. The optimization strategies employed are also presented. Mathematical formulation of the EEG inverse problem for a single dipole is presented in detail and computations are carried out for a three-shell spherical head model. The research carried out in this thesis does not include distributed source models.

Chapter 4 presents the RCD methodology. This numerical method is developed in response to the problem of spatial accuracy in EEG source analysis due to the uncertainty of the conductivity values. The method developed here, is based on the information provided by sensitivity analysis. A redefinition of the cost function including the sensitivity to the conductivity of the potentials is presented. Monte Carlo simulations are done with a first application to a single dipole and for a three shell spherical head model. The new cost function minimizes the influence of the conductivity on EEG inverse problems. Extensions of the new method are presented for multiple electrode configurations with improvement of the accuracy by a scale factor of 2 or 3. Good results are achieved in the case of noise in the measurements.

Chapter 5 presents a combined RCD and RAP-MUSIC methodology for the reconstruction of multiple dipoles. Here we assume a limited number of sources to model the electrical activity in the brain, and the selection strategy developed in the case of a single dipole is extended to multiple dipoles. The same assumptions of the RCD method are included in the RAP MUSIC algorithm. Then, Monte Carlo simulations are performed on the same spherical head model using three and five dipoles in the brain. Results of the simulations show that the theoretical work in chapter 4 on the useful information provided by sensitivity analysis, can be extended to multiple dipoles. The combination of RCD and RAP MUSIC shows that the new method is noise robust in the case of multiple dipoles when using a three shell spherical head model.

In **Chapter 6**, The last contribution of this thesis addresses a particularly challenging problem in EEG data processing: the multiple uncertainty of conductivity values when using spherical head models with multiple layers. A methodology is developed for reducing the reconstruction error of a single dipole in the case of multiple uncertainties.

Chapter 7 is the conclusion of the work. This chapter summarizes the main results and gives a more clear overview of the work carried out during the doctoral thesis. Finally there are some notes regarding further work where

future lines of research are suggested in order to extend the work done in this thesis.

Appendix A gives the formulas for computing the coordinates of the sensors positions for EEG source analysis.

In **Appendix B**, more details are provided on the computations of the potential first and second order derivatives towards the uncertainties used in the thesis. Two approaches are presented: the classical derivation and an alternative approach which is often used in the presented simulations.

Although the developed numerical techniques were evaluated throughout the main text of the thesis considering the spherical head models, the applicability of the RCD methodology towards realistic head models is shown in **Appendix C**.

CHAPTER 2

EEG Forward Problem

2.1. Introduction

Electroencephalography (EEG) is the recording along the scalp of the electrical activity arising from the neurons within the brain. The resulting signals of the electric activity of the brain over a short period of time, are recorded by a set of electrodes placed at the surface of the head [36]. The results of the measurements may be used to detect abnormalities related to electrical activity of the brain. During the recent years, an increasing use of EEG is observed as one of the main tools in the diagnosis of neurological disorders like epilepsy and in the research of brain functionality.

One of the major advantages of EEG source localization over other brain imaging techniques such as positron emission tomography (PET) or functional magnetic resonance imaging (fMRI) is its high temporal resolution. The spatial accuracy of EEG source analysis however is relatively small. Through the years, advances have been made in increasing the accuracy by using realistic geometrical modeling of the head and by incorporating anisotropic behavior of electrical conductivity. Two other sources of errors in EEG source analysis are more difficult to incorporate in the modeling: noise in the measurements and the uncertainties present in the head model.

EEG can be compared to other methods like invasive EEG (IEEG), depth electrodes technique and magnetoencephalography (MEG). At the opposite of EEG, the recordings in IEEG are made with electrodes that have been surgical implanted on the surface or within the depth of the brain. Such approach is highly accurate since the unknown skull conductivity does not have to be incorporated in the model. An obvious advantage of depth electrode recordings compared to scalp EEG is its low signal-to-noise ratio [37]. For

epileptic cases, the depth electrodes technique may be considered as the golden standard method for the identification of the epileptogenic zones [38]. This technique for which a numerical method is not needed, is also very accurate. But this procedure is surgically difficult and present some risks for the patients.

MEG which is also a non-invasive method used for localization of current sources in the brain, may be more accurate than EEG because the electrical conductivity does not influence so much the MEG source analysis results except for neural sources located near the boundary of adjacent tissues with different conductivities (e.g see, [39, 40]).

The EEG forward model mathematically expresses the relationship between a current dipole inside the volume conductor and the corresponding potentials at the surface of the head. Mathematical equations describing the EEG forward problem are based on the quasi-static approximation of Maxwell's equations from which a Poisson equation is derived. A Neumann boundary condition is coupled to this Poisson's equation.

The EEG forward problem as described in figure 2.1, requires as inputs: a head model (different geometries are available), the electrode positions on the head, a source and head material characteristics. The resulting output is an electrical field. The use of different electrode configurations is possible in the EEG forward problem, coupled to the fact that the conductivity of the head can be considered as isotropic (i.e. the conductivity is equal in all the directions) or anisotropic (i.e. the conductivity can differ depending on the direction on which the current flows).

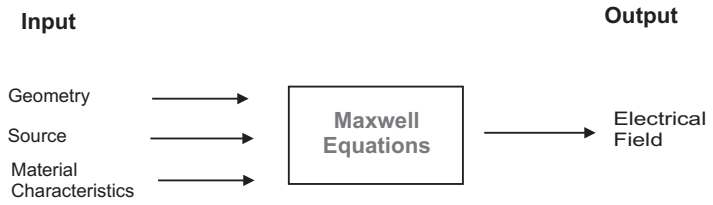

Figure 2.1: EEG forward problem simulation.

2.1.1 Source model

The two general approaches to EEG source estimation are equivalent dipole localization (parametric methods) and distributed source imaging [41]. The parametric methods typically assume that the sources can be represented by a few equivalent current dipoles (ECD) of unknown location $\mathbf{r}_d$ and moment or orientation $\mathbf{d}$ [42]. The assumption underlying this approach is that the potentials measured at the surface of the head, are produced by a small number of active regions in the brain. In the ECD source localization, it is assumed that dipoles are located somewhere in the brain and a fixed number of sources are used. The number of equivalent current dipoles (ECD), denoted by p, is fixed and each dipole i has a position $\mathbf{r}_{d,i} = [x_i, y_i, z_i]^{\mathrm{T}}$ and a moment $\mathbf{d}_i = [d_{xi}, d_{yi}, d_{zi}]^{\mathrm{T}}$. The dipole source model assumes that the number of dipoles p in the brain is smaller than the number of measurements (or sensors) N. One single current dipole is a widely used source model in EEG source analysis. Although this method gives a good estimate when the number of active areas is small, it is difficult to determine the appropriate number of dipole sources for complicated spatio-temporal activity.

The second approach models brain activity by a large number of sources that represent a continuous distribution of neural current generators .The distributed source imaging assumes distributed currents in the brain volume. Since the locations are fixed, only the orientation and amplitudes have to be determined, reducing the inverse problem to a linear one with strong similarities to those encountered in image reconstruction. The EEG inverse problem with distributed source models is strongly ill posed since the number of sensors N is less than the number of sources p e.g. the number of unknowns is much bigger than the number of equations. The problem is severely underdetermined, and regularization methods are required to restrict the range of allowable solutions. The ill-posedness of the inverse problem is most often tackled using regularization techniques, known from image restoration and reconstruction (e.g. see [41, 43] for extensive review).
The main difference between the two methods is whether a fixed number of dipoles is assumed a priori or not. Another important issue in EEG source imaging concerns the selection of the solution space within which the sources are allowed to be found. In most of the simple spherical head models, the whole volume within a certain radius of the sphere (excluding the space between the scalp and the brain) is accepted as solution space.

There exist also statistical techniques for estimating the number of dipoles in EEG data like the Information Criterion method (ICM) mentioned in [13, 14], which is a noninvasive method to determine the number of independent sources in the spatio-temporal model. It's also possible to determine the

number of sources through an analysis of the singular value decomposition (SVD) of the correlated matrix. In this phd thesis, the electrical sources to be reconstructed will be modeled as equivalent current dipoles with a focus on the improvement of the source estimations.

2.1.2 Conductivity model

The reliability of the EEG source analysis depends on the head geometry and accurate estimation of the conductivity. It is known that the conductivity plays a crucial parameter in EEG dipole analysis. Since the introduction of the equivalent current dipole inside a set of concentric spheres as a tool for performing EEG source localization, several attempts have been made to determine the electrical conductivity of the human skull. This has resulted in a large number of papers and a corresponding large number of different values for the conductivity [44]. Several approaches are used today by scientists to determine the conductivity with a certain accuracy. One of the main difficulties encountered in this process, is that the skull conductivity value varies highly among subjects. For a given patient or individual, the conductivity of a specific tissue, for example the skull, may be different from the average values listed in the literature. Moreover, it may vary as a function of position. For the purpose of better source estimation, it is essential to be able to estimate in vivo conductivities of head tissues. While the quantitative values of the electrical conductivity of the brain and the skull remain a very important parameter that attract a lot of debates in the EEG source analysis society, EEG source localization still suffers from a lack of its accuracy.

Many values have already been suggested in literature for the scalp, skull, cerebrospinal fluid and brain. In [5], it is stated that the soft to skull conductivity ratio was 80, 15 in [30], while in [32] the measured value is in the interval 10-40, and 20-50 in [31]. In [33] its measured value is 25. As noticed, there are considerable differences in the results. Moreover, the conductivity values may be patient and age dependent [34]. The large sensitivity of the EEG measurements to tissue conductivity have been reported e.g. in [22–25] and their influence on the EEG dipole source localization in realistic head models [27].
As found in the literature, many approaches are used for conductivity estimation. The methods can be classified into two broad categories as magnetic resonance imaging (MRI) and bioelectromagnetic excitation and measurement methods. MRI systems can be used to obtain conductivity tensors by using diffusion tensor imaging sequences [45] where its absolute value remains uncertain , see also [20]. In [46], it is stated that inclusion of tissue anisotropy information might improve source estimation procedures.

Electrical Impedance Tomography (EIT) consists in a current injection on the scalp through selected EEG electrodes, and conductivity values are then inferred from potential measurements at the remaining electrodes [47–49]. One drawback of EIT arises from the insulating effect of the skull, which forces most of the injected current to flow into the scalp, and so lowers the significance of EEG measurements [50]. In [51, 52], it is reported that the EIT method has less resolution compared to other anatomical imaging modalities, such as MRI.
It is possible to reference conductivities that have been measured in vivo on test subjects, or one can wish to estimate the conductivity for each subject using Electrical Impedance Tomography [53]. New methods to defined the conductivity with high accuracy are under development and are subject to improvement.

The in vivo conductivity values would be needed for obtaining the forward and inverse problem solution in EEG, but unfortunately they are at this time not measurable in living patients without surgery, and they must therefore be obtained from the wide range of values reported in the literature. Additionally, the conductivity is known to be anisotropic (in particular in white matter structures). Several studies have been carried out to quantify the influence of the inclusion of anisotropic conductivity on EEG source reconstruction [54,55]. Here, conductivity values of any model influence the lead fields of the forward problems and the solutions of the inverse problems.

2.2. Head model

2.2.1 Description of spherical head models

Methods for solving the forward problem in EEG, often require a volume head model. Until now, several approaches have been used to tackle this problem. Two types of models are mostly used to describe the human head: the concentric spherical head models, and the realistic head models. Other models include eccentric spheres.

From a geometric point of view, spherical head models are often used in analyzing EEG to approximate a real head, although they are only a local approximation. A first step towards head modeling is to consider the head as a set of nested concentric spheres. Each volume enclosed between two spheres is supposed to represent a different tissue with a constant isotropic conductivity.

Figure 2.2 is a fitting of a three-shell spherical head model into a real human head anatomy. This approximation of the human head by a three-shell spherical head model is widely used in research. It consists of the union of three concentric and symmetric regions R_i (i = brain, skull and scalp respectively) surrounded by air. Surfaces S_i denote the boundaries separating these regions from each other. The quantities: σ_{brain}, σ_{skull} and σ_{scalp} represent the conductivity values of each region, and $R_1 = R_{\text{brain}}$, $R_2 = R_{\text{skull}}$ and $R_3 = R_{\text{scalp}}$ the respective radii with the following numerical values: 8.0 cm, 8.6 cm and 9.2 cm. Spherical models allow fast computations of the potentials at the surface of the head.

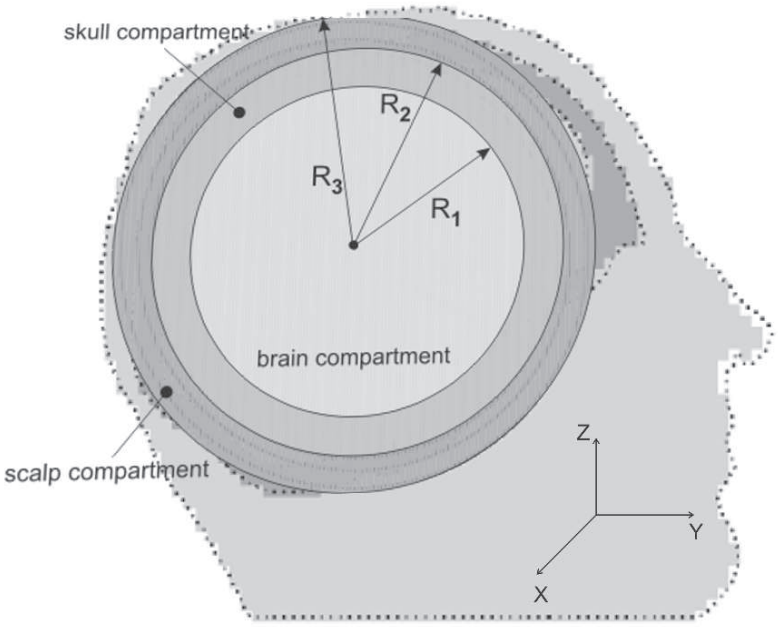

Figure 2.2: Fitting the spherical head model into a real head. The spherical head model consists of three layers: the scalp, the skull and the brain from [56].

In the head model, the electrical properties of the various tissues involved, namely the brain, the skull and the scalp, are assumed to be purely resistive due to the static approximation of the Maxwell's equations. The three or multiple (>3) shell spherical head model are widely used for solving the EEG forward and inverse problem. In practice, the head shape is clearly not spherical and can be approximated by using a more realistic head shape.

2.2.2 Realistic head models

Nowadays, realistically shaped head models are used: they can be developed from computed tomographic scans, Magnetic Resonance Imaging (MRI), radiographs, and physical measurements to approximate very closely the shape of an actual head. The realistic head geometry can be obtained from MRI data, where the volume was segmented and each tissue was labeled in the underlying voxels. This voxel structure can directly be used when considering a finite difference method for solving the Maxwell's equations. When using a finite element method, a space discretization based on tetrahedrons can be considered. The segmented head volume is then divided in tetrahedrons via a mesh generator that preserves the material classification when mapping the voxels to elements.
While fast analytic expressions exist for the potentials in spherical models, these solutions cannot be applied to realistic head models. Rather, a complete forward numerical solution must be computed in order to determine the electrode potentials due to each source. At the opposite of the previous model, many people tend nowadays to use realistic head models which are more accurate from a geometrical point of view for the evaluations of the potential distribution. It should be noted that the complexity of the corresponding potential calculations increases with the accuracy of the head description.

2.3. Electrode placement in EEG

2.3.1 Earlier stage of the number of electrodes in EEG

In order to measure the electric potentials generated by neuronal activity an EEG device consists of a set of electrodes that are positioned on the scalp so to establish electrical contact with the skin. During the first International EEG congress, held in London in 1947, it was recognized that a standard method of placement of electrodes used in electroencephalography (EEG) was needed. Possible methods to standardize electrode placement were studied by H.H. Jasper, which resulted in the definition of the 10-20 electrode system [57]. Since then, the 10-20 electrode system has become the de facto standard for clinical EEG. This system describes physical placement and designations of electrodes on the scalp. The head is divided into proportional distances from prominent skull landmarks (nasion, preauricular points, inion) to provide adequate coverage of all regions of the brain. This method was developed to ensure standardized reproducibility so that a subject's study could be compared over time and subjects could be compared to each other. This system is based on the relationship between the location of an electrode and

the underlying area of the cerebral cortex.

In 1985 an increase of the number of electrodes from 21 up to 74 was proposed [58]. This extended 10-20 system of electrode placement, also known as the 10% system was jointly accepted as the standard by the American Electroencephalographic Society and the International Federation of Societies for Electroencephalography and Clinical Neurophysiology [59] and [60]. First developed during the early twentieth century, the EEG electrode hardware continues to be improved. It is thought that this hardware will lead to a wide range of important discoveries both in basic brain function and cures for various neurological diseases.

2.3.2 Standard configuration of electrodes

Since 1958, the international 10-20 system has become the standard for clinical as well as non-clinical EEG [61]. On figure 2.3 the 10-20 system is shown on a simplified 2D head from above (see the right part of the figure). Electrodes are often held in fixed positions by an elastic cap. Each electrode carries a unique labeling, usually by a combination of letters and numbers as described in figure 2.3. The letters refer to a nearby lobe or fissure. Odd (even) numbers refer to the left (right) hemisphere. A label with a z instead of a number refers to a midline electrode. A label Fp refers to a prefrontal electrode. Letters may refer to the central fissure (C), or to the frontal (F), parietal (P), temporal (T), or occipital (O) lobe. Labels of other electrodes use a letter combination of nearby electrodes. Electrodes located between the earlier labeled electrodes are labeled frontocentral (FC), centroparietal (CP), parieto-occipital (PO), frontotemporal (FT), and temporoparietal (TP). Electrodes anterior to the frontal electrodes are labeled anterofrontal (AF). Additional electrodes between FC and C are referred to as FCC, et cetera. On figure 2.3 the 10-20 system is shown on a simplified 2D head viewed from above with the nose indicated at the top. However advancement in EEG studies has lead to multi-channel EEG hardware systems with a much larger number of electrodes.

The measured signal from each electrode is amplified, resulting in one recording channel for every electrode. For every electrode, the potential is expressed as the difference between the measured signal and a reference signal (computed per time step). For multichannel EEG with a large number of widely spread electrodes, an average reference is often applied which is the average of all measured scalp potentials. Alternatively, a common reference uses the signal of one selected electrode as a reference for all other electrodes, or it may

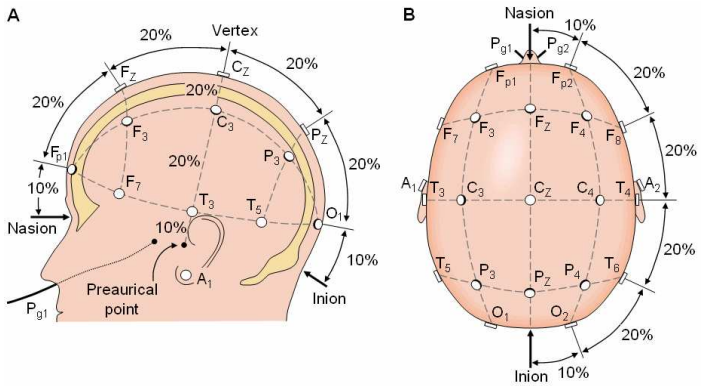

Figure 2.3: The 10-20 international system for the placement of the electrodes at the scalp to measure EEG potentials as described in [61].

combine two signals, e.g., recorded from electrodes attached to both ears. Potential differences between scalp electrodes are usually of the order of μ V.

2.3.3 Actual stage of the number of electrodes in EEG research

In recent years, recording high-resolution electroencephalograms (EEGs) from large electrode arrays has become a clear trend in brain research. Recent technological advances in electronic systems with the improvements in the EEG amplifier technology and computerized signal processing methods have allowed the EEG signals to be recorded from large electrode arrays.

Nowadays, laboratories specialized on EEG studies of brain activity have the possibility to use a greater number of channels than the original 21 channels. It is common today in many hospitals to measure EEG signal with 64 channels. Currently, it becomes common in research to move to a higher number of channels. The design of 128, 256 and even more channels by some companies around the world is already available in spite of the fact that the standard international 10-20 system is still widely used in clinical practice. Some research protocols can use up to 256 electrodes. Extensions of the 10-20 system have therefore been proposed with up to 345 electrode positions [62]. In a modern EEG system, the electrodes are connected to an amplifier and the signals are then digitized and stored on a computer. Using simulations as well as tests on real data, several authors showed that inter-electrode distances of around 2–3 cm are needed to avoid distortions of the scalp potential distribution as illustrated in [63].

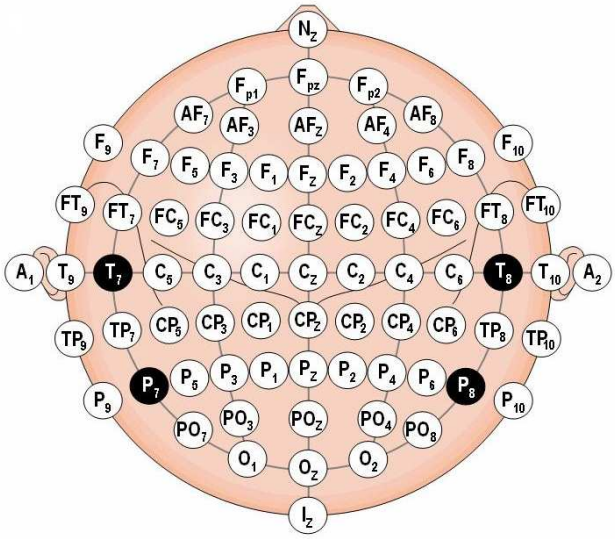

Figure 2.4: EEG configuration of 71 electrodes actually used for measurements according to the international 10-20 system from [61].

The increase of the number of the recording channels reduces the inter-electrode distance, thus increasing the spatial sampling density. With a larger number of electrodes in the EEG cap, more accurate information is gained regarding the potential distribution at the surface of the head.

During the last two decades several studies have investigated the benefits of increasing the number of EEG electrodes. The effect on the accuracy of both the forward solutions and inverse solutions has been evaluated and an increase in the number of electrodes to at least 128 has been shown to improve the accuracy of the results. Different factors affect the appropriate number of electrodes. These include, for example, the widely debated value of the skull's relative conductivity, which has a great impact on the accuracy of inverse solutions. Thus, for different EEG measurements conducted in different environments, the appropriate number of electrodes may vary considerably [64].

EEG source localization has to be split into two partial problems: the forward problem and the inverse problem. The forward problem is the calculation of the potential distribution resulting from a given source distribution in the brains by solving the Maxwell equations. As explained in figure 2.5 this requires a specification of the electrical brain activity, a modelization of the head geometry and the electrical properties of the different brain tissues as accurate as possible.

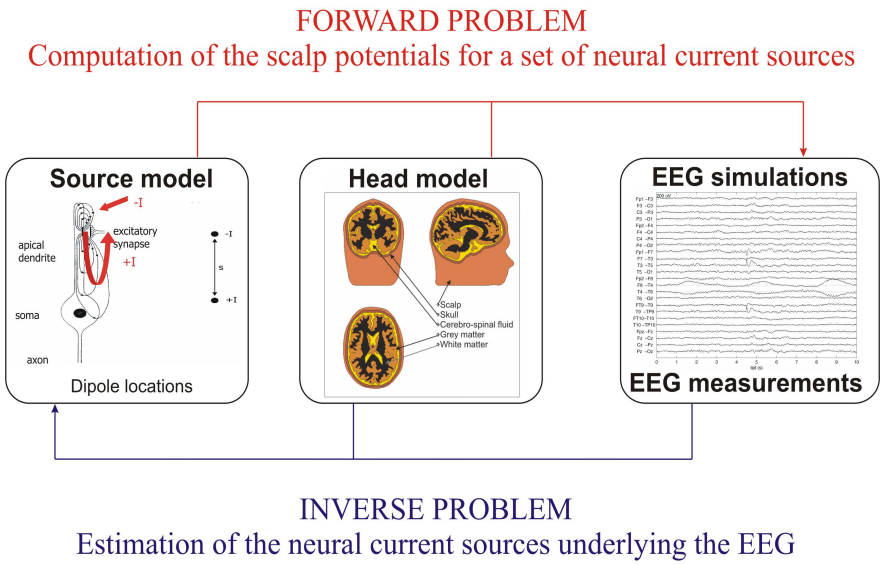

Figure 2.5: EEG forward and inverse problem.

2.4. Uncertainties in the forward model

The choice of head model and the assumption made on the nature of conductivity of the tissues, lead to uncertainties in the forward model. Many models of the head exist with the goal to produce the most accurate forward evaluations. Depending on the assumptions made, various numerical techniques exist to compute the potential values at the surface of the head. Some studies ([65, 66]) have been carried out in order to compare numerical values of the potentials predicted by analytical formulas V_a and those obtained by numerical methods V_n such as FEM, FDM, and BEM. The relative difference measure (RDM) between the analytical solutions and the numerical solutions methods is given by:

$$\text{RDM} = \frac{\|V_n - V_a\|}{\|V_a\|} \tag{2.1}$$

Depending on the dipole parameters (position and orientation) and the degree of discretization in the numerical methods, RDM varying between 5% and 10% was reported in [65, 67].

Influence of conductivity onto the forward EEG solution: The use of isotropic conductivity or anisotropic conductivity in the same head model will not produce the same outputs as well as a change of conductivity values when

computations are done with the same conditions. It is shown in [19–21] that anisotropically conducting compartments should be incorporated in the volume conductor head models. Finally, errors are introduced in each model due to the use of inaccurate absolute conductivity values of the different tissues in the volume conductor.

2.5. Mathematical description of EEG problems

2.5.1 Maxwell equations

Electromagnetic fields can be described by the Maxwell equations which can be written as:

$$\nabla \times \mathbf{H} = \frac{\partial \mathbf{D}}{\partial t} + \mathbf{J} \tag{2.2}$$

$$\nabla \times \mathbf{E} = -\frac{\partial \mathbf{B}}{\partial t} \tag{2.3}$$

$$\nabla.\mathbf{B} = 0 \tag{2.4}$$

$$\nabla.\mathbf{D} = \rho \tag{2.5}$$

where $\mathbf{E}$ $[V/m]$ and $\mathbf{B}$ $[Tesla]$ are respectively the electric and magnetic flux. $\mathbf{H}$ is the magnetic field strength , $\mathbf{D}$ is electric flux density and ρ is the charge density $[C/m^3]$ in a volume G. $\mathbf{J}$ is the current density $[A/m^2]$ which is the current per unit square passing through an elementary surface orthogonal to $\mathbf{J}$.

Applying the divergence operator to equation (2.2) and using the fact that $\nabla.(\nabla \times \mathbf{H}) = 0$, leads to the equation describing the preservation of the charges

$$\frac{\partial \rho}{\partial t} + \nabla.\mathbf{J} = 0 \tag{2.6}$$

This equation states that the change in charge inside a volume with time must correspond to a flow of charge through the surface of the volume. In other words, a current leaving or entering the volume conductor G causes a change in the total amount of charges in G.

2.5.2 Quasi-static conditions

Electromagnetic phenomena in the human head are in the frequency range up to 1 kHz [68]. Typically, the bandwidths of the signals considered in clinical

settings, range from less than 1Hz to 100 Hz. The neural sources change sufficiently slow in time, consequently the resulting electromagnetic fields depend only on the electrical conductivity of the head tissues (resistivity) and not on the complex impedance [69]. Thus, quasi-static conditions apply to the EEG forward problem.
It is shown in [70] that for the frequency range of the EEG signals, no electrical charge can be piled up in the conducting volume. Consequently, $\frac{\partial \rho}{\partial t} = 0$ which corresponds with stationary conditions for the electromagnetic fields.

2.5.3 Poisson equation

The sources of the EEG signals can be described by one or multiple dipole sources [10]. The current density in the head is the sum of the primary current $\mathbf{J}_p$, related to the original neural activity and a passive current flow $\sigma\mathbf{E}$ which results from the effect of an electric field on charge carriers in the conducting medium (Ohm's law)

$$\mathbf{J} = \mathbf{J}_p + \sigma\mathbf{E} \tag{2.7}$$

The primary current is generated by neural activity within the neuronal cells whereas the volume currents flowing passively in the medium are caused by conduction effects. The primary current also represents the source of the brain activity which we are trying to locate. Taking the divergence of both sides of equation (2.7) gives:

$$\nabla.\mathbf{J}_p + \nabla.(\sigma\mathbf{E}) = 0 \tag{2.8}$$

The divergence of the primary current density $\mathbf{J}_p(x,y,z)$ is defined as

$$\nabla.\mathbf{J_p}(\mathbf{r}) = \lim_{\mathbf{G}\to\mathbf{0}} \frac{\mathbf{1}}{\mathbf{G}} \oint_{\partial\mathbf{G}} \mathbf{J_p}.\mathbf{dS} \tag{2.9}$$

with G an infinitesimal small volume around **r**. For deriving a proper expression for the right hand side (2.9), we consider three cases.
In the first case we consider a small volume in the extracellular space not enclosing the current dipole. The current flowing into the infinitely small volume must be equal to the current leaving that volume. This is due to the fact that no charge can be piled up in the extracellular space. The surface integral of equation (2.9) is then zero, i.e. $\nabla.\mathbf{J_p} = \mathbf{0}$

In the second case we assume a volume enclosing the current sink with position parameters $\mathbf{r}_1(\mathrm{x}_1,\mathrm{y}_1,\mathrm{z}_1)$. The current sink represents the removal of positively charged ions at the apical dendrite of the pyramidal cell. The integral

of equation (2.9) remains equal to $-I$ while the volume in the denominator becomes infinitesimally small. This gives a singularity for the current source density. This singularity can be written as a delta function: $-I\delta(\mathbf{r}-\mathbf{r}_1)$. The negative sign indicates that current is removed from the extracellular volume. The delta function indicates that current is removed at one point in space.

For the third case we construct a small volume around the current source at position $\mathbf{r_2}(x_2, y_2, z_2)$. The current source represents the injection of positively charged ions at the cell body of the pyramidal cell. The current source density equals $I\delta(\mathbf{r}-\mathbf{r_2})$. The dipoles introduce singularities in the right-hand side of the Poisson's equation that need to be treated.

The head model is considered here as a volume conductor Ω with isotropic and position dependent conductivity, i.e. $\sigma \equiv \sigma$(x,y,z).
The electric field $\mathbf{E}$ is related to the electric potential V by the relation $\mathbf{E} = -\nabla V$. Thus inserting the three cases in equation (2.8), we have inside the head:

$$\nabla \cdot (\sigma(\mathbf{r}).\nabla V(\mathbf{r})) = I\delta(\mathbf{r}-\mathbf{r_2}) - I\delta(\mathbf{r}-\mathbf{r_1}) \quad \text{in} \quad \Omega \tag{2.10}$$

where $V(\mathbf{r})$ is the potential inside the head volume Ω, $\delta(.)$ is the delta Dirac function, $\mathbf{r_1}$ and $\mathbf{r_2}$ are the coordinates of the dipole current sink and source, respectively.

The right hand side of this Poisson's equation as mentioned in [71], represents the point current source and sink providing I and -I Ampere, at positions $\mathbf{r_2}$ and $\mathbf{r_1}$.

The boundary condition on the surface $\partial\Omega$ of the head i.e. scalp is given by $\sigma \frac{\partial V}{\partial \mathbf{n}}\Big|_{\partial\Omega} = 0$ with $\mathbf{n}$ the normal vector of the head model. This means that no current flows outside the head into the surrounding air i.e. the conductivity of air being equal to 0 ($\sigma_{\text{air}} = 0$).

For interfaces between non-air compartments, the potential is not subject to any discontinuity when crossing the interface. In this case, the potential remains the same $V_1 = V_2$ and the boundary condition here is the Dirichlet boundary condition. The Poisson equation describing the EEG problem in a more general way is an elliptic equation in the bounded domain Ω.

$$\begin{aligned} \nabla \cdot (\sigma(\mathbf{r}).\nabla V(\mathbf{r})) &= I\delta(\mathbf{r}-\mathbf{r_2}) - I\delta(\mathbf{r}-\mathbf{r_1}) \quad \text{in} \quad \Omega \\ \sigma \frac{\partial V}{\partial n} &= 0 \quad \text{on} \quad \partial\Omega \end{aligned} \tag{2.11}$$

2.6. Forward problem solutions in EEG

EEG problems can be stated as solving Poisson's equation of electrical conduction for the primary current sources. The forward problem in EEG is to compute the potential distribution V within the head and in particular on the electrode positions for a given source configuration (Upper part of figure 2.5). To get a good solution of the EEG forward problem, it is necessary to correctly model the shape of the head layers and their respective conductivities. To solve the forward problem described by equation (2.11), one needs to know the structure of the surfaces for the different volumes of the head. In the next paragraphs, we will give an overview of methods used to solve the EEG forward problem. We will first focus on analytical solutions for spherical head models and later, we will describe shortly numerical methods used for realistic and complex head models.

2.6.1 Solution for a dipole field in an infinite conductor

As stated in [72], the initial research in cortical surface mapping was limited to very simple geometric models, which provide analytical solutions to Poisson's equation. Two kinds of models were introduced: the infinite brain model and the concentric spherical models. The infinite brain model assumes that the head is infinite, homogeneous and isotropic. We introduce the potential field generated by a current dipole with moment $\mathbf{d} = d\mathbf{e}_d$ at position $\mathbf{r}_d$ in an infinite conductor with conductivity σ. For such a model, the solution of the Poisson's equation is:

$$V(\mathbf{r}, \mathbf{r}_d, \mathbf{d}) = \frac{\mathbf{d}.(\mathbf{r} - \mathbf{r}_d)}{4\pi\sigma\|\mathbf{r} - \mathbf{r}_d\|^3} \tag{2.12}$$

with $\mathbf{r}$ being the position where the potential is computed. If the dipole is located at the center of the Cartesian coordinate system and oriented along the z-axis, then the potential equals:

$$V(\mathbf{r}, 0, d\mathbf{e}_z) = \frac{\mathrm{d}\cos\theta}{4\pi\sigma\|r\|^2} \tag{2.13}$$

where θ represents the angle between the z-axis and the position $\mathbf{r}$. Note that $r = \|\mathbf{r}\|$. It is obvious that if V is a solution to the Poisson's equation, then $V + c$ where c is an arbitrary constant, is also a solution. Therefore, a reference potential must be chosen. One can choose to set one electrode to zero or one can opt for average referenced potentials. The latter results in electrode potentials having a mean value equal to zero. It is also reported in [72] that this model produces very approximate results and its use in clinical practice is limited.

2.6.2 Solutions for spherical head models in EEG

The most commonly used spherical head model assumes that it is made up of a set of concentric spheres, each with homogeneous and isotropic conductivity. Two approaches exist in the use of spherical head models. The first approach is to consider a simplified model. The human head is usually studied by considering a simple spherical head model consisting of three layers (M = 3) [73, 74]. This simplified model is widely used. The second approach consists to approximate the human head with a sphere with multiple layers (M > 3) since the structure of the head contains in reality many tissues. This model is known as the multishell case.

2.6.2.1 Case of simple spherical head models

Historically, the volume conductor head model assumes that the head consists of a set of three or four concentric homogeneous spherical shells, respectively, representing brain (white and gray matter), cerebrospinal fluid (CSF), skull, and scalp [6]. Analytic solutions exist for equation (2.10) constructed by spheres. Due to their simplicity and ease of computation these spherical head models have traditionally been used to approximate the human head [75]. Here, the choice of the Euclidean system $\mathbf{e}_x, \mathbf{e}_y, \mathbf{e}_z$ and the corresponding coordinate system in the spherical head model is defined in the following way: - point of origin is chosen at the centre of the concentric spheres. - the $\mathbf{e}_z$ axis is chosen in such a way that the electrical dipole is located on the e_z-axis. - the $\mathbf{e}_y$ axis is chosen in such a way that the position of the sensor under consideration lies in the yz plane.
The solution of the Poisson's equation for a dipole located in the inner sphere is given by:

$$V = \frac{1}{4\pi\sigma_{soft}R^2}\sum_{i=1}^{\infty}\frac{X(2i+1)^3}{g_i(i+1)i}l^{i-1}[id_rP_i(\cos\theta) + d_tP_i^1(\cos\theta)] \tag{2.14}$$

where

$$g_i = [(i+1)X+i]\left[\frac{iX}{i+1}+1\right] + (1-X)\left[(i+1)X+i\right](f_1^{i_1} - f_2^{i_1}) - i(1-X)^2(f_1/f_2)^{i_1}$$

The above solution to the Poisson's equation mainly depends in the case of spherical head models on the dipole location $\mathbf{r}_d$, and on the conductivity X. Notice that one choose $\sigma_{\text{scalp}} = \sigma_{\text{brain}}$ and X is defined as the ratio between the conductivity of the skull and the conductivity of the brain i.e. $X = \sigma_{\text{skull}}/\sigma_{\text{brain}}$. The remaining inputs are clearly known. The symbols introduced in the solution are given in table 2.1.

R	the radius of the outer shell [meter]
r_1	the radius of the inner shell [meter]
r_2	the radius of the middle shell [meter]
f_1	equals r_1/R
f_2	equals r_2/R
$l = \frac{B}{R}$	the relative distance of the dipole from the center, B is the distance from origin to the dipole position along the z-axis. [unitless]
σ_{soft}	the conductivity of the scalp and the brain tissue ($\sigma_{soft} \equiv \sigma_{scalp} \equiv \sigma_{brain}$) [Siemens/meter]
X	the ratio between the skull and soft tissue (electrical conductivity) [unitless]
θ	the polar angle between the z-axis and the axis through the origin and the point defined by the sensor position. [radians]
d_r	the dipole component along the z-axis (radial). [meter]
d_t	the dipole component along the x-axis (tangential). [meter]
$P_i(.)$	the Legendre polynomial,
$P_i^1(.)$	the associated Legendre polynomial
i	an index, $i_1 = 2i + 1$

Table 2.1: Parameters used in the solution of equation (2.14).

During the computation of the potential distribution, the infinite serie in (2.14) is truncated. In the present case, only the first 40 terms are used during the computations since a quadratic convergence of the infinite series described in equation (2.14) is reached. For high orders, the solution is more accurate but the computation is more expensive.

From the linearity of equation (2.11), it follows that the mapping from electric sources within the brain to the scalp recordings can be represented by a linear operator $\mathbf{L}$, the so-called lead field matrix.

Given the dipole parameters consisting of the dipole position $\mathbf{r}_d$ and the orientation of the dipole $\mathbf{d}$, the electrode potentials V_i, $i = 1, \ldots, N$ can be expressed as

$$\mathbf{V}(X, \mathbf{r}_d, \mathbf{d}) = \mathbf{L}(X, \mathbf{r}_d).\mathbf{d} \tag{2.15}$$

where ($\mathbf{L} \in \mathbb{R}^{N \times 3}$) is the lead-field matrix. The three columns correspond with the potentials for the N sensors when considering the x, y or z components, i.e. d_x, d_y, d_z, of the dipole respectively:

$$\mathbf{V}(X, \mathbf{r}_d, \mathbf{d}) = \mathbf{V}(X, \mathbf{r}_d, \mathbf{e}_x)d_x + \mathbf{V}(X, \mathbf{r}_d, \mathbf{e}_y)d_z + \mathbf{V}(X, \mathbf{r}_d, \mathbf{e}_z)d_z \tag{2.16}$$

with N the number of sensor locations.

In the case of EEG measurements, the electrode potentials contain noise that can be represented by the vector $\mathbf{N}$ (usually zero-mean Gaussian noise) in the system so that (2.15) becomes:

$$\mathbf{V}(X, \mathbf{r}_d, \mathbf{d}) = \mathbf{L}(X, \mathbf{r}_d)\mathbf{d} + \mathbf{N} \tag{2.17}$$

Equation (2.15) can be extended to p dipoles ($p > 1$) where we assume that the EEG signals use N electrodes and n_t time points. The spatio-temporal data matrix may be written as

$$\mathbf{V} = \Big[\mathbf{L}(\mathbf{r}_{d,1}), \mathbf{L}(\mathbf{r}_{d,2}), \ldots, \mathbf{L}(\mathbf{r}_{d,p})\Big]\Big[\mathbf{d}_1, \mathbf{d}_2, \ldots, \mathbf{d}_p\Big]^T \tag{2.18}$$

because a superposition of the potentials may be performed when using multiple dipoles, due to the linearity of the Maxwell's equations. $\mathbf{L}(\mathbf{r}_{d,i})$ is the $N \times 3$ lead field matrix mapping the ith dipole at the position $\mathbf{r}_{d,i}$. The $3 \times n_t$ matrix $\mathbf{d}_i$ represents the time course of the ith dipole moment. Here, we omit the notation of X within the lead fields for clarity reasons. If we assume that the p dipoles sources have fixed orientations as pointed out in [76], it is possible to rewrite $\mathbf{d}_i$ as:

$$\mathbf{d}_i = \mathbf{u}_i \mathbf{s}_i \tag{2.19}$$

where $\mathbf{u}_i$ is a 3×1 unit-norm dipole orientation vector and the $1 \times n_t$ vector $\mathbf{s}_i$ is the time course of the dipole strength of n_t time samples. The spatio-temporal matrix defined in equation (2.18) could be written as:

$$\mathbf{V} = \Big[\mathbf{a}(\mathbf{r}_{d,1}, \mathbf{u}_1), \mathbf{a}(\mathbf{r}_{d,2}, \mathbf{u}_2), \ldots, \mathbf{a}(\mathbf{r}_{d,p}, \mathbf{u}_p)\Big]\Big[\mathbf{s}_1, \mathbf{s}_2, \ldots, \mathbf{s}_p\Big]^T \tag{2.20}$$

or equivalently $\mathbf{V} = \mathbf{A}(\mathbf{r}_d, \mathbf{u})\mathbf{S}^T$ where $\mathbf{a}(\mathbf{r}_{d,i}, \mathbf{u}_i) = \mathbf{L}(\mathbf{r}_{d,i})\mathbf{u}_i$, and $i = 1, 2 \ldots\ldots p$. The set $\mathbf{r}_d \equiv \{\mathbf{r}_{d,1}, \mathbf{r}_{d,2}, \ldots, \mathbf{r}_{d,p}\}$ represents the location of the p dipoles and the set $\mathbf{u} \equiv \{\mathbf{u}_1, \mathbf{u}_2, \ldots, \mathbf{u}_p\}$ contains the corresponding unit norm vectors.

Since the signals are often contaminated by noise, we assume that a random $N \times n_t$ noise matrix, where the n_t are time slices i.e. $\mathbf{N} \equiv [\mathbf{n}(t_1), \mathbf{n}(t_2), \ldots, \mathbf{n}(t_{n_t})]$ is added to the data (2.20). Consequently, we obtain:

$$\mathbf{V} = \mathbf{A}(\mathbf{r}_d, \mathbf{u})\mathbf{S}^T + \mathbf{N} \tag{2.21}$$

The noise is commonly taken as zero-mean, white and uncorrelated,

$$\mathbf{E}\{\mathbf{n}(t_i)\mathbf{n}(t_i)^T\} = \sigma_n^2 \mathbf{I}_N, \quad i = 1, 2, \ldots, n_t \tag{2.22}$$

where $\mathbf{E}\{.\}$ is the mathematical expectation, and $\mathbf{I}_N$ is the N-dimensional identity matrix.

Head models that consist of concentric spherical shells representing tissues with different conductivity (brain, cerebrospinal fluid (CSF), skull and scalp), known as four shell spherical head models, are also widely used in modeling EEG signals. For this model, the solution is very similar to the one in equation (2.14).

2.6.2.2 Case of spherical head models with multiple layers

The advanced form of the spherical model consists of multiple number of spheres to represent layers of different conductivity. This mainly benefits EEG source analysis since including multi-layer conductivity information into the model reflects the actual composition tissue of conductivity in a much better way. The homogeneous sphere model, the three-or four-layered concentric model with isotropic or anisotropic conductivity are commonly used in the EEG forward and inverse problem. In the case of a dipole inside a sphere with anisotropic conductivity the potential on the surface can be computed as explained in [77].

$$V(R_0, D, R_e) = \frac{D}{4\pi\sigma_N R_e^2} \sum_{n=1}^{\infty} \frac{2n+1}{n} \Big(\frac{R_0}{R_e}\Big)^{n-1} \times \Big(f_n n \cos\alpha \mathrm{P_n}(\cos\gamma) + g_n \cos\beta \sin\alpha . \mathrm{P_n^1}(\cos\gamma) \Big) \quad (2.23)$$

The anisotropy information is embedded in the terms f_n and g_n. Detailed forms of the coefficients f_n and g_n can be found in [77].
This solution to the Poisson equation with a multi-sphere structure with N layers having an isotropic conductivity is reduced to:

$$V(R_0, D, R_e) = \frac{D}{4\pi\sigma_N R_e^2} \sum_{n=1}^{\infty} \frac{2n+1}{n} \Big(\frac{R_0}{R_e}\Big)^{n-1} \times f_n \Big(n \cos\alpha \mathrm{P_n}(\cos\gamma) + \cos\beta \sin\alpha . \mathrm{P_n^1}(\cos\gamma) \Big) \quad (2.24)$$

where D is the L_2 norm of the dipole moment $\mathbf{q}$, R_0 is the radius of dipole location, R_e is the radius of the electrode coordinates; note that $R_e = R_N$. α is the angle between the dipole position $\mathbf{r}_d$ and the dipole moment $\mathbf{q}$. γ is the angle between the dipole position $\mathbf{r}_d$ and the considered sensor position $\mathbf{r}_e$. η is the angle between the plane defined by $\mathbf{r}_d$ and $\mathbf{r}_e$ and the plane defined by $\mathbf{r}_d$ and $\mathbf{q}$.P_n and P_n^1 are the Legendre and associated Legendre polynomials respectively. Moreover

$$f_n = \frac{n}{nm_{22} + (1+n)m_{21}} \tag{2.25}$$

where the coefficients m_{21} and m_{22} are given by:

$$m_{21} = \frac{1}{(2n+1)^{N-1}} \prod_{k=1}^{N-1} n\Big(\frac{\sigma_k}{\sigma_{k+1}} - 1\Big)\Big(\frac{R_k}{R_e}\Big)^{2n+1} \tag{2.26}$$

$$m_{22} = \frac{1}{(2n+1)^{N-1}} \prod_{k=1}^{N-1} \Big(n + 1 + \frac{n\sigma_k}{\sigma_{k+1}}\Big) \tag{2.27}$$

$$m_{11} = \frac{1}{(2n+1)^{N-1}} \prod_{k=1}^{N-1} \Big(n + \frac{(n+1)\sigma_k}{\sigma_{k+1}}\Big)$$

$$m_{12} = \frac{1}{(2n+1)^{N-1}} \prod_{k=1}^{N-1} (n+1)\Big(\frac{\sigma_k}{\sigma_{k+1}} - 1\Big)\Big(\frac{R_e}{R_k}\Big)^{2n+1}$$

The conductivities are arranged from the innermost to the outer most sphere $\sigma_1, \sigma_2, \sigma_3, \ldots, \sigma_N$, corresponding to the radii of the various spheres $R_1, R_2, R_3, \ldots, R_N$ see figure 2.6.

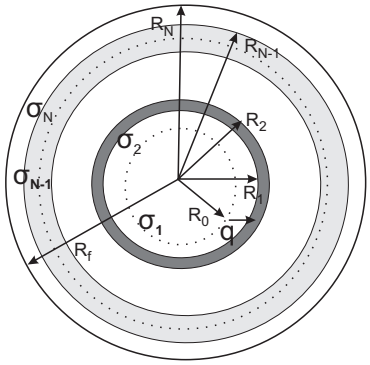

Figure 2.6: Human head approximated by a Multi-layer spherical head model.

The dipole is free to move inside the innermost sphere. A variant of this solution resulted in the form of De Munck formulas [78].

Other geometry (ellipsoids, eccentric spheres, etc) have been also considered in the EEG forward problem. Analytic solutions for these head models have been presented, such as prolate and oblate spheroids [79] or eccentric spheres [80]. Numerical solutions for narrow or wide ellipsoids are presented in [81].

The shortcomings of these spherical models is : genuine heads are not spherical, tissue layers have non-uniform thicknesses and conductivities. However, it is possible in these models to take into account anisotropy of the conductivity of the skull in order to model better the skull. In general, forward solutions when considering sphere-shaped head models are computationally fast. Due to their simplicity and ease of computation these spherical head models have traditionally been used to approximate the human head.
Several studies [67, 82–84] have shown that such simplified models cannot produce accurate results, and this constitutes limits of the spherical head models even if these models are widely used. A new tendency today in EEG research is to use realistic head models or more complex models. Such models do not allow analytical solutions and numerical solutions are used to compute the potentials.

2.6.3 Solutions for realistic head models in EEG forward problem

While fast analytic expressions exist for the potentials in spherical models, these solutions cannot be applied to realistic head models. Rather, a complete forward numerical solution must be computed in order to determine the electrode potentials due to each source. At the opposite of the previous model, many people tend nowadays to use realistic head models which are more accurate from a geometrical point of view in the evaluations of the potential distribution. Several numerical methods have been developed to solve the Poisson's equation of (2.10).

For realistic head models, the conductivity σ can be assumed anisotropic (i.e. the conductivity can differ depending on the direction the current flows). For that case, the conductivity is expressed as a tensor $[\sigma_{lm}]$ with $l, m = 1,2,3$. In reality the skull conductivity is anisotropic, and its tangential conductivity can be ten times higher than its radial conductivity. It has been shown that this anisotropy has an important influence on the results of the forward [85] and consequently also of the inverse problem. Moreover, with anisotropic conductivity, the Poisson's equation (2.11) becomes:

$$\nabla.\left(\begin{bmatrix}\sigma_{11} & \sigma_{12} & \sigma_{13}\\ \sigma_{21} & \sigma_{22} & \sigma_{23}\\ \sigma_{31} & \sigma_{32} & \sigma_{33}\end{bmatrix}.\begin{bmatrix}\partial V/\partial X\\ \partial V/\partial Y\\ \partial V/\partial Z\end{bmatrix}\right) = I\delta(\mathbf{r}-\mathbf{r_2}) - I\delta(\mathbf{r}-\mathbf{r_1}) \tag{2.28}$$

To improve the accuracy of the forward calculation one needs to consider more realistic head models. The geometry of such improved head models can be obtained from anatomical imaging modalities like the computed tomography (CT) or the functional magnetic resonance imaging (fMRI).

These realistic model forward solutions can be generated using the finite difference method (FDM), the finite element method (FEM) or the boundary element method (BEM), as described in [54].

2.6.3.1 The Finite Difference Method (FDM)

Finite difference methods provide numerical solutions to differential equations by approximating derivatives with finite differences. In 3D, a point r_0 has 6 neighbors r_i, (with $i = 1,2....6$), located at a distance of $+h$ and $-h$ in each direction. The finite difference approximation leads to:

$$\nabla.(\sigma\nabla V(r_0)) = \frac{1}{h^2}\Big(\alpha_0 V(r_0) - \sum_{i=1}^{6}\alpha_i V(r_i)\Big) \tag{2.29}$$

where the constants α_0 and α_i depend on the conductivities at the points r_0 and r_i. In equation (2.29) we assume an isotropic conductivity. We should note that this scheme corresponds exactly to Kirchhoffs law for the balance of currents, assuming that the points in the finite difference structure form a network of resistors. Generally, the head volume is discretized using a cubic grid with a regular spacing h. Therefore the scheme of (2.29) can be used at every point of the grid by computing differences between closest neighbors.

For the source, we need to approximate the divergence operator $\nabla.\mathbf{J}_p$ The primary currents are defined over the edges between the grid points. For example, a dipole can be represented as a small current flowing over the edge linking two points r^+ and r^-, so that the divergence is reduced to the source and sink, i.e.,$\nabla.J_p = I\delta r^+ - I\delta r^-$ where I is the amplitude of the current. Denoting by $[\mathbf{J}_i]$ the values of the primary currents between the neighboring grid points, the term $\nabla.\mathbf{J}_p$ can be written in matrix form as $\mathbf{B}[\mathbf{J}_i]$. By denoting [Vi] the values of the potential at grid points and plugging this expression into Kirchhoffs law, we get that the potential $[V_i]$ is the solution of the linear problem:

$$\mathbf{A}[V_i] = \mathbf{B}[J_i] \tag{2.30}$$

The matrices involved are typically very large since the whole head domain has to be discretized. However the matrix A that needs to be inverted is highly sparse, because it has at most seven nonzero elements per line, which implies that iterative methods are efficient.

The main drawback of the FDM method for EEG forward modeling is that, due to the cubic grid, the complex interfaces between brain structures and thin layers cannot be precisely modeled. Indeed, with a cubic grid,

the interfaces have to follow the grid points which leads to a "staircase" effect.

We should note here that numerical methods for anisotropic media (aFDM) have been recently developed in [86] and [87] with a cubic grid being defined on the domain Ω.

2.6.3.2 Finite Element Model

In the finite element method, the Poisson's equation is first reformulated in its variational form, also called weak form. Then, an approximate solution of the problem in its weak formulation is found by looking for a solution in a finite dimensional vector space. The second step requires to properly choose the finite dimensional space in order to guarantee the quality of the approximation. Once discretized, the problem leads to a linear system that is solved numerically. Contrary to the FDM, Finite Element Methods (FEM) do not suffer from the staircase effect [88].
The Finite Element Method for the EEG forward problem deals with the weak formulation of Poisson's equation in (2.31). We assume here that the potential V belongs in a certain Hilbert space E of regular functions. By multiplying both sides by a test function ϕ and then integrating over the whole computational domain, it follows using the divergence theorem that:

$$\int_{\Omega} \nabla.(\sigma \nabla V)\phi d\Omega = \int_{\Omega} \nabla.\mathbf{J}_p \phi d\Omega \tag{2.31}$$

Taking Green's first identity into account we have:

$$\int_{\partial\Omega} \phi(\sigma \nabla V).\mathbf{n} d\partial\Omega - \int_{\Omega} \sigma \nabla V.\nabla\phi d\Omega = \int_{\Omega} \nabla.\mathbf{J}_p \phi d\Omega \tag{2.32}$$

and by the boundary condition of (2.11) we obtain

$$-\int_{\Omega} \sigma \nabla V.\nabla\phi d\Omega = \int_{\Omega} \nabla.\mathbf{J}_p \phi d\Omega \tag{2.33}$$

The second step consists in finding an approximation for the solution of equation (2.31) in a finite dimensional subspace E_h of the Hilbert space E. An approximation for V in E_h denoted by V_h can be written as $V_h = \sum_{i=1}^{n} V_i \phi_i$ on the computational domain Ω. Let $\left(\phi_i\right)$, $i = 1,2,.....n$ be a basis of E_h, after replacing ϕ in equation (2.31) by ϕ_j, we have to find V_i, $i = 1,2,.....n$ such that:

$$-\sum_{i}^{n} V_i \int_{\Omega} \sigma \nabla\phi_i.\nabla\phi_j d\Omega = \int_{\Omega} \nabla \cdot \mathbf{J}_p \phi_j d\Omega, \quad \forall j = 1,2,.....n \tag{2.34}$$

The continuous integral equation is converted into a linear equation system and the FEM reduces the Poissons equation to a linear system:

$$\mathbf{A}V = \mathbf{b} \tag{2.35}$$

where the inputs of matrix $\mathbf{A}$ and vector $\mathbf{b}$ are:

$$A_{ij} = -\int_{\Omega} \sigma(r)\nabla\phi_i(r)\nabla\phi_j(r)d\Omega \tag{2.36}$$

$$b_j = \int_{\Omega} \mathbf{J}_p \nabla\phi_j(r)d\Omega = \int_{\Omega} \mathbf{q}\delta(r_0).\nabla\phi_j(r)d\Omega = \mathbf{q}\nabla\phi_j(r_0) \tag{2.37}$$

The finite element method (FEM) is often used for the forward problem, because it allows realistic representation of the complicated head volume conductor. The drawback of this method is the creation of a huge and sparse matrix, whose inverse is not easy to compute. Due to the sparsity of the matrix $[A_{ij}]$, iterative methods, like conjugate gradient methods are more appropriate as they perform well when solving this linear system.

2.6.3.3 Boundary element method

The boundary element method (BEM) is a numerical method for solving linear partial differential equations which have been transformed into integral equations defined over the boundaries of the different domains [89]. In the case of EEG, we can think at the white matter or the gray matter etc. In a first approximation, we can assume that the conductivity within the structures of the head is constant. In order to achieve such a reformulation of the problem, one needs to assume homogeneous conductivities in each domain.

The BEM is used to approximate each boundary of a domain such as brain, cerebrospinal fluid, skull and scalp using small surface elements. The original integral equation governing surface potentials is approximated as a summation of surface integrals over each element.The potential on each element is first assumed to be a linear function of nodal potentials. After choosing the interpolation functions and element geometry, the surface integral over each element is expressed in terms of unknown nodal potentials, and the original surface integral is reduced to a system of algebraic equations. The solution of the nodal potentials provides the potential at any point on the surfaces. The elements can have various shapes such as triangles or rectangles.

Let $S_1, S_2, \ldots, S_M$ denote the interfaces between the regions of different conductivities; with S_1 as the surface of the scalp. The electric potential V at $\mathbf{r}_d \in S_i$ for a dipole positioned in the medium with conductivity σ_0 (brain compart-

ment) obeys the integral equation [90]

$$(\sigma_i^- + \sigma_i^+)V(\mathbf{r}_d) = 2\sigma_0 V_0(\mathbf{r}_d) + \frac{1}{2\pi}\sum_{i=1}^{M}(\sigma_i^- - \sigma_i^+)\int_{S_i} V(\mathbf{r}'_d)\frac{\mathbf{r}_d - \mathbf{r}'_d}{\|\mathbf{r}_d - \mathbf{r}'_d\|^3}d\mathbf{S}_i \tag{2.38}$$

where S_i is the surface of the respective conductivity interface within the volume conductor, σ_i^- and σ_i^+ are the conductivities inside and outside the conductivity interface S_i respectively. $V_0(\mathbf{r}_d)$ is the potential caused by the current source in an infinite homogeneous medium given in equation (2.12). The surface S_i is discretized into N area elements and surface integration can be obtained as a sum of the surface integrals on these elements.

A significant advantage of the boundary element method (BEM) is that anisotropy and inhomogeneous media can be taken into account [91]. The boundary element method has the great advantage that it only requires computations on the boundaries and so does not need the entire volume to be meshed but only its describing surfaces.

It is important to mention here that the EEG forward problem is well-posed and has a unique solution. For a mathematical proof, one can refer to the following papers [92] and [93] for more details. The forward problem calculates the potential field at the scalp from known source locations, source strengths and given value of the conductivity. This is achieved when a configuration of electrodes is provided.

The accuracy of both analytic and numerical methods is, however, severely limited by incomplete knowledge of the electrical conductivity [94]. The different forward models described above in combination with different conductivity models could be used as input in the solution of the inverse problem.

2.7. Computations of the potential value **V**

As said previously, in order to use EEG for brain functional imaging, dedicated modeling and computations need to be done. It consists in quantifying the signal produced by the neuronal activities at the surface of the head. This involves physical considerations like the given set of sensors at the surface of the head and a head model. In what follows, we will consider a simple spherical head model including three concentric layers: the brain, the skull and the scalp. From a computational point of view, this head model is fast and is widely used in EEG research. The other reason leading to the choice of this spherical model is obviously simplicity. It is well known that the potential image on the scalp due to a dipole current source located anywhere inside can be predicted analytically [95].

For this simple head model, we will consider the analytic solution described by equation (2.14) for the computer simulations of the EEG potentials. That is, given the location parameters of the dipole, the mathematical formula given in equation (2.14) in a truncated form is used to compute the potential at any point on the surface of the model. Since the brain electrical activity of patients suffering from epilepsy are characterized by a limited number of electrical dipoles [10], we will not investigate here the influence of the used source model.

The computation of the forward solution requires specification of the EEG electrodes. In our case, a standard configuration of $N = 27$ electrodes following the International system 10-20 will be used for the computer simulations. Coordinates of the electrode positions using this standard configuration is given in Appendix A. In our computations of the EEG forward problem, presented in this section, only isotropic conductivities are considered (i.e. in each point the conductivity is equal in all directions). The chosen head model is divided into isotropic piecewise homogeneous compartments. The potential distribution V at the surface of the head is then a matrix of (27×3) elements and the values of the potential corresponding to a dipole oriented in each direction $\mathbf{e_x}, \mathbf{e_y}$ and $\mathbf{e_z}$, can be obtained separately.

Using figure 2.2 as the approximation of the head model, we fix $\sigma_{\text{scalp}} \equiv \sigma_{\text{brain}} = 0.33$ S/m and the conductivity is simply determined by X which is defined as the ratio between the conductivity of the skull and the one of the brain. The conductivity ratio is chosen within the interval $[1/40, \quad 1/9]$ as often found in the literature.

We denote by CS1, CS2, CS3 and CS4 the various case studies of the dipole located in the brain, corresponding to the cartesian coordinates in table 2.2. The cartesian coordinates of these dipoles located at different regions of the brain in the head model are given in the following table.
The first considered dipole CS1 is located almost at the center of the brain, the next two dipoles denoted by CS2 and CS3 are located inside the brain and the fourth dipole CS4 is located at the edge of the brain. In the computations of the potential values, we will display the potential $\mathbf{V}$ as a function of the conductivity ratio X.

Case Study (CS)	r_x (mm)	r_y (mm)	r_z (mm)
CS1	0.0	0.0	8.6
CS2	8.6	17.2	8.6
CS3	17.2	25.8	17.2
CS4	34.4	25.8	34.4

Table 2.2: Case studies of several dipoles located at different regions. The center of the head model is referenced as $\mathbf{r}_d = [0, \quad 0, \quad 0]$. The radii of the concentric spheres are $R_1 = 8.0$ cm, $R_2 = 8.6$ cm, $R_3 = 9.2$ cm.

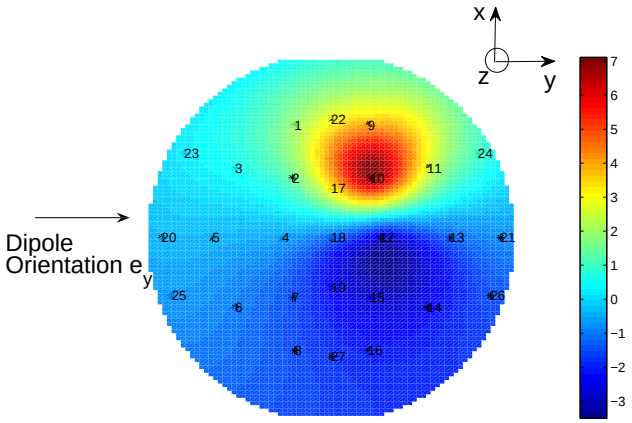

Figure 2.7: Potentials Distribution for dipole CS4 along the 27 electrodes with orientation $\mathbf{e_y}$.

Figures 2.9 and 2.10 give the potential distribution for different locations of the dipole in the brain for several conductivity values with specifications of the electrodes given at the right of these figures. The respective electrode positions where the potential value is computed, is referenced by letters at the right of the figures. A surface display of the potential is given in figures 2.7 and 2.8. Depending on the regions and the positions, some electrodes have a high potential value while others have a low potential value.

From figures 2.9 and 2.10, we can conclude that there is a change in potential values for most of the electrodes for a given source configuration when varying the conductivity ratio X. This change is more important for dipoles located at the edge of the spherical head model. For the other sensors in this

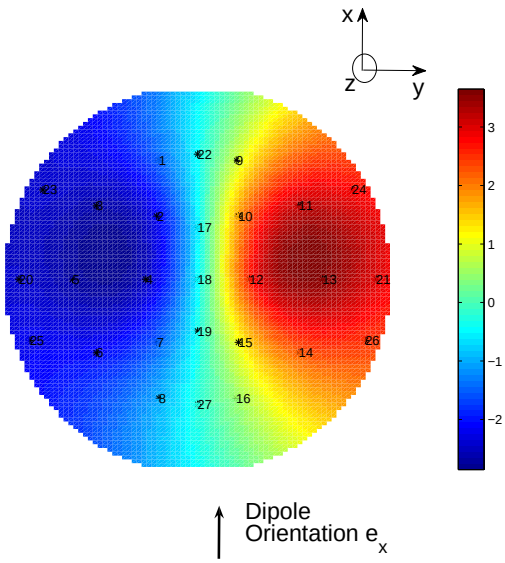

Figure 2.8: Potentials Distribution for dipole CS2 along the 27 electrodes with orientation $\mathbf{e_x}$.

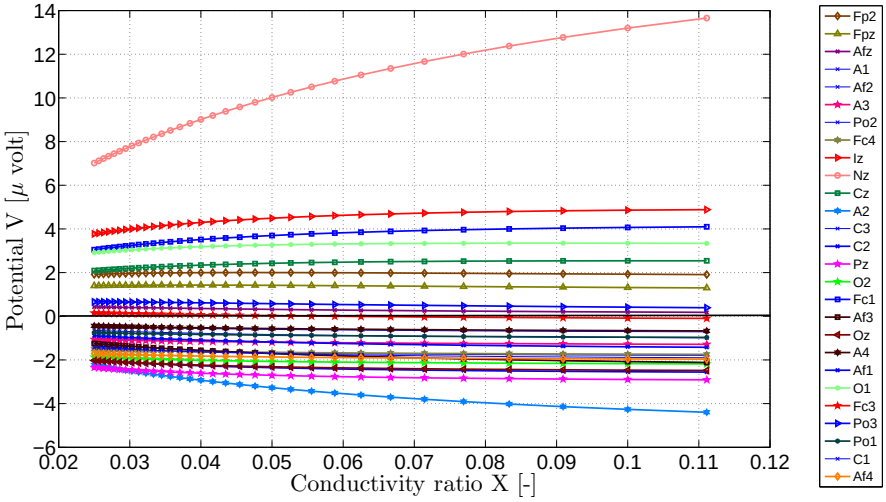

Figure 2.9: Potentials along the 27 electrodes vs the conductivity ratio for dipole CS4 with orientation $\mathbf{e_y}$.

case, a little change in the value of the potentials is observed when a variation

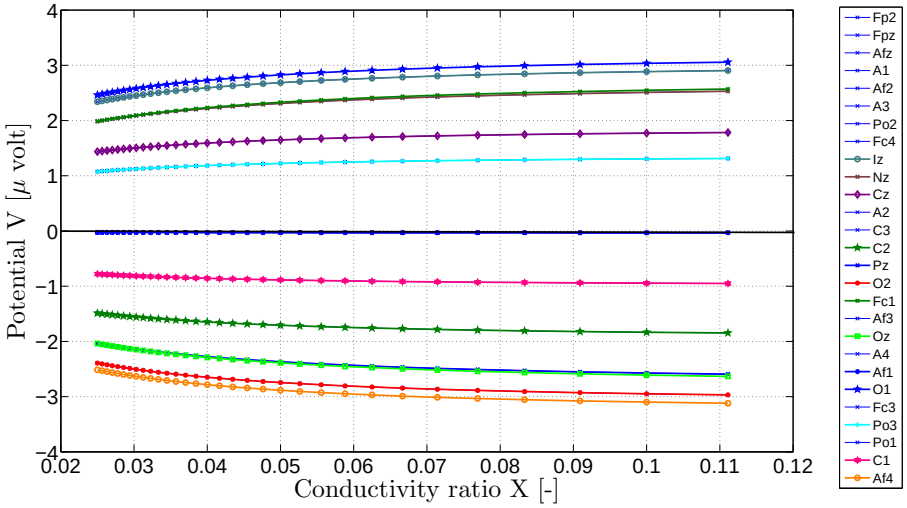

Figure 2.10: Potentials along the 27 electrodes with orientation $\mathbf{e_y}$ vs the conductivity ratio for dipole CS2 along the 27 electrodes.

of the conductivity ratio X is applied. This can be observed in all the regions of the dipole locations where the computations are carried out.

2.8. Sensitivity analysis

Sensitivity analysis is used to determine the influence of the brain to skull conductivity ratio towards the sensor potentials in the spherical head model. It is known that the forward model is sensitive to the conductivity as pointed out in [96]. Therefore, it is important to understand how the sensitivity of the conductivity can affect the dipole localization error (DLE) with the aim of using more accurate models. Such approach is useful because of the uncertainties introduced by the conductivity in the forward model evaluations.

Analytical formula resulting from the derivation of the solution of the Poisson's equation as described in Appendix B, are used for the computations of the sensitivity. These formula have been validated by the finite difference method (FDM). The sensitivity belonging to an EEG sensor is defined as the partial derivative of the sensor potential V_i to the electrical conductivity ratio:

$$\frac{\partial V_i}{\partial X}, \quad i = 1, \ldots, N \tag{2.39}$$

Three approaches will be used to display the sensitivity values in order to get the most reliable information: a 2D display of the sensitivity over the surface of the head, plots involving the potential and the sensitivity and finally plots involving the sensitivity in a specific region when several conductivity ratio values are used. Coordinates of the electrodes are given in appendix A.

2.8.1 2D display of the sensitivity

A 2D mapping of the sensitivity values over the surface of the head, shows to which extend sensors are sensitive or not. Figures 2.11 and 2.12 give a surface distribution of the sensitivity values for dipoles located respectively near the center (CS1) and inside the brain (CS2). The position of the sensitive electrodes are referenced by a number. We can observe from these figures that some sensors are very sensitive and other are not. The high sensitivity of the sensors to the conductivity ratio has an impact on the solution of the inverse problem since the conductivity is assumed to be uncertain, see chapter 3. Sensors which are very sensitive can be identified individually as we can see in figure 2.12.

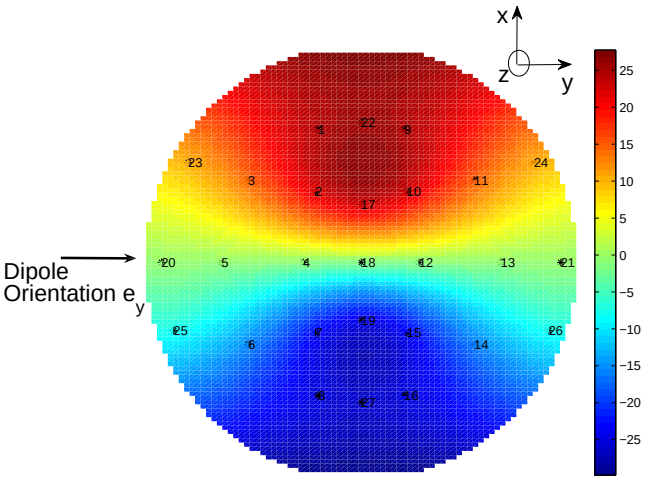

Figure 2.11: Sensitivity of the potential for the dipole CS1 in 2D for an assumed conductivity ratio $\widetilde{X} = \sigma_{skull}/\sigma_{brain} = 1/40$.

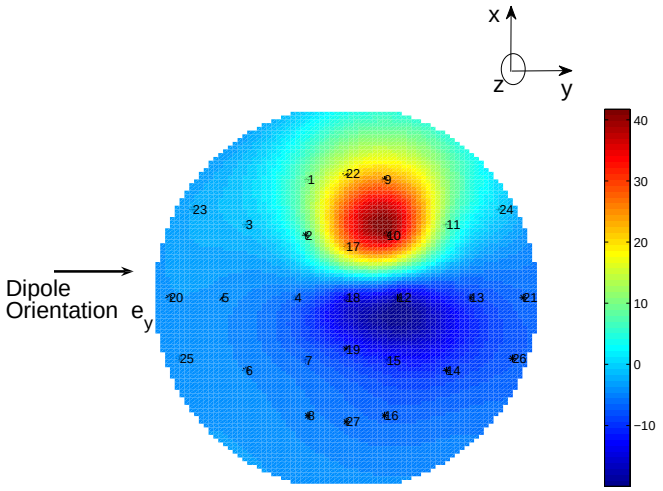

Figure 2.12: Sensitivity of the potential for the dipole CS2 in 2D for an assumed conductivity ratio $\widetilde{X} = \sigma_{skull}/\sigma_{brain} = 1/25$.

2.8.2 Potentials versus sensitivity values

In this section, a relation involving the potential value V and the sensitivity value $\partial V/\partial X$ is presented for different locations of the dipole. Such approach is done for a specific position of the dipole for only one conductivity ratio.
In figures 2.13 and 2.14, the highest value of the sensitivity (respectively 28 and 38 μ volt) is recorded along the 10^{th} electrode with the coordinates are ($\theta = 62°, \phi = 57°$). We should note here that other electrodes are also very sensitive.

Figures 2.13 and 2.14 show that the highest sensitivity values appear at the high potential-valued sensors. For the other dipole locations considered in this type of simulations, a similar trend has been observed but is not necessarily true in all cases.

For figure 2.14, there is a large difference in absolute value with the most sensitive sensor with the rest of the sensor, while this not the case in figure 2.13. Notice that the sensor corresponding with the highest sensitivity value is not necessarily the nearest sensor to the dipole as the potential distribution as well

as the sensitivity distribution depend not only on the location but also on the orientation of the dipole.

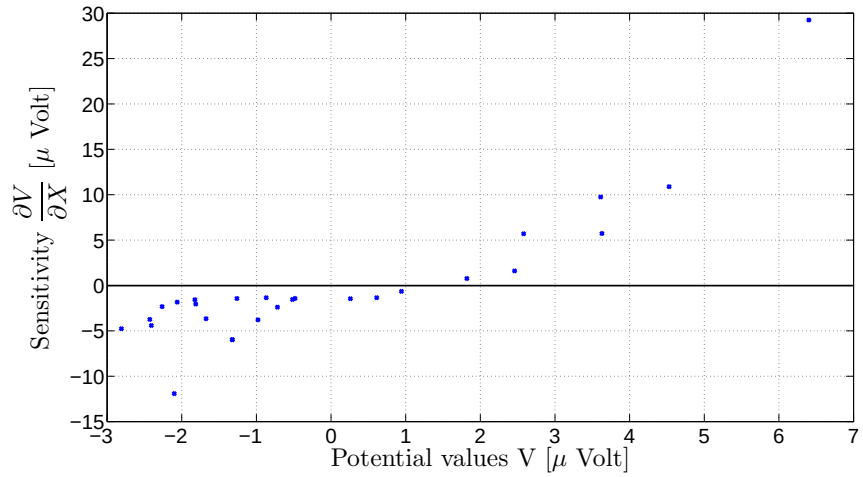

Figure 2.13: Potentials vs the sensitivity for dipole CS3 with orientation $\mathbf{e_y}$ for the 27 electrodes. The assumed conductivity ratio is $\widetilde{X} = 1/15$.

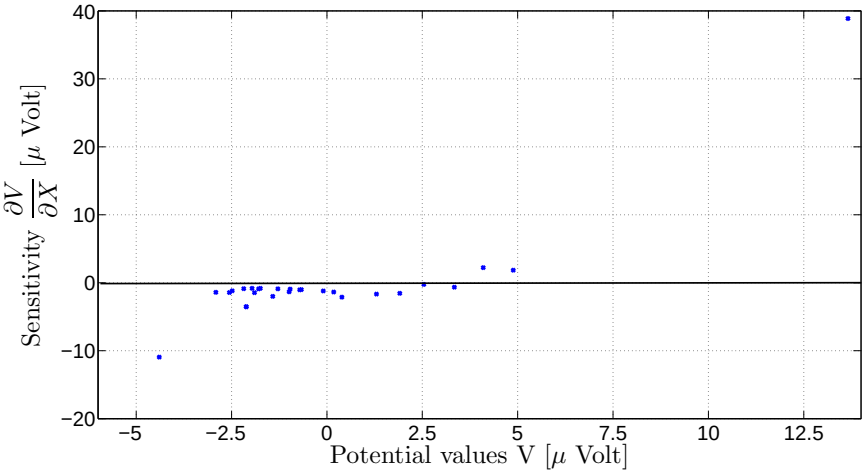

Figure 2.14: Potentials vs the sensitivity for dipole CS4 with orientation $\mathbf{e_y}$ for the 27 electrodes. The assumed conductivity ratio is $\widetilde{X} = 1/9$.

2.8.3 Sensitivity over the regions

The sensitivity of the potentials to conductivity ratio due to dipole orientation is also investigated by analyzing the distribution of the derivative values for the different sensors. This is done with several dipole locations with an orientation in the $\mathbf{e_x}$, $\mathbf{e_y}$ and $\mathbf{e_z}$ directions. The results for the dipoles located at CS1 and CS4 are shown in figures 2.17-2.20.

For dipoles located in the centre of the brain as well at the edge of the brain, we observe that not only the location but also the orientation influences the sensitivity of the sensors. Moreover, the sensor index belonging to the highest sensitivity can be different for a fixed location but for different orientations. This is also the case for the sensor index with the lowest sensitivity.
Remark that the ranking of the sensors with respect to their sensitivity value (from low to high value) is often independent from the conductivity ratio. However, this is not generally true as can be observed in figure 2.18 by the crossing sensitivity characteristics. Notice that the above observations will be used in the further developed techniques for solving the inverse problems in the following chapters.

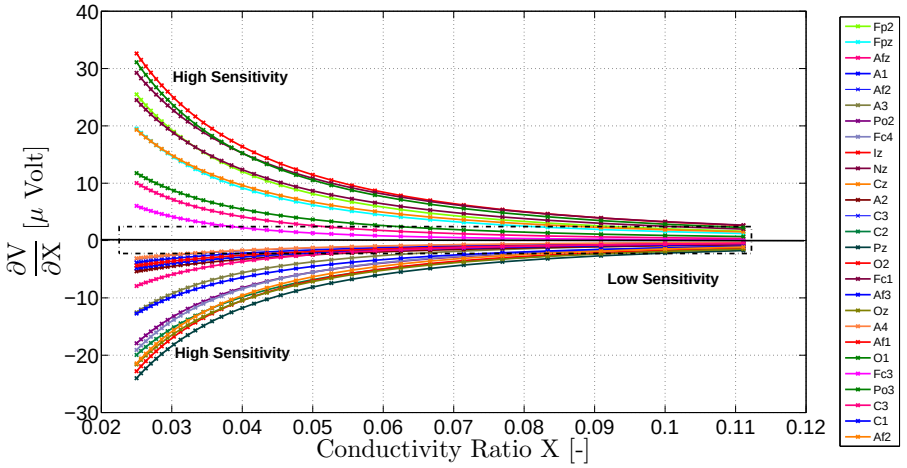

Figure 2.15: Sensitivity of potentials for the 27 electrodes vs conductivity ratio for dipole CS1 with orientation $\mathbf{e_x}$.

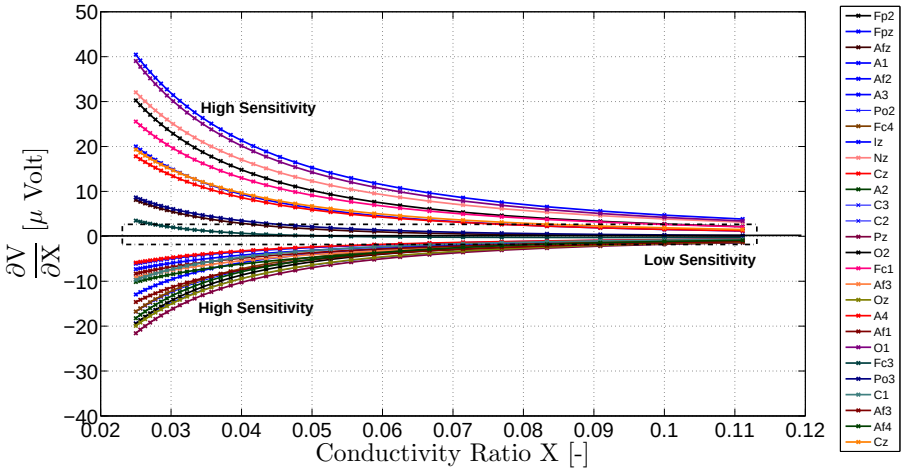

Figure 2.16: Sensitivity of potentials for the 27 electrodes vs conductivity ratio for dipole CS1 with orientation $\mathbf{e_y}$.

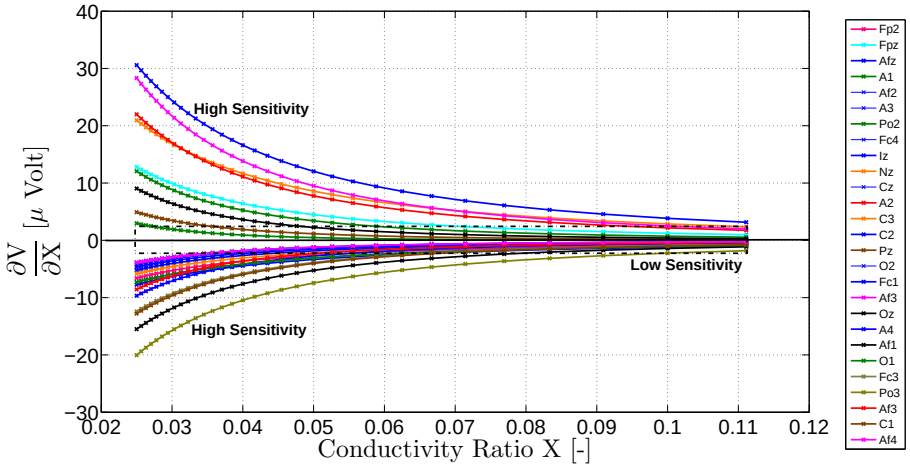

Figure 2.17: Sensitivity of potentials for the 27 electrodes vs conductivity ratio for dipole CS1 with orientation $\mathbf{e_z}$.

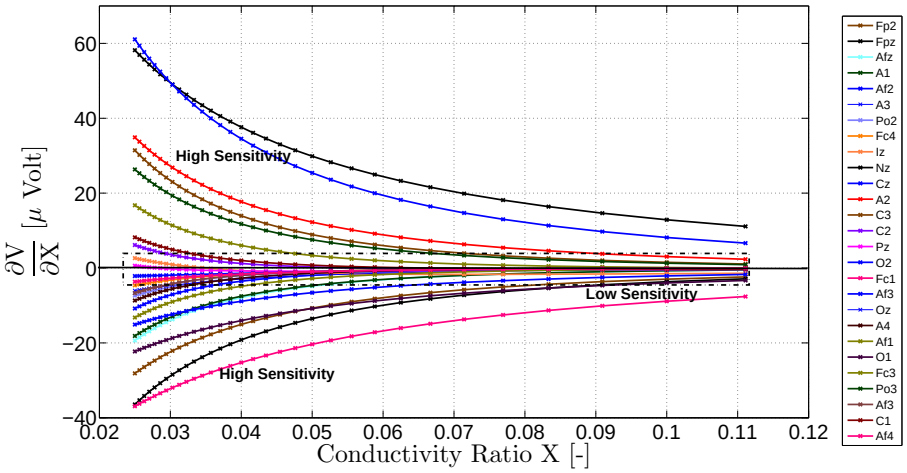

Figure 2.18: Sensitivity of potentials for the 27 electrodes vs conductivity ratio for dipole CS4 with orientation $\mathbf{e_x}$.

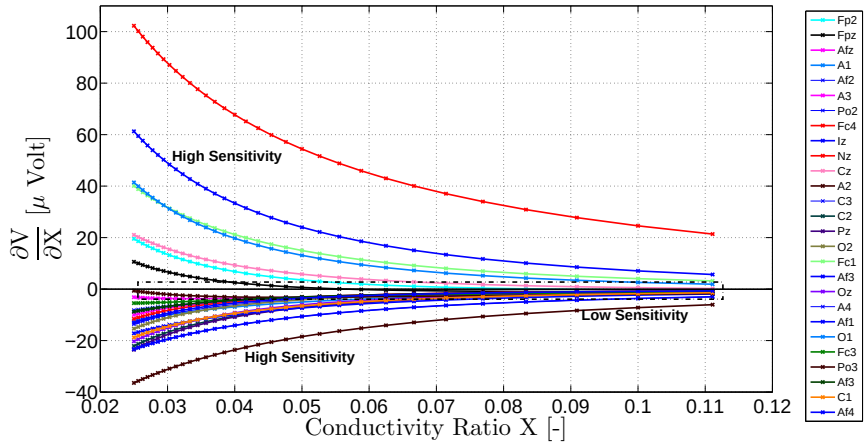

Figure 2.19: Sensitivity of potentials for the 27 electrodes vs the conductivity ratio for dipole CS4 with orientation $\mathbf{e_y}$.

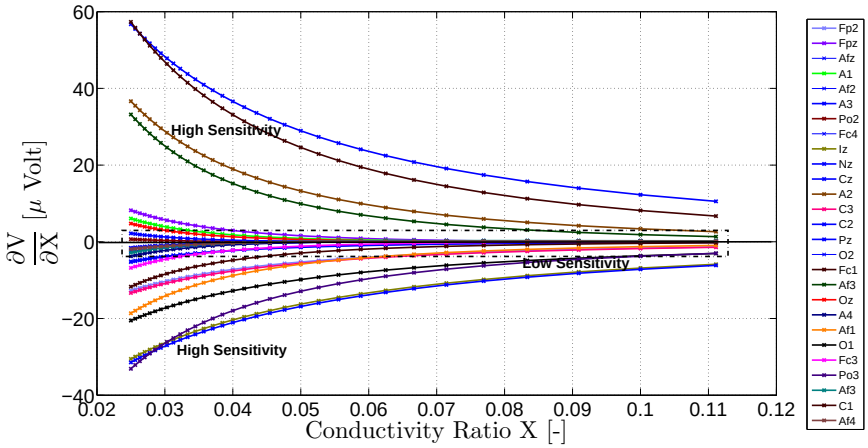

Figure 2.20: Sensitivity of potentials vs the conductivity ratio for dipole CS4 with orientation $\mathbf{e_z}$ along the 27 electrodes.

2.9. Conclusion

The EEG forward problem solution highly depends on the electrical conductivity values. In particular, for the three shell spherical head model, this is the case for the skull to soft tissue conductivity ratio X, see equation (2.14). In order to quantify this dependence, we defined and analyzed the sensitivity of the sensor to this conductivity ratio. It is possible using sensitivity analysis to analyze which sensors are highly affected by the conductivity and those who are not when considering a dipole source in a specific region. In the numerical simulations carried out, it was observed that the sensitivity of the sensor potentials is characterized by the position and orientation of the dipole in the brain and the specified value of the conductivity ratio.

In practice, it is difficult to measure the real value of the conductivity ratio value. Sensitivity analysis is thus a tool to determine the propagation of the uncertain conductivity onto the EEG forward problem. Therefore, it becomes important to study the effect of the skull to soft tissue conductivity ratio on the simulated potentials which need to be as accurate as possible, and later on to develop a strategy that will improve the accuracy of the solution of the inverse problem based on these two limitations.

CHAPTER 3

EEG Inverse Problem

3.1. Introduction

Over the past few decades, a variety of techniques for non-invasive measurement of brain activity has been developed. Among these, electroencephalography (EEG) is widely used for functional brain mapping. It is well known that this method is particularly suitable for neuroscience research and clinical practice, such as surgical planning for epilepsy patients [97].
It is common practice in cognitive research and in clinical routine to reconstruct current sources in the human brain by means of non-invasive field measurements outside the head. In order to use EEG for brain functional imaging, modeling and computation need to be done.

EEG uses measurements of electrical potentials (in the order of microvolts (μV)) at various locations on the scalp and then applies signal processing techniques to estimate the current sources inside the brain that best fit these data. Source localization in EEG is currently attracting intense research because it involves many difficulties.

The reconstruction of the dipole sources is called the inverse problem of EEG. One of the major advantages of EEG source reconstruction over other brain imaging techniques such as positron emission tomography (PET) or functional magnetic resonance imaging (fMRI) is its high temporal resolution. Solution of this EEG source localization or inverse problem typically requires a significant number of forward model evaluations. A first step towards the EEG inverse problem, is to solve the forward problem that consists in calculating the superficial potential for any possible configuration of the sources. The forward model should be accurate as possible as seen previously.

It is well known that source localization methods rely on mathematical models of the bio-electrical generators and the volume conductors within which they lie.

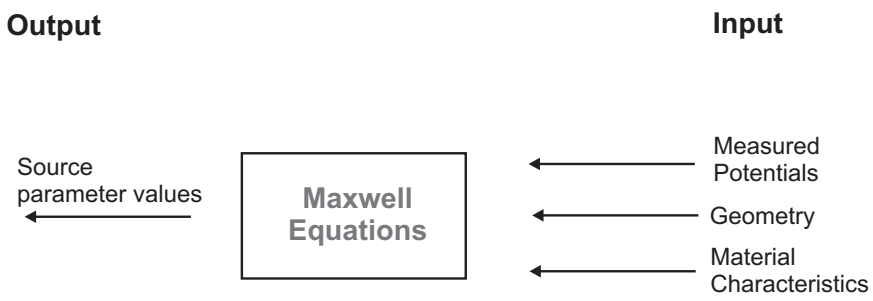

Figure 3.1: Schematic description of the EEG inverse problem.

The electrical activity in the brain is caused by some chemical actions within neurons. Neurons communicate with the displacements of electric charges that produce tiny currents. In order to produce electromagnetic fields detectable outside the head, multiple neurons within a same structure need to act simultaneously. In the case of epilepsy there are small zones inside the brain that give major contributions in the generation of the electric field. In order to measure the electric potentials generated by neuronal activity, an EEG device consists of a set of electrodes which are positioned on the scalp so to establish electrical contact with the skin. In clinical application, neurologists are interested in determining the location of the epileptogenic zones from the measured potentials on the scalp.

Starting from a given set of potential differences measured at the scalp, we can estimate the source responsible for the measured signals. This is known as EEG source localization. The reconstruction of the dipole location responsible for the measured EEG signals may be done by using a numerical technique. A head model and the conductivity model are the main inputs for the inverse problem as illustrated in figure 3.1.

3.2. Solving the inverse problem in EEG

The inverse problem is defined as the task to estimate the source position $\mathbf{r}_d$ from a given measurement $\mathbf{V}_{\text{meas}}$. The different steps leading to the reconstruction of the source are described in the lower side of figure 2.5. Thus starting from measurements of electrical potentials at the surface of the

head by means of electrodes, and making a choice of a given head model, we use a numerical technique to reconstruct dipole location responsible for the measured signals. The choice of the numerical technique depends on the various assumptions made. The EEG inverse problem for the reconstruction of electrical sources in the human brain, can be an ill-posed problem. This means that different source configurations can generate the same distribution of potential fields measured on the scalp.

The ill-posedness of the inverse problem is often tackled using regularization techniques, known from image restoration and reconstruction [11,43]. Among the other ones, imaging methods are sometimes addressed with a Bayesian stochastic framework [98]. Minimum norm solutions and Tikhonov regularization can also be seen as variational regularization methods for removing this indetermination.

There are many classes of methods for solving the EEG inverse problem, each one having its advantages and drawbacks. The two general approaches to EEG source estimation are equivalent dipole localization and distributed source imaging. The dipole fitting approaches assume that the measured data have been produced by a small number of active regions, each can be modeled by an equivalent current dipole (ECD). The number of sources p is fixed. In general, to have a unique solution, the number of parameters to estimate (6 per dipole) should not exceed the number of data. The main limitation with these methods is that the user has to fix a priori the number of active regions in the brain. As soon as the number of sources increases, i.e. $p > 1$, the number of local minima increases with the number of dipoles. The results of the non linear optimization problem could be inaccurate since solvers are easily trapped in local minima. Another approach to overcome the problem of local minima, is the use of scanning methods [99, 100].

Distributed sources usually exist as multiple dipoles uniformly distributed in the brain. Due to the linearity of Poisson's equation, the potential can be written as a superposition of the potential caused by each individual dipole source. An inverse problem with distributed source models is strongly ill posed since the number of sensors N is smaller compared to the number of sources p i.e. ($N < p$). The number of unknowns is much bigger than the number of equations. This leads to an undetermined system which has to be solved in the minimum norm sense and regularization techniques are needed [101–103].

In this thesis, we will solve the EEG inverse problem using single or multiple dipole source models and not using distributed source models because

the former source models lead to well-posed inverse problems and moreover these source models can be applied for analyzing the EEG of epileptic patients. Our goal of this thesis is to provide more efficient numerical methods for the accurate localization of the source for the treatment of epilepsy.

3.3. Cost function

The derivation of the forward model is the first step towards the solution of the inverse problem. Starting from Maxwell's equations in their quasi-static formulation which result into the Poisson's equation (see equation (2.11)) and from a physical model of the head, the forward problem predicts the measurements that would be obtained for a given configuration of current sources. These evaluations of the forward model are necessary to solve the inverse problem. The forward models can be obtained analytically or by numerical methods (FDM, BEM, FEM) as described in the previous chapter. The computational time required to solve the EEG inverse problem, partly depends on the methodology used in the forward evaluations. We should note that for spherical head models, the computation of forward and inverse problems is fast, while for realistic head models it is much more expensive. The inverse problem consists in the minimization of a cost function where the forward model solution is iteratively evaluated. A dipole estimation can be obtained using a minimization method.

For the solution of the inverse problem, several possibilities exist for the minimization of the EEG cost function. These cost functions depend on assumptions made on the electrical activity in the brain. Thus, assuming that the electrical activity in the brain can be modeled by the equivalent current dipole (ECD) or the distributed models, will lead to different cost functions in the minimization procedure. In the case of a current dipole, the source localization is made by the Least-Squares Method (LSM), scanning methods or by using a signal subspace scanning as explained in [54]. In the case of distributed sources in the brain, minimization methods include Minimum Norm Solution (MNS), the Low Resolution Tomography (LORETA) and its variants, the Local autoregressive average (LAURA), the EPIFOCUS, for a review see [104, 105]. Other methods exist like Image-based methods, the Bayesian method [106], and ELECTRA [107]. Other methods exist like Image-based methods, the Bayesian method, and ELECTRA. However the reliability of the solution depends on the validity of the assumptions made.

As stated in [108], for events like epileptic spikes or early stages of an epileptic seizure, a current dipole may be used as a source model. We will assume in this

chapter, that the electrical activity in the brain is modeled by a single ($p = 1$) current dipole.

3.3.1 Traditional least-squared method in EEG inverse problem

In EEG dipole source analysis, the neural source represented by an electrical dipole ($\mathbf{r}_d, \mathbf{d}$) is estimated by finding the dipole that best fits the measured potential distribution. The aim of the EEG inverse problem is to recover the neural dipole location $\mathbf{r}_d^*$ and orientation $\mathbf{d}^*$ that correspond the best to the measured EEG potentials $\mathbf{V}_{\text{meas}} \in \mathbb{R}^{N\times 1}$. For a single dipole, this is carried out by minimizing a least-squares cost function, the so-called relative residual energy (RRE) [109]:

$$\{\mathbf{r}_d^*, \mathbf{d}^*\} = \arg\min_{\mathbf{r}_d, \mathbf{d}} \text{RRE}(\mathbf{r}_d, \mathbf{d}) \tag{3.1}$$

with

$$\text{RRE}(\mathbf{r}_d, \mathbf{d}) = \frac{\|\mathbf{V}_{\text{meas}} - \mathbf{V}_m(X, \mathbf{r}_d, \mathbf{d})\|}{\|\mathbf{V}_{\text{meas}}\|} \tag{3.2}$$

Where $||.||$ is the L_2 norm, $\mathbf{V}_m \in \mathbb{R}^{N\times 1}$ denotes the potentials obtained from the forward model, see equation (2.11) with the lead field formulation (2.15), while $\mathbf{V}_{\text{meas}} \in \mathbb{R}^{N\times 1}$ represents the EEG signals measured by N electrodes at one time point. The cost function used here, is the energy norm of the difference between the measured potentials and the simulated potentials.
The data $\mathbf{V}_{\text{meas}}$ can correspond either to one time instant or to a block of time samples. The above inverse problem is formulated to solve the EEG inverse problem at a single time instant and can be extended (for multiple time instances) in a spatio-temporal way, e.g. as in [110, 111].
The number of parameters in this least-squares cost function can be reduced by considering the optimal dipole components:

$$\mathbf{d}_{opt} = \mathbf{L}^{\dagger} \cdot \mathbf{V}_{\text{meas}} \tag{3.3}$$

where $\mathbf{L}$ is the lead field matrix, see (2.15), and $\mathbf{L}^{\dagger}$ the Moore-Penrose pseudo inverse of the lead field matrix. Equation (3.2) becomes then, see e.g. [109]:

$$\text{RRE}(\mathbf{r}_d) = \frac{\|\mathbf{V}_{\text{meas}} - \mathbf{L}(X, \mathbf{r}_d)\mathbf{L}(X, \mathbf{r}_d)^{\dagger}\mathbf{V}_{\text{meas}}\|}{\|\mathbf{V}_{\text{meas}}\|}. \tag{3.4}$$

In this way, the dipole location is the only remaining parameter to be reconstructed by minimizing the relative residual energy (RRE). And consequently, the relative residual energy is only dependent on the dipole position $\mathbf{r}_d$.
The widely-used Nelder-Mead simplex method is implemented here to find the global minimum of the Relative Residual Energy (RRE) in equation (3.4).

See e.g. [111, 112]. The minimization of the cost function is performed by the algorithm until a global minimum is obtained. The values of the reconstructed dipole correspond to this global minimum.

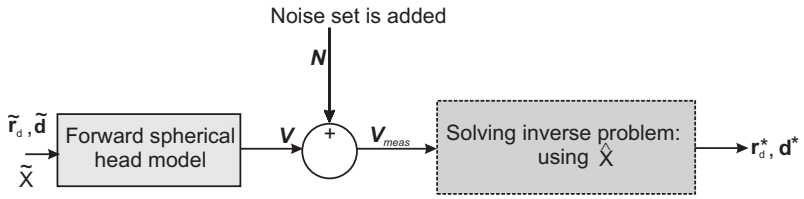

Figure 3.2: Simulation setup for solving the EEG inverse problems.

The analysis of spatial localization errors in EEG source analysis, is done by numerical experiments. Starting from an actual position of the dipole $\widetilde{\mathbf{r}}_d$, orientation of the dipole $\widetilde{\mathbf{d}}$ and actual value of the conductivity $\widetilde{X}$, we compute the corresponding potentials at the surface of the head denoted here by $\mathbf{V}$. See also figure 3.2. By adding noise to the computed $\mathbf{V}$, we obtain the signal $\mathbf{V}_{\text{meas}}$ which we can consider as measured signals and input for the inverse problem. See also equation (2.17). When solving the inverse problem, we assume a conductivity ratio $\widehat{X}$ that may be different from the actual one $\widetilde{X}$. Then using a numerical method we reconstruct the dipole location $\mathbf{r}_d^*$. In order to reconstruct the dipole position one needs to minimize the difference between the data and the forward model solution in the L_2 norm. If the difference does not satisfy a certain tolerance ϵ, then the source parameters are updated until the tolerance is reached. We will perform several Monte Carlo simulations using different assumed conductivity ratios $\widehat{X}$. Using the set of solutions it is possible to evaluate the accuracy by comparing the recovered dipole positions with the actual dipole positions $\widetilde{\mathbf{r}}_d$.

The reconstructed dipole location $\mathbf{r}_d^*$ may differ from the actual position of the dipole $\widetilde{\mathbf{r}}_d$ due to the presence of noise in the measurements and also because of the choice of the conductivity ratio $\widehat{X}$. The dipole position error (DPE) is the absolute difference in the L_2 norm between the actual dipole location $\widetilde{\mathbf{r}}_d$ and the reconstructed dipole location $\mathbf{r}_d^*$ provided by the solution of the inverse problem, expressed in the same normalized units.

$$\mathbf{DPE} = \|\widetilde{\mathbf{r}}_d - \mathbf{r}_d^*\| \tag{3.5}$$

It is important to mention here that the EEG cost function, when assuming a single dipole can be minimized using a locally convergent optimization algorithm. One of the limitations of these algorithms is the fact that they are

sometimes trapped in local solutions and they are very sensitive to the start value [112].

In general, the validation of an inverse procedure in EEG begins with choosing a head model and source, generating the forward solution, adding some random noise, resulting in the numerically obtained "measured EEG signals". Starting from these measured signals, we may run the inverse procedure to see if we can obtain an accurate guess close enough to the source. In order to test the robustness of the inverse procedure described previously, we will perform Monte-Carlo simulations. We will assume several values of the conductivity ratio as often found in the literature e.g. conductivity ratio values lying from $1/40$ to $1/9$.

3.3.2 Subspace correlation based methods

The least-squares method is no more suitable when the electrical activity of the brain is modeled by a limited number of dipoles i.e. $p > 1$. It is well known that inverse methods based on direct minimization of the squared error between the measured potentials $\mathbf{V}_{\text{meas}}$ and the forward model evaluations $\mathbf{V}_m$ through gradient-based optimization or simplex searches often lead to improper locations of the sources due to trapping in local minima which increases with the number of dipoles [12,113].

In order to overcome this problem, the signal subspace methods has been developed to handle more efficiently this difficulty. They are able to deal more accurately with the localization of multiple sources. These methods are based on signal classification between signal and noise via signal subspaces. The Multiple Signal Classification (MUSIC) is the most popular of these methods. The primary assumptions of this method are that the dipolar time series as defined by equation (2.21) are maximally uncorrelated among each other. To this, the fact that the number of time samples n_t is greater than the number of sensors N and the number of sources p is smaller than the number of sensors N is added. In the MUSIC algorithm the space spanned by the N measurements is divided into a signal subspace to identify the underlying components in the time series data and a noise subspace [76].

For more details concerning the subspace correlation based methods, we refer to chapter 5, section 5.2.

3.3.3 Other cost functions

In this section, we will give an overview of other cost functions that are often used in the EEG inverse problem. The list provided here is not complete, however the different cost functions mentioned below are chosen to explain the concept in EEG inverse problem and are for the case $p >> N$ (p denotes the number of dipoles, N the number of electrodes). In order to clearly define them, we will assume more generally that the orientations are fixed and that only the amplitudes of the dipoles $\mathbf{A} \in \mathbb{R}^{p \times n_t}$ need to be estimated (n_t denotes the number of time instants). The solution of the forward problem including noise with a specific noise level can then be written as:

$$\mathbf{M} = \mathbf{L}_g \mathbf{A} + \mathbf{N} \tag{3.6}$$

where $\mathbf{M} \in \mathbb{R}^{N \times n_t}$ corresponds to the measurements of the electric potential, $\mathbf{L}_g \in \mathbb{R}^{N \times p}$ stands for the lead field operator mapping the p sources (whole region under study) to the N measurement sites, $\mathbf{N} \in \mathbb{R}^{N \times n_t}$ is the noise matrix. Among these methods, are the minimum norm solution (MNS) [114], EPIFOCUS, Loreta, Local autoregressive average (LAURA), the Bayesian method, (POP-MUSIC, etc).

The standard Minimum-Norm solution as explained in [114, 115] is obtained by solving:

$$\mathbf{A}^* = \arg\min \mathbf{E(A)} = \arg\min_{\mathbf{A}} \|\mathbf{M} - \mathbf{L}_g \mathbf{A}\|_{\mathbf{F}}^2 + \lambda \|\mathbf{A}\|_{\mathbf{F}}^2,\ \lambda > 0 \tag{3.7}$$

Where $\|.\|_{\mathbf{F}}^2$ is the Frobenius norm. λ is the regularization parameter. It balances the reconstruction error and the regularity of the solution. The lower the level of noise present in the measurements, the smaller should be the reconstruction error. The solution of this unconstrained and differentiable problem is obtained by setting the derivative $d\mathbf{E}(\mathbf{A})/d\mathbf{A}$ equal to zero. The solution is simply:

$$\mathbf{A}^* = (\mathbf{L}_g^{\mathrm{T}} \mathbf{L}_g + \lambda \mathbf{I})^{-1} \mathbf{L}_g^{\mathrm{T}} \mathbf{M} \tag{3.8}$$

with $\mathbf{I}$ the identity matrix.

EPIFOCUS has mainly been developed for the analysis of focal epileptic activity where a single, dominant source with a certain spatial extent can be assumed. This method assumes a single focal source but differs from the equivalent dipole location in that it allows the source to have a spatial extent beyond a single point and avoids the non-linear optimization process required by dipole fitting [116]. When using EPIFOCUS, the inverse of the matrix is computed for each point independently in a very efficient way for

any given head model (e.g. realistic, spherical head model), and there is no need for regularization, i.e., one single inverse matrix can be used for all kind of data. It is a linear inverse method that scans the solution space and calculates the current density vector by projecting the scalp potential data on each solution point [116]. The results of this estimate can be interpreted as the probability of finding a single source at each specific point.

The Bayesian approach is a statistical method to incorporate a priori information into the estimation of the sources. The types of a priori information that have been incorporated in this approach include information on the neural current [117], the focal nature of the sources, combined spatial and temporal constraints [118], as well as strategies to penalize ghost sources [106]. Here assumptions are made in the form of probability distributions describing the neural current distribution and the signal noise which are assumed to be Gaussian variables with zero mean. Bayes' theorem enables detailed analytical computations to be made. Basic Gaussian distribution assumption gives a simple and robust algorithm. In general, this technique consists in finding an estimator $\mathbf{A}^*$ of $\mathbf{A}$ that maximizes the posterior distribution of $\mathbf{A}$ given the measurements $\mathbf{M}$ [118, 119]. This estimator can be written as

$$\mathbf{A}^* = \arg\max_{\mathbf{A}}[p(\mathbf{A}|\mathbf{M})] = \arg\max_{\mathbf{A}}[ln(p(\mathbf{M}|\mathbf{A})) + ln(p(\mathbf{A}))] \tag{3.9}$$

where $p(\mathbf{A}|\mathbf{M})$ denotes the conditional probability density of $\mathbf{A}$ given the measurements $\mathbf{M}$. This estimator is the most probable one with regards to measurements and a priori considerations.

LAURA, belongs to the class of distributed inverse solutions, which are capable of dealing with multiple simultaneously active sources. It is based on a Local Auto-Regressive Average model of the unknown current density in the brain. One advantage of this method is that, contrary to the single dipole model, there is no assumption made about the number of activated sources, which is a particularly useful attribute for analyzing cases of multi-focal epilepsy [116]. This solution is obtained by solving the following variational problem for the unknown vector $\mathbf{A}$.

$$\|\mathbf{M} - \mathbf{L}_g\mathbf{A} + \lambda \mathrm{R}(\mathbf{A})\| \tag{3.10}$$

where $\mathrm{R}(.)$ and λ represent the regularization operator and the regularization parameter respectively. The definition of the operator $R(.)$ is given explicitly in [120].

An alternative way to solve the inverse source localization problem as a minimization problem is to use genetic algorithms, which are a powerful tool solv-

ing problems and simulating natural systems in a variety of scientific fields. In this case dipoles are modeled as a set of parameters that determine the orientation and the location of the dipole and the error between the projected potential and the measured potentials is minimized by genetic algorithm evolutionary techniques. The minimization operation can be performed in order to localize multiple sources in the brain [121]. The advantage with Genetic algorithms is that they produce a large set of solutions which sample the solution-space globally but which can rapidly converge to a local or global minimum. One of the limitations is the computational time which involves a higher number of forward evaluations which typically must be done many thousands of time, combined to the construction and selection, crossover and mutation operations [122].
Other methods used so far are artificial neural networks (ANNs) [123], which solve the inverse problems in a very fast way but which are not very robust to noise . For a more complete literature review of all the methods used in EEG inverse problem, one can refer to [124].

3.3.4 Iterative schemes

The optimization strategies employed in EEG inverse problem vary from a large range of methods going from Levenberg-Marquardt, Nelder-Mead downhill simplex searches to global optimization schemes using multistart methods, genetic algorithms and simulated annealing [125]. The Nelder-Mead simplex method is one of the subroutines that can solve optimization problems with nonlinear constraints. It does not use any derivatives, and it does not assume that the objective function has continuous derivatives. In the simulations for the reconstruction of the source in the case of single dipole that will be treated later in this chapter, we will use this method which is a direct search method commonly used as a nonlinear optimization technique. It is known that this method is robust, and easy to implement [126].

Other methods like the gradient methods and the generic optimization algorithms could be used as a minimization tool in the EEG inverse problem. The problem with optimization methods is their efficiency in finding the global or the local minimum. In order to overcome this difficulty, one of the strategies is the use of multi-start values. This option tries local optimization from several starting positions and the solution is the one that best fits the measured data i.e the solution with the minimum residual.

For an EEG inverse problem with constraints in the parameters of the source, gradient-based methods and direct search methods can be used. Gradient-based methods use first derivatives (gradients) or second derivatives (Hes-

sians) of the cost function in the search of the global minimum. In this case, the function to optimize f should be convex, the derivative $\nabla f(x)$ should be Lipschitz continuous i.e

$$\forall x, y \in \mathbb{R}^n \quad \|\nabla f(x) - \nabla f(y)\|_{L_2} \leq K\|x - y\|_{L_2} \quad \text{with constant} \quad K > 0 \tag{3.11}$$

and the second order derivative should be bounded i.e. $\nabla^2 f(x) \leq K^\star$.

3.4. Source of errors in EEG source localization

3.4.1 Introduction

Several studies carried out have shown that dipole estimation errors are due to two major groups of errors: the data related errors and the model related errors. Data errors are due to additive noise in the recorded potentials on the scalp, while model related errors are due to geometrical errors (spherical head models, realistic head models and complex models) and errors in material properties such as conductivity. These errors lead to dipole location and orientation errors in the inverse procedure. A first class of model related errors are source modeling errors. A current dipole source is suitable because it represents an active pyramidal cell at microscopic level [10] but is only valid if the activity itself is limited to a focal region and stays focal over a period of time. For patients suffering from epilepsy, focal brain activity is mostly the case. In order to reduce these source modeling errors, it is possible to use more complex source models. Distributed source models can represent an alternative where the problem is highly under- determined and regularization methods are required, e.g. [11]. Another approach consists of limiting the parameters of the multidipolar sources to be less than the number of electrodes, e.g. the RAP-MUSIC algorithm as in [12].

A second model related error is the possible inaccurate geometrical modeling of the head. Recent studies in [127] have shown that due to inaccurate geometry modelling, scalp potentials are highly sensitive to the complexity of the head model. Since we can use patient-specific head models based on T_1 segmented magnetic resonance images, it is possible to have an accurate geometrical modeling of the head.
A third type of forward modeling errors can be electrode misplacements. The electrodes are placed at standard positions following the 10-20 international system. However, it is possible that certain electrode positions differ from the

standard positions due to inter-patient variability of the head geometry or due to inaccurate placement of the electrodes. One of the needs for recording good EEG signals is the type of electrodes used. Electrodes that make the best contact with a subject's scalp and contain materials that conduct EEG signals very well, provide the best EEG recordings. To solve this problem, high quality EEG electrodes as mentioned in [128], are actually designed and used to reduce noise. This leads to an improvement of a high quality of EEG signals which are needed for the inverse problem. However, by using correct EEG electrode placement techniques, it is possible to decrease that source of error [17], or by using more electrodes in the EEG source analysis problem [18].

Errors are also due to inaccurate modeling of conductivities of brain tissues. A new approach consists today to use anisotropic conductivity properties instead of isotropic conductivity properties as traditionally used for spherical head models, coupled to a realistic head model in order to improve the accuracy of the solution of the inverse problem.

In order to reduce noise in EEG measurements, a variety of methods are currently in use, including those based on linear filtering and adaptive noise cancelation, as well as subspace-based methods using singular value decomposition (SVD). In [129], EEG noise cancellation is obtained using a subspace method based on wavelet decomposition. Typically, their design is made in such a way that the movements of artifacts that usually distort EEG results, are reduced. A special technique of removal EEG noise and artifact using blind source separation was recently developed in [130].

3.4.2 Propagation of the uncertain conductivity to the inverse problem

It is known that the skull conductivity plays a crucial role in EEG dipole analysis. Since the introduction of the equivalent current dipole inside a set of concentric spheres as a tool for performing EEG source localization, attempts have been made to determine the electrical conductivity of the human skull [44]. This has resulted in a large number of papers and a corresponding large number of different values for the conductivity. This variability is caused by different approaches chosen in these various studies. Nevertheless, most researchers continue to take conductivity parameters from the standard references as found in the literature, presumably because there is no better method currently available.

The quality of the solution of the inverse problem is highly dependent on the values of these constants as pointed out in [131]. In the EEG case particularly, large systematic errors in the localization of the sources may arise due to errors in the values of the electrical conductivities.

In practice, the values of the electrical conductivities are taken from the literature [5] and they result from very few conductivity measurements which, most of the time, were performed on isolated samples of tissue. These values vary over a wide range and there might be a factor of 7 between the minimum and maximum conductivity values reported for a certain tissue [132]. This wide range of values might be due to several factors. The tissues are inhomogeneous and anisotropic and therefore differences in the measured conductivity coupled to variations in the orientation of the cells in the tissue, are to be expected. This is the case in e.g. brain tissue in which the measured conductivity is different if transversal or longitudinal fibres are considered. Also, the resistivity of the tissues depends on factors such as the water content, which might generate a change in the conductivity during measurement [133]. Physiological processes might also induce changes in the electrical conductivity of tissues. Finally, true inter-subject variations in the measured conductivity are to be expected due to the natural variation of the tissues from individual to individual.

The quantitative values of the electrical conductivity of the brain and the skull remain a very important parameter that attract a lot of debates in the EEG source analysis research field, see e.g. [5], [6]. A large number of methods to estimate the electrical conductivities of the head exist but uncertainties on the real values of conductivity of individuals are still an unresolved problem, thus introducing inaccuracies into forward model computations. This variability in results is in part caused by different approaches chosen in these various studies. Such situation leads to two options: the conductivity of the skull has to be either accurately measured by a reliable technique, or the uncertainties in the conductivity values should be reflected in uncertainty in the source location estimates.

Taking any average value of the conductivity as a basis for the forward model will obviously lead to unaccounted differences from subject to subject. In vivo measurements of individuals can partially solve the problem by providing subject-dependent data but measurement errors associated with this approach introduce uncertainty and such studies are difficult to conduct on a routine basis with existing EEG equipment [134]. It is important to understand this uncertainty and its propagation on results of forward models and inverse so-

lutions in order to have some confidence bounds on the solution and to have results that are consistent with the underlying source.

3.5. Results of traditional method

3.5.1 Introduction

In our numerical evaluation of the forward model, a standard configuration of 27 electrodes is used to compute the potential distribution given an actual value of conductivity ratio X as described in the expression of the solution of the Poisson's equation in equation (2.14). Conductivity values in this section, are taken from the standard references despite of the large variability in the available data. In the present case, the skull to soft tissue conductivity ratio is assumed to be in the interval $[1/40, 1/9]$. The reconstructed dipole positions $\mathbf{r}_d^*$ are then computed using the traditional method, i.e. solution of (3.1) using (3.4). The accuracy of the method is determined by the dipole localization error defined in (3.5) for different values of the conductivity ratio X in the chosen interval.
Results of the Monte Carlo simulations for various dipole locations using the previous set of conductivities and different dipole orientations are given in the next figures. The locations of the dipole $\mathbf{r}_d$ used in the computations are given in the table 2.2 of the previous chapter, and the orientations of the dipole are in the e_x, e_y and e_z directions.

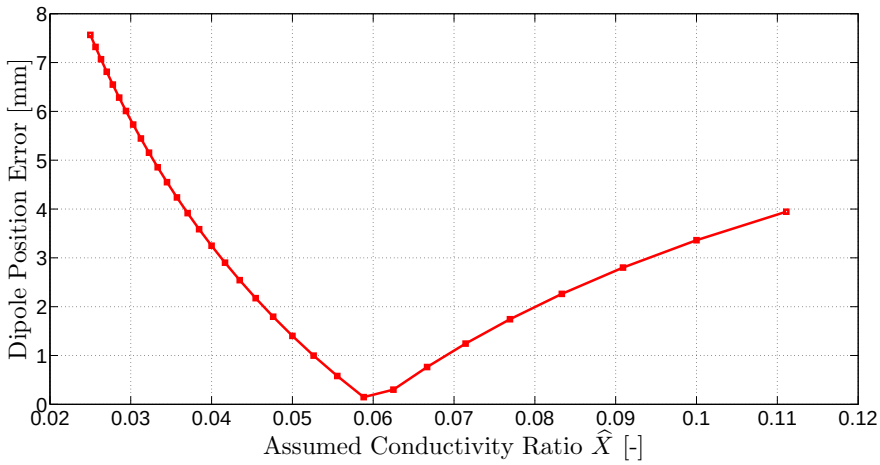

Figure 3.3: Results of inverse problem for dipole located at the edge of the head model CS4 with orientation $\mathbf{e}_y$.

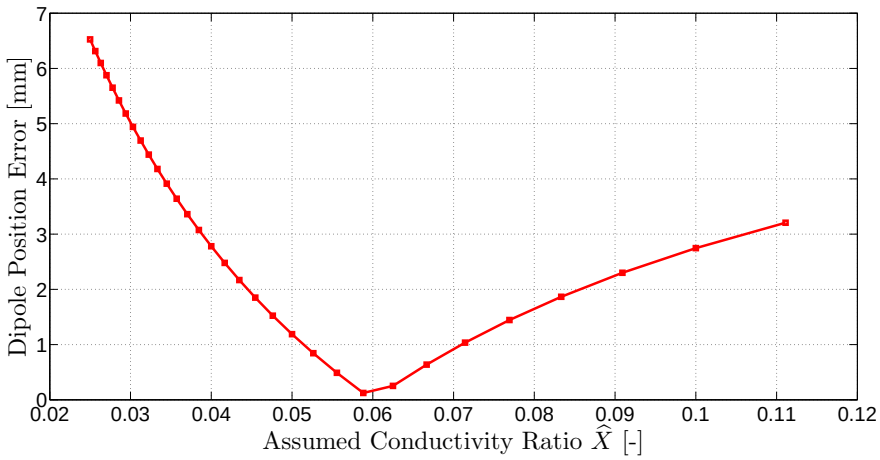

Figure 3.4: Results of inverse problem for dipole located inside the spherical head model CS3 orientation $\mathbf{e}_y$.

When the assumed conductivity ratio is equal to the actual one i.e. $\widetilde{X} = \widehat{X}$, then the reconstructed dipole is equal to the actual dipole position that is $\widetilde{\mathbf{r}}_d = \mathbf{r}_d^*$ (DPE = 0). When the value of the assumed conductivity ratio $\widehat{X}$ is very low for the case we are considering here, the error in dipole localization that could be made can be above 9 millimeters in the entire spherical head model. It was observed during the computations that this value remains high for any value of the actual conductivity value no matter of the regions in which the dipole is positioned in the head model. In the figures below, $\widetilde{X}$ denotes the actual value of the conductivity, while $\widehat{X}$ denotes the assumed value of the conductivity ratio.

We should remind here that the choice of the conductivity set is not unique. A large set of conductivities ranging from $1/80$ to $1/5$ can also be taken for evaluations. In such a case, the choice of a different value of the actual conductivity value $\widetilde{X}$ leads to the same structure of results. From the results of figures (3.3-3.5), we can conclude that the dipole localization error increases as we moved from the center to the edge of the spherical head model. This remark is true in general no matter of the orientation of the dipole and the chosen brain-skull conductivity ratio. There is a correlation between low conductivity ratio and high value in dipole localization error as explained above. The main remark coming out from various Monte Carlo simulations made when solving the EEG inverse problem is that the accuracy in the recovering of the neural dipole, depends on the conductivity and the dipole orientation in the brain. In the next section, sensitivity analysis is conducted and the impact of the results in the inverse problem for different models for

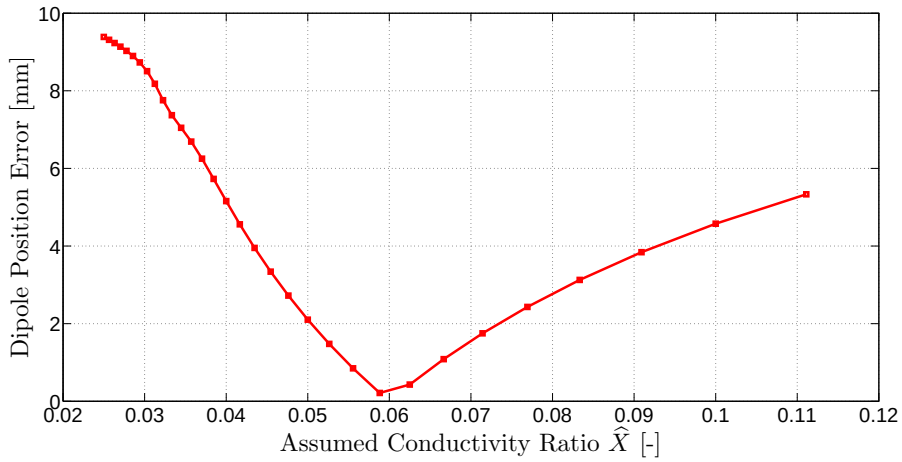

Figure 3.5: Results of inverse problem for dipole located at the edge of the head model for dipole CS4 with orientation $\mathbf{e}_x$.

the source is discussed

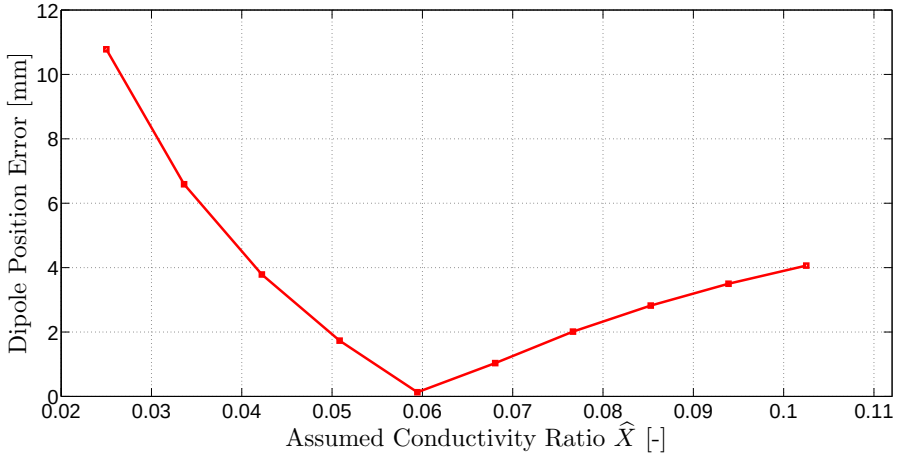

Figure 3.6: Dipole Localization error for dipole CS4 when $\widetilde{X} = 1/16$ with orientation $\mathbf{d} = \begin{bmatrix} 0.5, & 0.4, & 0.7 \end{bmatrix}$.

3.5.2 Influence of the conductivity on dipole localization error

As said already when solving the inverse problem, we assume a conductivity ratio $\widehat{X}$, that may differ from the actual value $\widetilde{X}$. The choice of $\widehat{X}$ may lead to a very significant value of the error as we can see below. For example, the error of 12 mm generated by the use of the conductivity ratio 0.025 instead of the actual conductivity ratio $\widetilde{X} = 0.06$, is bigger than the error generated by 50% of noise in the measurements ($\simeq 5$ mm) as observed in figures 3.6 and 3.7. White Gaussian noise with standard deviation Σ was incorporated using (2.17), see also figure 3.2. The noise values are uncorrelated between the scalp electrodes and are therefore called spatially white. We define the noise level as follows:

$$\mathrm{nl} = \frac{\Sigma}{V_{RMS}} \tag{3.12}$$

where V_{RMS} is known as the root mean square value of electric potential

$$\mathrm{V}_{RMS} = \sqrt{\frac{1}{N}\sum_{i=1}^{N} V_i^2} \tag{3.13}$$

with N the number of sensors.

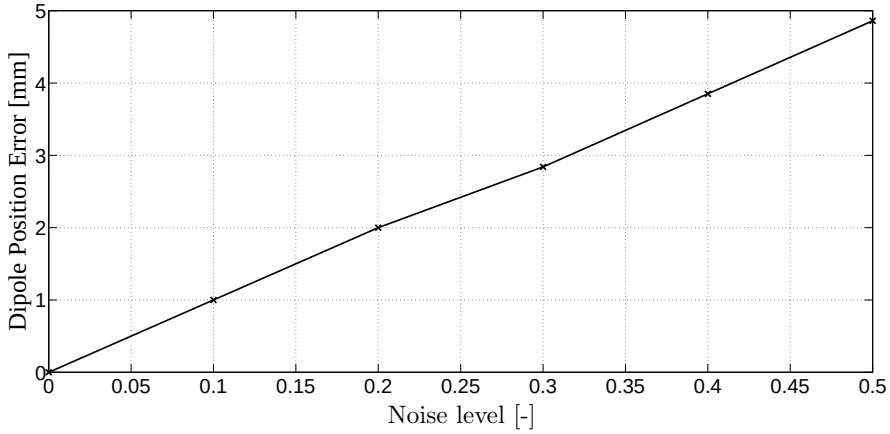

Figure 3.7: Error in the presence of noise for dipole CS4 when $\widetilde{X} = \widehat{X} = 1/16$ with orientation $\mathbf{d} = \begin{bmatrix} 0.5, & 0.4, & 0.7 \end{bmatrix}$.

3.6. Conclusion

The accuracy of the EEG inverse problem highly depends on the conductivity ratio X as observed in the simulations. We even observed that the influence of the conductivity ratio X can even exceed the influence due to noise for cases with a large discrepancy between the assumed and actual X. Results indicate that the source location error generally increases as the dipole moves away from the center of the head toward the boundary. In the case of the traditional method, the influence of the conductivity ratio uncertainty on the inverse solution is quite high and can be of the order of centimeters.
Results of sensitivity analysis in all the dipole positions have shown very high sensitivity values for low skull conductivity ratios. We can conclude from this study that potentials in the EEG forward problem are highly sensitive to the conductivity ratio X and influence the reconstruction accuracy of the neural source.

CHAPTER 4

EEG Single Dipole Analysis using Reduced Conductivity Dependence Method

4.1. Introduction

The estimated source locations starting from the EEG signals are highly sensitive to the electrical conductivity of the head tissue as observed in the results section of the previous chapter. We observed using numerical experiments that the uncertainty in the skull to soft tissue conductivity ratio may lead to high dipole localization errors. This chapter introduces a new approach – the Reduced Conductivity Dependence (RCD) method – for obtaining solutions of the inverse problem that are more accurate in the sense that the results are less degraded by the uncertain conductivity ratio. In order to obtain this improvement of the spatial accuracy of the EEG source localization, the fundamentals of the proposed method are the use of the sensitivity of the potentials at the various electrodes and the formulation of novel cost functions.

As explained in section 3.4, the solution of the EEG inverse problem mainly depends, next to the measurement noise, on three factors: the geometry of the head, the accuracy of the electrode placements, the accuracy of the conductivity values. The uncertainty of the conductivity values has been reported to be the most dominant uncertain factor in EEG source analysis e.g. [22, 24, 28, 39, 40, 96]. The geometry of the head can be modeled very accurately using segmented T1 Magnetic Resonance images and can be included in the forward numerical method, see also section 2.6.3. Moreover,

the electrodes can be placed nowadays very accurately and the introduced dipole localization errors are relatively smaller compared to the errors due to the use of wrong conductivity values [135]. In [20, 46, 86, 136] it is also shown that the inclusion of the anisotropic conductivity of the several tissues improves the dipole localization by a few centimeters. However, the solution still suffers from the uncertainty of the conductivity values and leads to high errors in the dipole locations.

From a clinical point of view, it is important to recall that values of the conductivity of the human tissues are not fixed for patients. Usually these values are located within a certain interval (see [30,32,34]). In addition to this, it is stated in [25] that in clinical practice, the skull conductivity value varies highly among subjects. See also section 2.1.2 for more details.

Increasing the localization accuracy of source localization is one of the main concerns in EEG: accurate electrode positioning systems, anisotropic realistic patient-specific head models, etc. The approach developed in this dissertation does not introduce alternative modeling of the forward model but uses alternative cost function formulations. Information available in the existing forward head models is used for obtaining more accurate dipole localization. In contrast to most previous works, we construct an algorithm that takes into account the sensitivity of the potentials in the inverse procedure. The proposed RCD method relies on the computation of the sensitivity values at the several electrodes (see section 2.8), at the opposite of the traditional method where this is not taken into account. In section 4.2 we describe the RCD method. Section 4.3 elaborates on the cost functions used in the RCD method. Section 4.4 shows the effect of the sensitivity on source localization and section 4.5 gives some computational aspects of the RCD method. Results and discussions are provided in sections 4.6 and 4.7.

4.2. Description of the RCD method

4.2.1 Introduction

The traditional EEG minimization method for the recovery of a single dipole has the drawback to have high errors in recovered dipole sources, see section 3.5, when using conductivity values which are different from the actual conductivity values. The results of the numerical experiments showed that this error depends on the location of the active region in the brain and the orientation of the electrical dipole. In clinical application, the epileptogenic zone should be located and identified with the best possible accuracy before

treatment and surgery. A high value of error is not in the interest of the patient suffering from epileptic seizures or refractory epilepsy.

This section explains the basic ideas of the RCD method, the used forward model and the iterative procedure of the RCD method.

4.2.2 Taylor expansion of the forward model

In order to handle the variability of the conductivity ratio, we use a Taylor expansion of the forward model that includes the derivative terms of the potentials to the conductivity. Hence for a given position $\mathbf{r}_d$ and orientation $\mathbf{d}$ of the dipole, we have:

$$\mathbf{V}_m(\widetilde{X},\mathbf{r}_d,\mathbf{d}) = \mathbf{V}_m(\widehat{X},\mathbf{r}_d,\mathbf{d}) + (\widetilde{X}-\widehat{X})\frac{\partial \mathbf{V}_m}{\partial X}\Big|_{X=\widehat{X}} + \frac{(\widetilde{X}-\widehat{X})^2}{2}\frac{\partial^2 \mathbf{V}_m}{\partial X^2}\Big|_{X=\widehat{X}} + \mathcal{O}(\mathrm{h}^3) \tag{4.1}$$

which relates the potentials of the actual conductivity ratio $\widetilde{X}$ with the potentials for the assumed conductivity ratio $\widehat{X}$. $\mathcal{O}(\mathrm{h}^3)$ denotes the error term with $\mathrm{h} = (\widetilde{X}-\widehat{X})$. When using a concentric three shell spherical head model, (2.14) can be used for the calculation of $\mathbf{V}_m$. This solution, involving the first and the second order derivatives, can be seen respectively as a linear and quadratic model of the potential distribution. This Taylor expanded model will be used in our subsequent evaluations instead of $\mathbf{V}_m(\widehat{X},\mathbf{r}_d,\mathbf{d})$ that is used in the traditional inverse method, see equation (3.2).

When evaluating the sensitivity distribution of the potential $\partial\mathbf{V}_m/\partial X$ and the second order derivative $\partial^2\mathbf{V}_m/\partial X^2$ in the forward problem, we are using a truncated Legendre series. See appendix B for an explicit formulation in equations (B.9) and (B.10). Due to the fast and quadratic convergence of the infinite series of the solution defined in (2.14) observed in the case of the potential $\mathbf{V}$, 40 terms are used during the computations of these derivatives to ensure convergence. The solution of the EEG forward problem given in (2.14) is iteratively used during the minimization of the cost function, see further section 4.2.4.

4.2.3 Effect of the sensitivity on source localization

As observed in section 2.8, the EEG forward potentials are highly sensitive to the conductivity ratio X. This was reported in figures 2.17, 2.18 and 2.19, especially for low conductivity ratios. Results of the EEG inverse problem have shown that this forward propagation leads to dipole position errors

(see section 3.5). These results can be explained by the high sensitivity values $\partial \mathbf{V}_m / \partial X$ that lead to a high difference between the potentials with the actual conductivity ratio $\mathbf{V}_m(\widetilde{X}, \mathbf{r}_d, \mathbf{d})$ and the potentials with the assumed conductivity ratio $\mathbf{V}_m(\widehat{X}, \mathbf{r}_d, \mathbf{d})$, see the above equation (4.1). It becomes clear that a strategy must be set out to make good use of the sensitivity information when trying to accurately localize the neural electrical dipoles.

The question to obtain more accuracy in the inverse solution with uncertainty of X arises at this point and needs to be addressed. The goal here is not to determine which regions of the brain are very sensitive, but to set out a strategy that provides better accuracy when taking into account the local sensitivity of the potentials. A first answer is to limit the propagation of the uncertainty of the conductivity X to the inverse solution. This is the aim of the RCD method, and this involves a reformulation of the inputs of the cost function as described in section 4.3 and the proposition of a new iterative procedure in the next section 4.2.4.

4.2.4 Iterative procedure of the RCD method

The RCD method proposes an alternative cost function that needs to be minimized for EEG source analysis. The main idea lies in the selection of electrodes that provide useful information in the sense that the electrodes which are selected, are minimally affected by the unknown conductivity in the forward model. Indeed, depending on the location of the electrical dipole and its orientation, some potentials are highly affected by the conductivity ratio X and others are not. This is seen in the results provided by the traditional methods in Figures 3.4 and 3.5. Such behavior of the potentials suggests to select only potentials that are less influenced by the sensitivity as a new approach in order to solve the inverse problem. The selection procedure needs to be performed in each iteration k of the minimization scheme, which is in this case the Nelder-Mead simplex method.
In the following, we present explicitly all iterative steps of the RCD method.

Step 1: Start value $\mathbf{r}_d^{(0)}$ is evaluated in the forward model, yielding the lead field matrix $\mathbf{L}(\mathbf{r}_d^{(0)})$, and simulated potential values

$$\mathbf{V}_m(\mathbf{r}_d^{(0)}) = \mathbf{L}(\mathbf{r}_d^{(0)})\mathbf{L}(\mathbf{r}_d^{(0)})^{\dagger}\mathbf{V}_{\text{meas}}. \tag{4.2}$$

Initialize $k = 0$.

Step 2: Calculate the sensitivity $\mathbf{W}$ of the simulated electrode potentials to the conductivity for an assumed conductivity ratio $\widehat{X}$:

$$\mathbf{W} = \frac{\partial \mathbf{V}_m(\mathbf{r}_d^{(k)})}{\partial X}\Big|_{X=\widehat{X}} \tag{4.3}$$

For the spherical head model, the computation of the sensitivity $\mathbf{W}$ is provided by the analytical solution described in section 2.2.1 of Appendix B. For realistic head models, this sensitivity can be computed using finite differencing.

Step 3: Selection of least sensitive electrodes, based on (4.3). Sensors with the largest sensitivity values are not considered in the EEG inverse problem, since their potential values are much influenced by the assumed value for the conductivity and may lead to large errors in the inverse problem. Here, a ranking of electrodes is carried out with respect to the sensitivity.

In order to compare simulated and measured EEG potentials, the same selection is carried out on the measured potentials $\mathbf{V}_{\text{meas}}$. A limited set of potential values are obtained:

$$\mathbf{S}_m = \text{sel}(\mathbf{V}_m) \in \mathbb{R}^{N_s \times 1}, \tag{4.4}$$

and the corresponding set of measured EEG potentials

$$\mathbf{S}_{\text{meas}} = \text{sel}(\mathbf{V}_{\text{meas}}) \in \mathbb{R}^{N_s \times 1} \tag{4.5}$$

where N_s is the number of selected potentials. A selection is also carried out on the lead field matrix:

$$\mathbf{M}(\mathbf{r}_d^{(k)}) = \text{sel}(\mathbf{L}(\mathbf{r}_d^{(k)})) \in \mathbb{R}^{N_s \times 3}. \tag{4.6}$$

The selection operator $\text{sel}(\cdot)$ reduces an $N \times 1$ vector or $N \times 3$ matrix to a $N_s \times 1$ vector or $N_s \times 3$ matrix respectively. The selection operator is defined by the ranking of the electrodes with respect to the sensitivity (4.3), i.e. N_s potentials with lowest sensitivity are selected.

Step 4 Calculation of updated value of dipole orientation which is less affected by the uncertainty of the conductivity ratio:

$$\mathbf{d}_{\text{opt}}^{(k)} = \mathbf{M}^{\dagger}(\mathbf{r}_d^{(k)})\mathbf{S}_{\text{meas}} \tag{4.7}$$

The optimal dipole orientations in a least squares sense are not computed anymore using (3.3) but using the selected measured potentials and computed lead field matrix $\mathbf{M}$.

Step 5: Calculation of RCD cost function $c^{(k)} \equiv \mathrm{RCD}(\mathbf{r}_d^{(k)})$ defined by (4.15) for the first order and (4.16) for the second order. For further details, see section 4.3.

Step 6: Based on the value of the cost function, the next iterate $\mathbf{r}_d^{(k+1)}$ can be computed. If the termination criteria of the minimization procedure are met, i.e. $c^{(k)} \equiv \mathrm{RCD}(\mathbf{r}_d^{(k)})$ reaches tolerance ε, then stop the algorithm. Otherwise, update $k = k + 1$ and go to *step 2*.

The selection procedure needs to be performed in each iteration k of the minimization scheme, which is in this case the Nelder-Mead simplex method. Different subsets of electrodes can be selected through this procedure.
It is also possible to set a certain threshold γ for sensitivity values where a subset of potentials is formed and used in the inverse procedure. In this case, we impose the following condition:

$$\frac{\partial \mathbf{V}_m(\mathbf{r}_d^{(k)})}{\partial X}\Big|_{X=\widehat{X}} \leq \gamma, \tag{4.8}$$

where γ is a threshold set by the user in the procedure. The start value of the minimization procedure is commonly provided by the user. A flowchart giving a clear description of this proposed RCD method step by step, is presented in figure 4.1.

4.3. Cost function of the RCD method

4.3.1 Incorporation of sensitivity in cost function formulations

Based on the conclusions drawn in 3.6 where the sensitivity of the sensors to the uncertain conductivity ratio are formulated and equation (4.1) that formulates an approximate relationship between the potentials of the actual conductivity ratio and the potentials of the assumed conductivity ratio, we derive here a novel cost function for solving the EEG inverse problem.

In the ideal case (no noise, no electrode mislocations, correct geometry and isotropic conductivities) we can theoretically state that the measured potentials equal the simulated potentials for the actual conductivity ratio $\widetilde{X}$ at the actual dipole position and orientation $\{\widetilde{\mathbf{r}}_d, \widetilde{\mathbf{d}}\}$:

$$\begin{aligned} \mathbf{V}_{\text{meas}} &\equiv \mathbf{V}_m(\widetilde{X}, \widetilde{\mathbf{r}}_d, \widetilde{\mathbf{d}}) && (4.9)\\ &\equiv \mathbf{L}(\widetilde{X}, \widetilde{\mathbf{r}}_d)\widetilde{\mathbf{d}} && (4.10)\\ &\equiv \mathbf{L}(\widetilde{X}, \widetilde{\mathbf{r}}_d)\mathbf{L}(\widetilde{X}, \widetilde{\mathbf{r}}_d)^{\dagger}\mathbf{V}_{\text{meas}} && (4.11) \end{aligned}$$

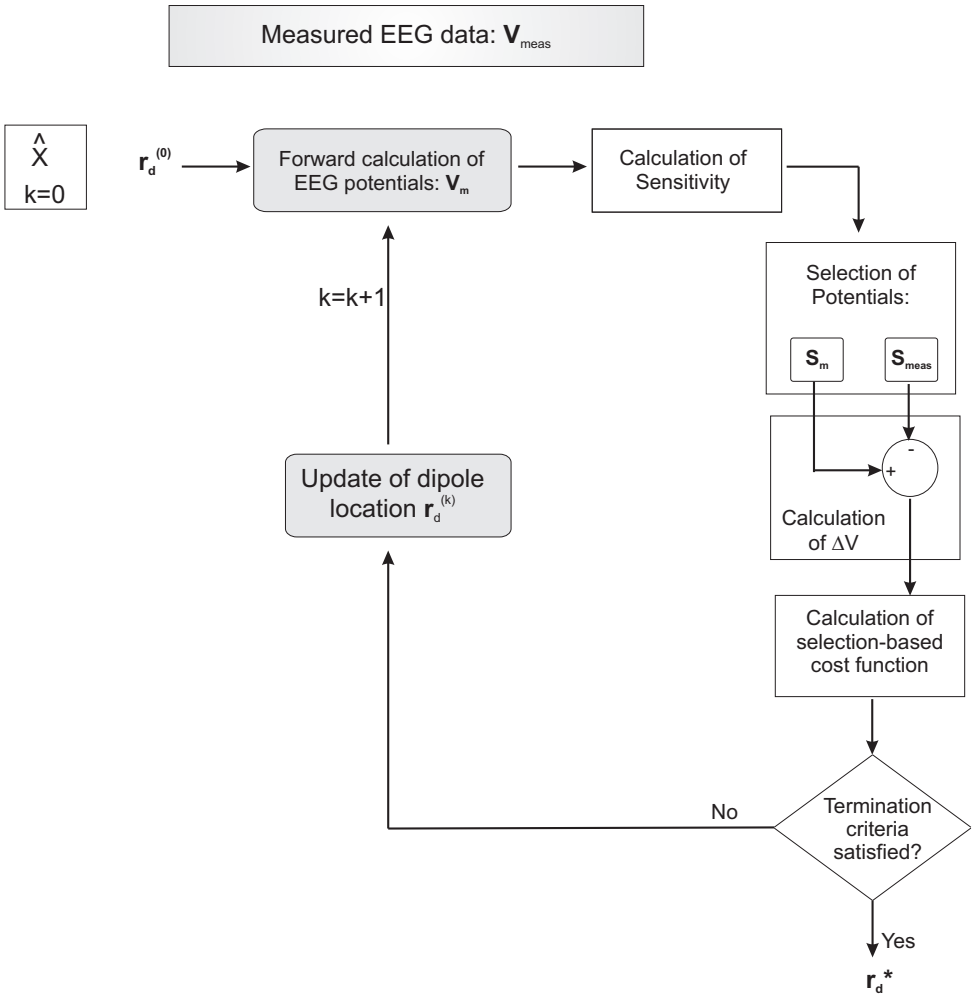

Figure 4.1: Flowchart of RCD method

When using however an assumed conductivity ratio $\widehat{X} \neq \widetilde{X}$, then a dipole location $\mathbf{r}_d^* \neq \widetilde{\mathbf{r}}_d$ corresponds with the measurement vector:

$$\mathbf{V}_{\text{meas}} \simeq \mathbf{V}_m(\widehat{X}, \mathbf{r}_d^*, \mathbf{d}^*) \tag{4.12}$$

where $\simeq$ is a symbolic notation for the closest $\mathbf{V}_m$ to $\mathbf{V}_{\text{meas}}$, meaning that $\|\mathbf{V}_{\text{meas}} - \mathbf{V}_m(\widehat{X}, \mathbf{r}_d^*, \mathbf{d}^*)\|$ is minimal for $\mathbf{r}_d^*$. The term on the right in (4.9) can

be approximated by the Taylor expansion (4.1):

$$\mathbf{V}_{\text{meas}} \simeq \mathbf{V}_m(\widehat{X}, \widetilde{\mathbf{r}}_d, \widetilde{\mathbf{d}}) + (\widetilde{X} - \widehat{X}) \frac{\partial \mathbf{V}_m(X, \widetilde{\mathbf{r}}_d, \widetilde{\mathbf{d}})}{\partial X}\Big|_{X=\widehat{X}} \tag{4.13}$$

where the second right hand side term depends on the propagation of the uncertainty to the forward problem. If one uses a certain assumed conductivity ratio $\widehat{X}$, then (4.13) would be a sufficient forward model, but the Taylor coefficient $\widetilde{X}$ is however unknown. We refer to the next section 4.3.2 for approximating the Taylor coefficient

$$\alpha = \widetilde{X} - \widehat{X} \tag{4.14}$$

The traditional RRE cost function (3.2) for EEG single dipole reconstruction is now reformulated using the above ideas. We formulate the first order RCD cost function as follows:

$$\text{RCD}_1(\mathbf{r_d}, \mathbf{d}) = \frac{\|\mathbf{V}_{\text{meas}} - \mathbf{V}_m(\widehat{X}, \mathbf{r}_d, \mathbf{d}) - \alpha \frac{\partial \mathbf{V}_m}{\partial X}|_{X=\widehat{X}}\|}{\|\mathbf{V}_{\text{meas}}\|} \tag{4.15}$$

and for the second order RCD cost function:

$$\text{RCD}_2(\mathbf{r_d}, \mathbf{d}) = \frac{\|\mathbf{V}_{\text{meas}} - \mathbf{V}_m(\widehat{X}, \mathbf{r}_d, \mathbf{d}) - \alpha \frac{\partial \mathbf{V}_m}{\partial X}|_{X=\widehat{X}} - \frac{\alpha^2}{2} \frac{\partial^2 \mathbf{V}_m}{\partial X^2}|_{X=\widehat{X}}\|}{\|\mathbf{V}_{\text{meas}}\|} \tag{4.16}$$

(4.15) and (4.16) can be formulated in a least squares sense using the optimal dipole components (3.3) in the same way that $\text{RRE}(\mathbf{r}_d, \mathbf{d})$ in (3.2) can be formulated as $\text{RRE}(\mathbf{r}_d)$ in (3.4). We have thus for (4.15), that $\text{RCD}_1(\mathbf{r_d})$ equals:

$$\frac{\|\mathbf{V}_{\text{meas}} - \mathbf{L}(\widehat{X}, \mathbf{r}_d)\mathbf{L}(\widehat{X}, \mathbf{r}_d)^\dagger \mathbf{V}_{\text{meas}} - \alpha \frac{\partial [\mathbf{L}(X, \mathbf{r}_d)\mathbf{L}(X, \mathbf{r}_d)^\dagger \mathbf{V}_{\text{meas}}]}{\partial X}|_{X=\widehat{X}}\|}{\|\mathbf{V}_{\text{meas}}\|} \tag{4.17}$$

with measured potentials $\mathbf{V}_{\text{meas}}$. The second order RCD cost function can be derived in a similar way. Remark that the basic difference between the traditional RRE and the (first order) RCD cost function is the following:

$$\text{RRE}(\mathbf{r}_d) = \frac{\|\Delta \mathbf{V}\|}{\|\mathbf{V}_{\text{meas}}\|}, \qquad \text{RCD}(\mathbf{r}_d) = \frac{\|\Delta \mathbf{V} - \alpha \frac{\partial \mathbf{V}_m}{\partial X}|_{X=\widehat{X}}\|}{\|\mathbf{V}_{\text{meas}}\|} \tag{4.18}$$

with

$$\Delta \mathbf{V} = \mathbf{V}_{\text{meas}} - \mathbf{V}_m(\widehat{X}, \mathbf{r}_d, \mathbf{d}) \tag{4.19}$$

In *steps 3* and *5* of the iterative RCD algorithm given in section 4.2.4, selection is carried out on the potentials, so that the RCD cost function in (4.18) becomes:

$$\mathrm{RCD}_1^s(\mathbf{r}_d) = \frac{\|\Delta\mathbf{S} - \alpha\, \frac{\partial \mathbf{S}_m}{\partial X}|_{X=\widehat{X}}\|}{\|\mathbf{S}_{\mathrm{meas}}\|} \tag{4.20}$$

with definitions (4.4), (4.5), (4.6) and

$$\Delta\mathbf{S} = \mathbf{S}_{\mathrm{meas}} - \mathbf{S}_m \tag{4.21}$$

As in the case of the traditional method (3.1), the electrical dipole coordinates $\mathbf{r}_d^*$ need to be determined using

$$\mathbf{r}_d^* = \arg\min_{\mathbf{r}_d} \mathrm{RCD}(\mathbf{r}_d) \tag{4.22}$$

with the adaptive cost function $\mathrm{RCD}(\mathbf{r}_d)$ elaborated above. The dipole locations are iteratively updated (see *step 6* in section 4.2.4) in the minimization (4.22) using the Nelder-Mead simplex method.

4.3.2 Fitting procedure in the RCD method

The kth iterate $\mathbf{r}_d^{(k)}$ in the minimization (4.22) and for given set of measured EEG potentials yields the following data set:

$$\Delta\mathbf{V}^{(k)} = \mathbf{V}_{\mathrm{meas}} - \mathbf{L}(\widehat{X}, \mathbf{r}_d^{(k)})\mathbf{L}(\widehat{X}, \mathbf{r}_d^{(k)})^{\dagger}\mathbf{V}_{\mathrm{meas}} \tag{4.23}$$

and the sensitivity data set:

$$\mathbf{W}^{(k)} = \frac{\partial[\mathbf{L}(X, \mathbf{r}_d^{(k)})\mathbf{L}(X, \mathbf{r}_d^{(k)})^{\dagger}\mathbf{V}_{\mathrm{meas}}]}{\partial X}|_{X=\widehat{X}} \tag{4.24}$$

We aim at fitting the above N-dimensional data sets (4.23) and (4.24) that yields the fitting constant α. Since in the iterative minimization, $\mathbf{r}_d^{(k)} \neq \widetilde{\mathbf{r}}_d$, this fitting is not linear so that errors are made with respect to the approximation of α. This is observed in figure 4.2, where we relate the absolute values of $\Delta\mathbf{V}^{(k)}$ with $\mathbf{W}^{(k)}$. The iterate $\mathbf{r}_d^{(k)}$ is here approximately 2 mm away from $\widetilde{\mathbf{r}}_d$. In the case of real measured potentials with noise, this difference can become larger and that the residual of the linear fit becomes also larger. When $\mathbf{r}_d^{(k)}$ approaches $\widetilde{\mathbf{r}}_d$ the Taylor coefficient (4.14) is approximated in a more accurate way. This is illustrated in figure 4.3.

The figures 4.2 and 4.3 illustrate the correlation between the potential difference and the sensitivity. The measured potentials correspond here with $\widetilde{X}$

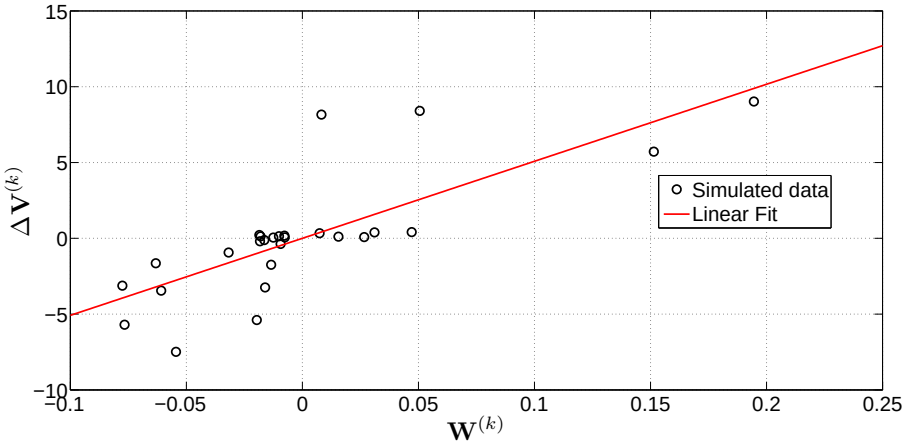

Figure 4.2: Fitting procedure of first order for the dipole position CS3 along the 27 electrodes with an orientation in the $\mathbf{e}_y$ direction with $\widehat{X} = 1/9$ and $\widetilde{X} = 1/16$. $\mathbf{r}_d^{(k)}$ and $\widetilde{r}_d$ are located far from each other.

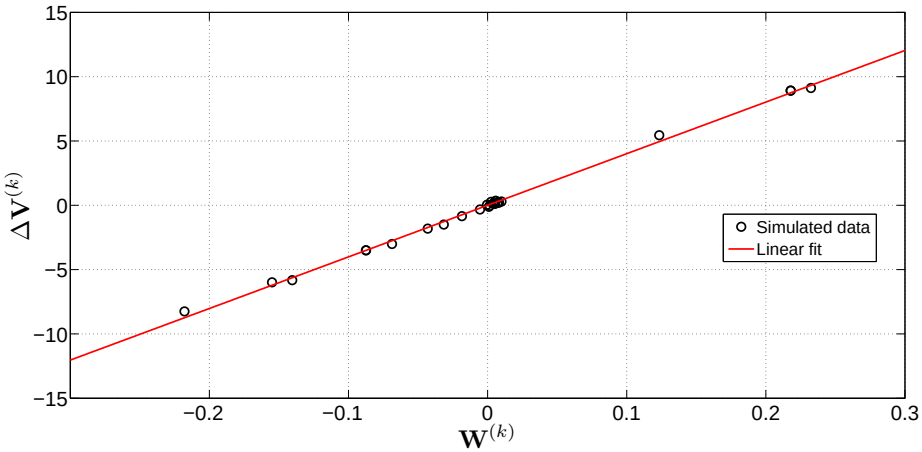

Figure 4.3: Fitting procedure of first order for the dipole position CS3 along the 27 electrodes with an orientation in the $\mathbf{e}_y$ direction with $\widehat{X} = 1/9$ and $\widetilde{X} = 1/16$. $\mathbf{r}_d^{(k)}$ and $\widetilde{r}_d$ are located close to each other.

($\mathbf{V}_{\text{meas}} = \mathbf{V}_m(\widetilde{X}, \widetilde{\mathbf{r}}_d)$), while the forward model is computed with $\widehat{X} \neq \widetilde{X}$. The Taylor coefficients can be determined by performing a linear fitting.

When using the RCD method with the Taylor expansion as a second order expansion (see equation (4.16)), then α needs to be determined by the following:

$$\alpha = \arg\min_{\overline{\alpha}} \|\Delta\mathbf{V}^{(k)} - \overline{\alpha}\mathbf{W}^{(k)} - \overline{\alpha}^2\mathbf{H}^{(k)}\| \tag{4.25}$$

with

$$\mathbf{H}^{(k)} = \frac{1}{2}\frac{\partial^2[\mathbf{L}(X,\mathbf{r}_d^{(k)})\mathbf{L}(X,\mathbf{r}_d^{(k)})^{\dagger}\mathbf{V}_{\text{meas}}]}{\partial^2 X}\Big|_{X=\widehat{X}}. \tag{4.26}$$

This is illustrated by figures 4.4 and 4.5. A fitting is here performed within a plane. Higher order fittings are possible by fitting the data within a hyperplane which can become necessary when the influence of the uncertainty is highly nonlinear upon the output, which is not the case for conductivity in EEG source analysis.

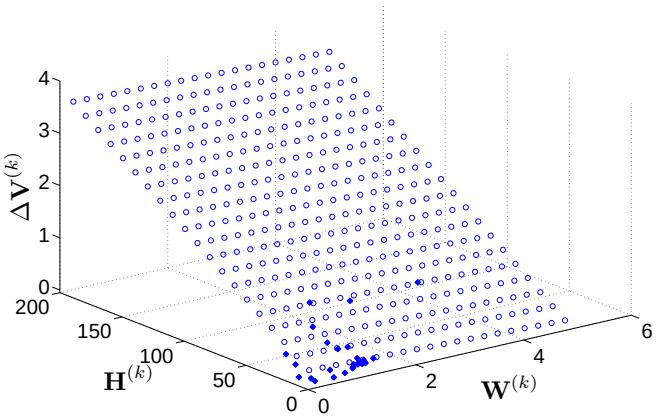

Figure 4.4: Fitting procedure of second order for the dipole position CS3 with orientation $\mathbf{e}_y$. $\mathbf{r}_d^{(k)}$ and $\widetilde{r}_d$ are located far from each other.

We note that when $\widehat{X} \to \widetilde{X}$ the RCD method converges to the RRE method, see (4.18). The fitted line is then close to the $\mathbf{W}^{(k)}$-axis in figures 4.2 and 4.3, while in the second order fitting procedure the fitted plane corresponds with the $(\mathbf{W}^{(k)},\mathbf{H}^{(k)})$-plane in figures 4.4 and 4.5.

4.3.3 Selection procedure of the RCD method

The RCD method offers the possibility to choose a certain number of electrodes out of the given electrode configuration setup, in order to solve the inverse problem. The selection is based on the ranking of the electrodes with

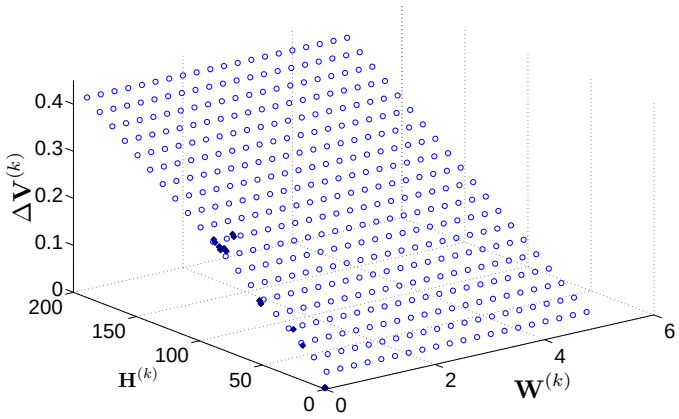

Figure 4.5: Fitting procedue of second order for the dipole position CS1 and with orientation $\mathbf{e}_y$. $\mathbf{r}_d^{(k)}$ and $\widetilde{r}_d$ are located close to each other.

respect to the sensitivity, see *step 2* in 4.2.4 with the selection operator sel$(\cdot)$. Here, the number of selected potentials N_s out of the total set of N electrodes is taken fixed. In section 4.5.3.4 we investigate the influence of the number of selected potentials upon the solution of the inverse problem.

Through the use of a suitable selected set of potentials, the dipole orientation (4.7) can be determined in a more accurate way compared to using (3.3). This is because the lead field components and measured signals that are most affected by the uncertain conductivity value are not included in the determination of the dipole orientation.

In a more general way it is possible to formulate the selection procedure as a weighting of the simulated potentials and measured signals so that (4.4) and (4.5) become:

$$\mathbf{S}_m = \mathbf{K}\mathbf{V}_m \tag{4.27}$$

$$\mathbf{S}_{\text{meas}} = \mathbf{K}\mathbf{V}_{\text{meas}} \tag{4.28}$$

with weighting matrix $\mathbf{K}$. A choice for the i-th diagonal element $K_{i,i}$ could be reciprocal to the sensitivity of the i-th potential.

Here, we use $K_{i,i} = 1$ if the i-th potential is among the N_s least sensitive potentials with ($N_s < N$). Otherwise, $K_{i,i} = 0$. The RCD cost function (4.17) becomes then

$$\text{RCD}_w(\mathbf{r}_d) = \frac{\|\mathbf{K}\mathbf{V}_{\text{meas}} - \mathbf{K}\mathbf{V}_m(\widehat{X}, \mathbf{r}_d) - \mathbf{K}\mathbf{W}(\widehat{X}, \mathbf{r}_d)\|}{\|\mathbf{K}\mathbf{V}_{\text{meas}}\|}. \tag{4.29}$$

When using the approach $K_{i,i} = 1$ or 0 has an advantage: the dipole orientation (4.7) can de determined in a better way, while this is not possible when using continuous $K_{i,i}$ varying values. Furthermore, a more correct comparison between measured and simulated potentials can be performed.

The selected potential subset $\mathbf{S}_m$ is minimally influenced by the skull to soft tissue conductivity ratio. Such choice based on the sensitivity value of the potentials $\mathbf{W}$ provides a more suitable approach in the use of the data during the computations when trying to reconstruct the source. The use of this approach is a direct consequence of the sensitivity analysis, see section 2.8. The advantage of this choice is to limit the effect of the sensitivity of the potentials with respect to the conductivity ratio in the solution of the inverse procedure, since it is known in EEG source analysis that some electrodes are very sensitive to the conductivity ratio X as was observed e.g. in figure 2.13.

The RCD method offers the possibility to choose a minimum of 8 electrodes out of a standard configuration of 27 electrodes actually used, to solve the inverse problem. Below this number, the problem becomes ill-posed since the number of parameters of the dipole i.e. 6 (position $\mathbf{r}_d$ and orientation $\mathbf{d}$) to be recovered should be inferior to the number of sensors N in the inverse procedure. Also, the dipole orientations (4.7) can not be computed accurately. The selection of potentials is chosen to limit the influence of sensitivity on the dipole localization error. And with this option, we can expect a more accurate solution of the EEG inverse problem.

4.3.4 Computation of the sensitivity in spherical head model

In section 4.3.1 we showed that the cost function can be formulated by equation (4.15) where the sensitivity is computed using $\frac{\partial \mathbf{V}_m}{\partial X}$. In appendix B section 2.1 we give an analytical derivation for the calculation of this term in the cost function for the concentric three-shell spherical head model. An alternative cost function formulation uses $\frac{\partial [\mathbf{L}(X, \mathbf{r}_d)\mathbf{L}(X, \mathbf{r}_d)^{\dagger}\mathbf{V}_{\text{meas}}]}{\partial X}|_{X=\widehat{X}}$, see equation (4.17). We refer to section 2.2 in the appendix B for a direct formulation for the calculation of the derivatives. Both approaches presented in that appendix have been validated by finite differencing.

4.4. Results and discussion for EEG single dipole analysis

4.4.1 Introduction

Numerical experiments using Monte Carlo simulations are performed here so to investigate the performance and accuracy of the traditional and RCD method. The simulation setup shown in figure 3.2 is carried out. The dipole localization error (3.5) is a measure for the accuracy of the inverse methods. The RCD algorithm is performed in the same conditions as the traditional method. This includes the same starting point, the same stopping criteria ε and the same maximum number of iterations in the Nelder-Mead simplex method.

In the computations, we use a certain synthetic measured EEG set that is generated for an actual dipole position $\widetilde{\mathbf{r}}_d$, orientation $\widetilde{\mathbf{d}}$ and actual conductivity ratio $\widetilde{X}$: $\mathbf{V}_{\text{meas}} = \mathbf{V}_m(\widetilde{X}, \widetilde{\mathbf{r}}_d)$. When solving the inverse problem, we use a forward model with certain assumed conductivity ratio $\widehat{X}$. The lead fields computed in that forward model are $\mathbf{L}(\widehat{X}, \mathbf{r}_d^{(k)})$ with $\mathbf{r}_d^{(k)}$ the kth iterate in the minimization procedure. We solve different inverse problems, each time with a varied assumed conductivity ratio $\widehat{X}$. We consider the interval $[1/40, 1/9]$ for the assumed conductivity ratio as the numerical experiments carried out in 3.5. See also section 2.1.2 for further details. Moreover, these Monte Carlo simulations are carried out for different $\widetilde{\mathbf{r}}_d$ that correspond with various regions that are active within the spherical head model. See table 2.2 for the different case studies.

We perform experiments in the case of no noise in the data, see section 4.4.2 and in the case of noise in the data, see section 4.4.3, each time without selection and with selection of the electrodes. In section 4.4.4 we define the efficiency of the method. Finally in 4.4.5 we provide a convergence history of the results.

Results obtained in this section when using the spherical head model can be extended to realistic head models with isotropic and anisotropic conductivities. We refer to Appendix C for the results when using a realistic head model.

4.4.2 Results in the no noise case

4.4.2.1 No selection of the electrodes

Figures 4.6-4.9 show the results for the four different case studies when using the RCD cost function. We are using here no selection of the potentials

($N_s \equiv N$ in *step 3* of the RCD method with $N = 27$ the total number of electrodes). The numerical experiments are carried out here for dipoles with a random orientation $\widetilde{\mathbf{d}} = [0.5; \quad 0.4; \quad 0.7]$. We observe an improvement in the accuracy of 7 mm for dipoles located near the edge of the brain in the case of assuming low conductivity ratios $\widehat{X}$. For other dipole positions, an accuracy of 1 mm to 6 mm was recorded. Notice here that when the assumed conductivity $\widehat{X}$ is close or equal to the actual conductivity $\widetilde{X}$, the error becomes zero due to the fact that the RCD method converges to the traditional method.

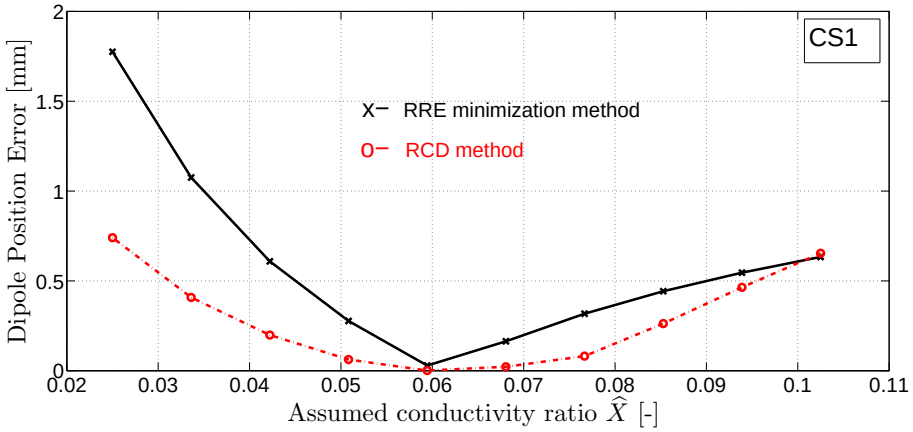

Figure 4.6: Dipole position error for CS1 using the traditional least squares minimization of the RRE and the RCD method ($N = N_s = 27$). The actual conductivity ratio of the simulated $\mathbf{V}_{\text{meas}}$ is chosen as $\widetilde{X} = 1/16$.

The results show that the influence of the uncertain conductivity towards the inverse solutions is reduced, even when selection is not carried out. This is because we are including in the RCD cost function the sensitivity and the fitting procedure. The altered forward model is in this way representing more accurately the system where the measurements are carried out. However, we are observing that the reduction is not always very drastic. Therefore we include in the following, selection of the electrodes $N_s < N$.

4.4.2.2 Selection of the electrodes

The RCD method gives the possibility to select a certain number of potentials that are less affected by the conductivity ratio X when solving the inverse problem. The minimum in our case is $N_s = 8$, otherwise the problem becomes

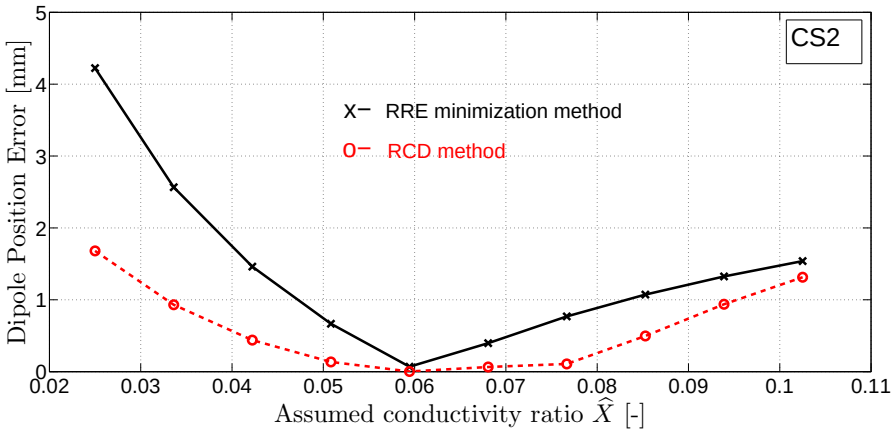

Figure 4.7: Dipole position error for CS2 using the traditional least squares minimization of the RRE and the RCD method ($N = N_s = 27$). The actual conductivity ratio of the simulated $\mathbf{V}_{\text{meas}}$ is chosen as $\widetilde{X} = 1/16$.

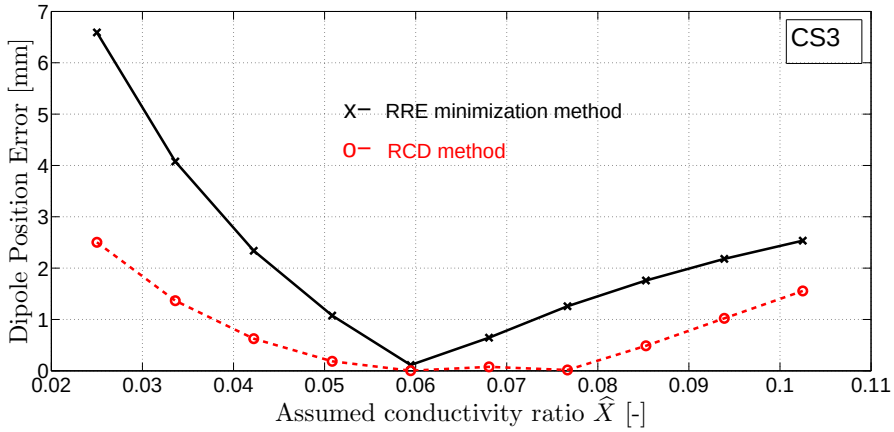

Figure 4.8: Dipole position error for CS3 using the traditional least squares minimization of the RRE and the RCD method ($N = N_s = 27$). The actual conductivity ratio of the simulated $\mathbf{V}_{\text{meas}}$ is chosen as $\widetilde{X} = 1/16$.

ill-posed. It should be noted that the selection criterion is here based on fixing the number of selected potentials N_s in each iteration. It is also possible to consider another selection criterion by using e.g. $\mathbf{W}^{(k)} \leq \gamma$ with selection threshold γ. Since $\mathbf{W}^{(k)}$ contains measurements that can contain noise, this criterion is not universally valid. The number of selected electrodes will in this case be dynamic in each iteration (i.e. N_s may change in each kth iteration

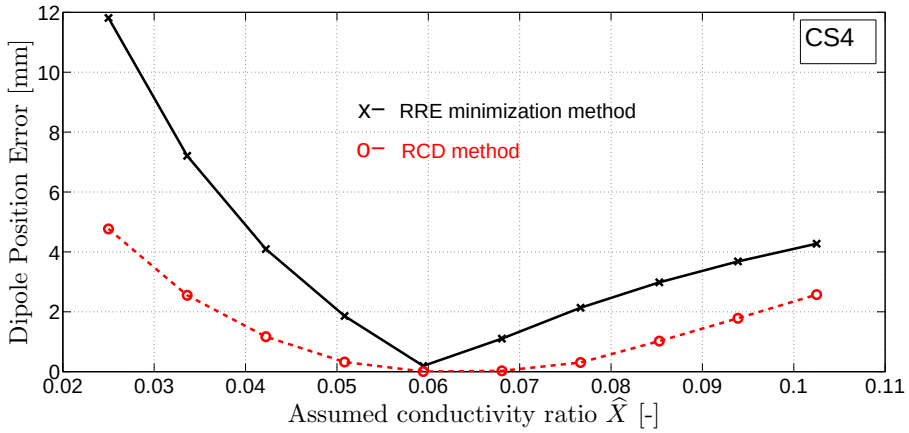

Figure 4.9: Dipole position error for CS4 using the traditional least squares minimization of the RRE and the RCD method ($N = N_s = 27$). The actual conductivity ratio of the simulated $\mathbf{V}_{\text{meas}}$ is chosen as $\widetilde{X} = 1/16$.

of the minimization). In order to investigate the influence of the selection of the electrodes, we fix the number of selected potentials in each iteration of the RCD method.

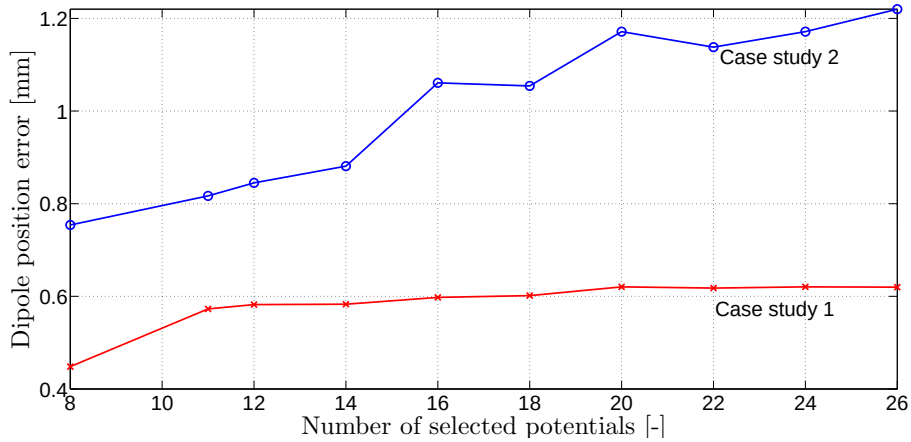

Figure 4.10: Results of RCD Method using selection of electrodes for case study CS1 and CS2 with $\widehat{X} = 1/9$ $\widetilde{X} = 1/16$.

In figure 4.10 we show the results of the RCD method for the two case studies CS1 and CS2 when varying $N_s < N$. The inverse problem is solved with assumed conductivity ratio $\widehat{X} = 1/9$ starting from a no noise data set that

was generated with the actual conductivity ratio $\widetilde{X} = 1/16$. We observe that a better accuracy is achieved when incorporating the selection of the potentials. The results are not monotonically decreasing for decreasing N_s because of numerical instability caused by the fitting procedure within the RCD method. But the general trend is a decreasing error. We show in figure 4.11 the same trend, but then for a dipole CS4 and for a different $\widehat{X}$. The traditional method gives an error of 11.8 mm for this same simulation setup and a decrease in error is again observed.

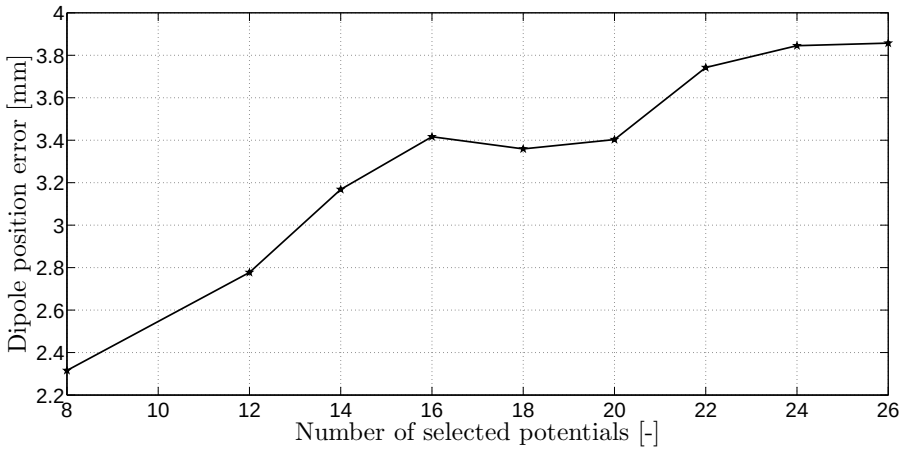

Figure 4.11: Results of RCD Method using selection of electrodes for case study CS4 (with $\widetilde{X} = 1/16$). The inverse problem is solved with assumed $\widehat{X} = 1/40$.

Simulations were performed over a uniform distributed grid of dipoles. We placed dipoles in each voxel (voxel discretization of $\approx$ 4.6mm) and solved the inverse problem for the EEG potential corresponding with that dipole. The EEG cap consisted of $N = 27$ electrodes. The inverse problem was solved using the RCD methodology with number of selected electrodes $N_s = 10$ electrodes. Figures 4.12 - 4.14 show the dipole position errors in mm when using the traditional methodology and when using the RCD methodology for dipoles located in a transversal plane that are $\mathbf{e}_x$, $\mathbf{e}_y$ and $\mathbf{e}_z$ directed. Figures 4.15 - 4.17 show the dipole position errors for dipoles located in a sagittal plane (y=1cm). We observe that overall the dipole position errors are decreased when using the RCD methodology compared to the traditional methodology.

In order to quantify the ratio of increase in accuracy when using the RCD methodology compared to the traditional methodology, we carried out

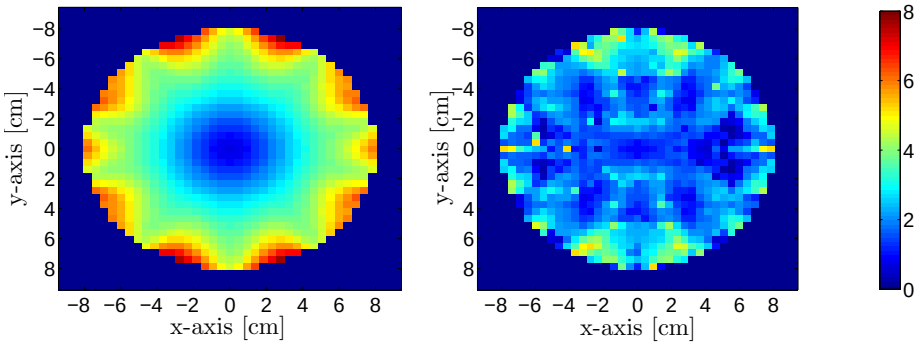

Figure 4.12: Dipole position errors (mm) when using the traditional methodology (left) and when using the RCD methodology (right). $\mathbf{e}_x$-oriented dipoles are placed in each voxel and starting from corresponding EEG potentials, the corresponding inverse problem is solved. The considered slice is transversal, i.e. in the z≈1cm-plane. $N_s = 14$ out of $N = 27$.

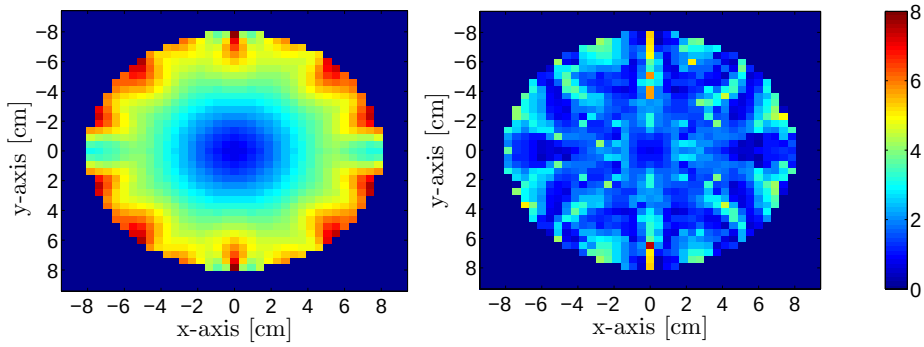

Figure 4.13: Dipole position errors (mm) when using the traditional methodology (left) and when using the RCD methodology (right). $\mathbf{e}_y$-oriented dipoles are placed in each voxel and starting from corresponding EEG potentials, the corresponding inverse problem is solved. The considered slice is transversal, i.e. in the z≈1cm-plane. $N_s = 14$ out of $N = 27$.

numerical experiments with test dipoles located in a three-dimensional grid. This ratio was defined as the ratio of dipole position errors when using the traditional method to the dipole position errors when using the RCD methodology. Again, starting from each dipole location forward EEG signals were simulated and the corresponding inverse problem was solved. In total, 21060 inverse problems were solved. Figure 4.18 shows the histogram of the ratio of increase, i.e. the number of counts (here expressed in percentage) that lie within a certain interval of ratio of increase. We can observe that the ratio of increase in accuracy has a maximal value at about 1.6 and can rise to a

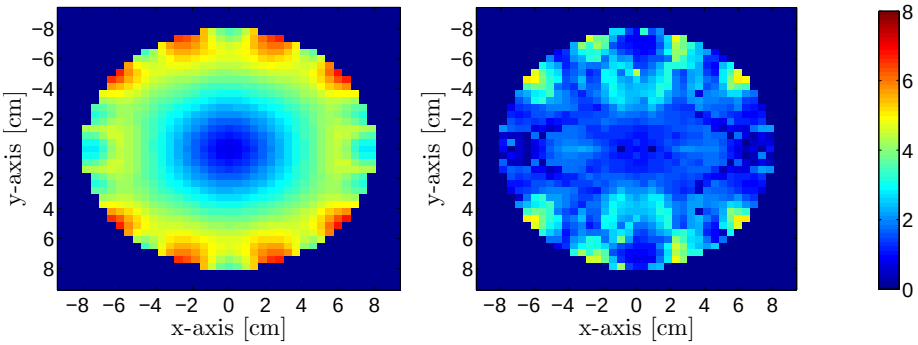

Figure 4.14: Dipole position errors (mm) when using the traditional methodology (left) and when using the RCD methodology (right). $\mathbf{e}_z$-oriented dipoles are placed in each voxel and starting from corresponding EEG potentials, the corresponding inverse problem is solved. The considered slice is transversal, i.e. in the z≈1cm-plane. $N_s = 14$ out of $N = 27$.

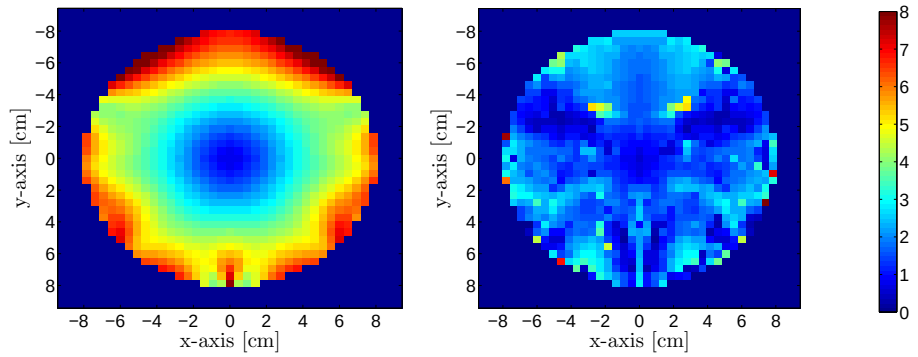

Figure 4.15: Dipole position errors (mm) when using the traditional methodology (left) and when using the RCD methodology (right). $\mathbf{e}_x$-oriented dipoles are placed in each voxel and starting from corresponding EEG potentials, the corresponding inverse problem is solved. The considered slice is sagittal, i.e. in the y≈1cm-plane. $N_s = 14$ out of $N = 27$.

factor of about 5.

4.4.3 Results in the noise case

4.4.3.1 No selection of electrodes

Real measured EEG signals contain noise, environmental noise and the background noise of the brain activity. As pointed out in section 3.4.1, noise limits

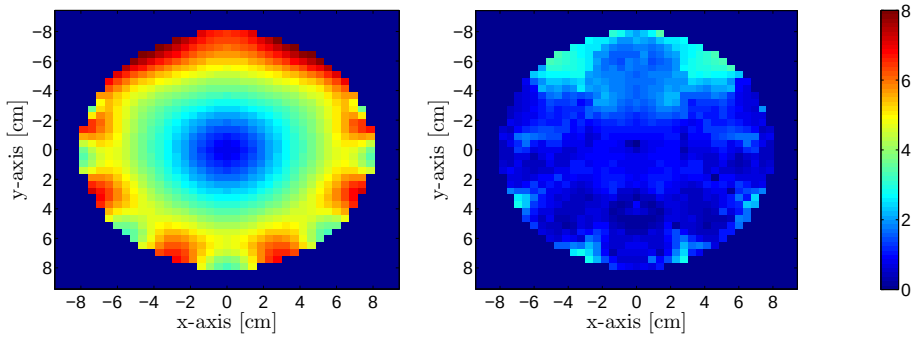

Figure 4.16: Dipole position errors (mm) when using the traditional methodology (left) and when using the RCD methodology (right). $\mathbf{e}_y$-oriented dipoles are placed in each voxel and starting from corresponding EEG potentials, the corresponding inverse problem is solved. The considered slice is sagittal, i.e. in the y≈1cm-plane. $N_s = 14$ out of $N = 27$.

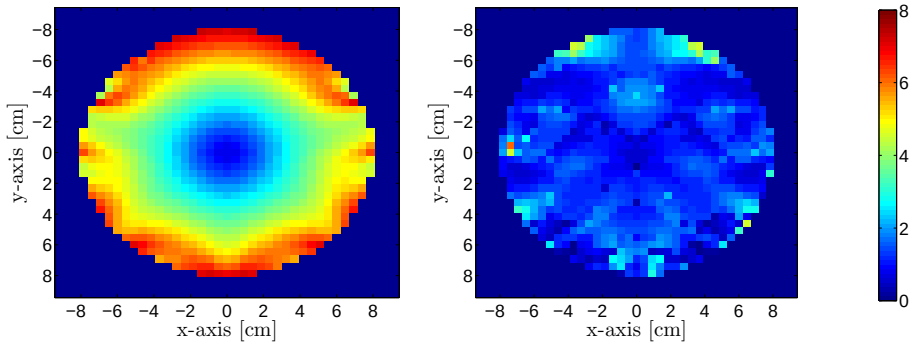

Figure 4.17: Dipole position errors (mm) when using the traditional methodology (left) and when using the RCD methodology (right). $\mathbf{e}_z$-oriented dipoles are placed in each voxel and starting from corresponding EEG potentials, the corresponding inverse problem is solved. The considered slice is sagittal, i.e. in the y≈1cm-plane. $N_s = 14$ out of $N = 27$.

the resolution of EEG source analysis. In this section we assume the noise to be white Gaussian noise, i.e. zero mean with certain standard deviation. See equation (2.17) and figure 3.2. In figure 3.7 we showed the influence of noise upon the accuracy when using the traditional method. The noise level of the Gaussian noise is defined by (3.12). The so-called measured potentials that are simulated here is given by

$$\mathbf{V}_{\text{meas}} = \mathbf{V}_m(\widetilde{X}, \widetilde{\mathbf{r}}_d, \widetilde{\mathbf{d}}) + \mathbf{N} \tag{4.30}$$

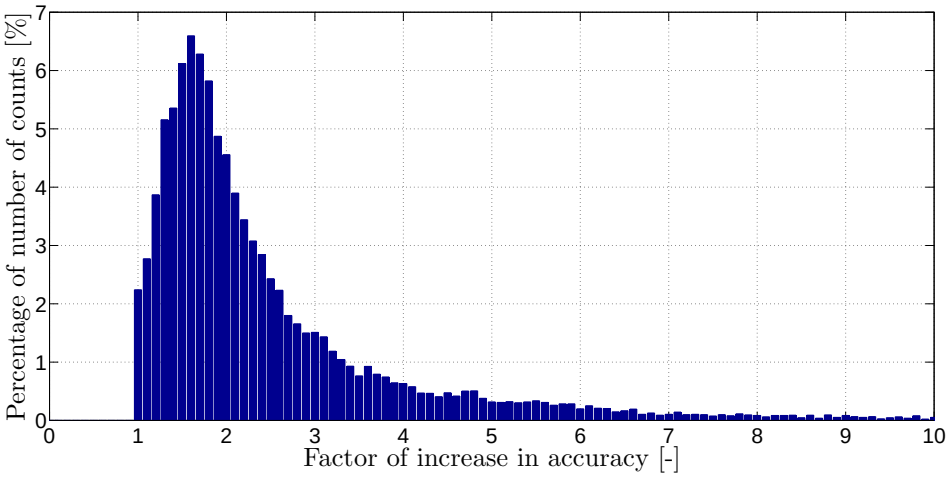

Figure 4.18: Histogram depicting the ratio of increase in accuracy when using the RCD methodology compared to the traditional methodology. Starting from each dipole location, forward EEG signals were simulated and the corresponding inverse problem was solved. In total, 21060 inverse problems were solved. $N_s = 14$ out of $N = 27$ in the RCD method.

with noise vector **N**. In order to have a correct representation of the influence of noise upon the solution, multiple (about 50) data sets are generated with the same noise level. Seven degrees of noise levels (nl) expressed by a percentage will be used in the numerical experiments: nl $= [0\ 0.025\ 0.05\ 0.1\ 0.2\ 0.3\ 0.4]$. The dipole position errors shown here are averaged over the 50 inverse problems that were solved. In the results below, no selection of the potentials is carried out of the standard configuration ($N_s \equiv N$) when using the RCD method. The case nl $= 0$ corresponds to the situation where there is no noise in the potentials, while 0.4 means 40% of noise in the measurements. We will perform our evaluations for the dipole localization error using assumed conductivity ratios in the interval [1/40, 1/9] as illustrated in figure 4.19. We observe a reduction in dipole localization error when using the RCD method in the noise case. For the different assumed conductivity ratios, the RCD method improves the accuracy. As observed here, the best accuracy is recorded in the RCD method for low conductivity ratios $\widehat{X}$.

The next simulation corresponds with the estimation of the average dipole position errors for varying noise levels. The results are shown in figures 4.20 and 4.21 for different locations of the active electrical dipole. It is important to mention here that the residual of the linear fitting procedure becomes larger compared to the case where potentials are without noise. Due to these errors

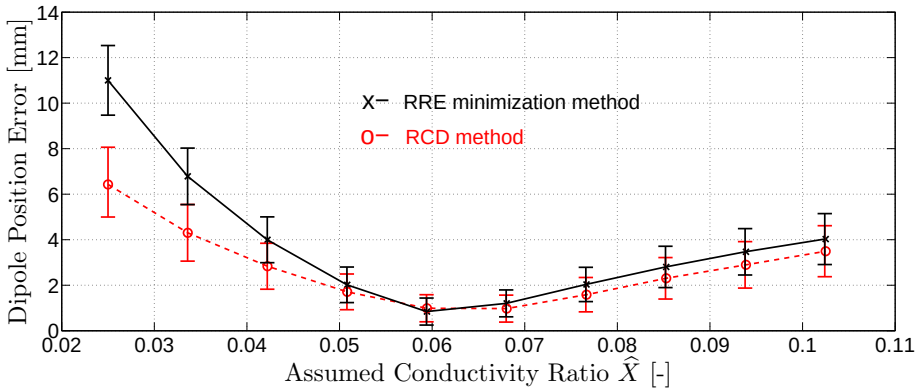

Figure 4.19: Results of RCD Method for noise level nl=0.025 for several conductivities for the dipole located in CS4 with actual conductivity $\widetilde{X} = 0.06$. $N = N_s = 27$.

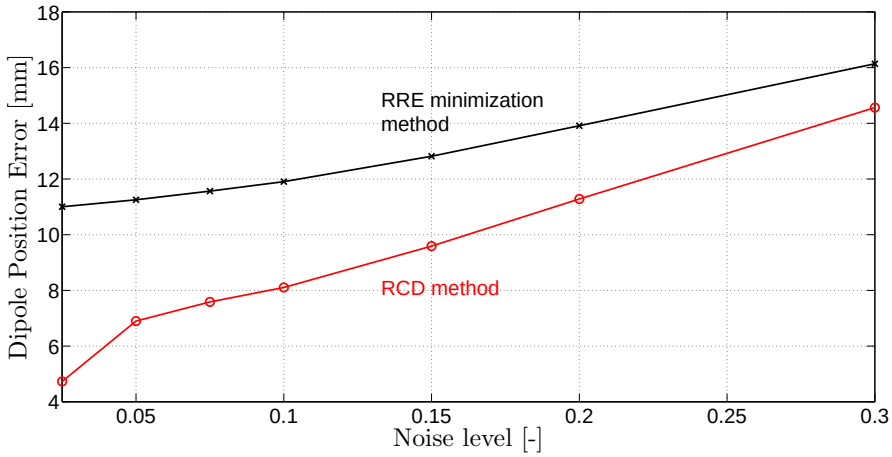

Figure 4.20: Results of RCD Method for various noise levels for Case study CS3,with $\widehat{X} = 1/9$ and $\widetilde{X} = 1/25$. $N = N_s = 27$.

in fitting, the relative increase in accuracy is less for high noise levels than for low noise levels, as we can observe in the provided figures. We refer to section 4.4.4 for defining the efficiency of the RCD method. We provide solutions to increase the accuracy of the RCD method in the case of noise in chapter 5.

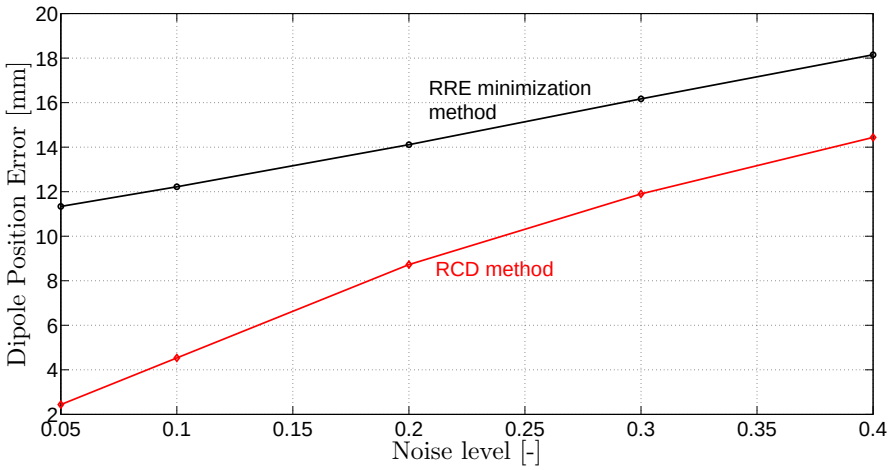

Figure 4.21: Results of RCD Method for various noise levels for Case study CS4, with $\widehat{X} = 1/9$ and $\widetilde{X} = 1/40$. $N = N_s = 27$.

4.4.3.2 Selection of electrodes

We implement now selection of electrodes $N_s < N$ in the case of noisy data sets. Figure 4.22 shows the improvement of the RCD method when incorporating selection. Notice that when using the traditional method, the average dipole localization error is 14.7 mm. When incorporating selection, the resolution is improved by few millimeters as observed in the figure. The reason for this small decrease in dipole localization error is again due to the use of the fitting procedure within the RCD methodology. The total number of electrodes where selection can be performed upon is limited ($N = 27$) here. We refer to section 4.5 of this chapter for increasing the accuracy using selection with a high number of electrodes. Also, chapter 5 shows how the efficiency of the RCD methodology can be increased in the case of noisy data sets.

A numerical instability is observed between $N_s = 15$ and $N_s = 20$, resulting in a decrease in the value of the error. The reason behind this is that the minimization of the RCD cost function does not always result in a global optimum, especially because of the efficiency of the fitting procedure. This is the main drawback of the RCD method: global minimization techniques are needed and the accuracy of the fitting procedure needs to be increased. For the global minimization, the use of multiple start values is an alternative. More generally, we observed that the selection in the noise case provides an improvement of 3 mm for high level of noise to 7.5 mm for small amount of

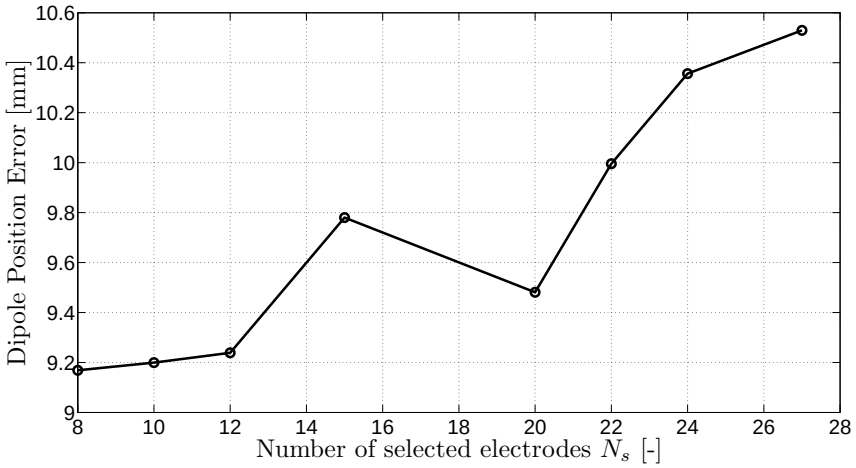

Figure 4.22: Dipole position error for CS3 with noise level nl $= 0.2$. Assumed conductivity ratio $\widehat{X} = 1/30$ and actual conductivity ratio $\widetilde{X} = 1/16$.

noise compared to the traditional solution.

4.4.4 Efficiency of the RCD method

We observed in the previous section that the value of the error for a dipole with location $\widetilde{\mathbf{r}}_d$ and orientation $\widetilde{\mathbf{d}}$ depends on the conductivity ratio X and the amount of noise in the measurements. Taking the error as a function of these two parameters, we define the efficiency of the RCD method as follows:

$$\eta(\mathrm{nl},\mathrm{X}) = \frac{\|\mathrm{E}_{\mathrm{TRAD}}(\mathrm{nl},\mathrm{X}) - \mathrm{E}_{\mathrm{RCD}}(\mathrm{nl},\mathrm{X})\|}{\|\mathrm{E}_{\mathrm{TRAD}}(\mathrm{nl},\mathrm{X})\|} \times 100\% \tag{4.31}$$

where nl is the noise level defined in equation (3.12). $\mathrm{E}_{\mathrm{TRAD}}$ and $\mathrm{E}_{\mathrm{RCD}}$ are the dipole localization errors when using the traditional method and the RCD method respectively.

In the tables 4.1 and 4.2 we give the results of this efficiency for two regions of the active dipole. The first table is for a dipole located at the edge of the brain with no noise in the potentials. The efficiency is given for several assumed conductivity ratios $\widehat{X}$. The second table is the efficiency for a dipole located inside the brain for several noise levels. Results are here displayed for only one assumed conductivity ratio $\widehat{X}$.

$\widehat{X}$	$\widehat{X}_1 = 0.025$	$\widehat{X}_2 = 0.03361$	$\widehat{X}_3 = 0.0422$	$\widehat{X}_4 = 0.05083$
η	59.64 %	64.63%	71.49%	82.63%
$\widehat{X}$	$\widehat{X}_5 = 0.306$	$\widehat{X}_6 = 0.08528$	$\widehat{X}_7 = 0.09389$	$\widehat{X}_8 = 0.10250$
η	85.65%	65.79%	51.52%	39.78%

Table 4.1: Efficiency of the RCD method when $\widetilde{X} = 1/16$ and many assumed conductivity ratios $\widehat{X}$ for dipole CS4.

Noise Level	5%	10%	20%	30%	40%
η	78.48%	62.89%	38.16%	26.41%	20.44%

Table 4.2: Efficiency of the RCD method when $\widehat{X} = 1/9$ and $\widetilde{X} = 1/40$ for dipole CS3.

When nl $= 0$, the RCD method has an efficiency going from 12% to 81.5%, depending on the number of electrodes that is used to solve the inverse problem. When the measured potentials contain noise, an efficiency of 10% up to 80.00% was recorded in the entire spherical head model depending on the noise level and the location of the dipole. Using measure (4.31) it becomes clear that it is necessary to increase the efficiency of the RCD method in the noise case but that the high efficiency in the no noise case is sufficient.

4.4.5 Convergence history

For recovering the location of the electrical dipole, a common starting point is used each time: $\mathbf{r}_d^{(0)} = [0 \quad 0 \quad 0.1]^{\mathrm{T}}$ that is located close to the center of the spherical head model. As mentioned in the description of the RCD method 4.2.4, the iterates $\mathbf{r}_d^{(k)}$ are updated using the RCD cost function. See also figure 4.1.

The selection procedure is dynamic along all the sensors of the given configuration within the minimization process as illustrated in figure 4.23. This figure shows that in each iteration, a different subset of electrodes are selected within the minimization procedure of the RCD cost function. The number of selected electrodes in the figure is here $N_s = 10$. Note that in the beginning of the minimization procedure the labels of selected potentials are varying to a large extend. When reaching the optimum, the selection is not varying much because the locations $\mathbf{r}_d^{(k)}$ are not varying much anymore.

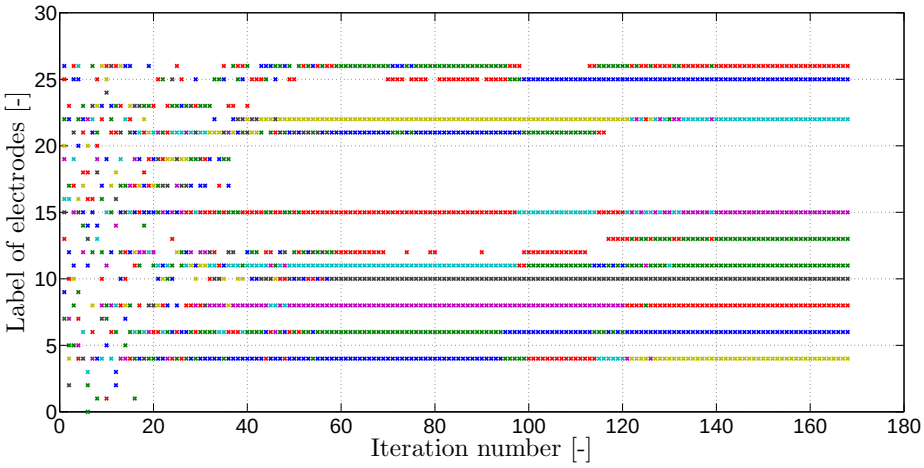

Figure 4.23: Indices of selected potentials during minimization of RCD cost function with $\widetilde{X} = 1/20$, $\widehat{X} = 1/16$. Recovery of dipole CS2 with $N_s = 10$ electrodes during the minimization of the RCD cost function.

A maximum number of 500 iterations was fixed in the recovering of the dipole when solving the inverse problem using the traditional and the RCD method. The iterative procedure needs approximately 50-100 forward function evaluations in order to minimize the RCD cost function. Since the selection of potentials leads to the use of a subset whose number is always less than the number of measurements in the initial configuration, the norm of the RCD cost function is always less than the one of the traditional case. However, these norms are equal when the assumed conductivity $\widehat{X}$ is equal to the conductivity $\widetilde{X}$. They also require the same number of iterations in this case to converge towards the same optimal solution. Remark that other minimization procedures can be implemented. The RCD method can be implemented in any possible iterative minimization procedure.

Figure 4.24 shows us the convergence history of both methods for dipole CS3 with the assumed conductivity ratio $\widehat{X} = 1/40$ starting with potentials that are generated with the actual conductivity ratio $\widetilde{X} = 1/25$. The dipole location that corresponds with the minimum of the RCD method gives a better solution since its error is lower, compared to the one of the RRE cost function. We deduce from this figure that the RRE value is large when we are close to the accurate solution. As illustrated in figure 4.10, an improvement of the spatial resolution is also obtained with the selection of potentials. Moreover, the minimal value of the RCD method does not correspond with the minimal value of the RRE method. This shows that for the traditional RRE method a

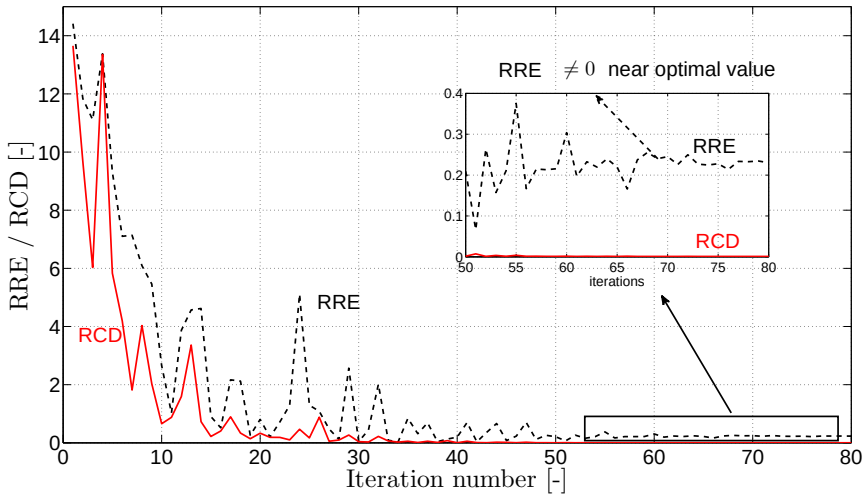

Figure 4.24: Convergence history of both methods.

solution closer to the actual dipole has a higher cost and thus recovers dipoles further away from the actual dipole. In general, the minimal value of the RCD method does not correspond with the one of the traditional method when the stopping criteria ε is reached.
It is essential to mention that the RCD method requires more computational time than the traditional method in order to reach the global minimum. The main reason is that the RCD method needs various evaluations of the derivatives associated to the RCD cost function.

4.5. Applications of RCD method to a higher number of electrodes

4.5.1 Introduction

A first step towards increasing the spatial accuracy of the EEG inverse problem has been made in the previous sections. We observed that an increase is observed but that the selection procedure is suboptimal when using a limited number of measurement electrodes, see section 4.4.3.2. Indeed, the RCD method, improves the source localization accuracy approximately two to three times, depending on the location of the dipole, for a standard configuration of 27 electrodes when using a three-shell spherical head model.

In this section, results of the RCD method are presented for a higher number of electrodes configurations. The RCD cost function remains the same, and the number of electrodes initially set at 27 electrodes increases up to 148

electrodes. The coordinates of the various systems of electrodes are given in Appendix A.

We will apply the RCD methodology to a higher set of electrodes than the set of 27 electrodes previously used. We will compare the improvement of the spatial accuracy when using the RCD method onto different EEG caps. Numerical experiments using Monte Carlo simulations will be performed in the same conditions as previously defined.

4.5.2 Sensitivity analysis

When increasing the number of electrodes, the inter-electrode distance is reduced compared to the 10-20 international system as observed in figure 2.4. In our simulations, the potential distribution $\mathbf{V}$ on the spherical head model is computed for several electrode configurations. For each electrode configuration we investigate the impact on the EEG source localization accuracy.

All configuration systems follow the widely used International standard 10–20 system. Computations of the EEG potentials over the head are done for 56, 64, 74, 112 and 148 electrodes. As an example we show the potentials for the setup with 56 and 74 electrodes in figures 4.25, 4.26 for dipole position CS2. It is clear that a better sampling is made on the scalp of the electrical activity within the brain when using a higher number of electrodes.

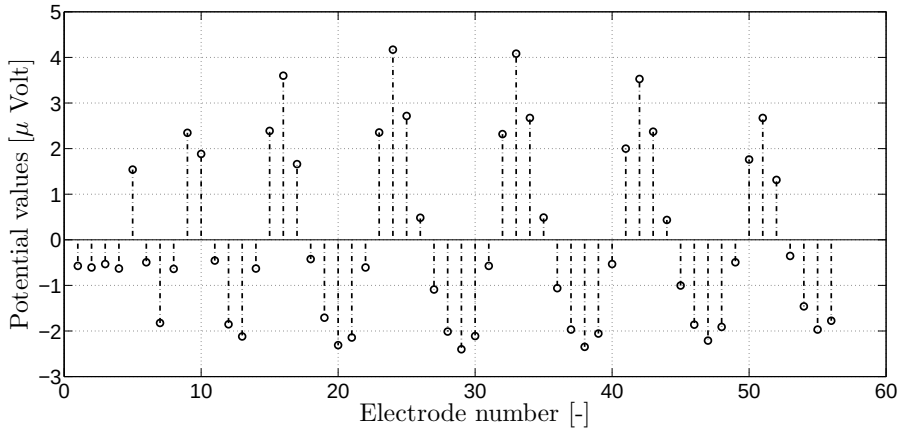

Figure 4.25: EEG Potential for 56 electrodes with actual conductivity ratio $\widetilde{X} = 1/40$ for dipole position CS2 with orientation $\mathbf{e}_y$.

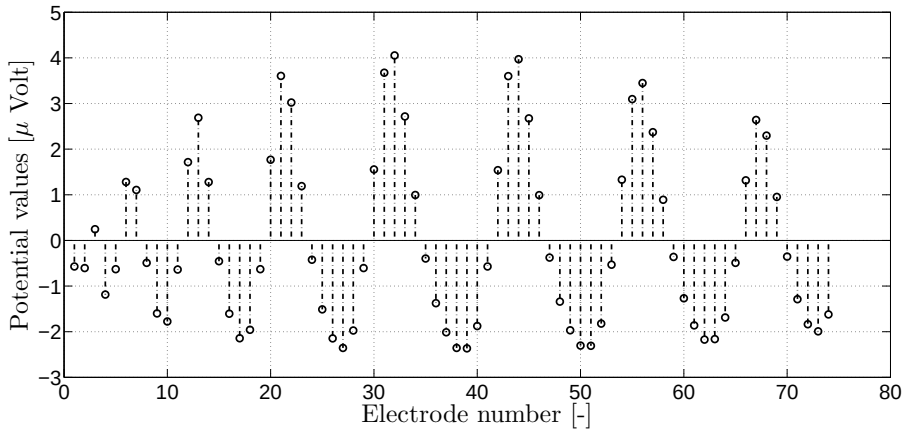

Figure 4.26: EEG Potential for 74 electrodes with actual conductivity $\widetilde{X} = 1/40$ for dipole position CS2 with orientation $\mathbf{e}_y$.

Figures 4.27 and 4.28 display the potential values $\mathbf{V}_m$ when using 56 and 112 electrodes. Computations are performed for 32 conductivities in the interval $[1/40, \quad 1/9]$. We can observe that more electrodes can have a smaller sensitivity when using 112 electrodes instead of 56 electrodes. From these figures, we can conclude that the potential values of various electrodes fall in the same range of values. In terms of L_∞-norm of the potential value V, the difference between different subsets is very small. This difference does not exceed ± 1.5 μ volt.

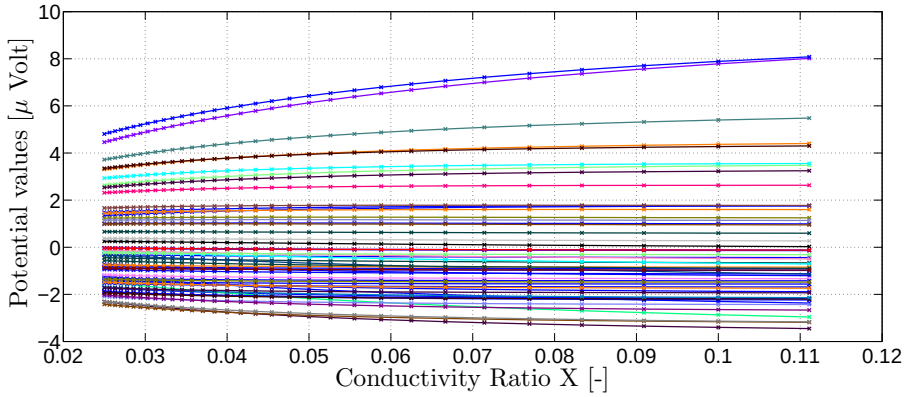

Figure 4.27: EEG Potential distribution using 56 electrodes for dipole position CS3 with orientation $\mathbf{e}_x$.

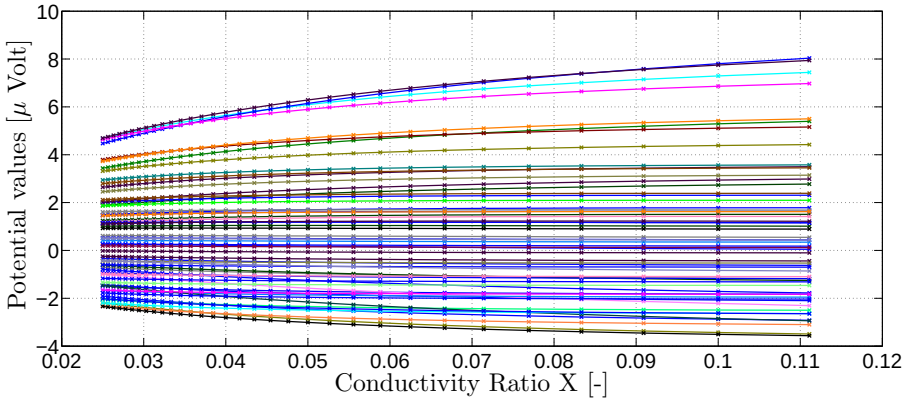

Figure 4.28: EEG Potential distribution using 112 electrodes for dipole position CS3 with orientation $\mathbf{e}_x$.

When introducing a high number of channels in the EEG inverse problem, it is important to make a comparison between the sensitivity analysis of the standard configuration of 27 electrodes and the new configuration for the same spherical head model. We therefore give in figure 4.29 the distribution of sensitivity values for four subsets of electrodes for a small conductivity ratio ($X = 1/20$). The number of electrodes whose sensitivity values are close to zero increases with the number of electrodes in the configuration.

From a numerical point of view, it becomes clear that the use of configurations containing a higher number of electrodes can be useful for the selection procedure in the RCD method. The main reason is that the number of sensors with low sensitivity values is high and increases with the number of electrodes used in the configuration. This is true for every conductivity ratio X used. This was observed for all locations in the head model.

From figure 4.29 it is clear that more electrodes have a low sensitivity in configurations with $N > 27$. A selection procedure with a higher number of electrodes less affected by the conductivity ratio X, in comparison to the standard configuration of 27 electrodes, becomes with such approach a good option for solving the inverse problem. Moreover, higher degrees of freedom are possible in selecting the potentials with lowest sensitivity in each iteration of the RCD method.

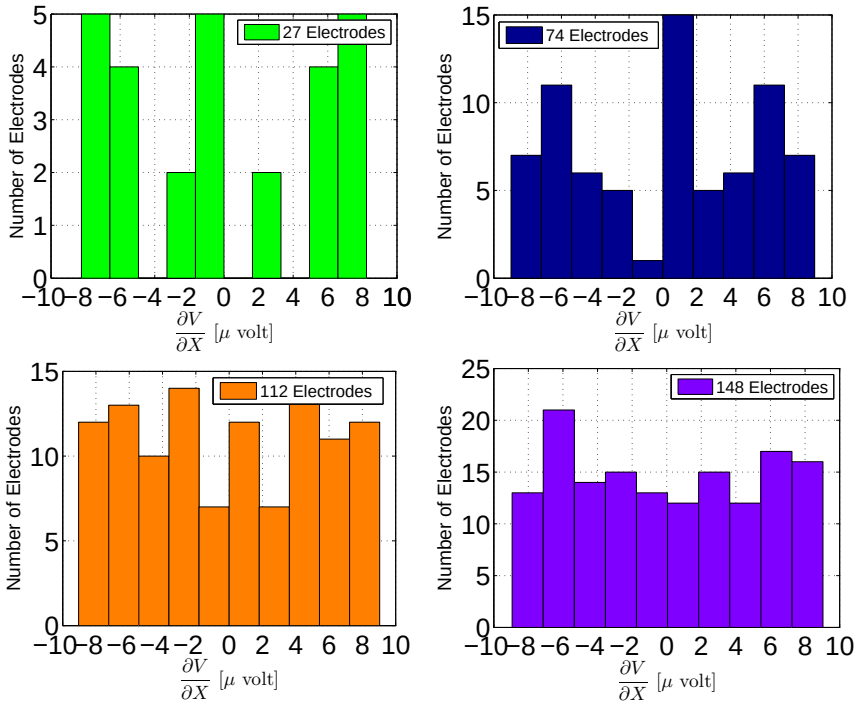

Figure 4.29: Sensitivity Distribution for assumed skull to soft tissue conductivity ratio $\widetilde{X} = 1/20$ for dipole position CS1 for several configurations of electrodes.

4.5.3 Results and Discussion

4.5.3.1 Simulation setup

We carry out numerical experiments following figure 4.30. In the numerical experiments we can vary the number of electrodes N in the EEG cap ($N = 27,56,64,74,112,148$). For the various configurations of electrodes used here, the disposition on the head follows the 10-20 international system, with three electrodes on each of the interior temporal regions. The number of electrodes in these configurations are uniformly distributed on the spherical head model, as described in [137]. The inverse problem is solved using the traditional method and using the RCD method. We investigate here in detail the influence of the number of selected electrodes N_s on the accuracy of the inverse problem. Moreover, the influence of the used EEG cap with certain number of electrodes N on the accuracy is investigated. The same numerical experiments are carried out as in section 4.4.

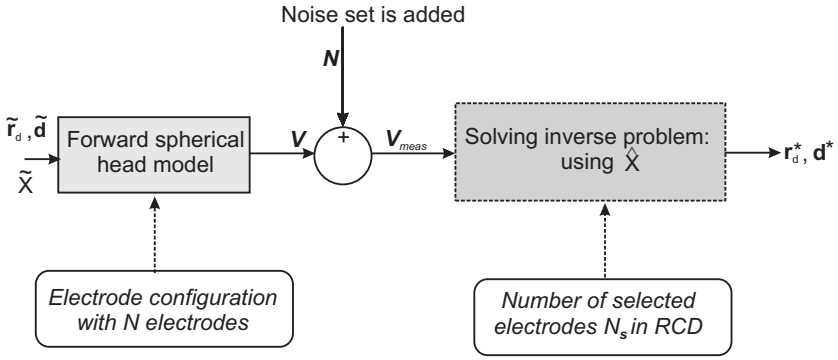

Figure 4.30: Numerical experiments with multiple electrodes.

4.5.3.2 Fitting parameters for large electrode configurations

Here we examine the fitting procedure for approximating the first order Taylor coefficient α (4.14) in the fitting of data sets (4.23) and (4.24). We will compare the residuals of the fitting procedure and perform this for 2 different regions in the spherical head model.

Tables 4.3 and 4.4 give the Taylor coefficient for the first order derivative when using six electrode configurations for a dipole located respectively inside and at the edge of the brain.

Inputs	$\widetilde{X}$	$\widehat{X}$	Linear Fit	Residual
27 Electrodes	1/16	1/40	0.0157	8.985×10^{-9}
56 Electrodes	1/16	1/40	0.01569	2.244×10^{-8}
64 Electrodes	1/16	1/40	0.0157	4.118×10^{-14}
74 Electrodes	1/16	1/40	0.0157	2.3×10^{-14}
112 Electrodes	1/16	1/40	0.01571	2.789×10^{-13}
148 Electrodes	1/16	1/40	0.0157	9.53×10^{-13}

Table 4.3: Taylor coefficient used in the RCD Method for the dipole CS1 located inside the brain.

These tables show that, the residual of the fitting goes to zero when the number of electrodes increases. Similar results were obtained for all the dipole locations where numerical experiments were conducted.

Inputs	$\widetilde{X}$	$\widehat{X}$	Linear Fit	Residual
27 Electrodes	1/25	1/9	0.1632	6.528×10^{-2}
56 Electrodes	1/25	1/9	0.1782	3.42×10^{-2}
64 Electrodes	1/25	1/9	0.1731	5.001×10^{-2}
74 Electrodes	1/25	1/9	0.1666	5.347×10^{-2}
112 Electrodes	1/25	1/9	0.165	5.144×10^{-2}
148 Electrodes	1/25	1/9	0.1645	5.402×10^{-2}

Table 4.4: Taylor coefficient used in the RCD Method for the dipole CS3 located near the edge of the brain.

4.5.3.3 Effect of the number of electrodes on source localization

An important question concerns the number of electrodes that are required for performing accurate EEG source reconstruction. The sensitivity analysis presented in figure 4.29 show that higher electrode configurations may provide useful data for the inputs of the RCD algorithm. We perform numerical experiments in the case $\mathbf{V}_{\text{meas}}$ contains no noise and in the case the set does contain noise.

No noise case:

Figure 4.31 illustrates the reduction of the source localization error when increasing the number of electrodes N in the EEG inverse problem when performing Monte Carlo simulations. For clarity, the dipole localization error of the RCD method is depicted in percents relatively to the traditional method. The assumed skull to soft tissue conductivity value ratio is $\widehat{X} = 1/9$, while the actual conductivity value ratio is $\widetilde{X} = 1/25$.

Figure 4.32 shows the source localization error for different assumed conductivity ratio values when using the traditional minimization method with $N = 112$ electrodes. Moreover, the error is given when selecting a different number of electrodes N_s of the total of N electrodes. In the Monte Carlo simulations, the assumed value of the conductivity $\widehat{X}$ is taken in the interval $[1/40, \quad 1/9]$. As observed here, small values of conductivity introduce a large error in the RCD method as with the traditional method.

The introduction of multi-channel electrodes when using traditional method when solving the inverse problem, does not improve the accuracy of the localization of the dipole as we can see in figure 4.31. This figure illustrates the reduction of the source localization error when increasing the number of electrodes N in the EEG cap for the implemented selection procedure. The reason for this decrease in error is because the fitting parameter α can be determined in a better way. Moreover, a larger set N_s of electrodes can be

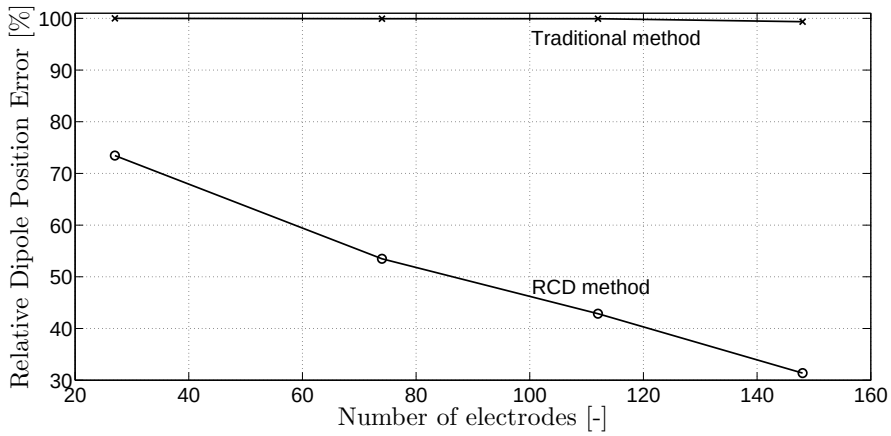

Figure 4.31: Source localization error when using the traditional minimization method and the selection method with actual $\widetilde{X} = 1/25$ and assumed $\widehat{X} = 1/9$. The dipole CS2 is situated inside the brain.

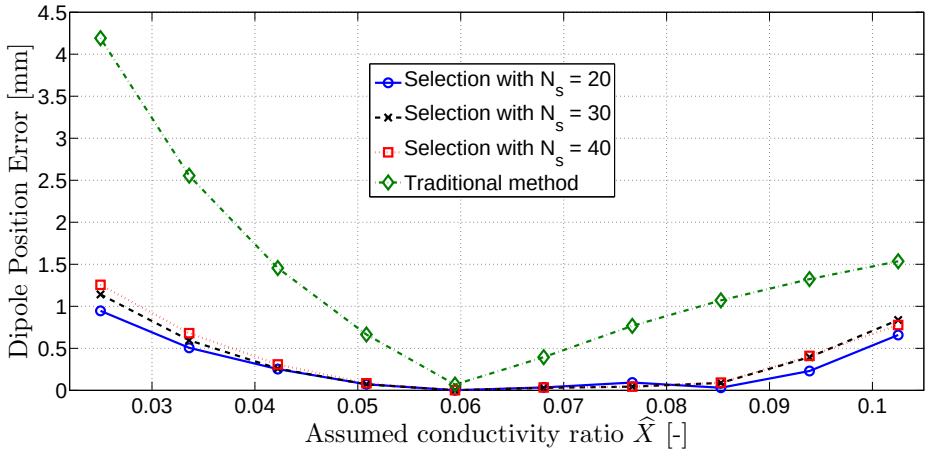

Figure 4.32: Source localization error for different assumed conductivity ratios $\widehat{X}$ with actual $\widetilde{X} = 1/16$. A dipole near the middle of the brain needs to be recovered. $N = 112$ and the number of electrodes that are selected in each iteration are varied, no noise case.

found which have a lower sensitivity of potentials to the conductivity, i.e. $\mathbf{W}^{(k)}$ contains relatively lower values when using higher N. It is important to mention here, that a different choice of the actual value of the conductivity ratio $\widetilde{X}$ will produce a similar behavior of the dipole localization error.

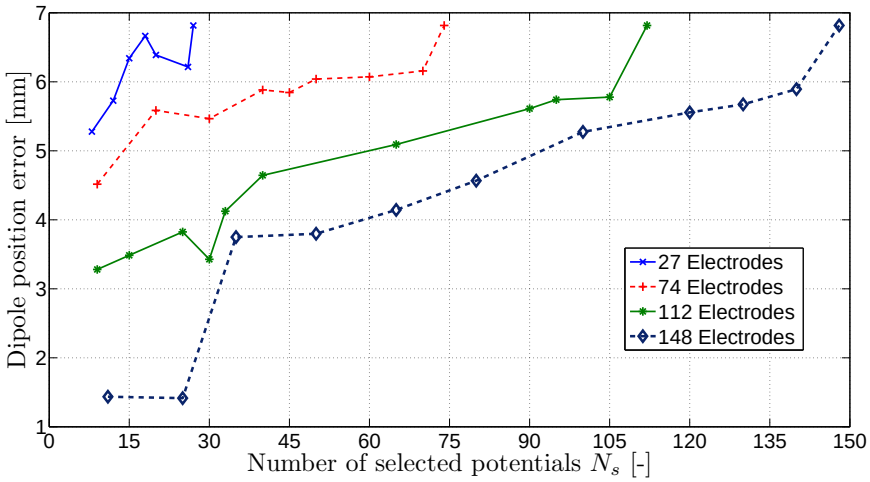

Figure 4.33: Source localization error for actual conductivity $\widetilde{X} = 1/20$ and assumed conductivity $\widehat{X} = 1/16$ for dipole location CS2 using various electrodes configurations.

As observed during the sensitivity analysis and illustrated in the various histograms, the number of sensors whose sensitivity values are close to zero increases with the number of electrodes in the EEG cap. Figure 4.33 shows the improvement made in the recovering of the dipole position for different subsets of electrodes for a dipole located near the center of the brain. The small value of error recorded in figure 4.33 is due to the fact that the actual conductivity value is so close to the assumed conductivity value when solving the inverse problem. When the difference between the actual and the assumed conductivity ratio is high, a great dipole localization error is observed either in the traditional and the RCD method.

A better accuracy is always recorded whenever a selection procedure is carried out in any configuration of electrodes. The non-linearity of the behavior of the error due to selection observed on the picture can be due to the minimization procedure that does not always result into a global minimum. The use of a minimization procedure that starts from different start values could tackle this problem.

Noise case:

The performance of the RCD method is evaluated under different noise levels using different subsets of electrodes. When using noisy data, that is nl > 0 in the numerical experiments as in figure 4.34, we observe an increase of

the dipole position error with both methods when noise increases in the measurements. When increasing the number of electrodes in the EEG cap, the RCD method yields lower dipole position errors compared to the traditional method as illustrated in this figure. The number of selected potentials is $N_s = 20$.

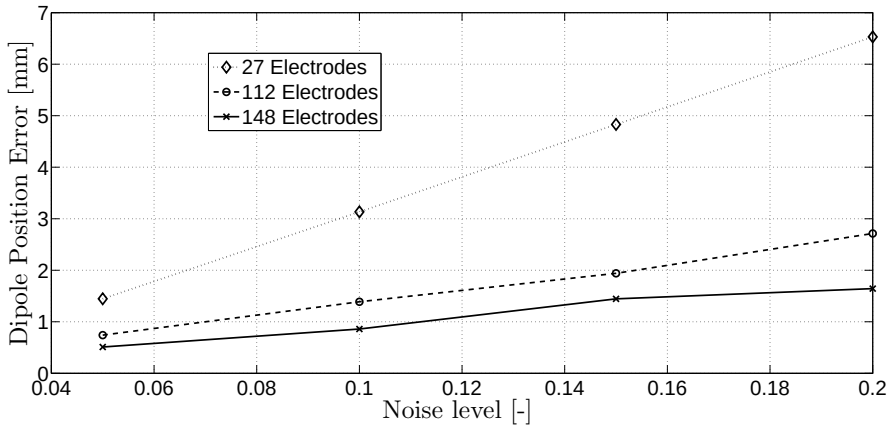

Figure 4.34: Source localization error using the RCD method for assumed conductivity $\widehat{X} = 1/40$ and actual conductivity $\widetilde{X} = 1/13$ for dipole location CS1 using various electrode configurations ($N = 27, 112, 148$) and noise levels. Number of selected electrodes is $N_s = 20$.

The RCD method offers for a large set of electrodes and for a large set of conductivity ratios, a better spatial resolution as observed in figure 4.35. Computations are done here for a noise level of 10% in the measurements. It should be noted here that the result displayed in figure 4.35 is obtained without selection of the potentials, i.e. when all the electrodes are used in the RCD method.

4.5.3.4 Influence of the selection of potentials N_s on the solution

One of the internal parameters of the RCD method which influences the spatial resolution is the number of selected potentials N_s. It was observed in the case of a standard configuration of 27 electrodes that a better spatial resolution is achieved when performing a selection N_s on the number of electrodes less influenced by the conductivity ratio.
In this section, we will analyze how the spatial resolution of the EEG inverse problem could be increased by altering N_s when using a large set of electrodes. Numerical experiments are first carried out in the no noise case.

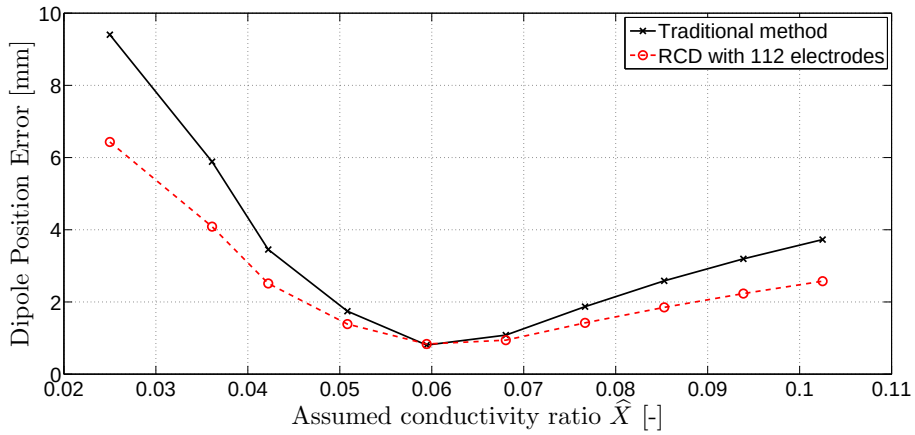

Figure 4.35: Source localization error of dipole CS3 for different assumed conductivity ratios $\widehat{X}$ with actual conductivity $\widetilde{X} = 1/16$, using a fixed number of electrodes with noise level 0.1. The traditional and RCD method are solved using an EEG cap with 112 electrodes. The number of selected electrodes is $N_s = N$.

Figure 4.32 shows the source localization error for different assumed skull to soft tissue conductivity values when using the traditional minimization method with $N = 112$ electrodes. Moreover, the error is given when selecting with a different number of electrodes N_s from the total number N in the RCD method. This figure illustrates that decreasing N_s yields lower dipole position error for all assumed conductivity ratio values.
The effect of electrode configuration was assessed by comparing the source localization accuracy produced by various electrode configurations as seen in figure 4.36 and 4.37 respectively. The localization error when using a minimum of 8 selected electrodes for each configuration has shown an increase of the accuracy of the spatial resolution for different conductivity values. These simulations revealed an influence of the number of selected electrodes on source localization that could be completely linear if some instabilities due to the minimization method were not observed for certain values of N_s.

Figure 4.36 shows that both increasing the number of electrodes in the EEG cap and decreasing the number of selected potentials N_s, result in an increase of spatial resolution. For $N = 27$, the error decreases from ≈4.1 mm to ≈2.1 mm while for $N = 148$ the error decreases from ≈4.1 mm to ≈1 mm. A global decrease of the dipole position error is observed for decreasing N_s. However, in some cases a small relative increase of error is observed. This is because the minimization of the RCD cost function does not always result in the global op-

timum. The implementation of a multi start (start values randomly distributed in the head) minimization method can provide a solution to this problem.

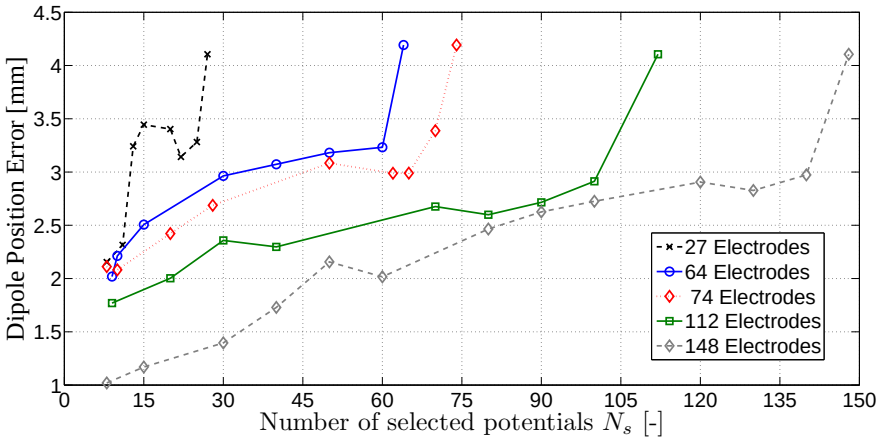

Figure 4.36: Source localization error for assumed conductivity $\widehat{X} = 1/25$ and actual conductivity $\widetilde{X} = 1/9$ for dipole location $\widetilde{r}_d$ = CS3 using various electrodes configurations in the no noise case.

For some cases (i.e. higher number of electrodes) as illustrated in figure 4.34 where a difference of 3.7 mm for $N = 112$ electrodes and 4.8 mm for $N = 148$ electrodes is recorded for a noise level of $n = 0.2$ in comparison to the error generated for $N = 27$ electrodes, the efficiency can be much higher. It should be noticed here that the difference between the actual and the assumed conductivity ratio is significant.

When using noisy data in the numerical experiments, a global decrease of the dipole position error is also observed, see figure 4.37. We observe in this figure that an increase of spatial resolution of factor 2 can be attained for this specific data set. In the noise case the improvement of accuracy is much more limited than in the no noise case.

Additional simulations were performed over a uniform distributed grid of dipoles. We placed dipoles in each voxel (voxel discretization of $\approx$ 4.6mm) and solved the inverse problem for the EEG potential corresponding with that dipole. The EEG cap consisted of $N = 27$ electrodes. The inverse problem was solved using the RCD methodology with number of selected electrodes $N_s = 27$ and $N_s = 10$. In figure 4.38 a histogram of the factor in increase in spatial resolution, i.e. the ratio of the dipole position error when using RCD method using $N_s = 27$ and when using $N_s = 27$, is shown where approximately 1700 inverse problems were solved. This figure shows that an overall

increase in accuracy is attained when using a smaller number of selected electrodes (i.e. 10 instead of 27 out of the total of 27 electrodes). Notice that for a small number of test dipoles the ratio was less than 1. This is because the minimization methodology (with $N_s = 10$) was trapped in a local minimum and was not converging towards the global minimum.

However, the above results show that when using the RCD method, the manufacturers of EEG hardware should aim at EEG caps with the number of electrodes as high as possible. In the numerical RCD algorithm, the internal parameter N_s should be taken as low as possible. In this way, more accurate EEG source analysis can be carried out for the analysis of EEG samples. Note that the above conclusions can be extended when using spatio-temporal data, i.e. $\mathbf{V}_{\text{meas}} \in \mathbb{R}^{N \times p}$ with p time samples [109].

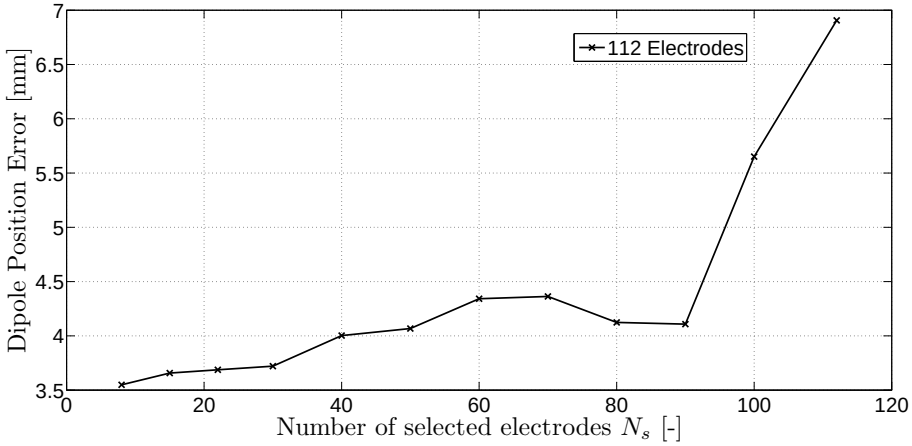

Figure 4.37: Source localization error for assumed conductivity $\widetilde{X} = 1/30$ while actual $\widehat{X} = 1/16$ using selection for dipole $\widetilde{r_d}$ = CS4 for $N = 112$ electrodes configuration and noise level 0.2.

The non-linear behavior of the error observed in figure 4.37 in the presence of noise when a selection procedure N_s is carried out, is similar to the case when the potentials do not contain noise in the measurements. The value of the error recorded for $N_s = 80$ and $N_s = 90$ is linked to numerical instabilities of the minimization procedure. But in general for noise case, a selection of N_s electrodes, minimally influenced by the conductivity, leads to a better accuracy in the reconstruction of the source.

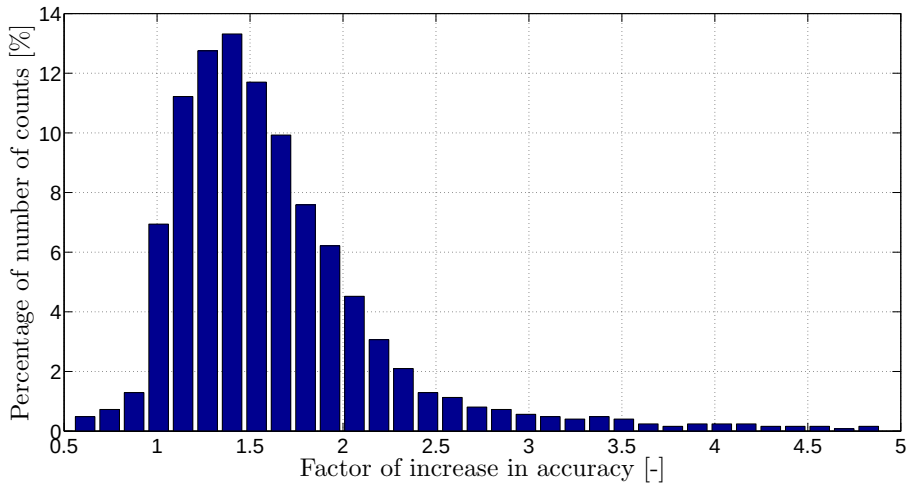

Figure 4.38: Histogram depicting the factor of increase when using the RCD with $N_s = 10$ compared to the RCD with $N_s = 27$ electrodes. 1700 inverse problems were solved. $N = 27$.

4.5.3.5 Efficiency of the RCD method with high number of measurement channels

The number of EEG electrodes in the EEG cap has no significant influence when using the traditional method as observed in figure 4.34 where no improvement of the accuracy in dipole position error was recorded. Given that numerical experiments are carried out for a specific position of the dipole, a local efficiency of the RCD inverse methodology can be presented for several electrode configurations. Different results at this level, could be obtained depending on the choice of the actual value $\widetilde{X}$ and assumed conductivity ratio $\widehat{X}$ used to solve the inverse problem.
As seen during the computations all over the spherical head model, a large set of electrodes always provides the best spatial resolution for the EEG inverse problem compared to the traditional set of 27 electrodes. The efficiency η as defined in equation (4.31), varies from 30% to 75% and an average efficiency of 30% is obtained in the case of noise in the measurements. More generally, using a higher number of electrodes with the RCD method gives better results compared to the traditional configuration of 27 electrodes.

4.5.4 Conclusion for configurations high number of electrode configurations

It was assumed that a high number of electrodes in an EEG cap does not increase the spatial resolution for the traditional approach. However, a larger number of electrodes together with the selection strategy increases sufficiently the spatial resolution in the EEG dipole localization. Solving the inverse problem by selecting the electrodes which are less sensitive to the conductivity ratio lead to an improvement of the spatial resolution. Numerical results show that we can even improve the spatial resolution by choosing a high number of electrodes in the EEG measurement hardware and by selecting a lower number of electrodes in the inverse problem. The results show that the EEG inverse problem can be solved with considerably improved quality.

4.6. Conclusions

We presented in this chapter the novel Reduced Conductivity Dependence method. We formulated the RCD cost function that, contrary to state of the art techniques, incorporates the sensitivity of the sensors to the uncertain skull to soft tissue conductivity ratio. Moreover, we proposed a selection procedure that removes the sensors that are highly influenced by the uncertain conductivity ratio. Numerical experiments were performed for different active electrical dipoles, different actual and assumed conductivity ratios. The results show that a reduction in dipole localization error is obtained up to 60-80% in the case that no noise is available in the measured data sets. However, when the data sets contain noise, then the efficiency of the RCD method is only 20-60%, depending on the noise level in the data sets used for solving the inverse problem. The reason for the less efficiency in the noise case is because the fitting procedure, needed within the RCD method for approximating the Taylor coefficients, is not performing well when noise is to a large extend available in the data sets.

We also investigated the use of the RCD method in the case of using a higher number of electrodes within the EEG cap. Contrary to the traditional method, a reduction in dipole localization error is observed when increasing the number of electrodes within the EEG cap. We state that the RCD method has an important advantage compared to state of the art methods when the EEG cap contains dense sensing electrodes. This is due to the fact that a higher variety of sensors can be selected within the RCD method. Moreover, the fitting procedure within the RCD procedure works in a more accurate way.

The RCD method developed is innovative in the sense that for a given configuration of 27 electrodes, spatial resolution can be improved not by increasing the number of electrodes as often suggested but instead by making a selection of potentials less affected by the sensitivity. With such approach, it becomes important to test the efficiency of the RCD method by including when solving the inverse problem, other configurations of the electrodes and compare results to those of the standard 27 electrodes actually used for the numerical experiments on the spherical head model.

A general conclusion that can be drawn is that the methodology mentioned in this chapter can be used for other (bio-)electromagnetic applications where a numerical uncertain inverse problem needs to be solved starting from a certain set of sensors.

CHAPTER 5

EEG Multiple Dipole Analysis using RCD RAP-MUSIC Method

5.1. Introduction

A current dipole model may be used to represent well-localized activated neural sources for events like epileptic spikes or early stages of an epileptic seizure [9]. A simple and in many cases valid model of brain electrical activity assumes a focal source. The single current dipole is then adequate to model the location in space, as well as the magnitude and orientation of the neural activity (see section 2.1.1). However, several simultaneously active sources are better modeled by multiple dipoles. Two cases are possible: a limited number of dipoles in the sense that the number of these dipoles are smaller than the number of sensors ($p < N$) and distributed source models ($p >> N$). For details concerning the solution of the corresponding inverse problems, see sections 3.3.2 and 3.3.3 respectively.

Multiple equivalent current dipoles are often sufficient to accurately represent sources of the measured scalp potential data in epilepsy patients with focal origin in comparison to distributed source models [138]. Moreover, most spikes and seizures are well modeled by equivalent dipoles, see e.g. [139]. As pointed out in [140], one of the major problems in clinical neurophysiology has been the investigation of physiological as well as pathological processes involving multiple simultaneously active brain regions when using electrical measurements.

The above is the main reason for extending the applicability of the RCD method as elaborated in previous chapter (for single dipole reconstruction)

towards the reconstruction of a limited number of multiple dipoles. In this way, a more approximate reconstruction of the neural activity can be made. The least squares cost function, as defined in (3.4) for single dipole localization, is not suitable for multiple dipole localization [12]. Subspace-based methods are able to locate multiple sources in an accurate way [12]. The aim of this chapter is to incorporate the RCD methodology within subspace-based methods, more specifically within the Recursively Applied and Projected (RAP) - Multiple Signal Classification (MUSIC) algorithm. We alter the traditionally known RAP-MUSIC subspace-based cost function and incorporate selection of sensors based on the sensitivity. Numerical experiments in the no noise and noise case are performed so to establish the performance of the proposed RCD RAP-MUSIC method. Contrary to previous chapter where spatial-only data sets (EEG potentials at a single time instant) were used for solving the inverse problem (potentials of the form (2.17)), we examine the performance of the proposed algorithm using spatio-temporal data sets (window of multiple EEG data sets that vary in time) of the form (2.21).

In section 5.2 we shortly review the traditional RAP-MUSIC algorithm while in section 5.3 we propose the RCD RAP-MUSIC methodology. Finally, results and discussion are given in section 5.4.

5.2. Traditional RAP-MUSIC

5.2.1 Introduction

The estimation of multiple dipole parameters is known as a difficult nonlinear minimization problem because the cost functional contains many local minima. A least squares cost function can be constructed in a similar way as cost function (3.4):

$$\mathrm{RRE}(\mathbf{r}_d) = \frac{\|\mathbf{V}_{\mathrm{meas}} - \mathbf{L}_{\mathrm{all}}\mathbf{L}_{\mathrm{all}}^{\dagger}\mathbf{V}_{\mathrm{meas}}\|}{\|\mathbf{V}_{\mathrm{meas}}\|}. \tag{5.1}$$

when using the spatio-temporal formulation (2.18)

$$\mathbf{L}_{\mathrm{all}} = \Big[\mathbf{L}(\mathbf{r}_{d,1}), \mathbf{L}(\mathbf{r}_{d,2}), \ldots\ldots\ldots \mathbf{L}(\mathbf{r}_{d,p})\Big] \tag{5.2}$$

for p dipoles. In the case $p < N$, the inverse problem with (5.1) is not ill-posed. For the minimization of these cost functions many strategies have been developed such as the use of simulated annealing [141]. These methods however, can not accurately locate several dipole soures, contrary to the subspace-based methods introduced in EEG source localization [142]. The so-called MUltiple Signal Classification (MUSIC) algorithm was adopted

from radar and sonar applications for the localization of multiple dipoles. In [11, 12], it is illustrated that the Recursively Applied and Projected (RAP)-MUSIC algorithm has better source localization properties due to the use of sequential cost functions that are adapted for the localization of each dipole.

MUSIC employs a scanning technique instead of solving the difficult multidimensional nonlinear minimization problem of (5.1) [143]. Scanning is necessary for finding the p peaks in the MUSIC cost function. Each of these peaks corresponds then with the sources to be estimated. MUSIC partitions the N-dimensional measurement space into a signal subspace and a noise subspace.

When using the spatio-temporal dipole model in equation (2.21), the singular value decomposition (SVD) of the spatial correlation matrix $\mathbf{R_V}$ can be considered:

$$\begin{aligned} \mathbf{R_V} &= E\{\mathbf{V}_{\text{meas}}\mathbf{V}_{\text{meas}}^T\} \\ &= [\Phi_S \Phi_N] \begin{bmatrix} \Lambda_S & 0 \\ 0 & \Lambda_N \end{bmatrix} [\Phi_S \Phi_N]^T \end{aligned} \tag{5.3}$$

where Λ_S and Λ_N are diagonal matrices with the singular value of $\mathbf{V}_{\text{meas}}$ associated with the signal subspace Φ_S and the noise subspace Φ_N, respectively. MUSIC searches throughout the brain volume for source locations that satisfy the condition that the topography of the dipoles lie in the signal subspace. This can be carried out by projecting the topographies onto the signal subspace with projection matrix $\mathbf{P}_S = \Phi_S \Phi_S^T$ onto the signal subspace. The dipole source locations with the largest projections on the signal subspace are the active sources [12] using the following cost function:

$$\frac{\|\mathbf{P}_S \mathbf{L}(\mathbf{r})\mathbf{e}\|}{\|\mathbf{L}(\mathbf{r})\mathbf{e}\|} \tag{5.4}$$

where $\mathbf{e} = \frac{\mathbf{d}}{\|\mathbf{d}\|}$ is determined by two parameters (the magnitude of the dipole orientation does not need to be given). When the dipole positions and orientations are determined, i.e. the parameters of matrix $\mathbf{A}$, by the minimization of (5.4), then the dipole time series can be determined by

$$\mathbf{S}_{\text{opt}}^T = \mathbf{A}^{\dagger}\mathbf{V}_{\text{meas}} \tag{5.5}$$

with spatio-temporal model (2.21).

5.2.2 Recursively Applied and Projected MUSIC

The RAP-MUSIC algorithm was proposed in [12] and is based on a modification of the MUSIC algorithm. In MUSIC, the array manifold is projected onto an estimate of the signal subspace. The MUSIC algorithm however has difficulty finding several local minima as the dimension p of the number of sources increases. RAP-MUSIC overcomes the problems MUSIC has to deal with by employing a recursive procedure in which each source $\mathbf{r}^*_{d,l}$ $(l = 1,\ldots,p)$ is found as the global maximizer of a different objective function:

$$\mathbf{r}^*_{d,l} = \arg\max_{\mathbf{r}_d}(subcorr(\Pi^{\perp}_{\mathbf{A}_{l-1}}\mathbf{L}(\mathbf{r}_d),\Pi^{\perp}_{\mathbf{A}_{l-1}}\Phi_S)_1) \tag{5.6}$$

with

$$\Pi^{\perp}_{\mathbf{A}_{l-1}} = (\mathbf{I} - \mathbf{A}_{l-1}\mathbf{A}^{\dagger}_{l-1}) \tag{5.7}$$

the projection matrix constructed by $\mathbf{A}_{l-1}$, a matrix containing in each column the topographies of the already found $l-1$ sources [12], and Φ_S is the signal subspace. The RAP-MUSIC method is an improvement to the original MUSIC scanning method because it refines the MUSIC cost function after each source is found by projecting the signal subspace and the lead field matrix $\mathbf{L}(\mathbf{r}_d)$ away from the topographies of the already found sources, i.e. $\Pi^{\perp}_{\mathbf{A}_{l-1}}$ [12].

The subspace correlation method $subcorr(\cdot)_1$ computes the correlation between the subspaces spanned by the columns of $\mathbf{L}(\mathbf{r}_d)$ and Φ_S. As stated in [144], the subspace source localization approach scans the entire possible source space and calculates the subspace correlation of two subspaces. Contrary to the MUSIC scanning search approach, the sources can be estimated using p maximization procedures (5.6). Remark that minimization is possible of $-(subcorr(\Pi^{\perp}_{\mathbf{A}_{l-1}}\mathbf{L}(\mathbf{r}_d),\Pi^{\perp}_{\mathbf{A}_{l-1}}\Phi_S)_1)$ where the Nelder-Mead simplex methodology can be employed for the minimization of the cost function.

5.3. Description of the RCD RAP-MUSIC algorithm

5.3.1 Introduction

In previous chapter we showed that it is possible to redefine the traditional cost function, see (4.18), so that the minimization is more robust to the uncertain conductivity value. Using the Taylor expansion of the simulated potentials, we include in the cost function the sensitivity of the potentials to the conductivity in the cost function. Moreover, selection of sensors was carried out in each iteration of the minimization procedure. We aim here to include the RCD methodology within the RAP-MUSIC cost function (5.6) so

to have an accurate multiple dipole reconstruction procedure. In this section we alter the traditionally known RAP-MUSIC cost function and define the RCD RAP-MUSIC scheme.

5.3.2 RCD RAP-MUSIC cost function

The RCD RAP-MUSIC cost function that we propose is elaborated for the reconstruction of the lth dipole, and in the kth iteration of the minimization of the cost function. Based on the analysis performed in section 4.3 we alter the following cost function

$$subcorr(\Pi^{\perp}_{\mathbf{A}_{l-1}}\mathbf{L}(\mathbf{r}^{(k)}_{d,l}),\Pi^{\perp}_{\mathbf{A}_{l-1}}\Phi_S)_1 \tag{5.8}$$

and perform the following transformation:

$$\mathbf{L}(\mathbf{r}_d) \rightarrow \mathbf{L}(\mathbf{r}_d) + \alpha\mathbf{W}(\mathbf{r}_d) \tag{5.9}$$

with $\mathbf{W}(\mathbf{r}_d) \in \mathbb{R}^{N\times 3}$ defined here as the sensitivity of the lead field matrix to the conductivity ratio:

$$\mathbf{W}(\mathbf{r}_d) = \frac{\partial \mathbf{L}(\mathbf{r}_d)}{\partial X}|_{X=\widehat{X}} \tag{5.10}$$

evaluated for the assumed conductivity ratio $\widehat{X}$. Contrary to the vector (4.3) for RCD single dipole reconstruction, the sensitivity is now a $N \times 3$ matrix. α is again the Taylor coefficient (4.14) that is again approximated through a fitting procedure. We have the following basic cost function:

$$subcorr(\Pi^{\perp}_{\mathbf{A}_{l-1}}(\mathbf{L}(\mathbf{r}^{(k)}_{d,l}) + \alpha\mathbf{W}(\mathbf{r}_d)),\Pi^{\perp}_{\mathbf{A}_{l-1}}\Phi_S)_1 \tag{5.11}$$

that needs to be minimized within the RCD RAP-MUSIC methodology. In (5.11), no selection of sensitive sensors is yet performed.

5.3.3 Iterative scheme of the RCD RAP-MUSIC algorithm

We reformulate the basic principles for RCD single dipole analysis as elaborated in section 4.3.1 to multiple dipole localization. Figure 5.1 shows the iterative scheme of the proposed RCD RAP-MUSIC scheme. When incorporating the RCD methodology within the RAP-MUSIC framework, the steps 1-6 given in section 4.2 in chapter 4 can be executed in a similar way.

The sensitivity of the simulated potential values to the conductivity in step 2, needs to be altered. We consider a different measure for the sensitivity to the

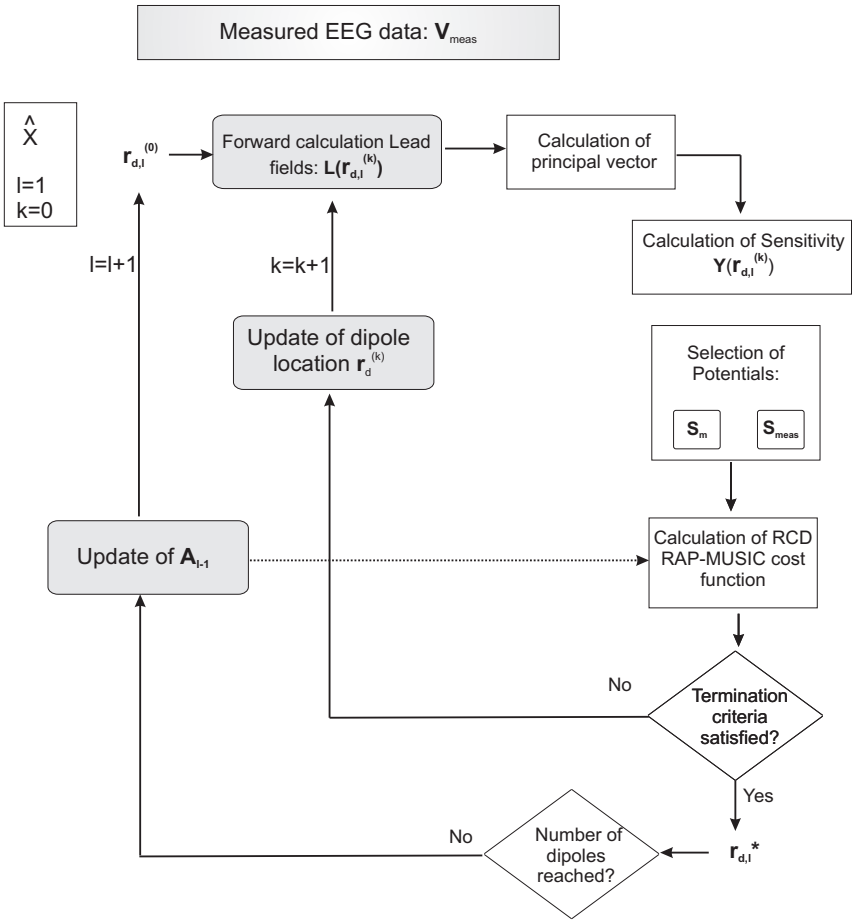

Figure 5.1: Iterative scheme of the RCD RAP-MUSIC methodology.

conductivity ratio, namely the sensitivity to the conductivity ratio of the principal vector $\mathbf{U} \in \mathbb{R}^{m\times 1}$ that is associated to the principal angle of the subspace correlation function. This principal vector can be computed following [145] and depends in the k-th iteration of the minimization procedure upon Φ_s and $\mathbf{L}(\mathbf{r}_{d,l}^{(k)})$ (and consequently also upon the conductivity ratio X). So, instead of using (4.3), the following sensitivity to conductivity ratio is computed in each iteration

$$\mathbf{Y}(\mathbf{r}_{d,l}^{(k)}) = \frac{\partial \mathbf{U}(\mathbf{r}_{d,l}^{(k)})}{\partial X}\Big|_{X=\widehat{X}}. \tag{5.12}$$

This can be computed in a finite difference way.

Selection of N_s electrodes with selection operator $\text{sel}(\cdot)$ is carried out on the basis of (5.12), similar to step 3 in section 4.2. By ranking $\mathbf{Y}(\mathbf{r}_{d,l}^{(k)})$, i.e. ordering the values from lowest to the highest values, it is possible to select those sensors with lowest sensitivity and in each kth iteration for the recovery of the lth dipole, the selection operator $\text{sel}(\cdot)$ is defined. In this way the cost function (5.11) becomes:

$$subcorr(\text{sel}(\,\Pi^{\perp}_{\mathbf{A}_{l-1}}(\mathbf{L}(\mathbf{r}_{d,l}^{(k)}) + \alpha\mathbf{W}(\mathbf{r}_d))\,), \text{sel}(\,\Pi^{\perp}_{\mathbf{A}_{l-1}}\Phi_S\,))_1 \tag{5.13}$$

Remark that in (5.13) the first order derivative (5.10) is used and not the sensitivity (5.12) because we use the first order expanded Taylor approximation.

5.4. Results and Discussion

5.4.1 Simulation set up

The performance of the proposed RCD RAP-MUSIC methodology is investigated using numerical experiments. Spatio-temporal EEG data is used as input to solve the inverse problem. These time varying potentials are represented by (2.21). The simulation setup for the recovery of multiple dipoles consists in the recovery of $p = 2$, $p = 3$ and $p = 5$ different dipoles. For the location of the dipoles used in the simulation study, see table 5.1.
In the case of $p = 2$, we assume that the first dipole is located at DL1 which represents an epileptic spike of 0.2s with onset at 0.4s (defines waveform $\mathbf{s}_1$), and that the second dipole is located at DL2 with rhythmic activity (sinusoidal waveform $\mathbf{s}_2$ at 10Hz). For the case $p = 3$, the third dipole is located at DL3 with rhythmic activity (cosinusoidal waveform $\mathbf{s}_3$ at 10 Hz). For $p = 5$, a dipole at DL4 (sinusoidal waveform $\mathbf{s}_4$ at 5Hz) and a dipole located at DL5 (cosinusoidal waveform $\mathbf{s}_5$ at 5Hz) is added. Using the forward model, a spatio-temporal matrix was generated with a certain conductivity ratio value $\widetilde{X}$:

$$\mathbf{V}_{\text{meas}} = \left[\mathbf{L}(\widetilde{X},\widetilde{\mathbf{r}}_{d,1}), \mathbf{L}(\widetilde{X},\widetilde{\mathbf{r}}_{d,2}), \ldots, \mathbf{L}(\widetilde{X},\widetilde{\mathbf{r}}_{d,p})\right]\left[\widetilde{\mathbf{d}}_1, \widetilde{\mathbf{d}}_2, \ldots, \widetilde{\mathbf{d}}_p\right]^T \tag{5.14}$$

with

$$\mathbf{d}_i = \widetilde{\mathbf{u}}_i\widetilde{\mathbf{s}}_i \tag{5.15}$$

where $\mathbf{s}_i$ is the waveform of the dipole strength of n_t time samples as defined above for each dipole. To the matrix (5.14) white Gaussian noise $\mathbf{N}$ was added with varying noise levels. Figure 5.2 shows an example of the EEG data (1 second) used during the simulation experiments. The total number of EEG electrodes is here also $N = 27$ (see section 2.7).

Dipole Location (DL)	r_x (mm)	r_y (mm)	r_z (mm)
DL1	17.2	34.4	25.8
DL2	25.8	43.0	8.6
DL3	8.6	17.2	17.2
DL4	17.2	25.8	17.2
DL5	25.8	25.8	8.6

Table 5.1: Dipole locations at different regions in the case of multiple dipole localization. The center of the head model is referenced as $\mathbf{r} = [0,0,0]$.

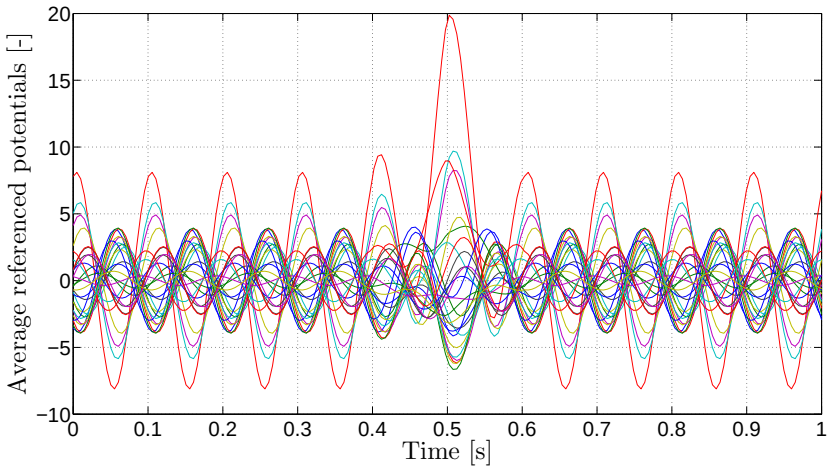

Figure 5.2: Sample of average referenced EEG data. These EEG data results from $p = 3$ dipoles (located at DL1, DL2, and DL3).

The dipole position error (DPE_i) for the ith ($i = 1,\ldots,p$) dipole is the absolute difference in the L_2 norm between the actual dipole location $\widetilde{\mathbf{r}}_{d,i}$ and the reconstructed dipole location $\mathbf{r}^*_{d,i}$ provided by the solution of the inverse problem:

$$\mathrm{DPE}_i = \|\widetilde{\mathbf{r}}_{d,i} - \mathbf{r}^*_{d,i}\| \tag{5.16}$$

5.4.2 Accuracy of the RCD-RAP MUSIC

5.4.2.1 Results in the no noise case

The RCD RAP-MUSIC methodology explained in previous section 5.3 is used as inverse algorithm and compared to the traditional RAP-MUSIC algorithm. In the inverse algorithm, the forward calculations use the assumed conductivity ratio $\widehat{X}$ that may differ from the actual conductivity ratio $\widetilde{X} = 1/24$ that

is used for generating the measured spatio-temporal data set (5.14). No noise was added here to the data set.

Figures 5.3 and 5.4 depict the dipole position errors defined in (5.16) for respectively $p = 2$ and $p = 3$ dipoles when using the traditional RAP-MUSIC cost function (denoted as 'Traditional') and when using the RCD methodology during the maximization of cost function (5.13) in the no noise case. Results are displayed here for conductivity ratios in the interval $[1/60, 1/25]$ where more small conductivity ratios are used in the computations. The RCD RAP-MUSIC can improve the source localization with 5 mm for both dipoles.

The results here show that it is possible to reduce the dipole position errors introduced by the use of the wrong conductivity ratio ($\widehat{X} \neq \widetilde{X}$) in the forward model. It is thus possible to extend the traditional RAP-MUSIC algorithm to the RCD RAP-MUSIC with reduction of DPE_i. The reduction is of the same order as the RCD algorithm for single dipole localization for the no noise case.

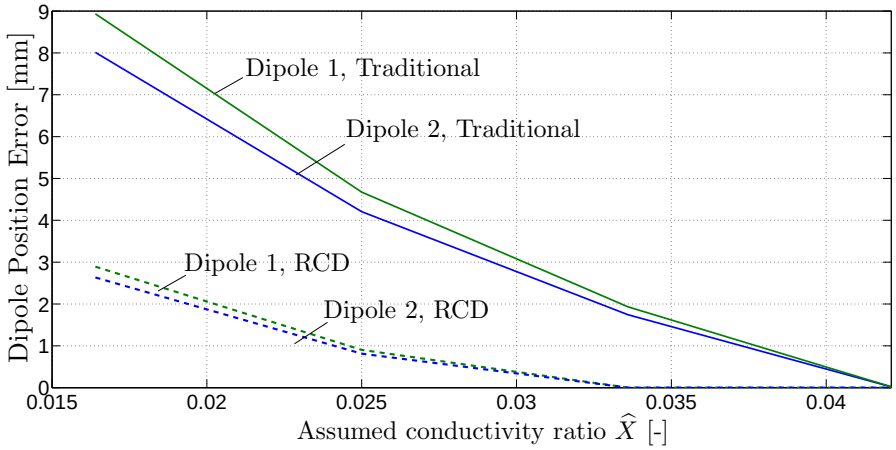

Figure 5.3: Dipole position errors for dipoles located at DL1 and DL2 when assuming different conductivity ratios. The number of selected electrodes is here $N_s = 12$. EEG cap has $N = 27$ electrodes.

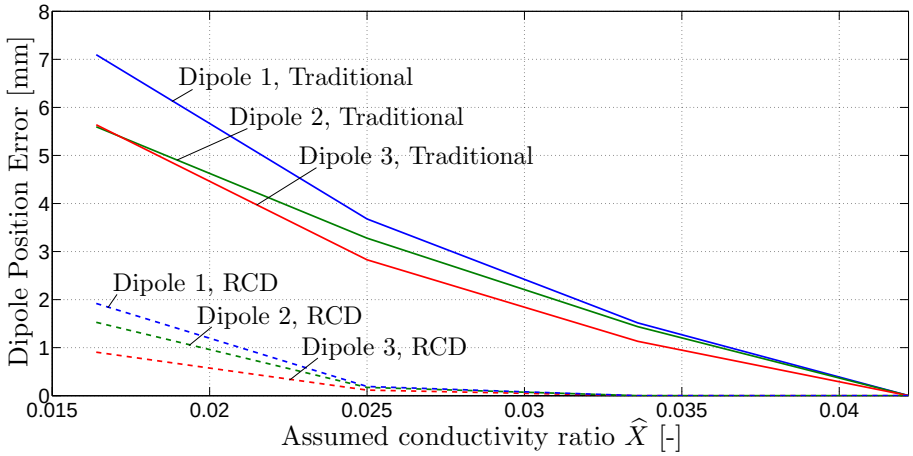

Figure 5.4: Dipole position errors for dipoles located at DL1, DL2 and DL3 when assuming different conductivity ratios. The number of selected electrodes is here $N_s = 12$. EEG cap has $N = 27$ electrodes.

5.4.2.2 Results in the noise case

In the simulations carried out here, noise **N** was added to (5.14) with varying noise levels. Figure 5.5 shows the total dipole localization error, i.e.

$$\sum_{i=1}^{p} \mathrm{DPE}_i \tag{5.17}$$

versus the noise level in the case of $p = 3$. DPE_i is here the average of 100 EEG samples with certain noise level. The same results were obtained when recovering $p = 5$ different dipoles, see figure 5.6. We observe here an important trend: the dipole position errors of the RCD RAP-MUSIC follow the same trend as the traditional RAP-MUSIC method. This is different to the results shown in section 4.4.3 for RCD single dipole localization.

In figures 4.20 and 4.21, we observed that the efficiency of the RCD method with the cost function defined in equation (4.20) was drastically reduced compared to the no noise case in the recovery of a single dipole. However, when we compare these results for single dipole reconstruction with figures 5.10 and 5.6 for multiple dipole reconstructions, we observe that the RCD with cost function (5.13) is more robust to noise. The underlying reason for this is that the fitting constant α is much better approximated when using as data **U** and **Y**. The principal vectors and corresponding sensitivity in equation (5.12) are less affected by noise. Figure 5.7 shows the average dipole position

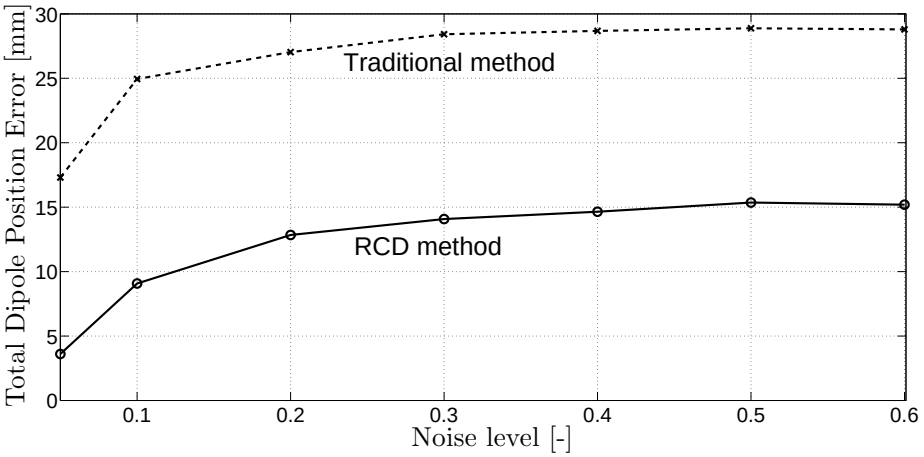

Figure 5.5: Total dipole position error when recovering $p = 3$ dipoles (DL1, DL2, DL3) with $\widetilde{X} = 1/24$, $\widehat{X} = 1/60$ and $N_s = 12$ with several noise levels. EEG cap has $N = 27$ electrodes.

errors for the three different dipoles separately when using the traditional methodology and the RCD methodology. An overall decrease in dipole position errors of the different dipoles can be observed.

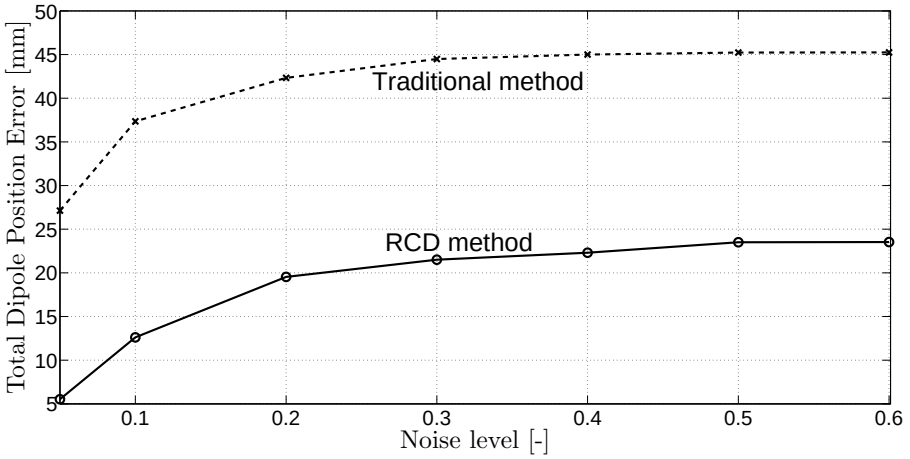

Figure 5.6: Total dipole position error when recovering $p = 5$ dipoles (DL1, DL2, DL3,DL4,DL5) with $\widetilde{X} = 1/24$, $\widehat{X} = 1/60$ and $N_s = 12$ with several noise levels. EEG cap has $N = 27$ electrodes.

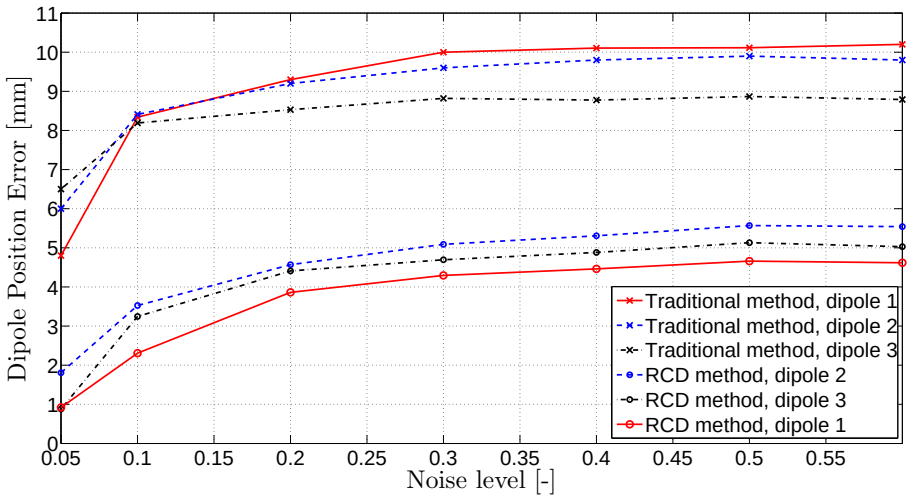

Figure 5.7: Average dipole position errors when recovering $p = 3$ dipoles (DL1, DL2, DL3) with $\widetilde{X} = 1/24$, $\widehat{X} = 1/60$ and $N_s = 12$ with several noise levels. EEG cap has $N = 27$ electrodes.

Indeed, we applied the RCD RAP-MUSIC cost function (5.13) onto the localization of a single dipole CS4 and added several levels of noise (same data as in figure 4.20). The used data is here spatial-only, i.e. the data used for solving the inverse problem is recorded at a single time instant. When using the RCD RAP-MUSIC cost function, we used as input for the signal subspace: $\Phi_S \equiv \mathbf{V}_{meas}$ with $\mathbf{V}_{meas}$ the potentials at a single time instant. The results of the reconstruction of the source are better than those observed in the case of RCD method in the previous chapter. Figure 5.8 shows indeed a more robust behavior of the RCD method towards noise when using the subspace correlation function (5.13).

In figure 5.8 no singular value decomposition or principal component analysis (PCA) was applied. We also applied the RAP-MUSIC and the RCD RAP-MUSIC methodology upon spatiotemporal dataset where the same dipole CS4 is a spike. When using these methodologies, PCA is carried out beforehand for determining the signal subspace. Figure 5.9 shows the average dipole position errors when using RAP-MUSIC (denoted as Subcorr) and the RCD RAP-MUSIC method (denoted as RCD-Subcorr). We observe here the denoising effect of PCA.

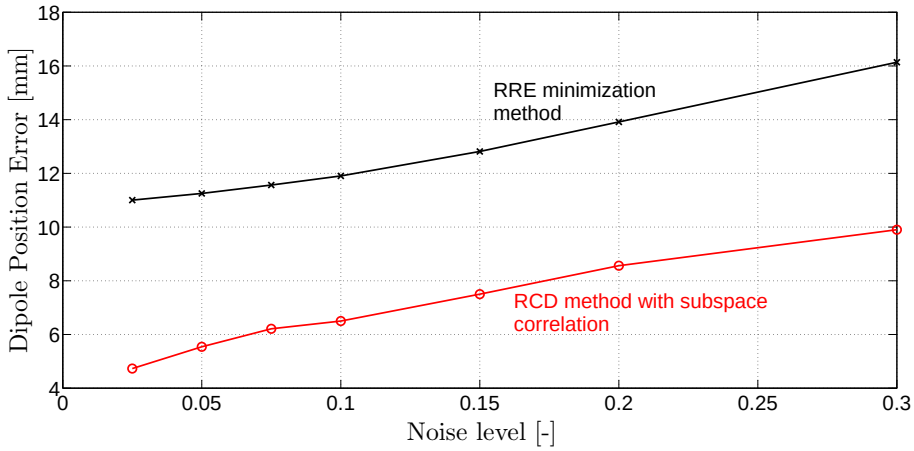

Figure 5.8: Dipole position error for $p = 1$ dipole located at CS4 using spatial only EEG data of figure 4.20.

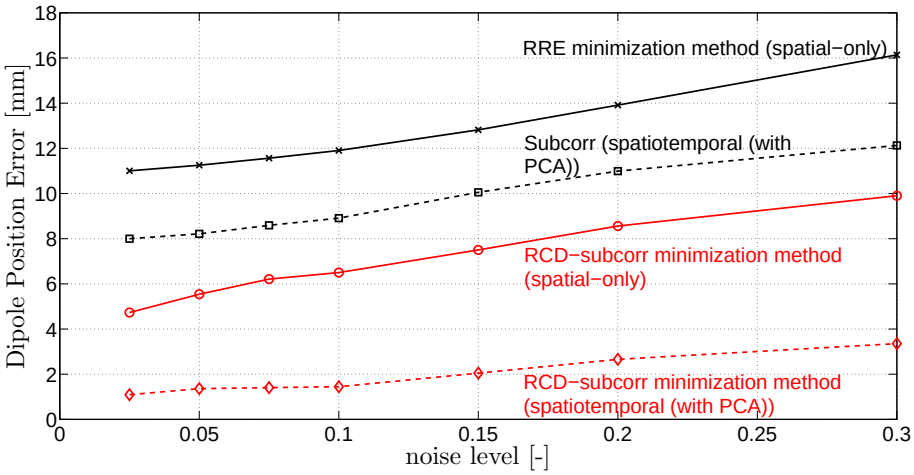

Figure 5.9: Dipole position error for $p = 1$ dipole located at CS4 using spatial-only EEG data of figure 4.20 and when using spatiotemporal EEG data of the same dipole with the time signal being a spike.

5.4.3 Influence of selected number of potentials

Figure 5.10 shows the decrease in Total Dipole Position Error when decreasing the number of selected electrodes N_s. EEG data (figure 5.2) was generated for $p = 3$ dipoles (DL1, DL2, DL3) with noise level $n = 0.3$. Each data point is

computed as the average of 100 EEG samples.

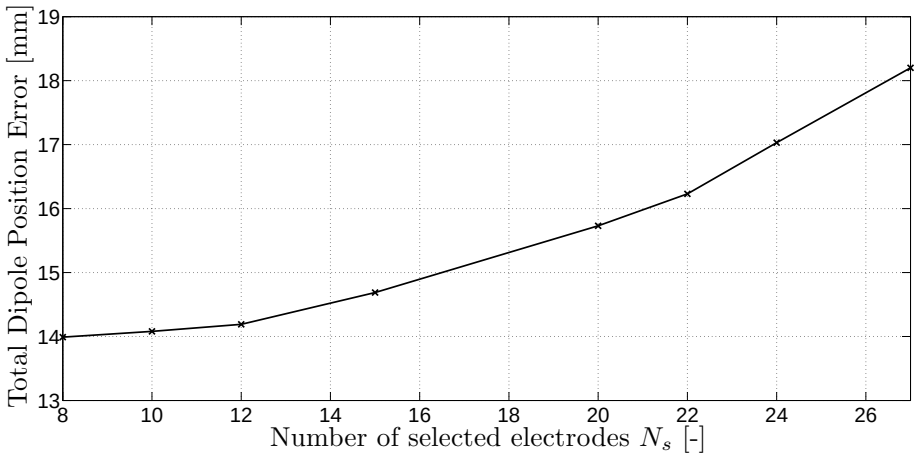

Figure 5.10: Total dipole position error with assumed conductivity ratio $1/60$ and actual conductivity ratio of about $1/24$ with noise level $n = 0.3$ for three dipoles (DL1, DL2, DL3). $N_s = 12$.

In the case of using the RCD methodology for the recovery of multiple dipoles, the same conclusion as in the case of single dipole can be drawn with respect to the influence of N_s on the accuracy. The selection leads also in this case to an improvement in the dipole localization error. Remark that for a certain number of selected electrodes the improvement is marginal when decreasing the number of selected electrodes. When decreasing the number of selected electrodes we observed that the computation time for recovering the dipole was also increasing because the cost function is fluctuating much more.

Accurate results are obtained in the case of noise in the measurements, even at a high level. From figure 5.6, an efficiency of almost 60% is recorded in the presence of noise and indeed such accuracy is satisfactory.

5.4.4 Convergence history

In figure 5.11, the cost function of both methods is displayed for dipoles located at DL2, DL3 (See table 5.1). As in the case of a single dipole, the cost function of the RCD method is lower than the cost of the traditional method in the L_2 norm. It should be noted that the RCD method with a single dipole is not globally minimizing the cost function. It was observed during the computations that the starting location used can influence the solution found. In

the case of multiple dipoles, this remains true.
The dipole location that corresponds with the minimum of the RCD-RAP MUSIC method gives a better solution, compared to the minimum of the traditional approach. The minimal value of the RCD method does not correspond with the minimal value of the traditional method as observed in the figure. Figure 5.11 shows the convergence history for a starting value of the dipole close to the actual dipole position, while for figure 5.12 the starting value is near the center of the spherical head model (See table 5.1).

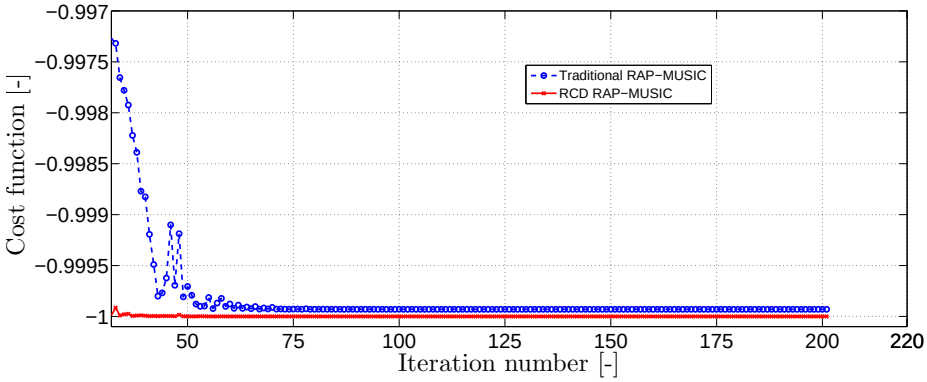

Figure 5.11: Convergence history when recovering the dipole located at DL3 with $\widehat{X} = 1/60$ and $\widetilde{X} = 1/24$. The difference between the first point (e.g. -0.99) and the last point (close to -1) is very small because of the use of a start value close to the actual dipole.

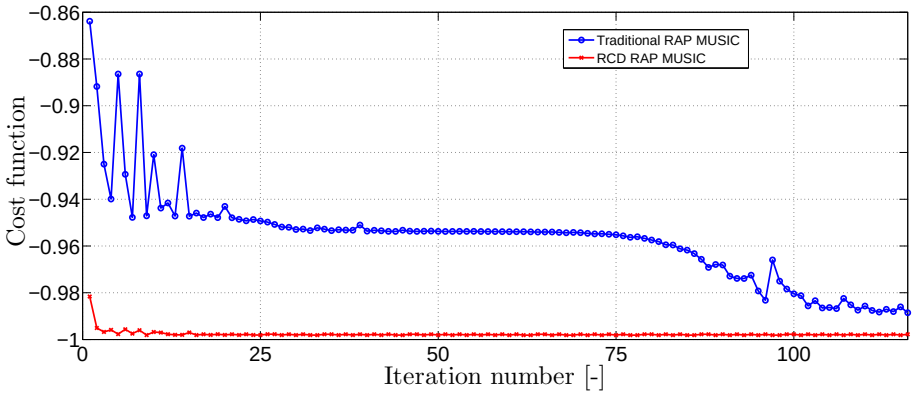

Figure 5.12: Convergence history when recovering dipole located at DL2 with $\widehat{X} = 1/50$ and $\widetilde{X} = 1/30$. The difference between the first point (e.g. -0.86) and the last point (close to -1) is relatively high because the start value is located at the center of the head model.

5.5. Conclusions

In this chapter we extended the traditional RAP-MUSIC with the RCD methodology. We altered the subspace correlation cost function and incorporated selection of the electrodes within the methodology. Results of the numerical experiments with no noise data sets showed similar results as in the case of the RCD methodology elaborated in chapter 4 for the localization of a single dipole. The RCD RAP-MUSIC is more robust to the uncertain conductivity ratio compared to the widely used RAP-MUSIC method. However, in the case of the presence of noise in the data sets, the performance of the RCD RAP-MUSIC is relatively similar to the performance of the traditional RAP-MUSIC methodology and contrary to the RCD methodology for single dipole localization, the RCD RAP-MUSIC method is robust to noise. This was proven by comparing the results of the RCD RAP-MUSIC method for the recovery of a single dipole with the results of the RCD method elaborated in chapter 4. The robustness to noise is mainly because a robust fitting is performed here by using the principal vectors of the subspace correlation cost function.

The methodology presented in this chapter is able to localize a limited number of dipoles ($p < N$) in a noise robust way and is more robust to the uncertain conductivity ratio compared to state of the art methodologies.

CHAPTER 6

EEG Source Analysis with Multiple Uncertainties

6.1. Introduction

In chapter 4, we developed the novel RCD methodology for the recovery of a single dipole where the spatial accuracy was increased by limiting the propagation of the uncertain skull to soft tissue conductivity ratio to the inverse problem solution. In chapter 5, we showed that the RCD methodology can be used for the recovery of multiple dipoles with decrease of localization errors and with robustness to the noise in the measurements. In both previous chapters, only a single uncertainty was considered: the skull to soft tissue conductivity ratio $X = \sigma_{skull}/\sigma_{\text{soft tissue}}$, ($\sigma_{brain} = \sigma_{scalp} = \sigma_{\text{soft tissue}}$).

Next to the three shell spherical head model elaborated in 2.6.2.1, it is possible to implement a multilayered spherical head model, see section 2.6.2.2. It is possible to assign to each layer different conductivities which may differ from each other and which are uncertain. In this chapter, we focus on the formulation of a RCD methodology for the reduction of the propagation of multiple (≥ 2) uncertainties towards the EEG inverse solutions. We employ a five shell spherical head model for performing the analysis of the proposed methodology. The analysis is performed for a single dipole and extension is possible using the methodologies developed in previous chapter.

In section 6.2 we define the used forward model and the simulation setup. Section 6.3 illustrates the sensitivities of the forward solutions to the multiple uncertainties. In section 6.4 we propose the RCD methodology for dealing

with multiple conductivity uncertainties and the results and discussion of the numerical experiments are given in section 6.5.

6.2. Forward model and simulation setup

6.2.1 Introduction

In the previous chapters, a simplified model consisting of three layers - the scalp, the skull and the brain, ($\sigma_{brain} = \sigma_{scalp} = \sigma_{\text{soft tissue}}$) - was used in the computations. With this simplified model, we have shown that the reconstruction of the source mainly depends on the sensitivity of the sensor potentials to the conductivity ratio of the skull $X = \sigma_{skull}/\sigma_{\text{soft tissue}}$. Moreover, the source is better estimated with the inclusion of sensitivity to the single uncertainty X in the cost function. However, the head contains in reality several tissues with different conductivity values. In order to improve the quality of the forward model solutions, multiple layers have been proposed among which, the four and the five shell spherical head models. Here, we implemented a five layered spherical head model, see [146].

6.2.2 Geometry

The five layer spherical head model of [146] takes into account the scalp, the skull, the cerebro-spinal fluid (CSF) layer, the gray and the white matter, see figure 6.1.

The geometrical parameters in the implemented head model are the following: scalp (radius=96mm), skull(radius=86mm) and CSF(radius=80mm), gray matter (GM)(radius=70mm) and white matter (WM)(radius=20mm).

6.2.3 Conductivity values of the tissues

In the present study, we assume the conductivity to be isotropic within the five layered spherical head model depicted in figure 6.1. We denote σ_{scalp} as the conductivity of the scalp, σ_{skull} as the conductivity of the skull, σ_{csf} as the conductivity of the cerebro-spinal fluid (CSF), σ_{gray} as the conductivity of the gray matter (GM), and σ_{white} as the conductivity of the white matter. In order to validate the RCD method for multiple uncertainties, we set

$$\sigma_{gray} = \sigma_{\text{soft tissue}} = 0.33 S/m \tag{6.1}$$

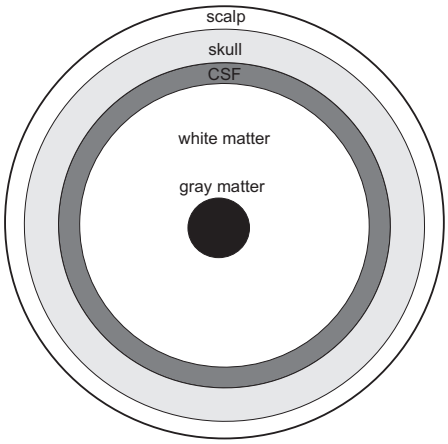

Figure 6.1: Human head approximated by 5 layer spherical head model. The volume model consists of the following layers: the scalp, the skull, the CSF, the white matter and the gray matter.

and we define the conductivity ratio of the scalp ($X_{c,1}$), skull ($X_{c,2}$), CSF ($X_{c,3}$) and white matter ($X_{c,4}$) as:

$$\begin{aligned} X_{c,1} &= \sigma_{scalp}/\sigma_{\text{soft tissue}}, \quad X_{c,2} = \sigma_{skull}/\sigma_{\text{soft tissue}}, \\ X_{c,3} &= \sigma_{CSF}/\sigma_{\text{soft tissue}}, \quad X_{c,4} = \sigma_{white}/\sigma_{\text{soft tissue}} \end{aligned} \tag{6.2}$$

We assume that these conductivity ratios are uncertain and that they can be taken in the respective intervals: $X_{c,1} \in [0.6, \quad 1.4]$, $X_{c,2} \in [1/60, \quad 1/8]$, $X_{c,3} \in [0.6, \quad 1.4]$ and $X_{c,4} \in [0.6, \quad 1.4]$.

6.2.4 Solution of Poisson's equation

In this chapter, we will make use of the widely used De Munck approximation [147] to compute the potentials using the spherical head model described above. Hence, the solution to the Poisson's equation (2.11)is given by [147]:

$$V = \frac{1}{4\pi} \sum_{n=0}^{\infty} (2n+1) R_n(\mathbf{r_0}, \mathbf{r_e}, X_{c,1}, X_{c,2}, X_{c,3}, X_{c,4}) P_n \cos w_{0_e} \tag{6.3}$$

$\mathbf{r_e}$ is the electrode position and $\mathbf{r_0}$ is the source position. P_n are the Legendre polynomials, and w_{0_e} is the angular distance between the electrode and source point. The explicit value of the coefficient $R_n(\mathbf{r_0}, \mathbf{r_e}, X_{c,1}, X_{c,2}, X_{c,3}, X_{c,4})$ containing the conductivity ratio terms, is given in detail in [147].

Notice that the solution provided by the De Munck's model (equation (6.3)) and the one provided by Sarvas model (equation (2.14)), give the same results for the sensor potentials when $X_{c,1} = X_{c,3} = X_{c,4} = 1$ in the former model. In the computations of the forward model, we are using 256 electrodes with cartesian coordinates given in Appendix A.

6.2.5 Numerical experiments

Starting from the actual position of the dipole $\widetilde{\mathbf{r}}_d$ and actual values of the conductivity ratios $\widetilde{X}_{c,1}$, $\widetilde{X}_{c,2}$, $\widetilde{X}_{c,3}$, and $\widetilde{X}_{c,4}$, we compute the forward solution using the five layered spherical head model (6.3). When solving the inverse problem, we vary the assumed conductivity ratios $\widehat{X}_{c,1}$, $\widehat{X}_{c,2}$, $\widehat{X}_{c,3}$ and $\widehat{X}_{c,4}$.

We investigate the performance of the proposed RCD for multiple uncertainties by comparing the reconstructed $\mathbf{r}_d^*$ with the a priori chosen actual position $\widetilde{\mathbf{r}}_d$. The dipole position error is again defined as the difference in the L_2-norm of these dipole positions, see equation (3.5). The numerical experiments are performed similar to figure 3.2 but with inverse solutions solved for different $\widehat{X}_{c,i}$ $(i = 1, \ldots, 4)$.

6.3. Sensitivity to the conductivity tissues

6.3.1 Introduction

We showed in section 2.8 that the potential values computed using the three shell spherical head model are very sensitive to the skull to soft tissue conductivity ratio. In this section, we investigate the forward propagation of the uncertain conductivity ratios $X_{c,1}$, $X_{c,2}$, $X_{c,3}$, and $X_{c,4}$ to the forward solution in the five shell spherical head model. Previous studies in this direction were done in [148] using a statistical approach with a finite element method as forward model. The study of the derivatives of the sensor potentials to the conductivity ratios $X_{c,1}$, $X_{c,2}$, $X_{c,3}$ and $X_{c,4}$ will be investigated here, similar to the study in section 2.8. We employ a finite difference approach for calculating the derivatives.

6.3.2 Sensitivity

Sensitivity to variations of the scalp's conductivity ratio $X_{c,1}$: Figure 6.2 gives the values of the sensitivity evaluated for a conductivity ratio $X_{c,1} = 1$. As ob-

served here, most of the sensors have an absolute sensitivity value close to 0.5 except for a limited number of sensors whose absolute sensitivity values are between 0.5 and 1.5 μ volt. Here, we see that for the considered case, the sensor potential values will not change considerably when changing the scalp conductivity ratio $X_{c,1}$.

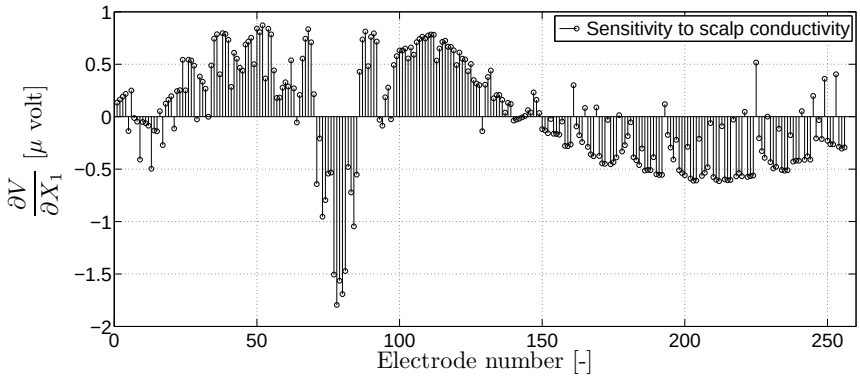

Figure 6.2: Sensitivity of the potentials with respect to the scalp conductivity ratio $X_{c,1}$, for $X_{c,1} = 1$, $X_{c,2} = 0.06$, $X_{c,3} = 1$, $X_{c,4} = 1$ for dipole $\mathbf{r}_d$=[52.5, 15.5, 7.7]mm with orientation $\mathbf{e}_x$.

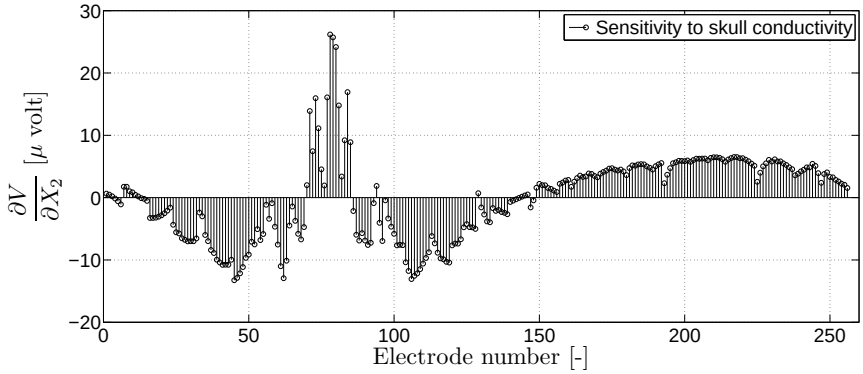

Figure 6.3: Sensitivity of the potentials with respect to the skull conductivity ratio $X_{c,2}$, for $X_{c,1} = 1$, $X_{c,2} = 0.06$, $X_{c,3} = 1$, $X_{c,4} = 1$ for dipole $\mathbf{r}_d$=[52.5, 15.5, 7.7]mm with orientation $\mathbf{e}_x$.

Sensitivity to variations in the Skull's conductivity ratio $X_{c,2}$: Figure 6.3 gives the sensitivity of the potentials to the skull conductivity ratio $X_{c,2}$ for the same dipole position as previously. Much higher values for the sensitivities are recorded here, compared to the sensitivity values for the scalp conductivity

ratio $X_{c,1}$. Consequently, as observed in the case of the three-shell spherical head model in previous chapters, the potential values in the five shell spherical head model are also very sensitive to the skull conductivity ratio $X_{c,2}$. A similar behavior is observed for other dipole positions in the head model.

Sensitivity to variations in the CSF's conductivity ratio $X_{c,3}$: the importance to model the cerebro-spinal fluid (CSF) in the forward EEG models has been underlined in [149, 150]. Following the same strategy as for the scalp and skull conductivity ratio sensitivity, we investigate the CSF conductivity ratio sensitivity values within the five shell spherical head. As observed in figure 6.4, some sensors have a relatively high sensitivity value even if the majority of the sensors have a sensitivity value close to zero.

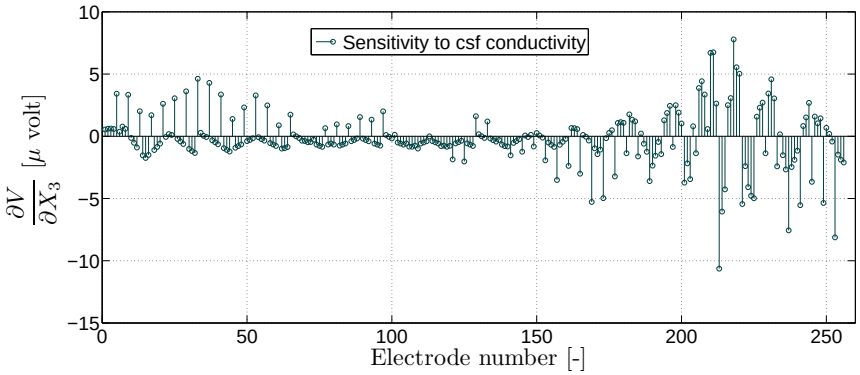

Figure 6.4: Sensitivity of the potentials to the cerebro-spinal fluid conductivity ratio $X_{c,3}$, for $X_{c,1} = 1$, $X_{c,2} = 0.06$, $X_{c,3} = 1$, $X_{c,4} = 1$ for dipole $\mathbf{r}_d$=[52.5, 15.5, 7.7]mm with orientation $\mathbf{e}_x$.

Sensitivity to variations in the White matter's conductivity ratio $X_{c,4}$: this layer like the skull has an anisotropic structure. In [151], the authors studied the effect of white matter anisotropy for the forward EEG computations. In the five layer model used here, we assume an isotropic conductivity of this layer. Figure 6.5 shows the sensitivity value to the white matter conductivity ratio X_4 for the same dipole position as in the case of the previous layers. Some sensors (less than 15) also have a relatively high sensitivity value.

Such behavior of the sensor sensitivities related to the conductivity of the skull, the CSF and the white matter layers suggests to take into account other sensitivities than those associated to $X_{c,2}$ when solving the inverse problem.

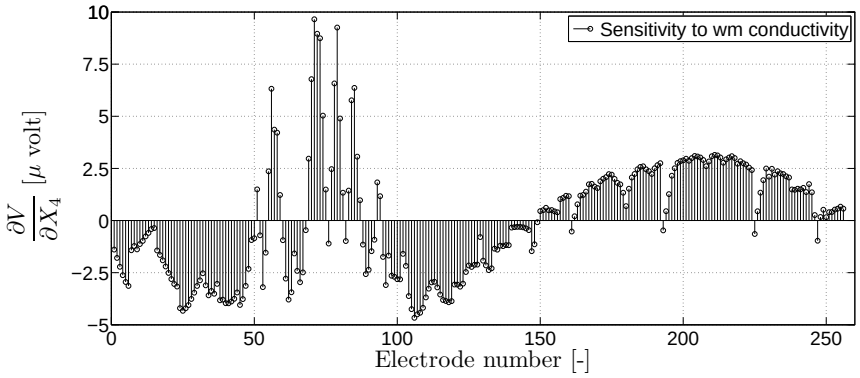

Figure 6.5: Sensitivity of the potentials to the White matter conductivity ratio $X_{c,4}$ for $X_{c,1} = 1$, $X_{c,2} = 0.06$, $X_{c,3} = 1$, $X_{c,4} = 1$ for dipole $\mathbf{r}_d$=[52.5, 15.5, 7.7]mm with orientation $\mathbf{e}_x$.

6.3.3 Discussion

Results show that for the considered numerical experiments the sensor potential values are almost not sensitive to the scalp conductivity ratio. For the CSF and white matter conductivity ratio, relatively high values of the sensitivities were recorded for a limited number of sensors, while the highest values were recorded for the skull. Here, different dipole positions were considered in the gray and white matter region.

The fact that the highest values of the sensitivity is related to skull conductivity ratio, suggests for solving the EEG inverse problem, an extension of the RCD method taking into account multiple uncertainties. Here we may consider for the extended RCD method different combinations, such as combining respectively skull and CSF, skull and white matter.

6.4. RCD methodology for multiple conductivity uncertainties

6.4.1 Introduction

In this section, we propose an extension of the RCD method for solving the EEG inverse problem by extending the cost function towards multiple uncertainties. We introduce modifications with respect to the original RCD formulations in chapter 4. We start with the iterative procedure in section 6.4.2, propose the RCD cost function in section 6.4.3 and present the selection procedure in section 6.4.4. We formulate the methodology in an as general as possible way for limiting the propagation of N_u uncertainties. We denote the

N_u uncertain conductivity ratios as $\widehat{X}_i$, $i = 1, \ldots, N_u$.

6.4.2 Iterative procedure of the RCD method for multiple uncertainties

The original iterative procedure given in section 4.2.4 can be adapted for dealing with multiple uncertainties. In the following, we present explicitly all iterative steps of the RCD method.

Step 1: Start value $\mathbf{r}_d^{(0)}$ is evaluated in the forward model, yielding the lead field matrix $\mathbf{L}(\mathbf{r}_d^{(0)})$, and simulated potential values $\mathbf{V}_\mathrm{m}(\mathbf{r}_d^{(0)}) = \mathbf{L}(\mathbf{r}_d^{(0)})\mathbf{L}(\mathbf{r}_d^{(0)})^\dagger \mathbf{V}_\mathrm{meas}$. Initialize $k = 0$.

Step 2: Calculate the sensitivities $\mathbf{W}_i$, $i = 1, \ldots, N_u$ of the potentials to the conductivity ratios $\widetilde{X}_i$:

$$\mathbf{W}_i^{(k)} = \frac{\partial \mathbf{V}_\mathrm{m}(\mathbf{r}_d^{(k)})}{\partial X_i}\Big|_{X_i = \widehat{X}_i} \tag{6.4}$$

When using the spherical head model, (6.4) can be computed using the analytical solution described in equation (6.3). For the case considered here, the sensitivity to conductivity ratio may concern the skull, the CSF or the white matter associated conductivity ratio. For realistic head models, this sensitivity can be computed through finite differentiation.

Step 3: Selection of least sensitive electrodes based on (6.4). For further details concerning the definition of the selection operator $\mathrm{sel}(\cdot)$, see section 6.4.4. In order to compare simulated and measured EEG potentials, the same selection is carried out on the measured potentials $\mathbf{V}_\mathrm{meas}$. A limited set of potential values are obtained: $\mathbf{S}_\mathrm{m} = \mathrm{sel}(\mathbf{V}_\mathrm{m}) \in \mathbb{R}^{N_s \times 1}$, and the corresponding set of measured EEG potentials $\mathbf{S}_\mathrm{meas} = \mathrm{sel}(\mathbf{V}_\mathrm{meas}) \in \mathbb{R}^{N_s \times 1}$ where N is the number of selected potentials. A selection is also carried out on the lead field matrix $\mathbf{M}(\mathbf{r}_d^{(k)}) = \mathrm{sel}(\mathbf{L}(\mathbf{r}_d^{(k)})) \in \mathbb{R}^{N_s \times 3}$.

Step 4 Calculation of updated value of dipole orientation which is less affected by the uncertainty of the conductivity ratio.

$$\mathbf{d}_\mathrm{opt}^{(k)} = \mathbf{M}^\dagger(\mathbf{r}_d^{(k)})\mathbf{S}_\mathrm{meas} \tag{6.5}$$

Step 5: Calculation of RCD cost function, see next section 6.4.3.

Step 6: Based on the value of the cost function, the next iterate $\mathbf{r}_d^{(k+1)}$ can be computed. If the termination criteria of the minimization procedure are met, i.e. $c^{(k)}$ reaches tolerance ε, then stop the algorithm. Otherwise, update $k = k + 1$ and go to step 2.

The selection procedure needs to be performed in each iteration k of the minimization scheme, which is in this case the Nelder-Mead simplex method.

6.4.3 Cost function of the RCD method

In this section we elaborate how to redefine the RCD cost function that needs to be evaluated in *step 5* of the iterative RCD scheme. In the general case of a spherical head model with multiple layers, the potential values V_k, $k = 1, \ldots, N$ recorded at a certain electrode is a function of N_u uncertain variables $(X_1, X_2, \ldots, X_{N_u})$:

$$\mathbf{V}_\mathrm{m}(X_1, X_2, \ldots, X_{N_u}, \mathbf{r}_d, \mathbf{d}) = \mathbf{L}(X_1, X_2, \ldots, X_{N_u}, \mathbf{r}_d)\mathbf{d} \tag{6.6}$$

Using optimal dipole components in a least squares sense (3.3), (6.6) becomes

$$\mathbf{V}_\mathrm{m}(X_1, X_2, \ldots, X_{N_u}, \mathbf{r}_d) = \mathbf{L}(X_1, X_2, \ldots, X_{N_u}, \mathbf{r}_d)\mathbf{L}^\dagger(X_1, X_2, \ldots, X_{N_u}, \mathbf{r}_d)\mathbf{V}_\mathrm{meas} \tag{6.7}$$

We formulate the first order RCD cost function for multiple uncertainties, denoted here as mRCD, as follows:

$$\mathrm{mRCD}(\mathbf{r_d}, \mathbf{d}) = \frac{\|\mathbf{V}_\mathrm{meas} - \mathbf{V}_\mathrm{m}(\widehat{X}_1, \widehat{X}_2, \ldots, \widehat{X}_{N_u}, \mathbf{r_d}, \mathbf{d}) - \sum_{i=1}^{N_u} \alpha_i \frac{\partial \mathbf{V}_\mathrm{m}}{\partial X_i}|_{X_i = \widehat{X}_i}\|}{\|\mathbf{V}_\mathrm{meas}\|} \tag{6.8}$$

where in the cost function a certain value for the conductivity ratios are assumed. α_i in (6.8) are the Taylor coefficients:

$$\alpha_i = \widetilde{X}_i - \widehat{X}_i, \quad i = 1, \ldots, N_u \tag{6.9}$$

which are approximated using a fitting procedure, see further equation (6.17). Using (6.7), the mRCD cost function in (6.8) can be formulated to be dependent on $\mathbf{r}_d$. The above cost function is obtained by expressing the simulated potential value with actual conductivity ratios $\widetilde{X}_i$, $i = 1, \ldots, N_u$ as a Taylor expansion around the assumed conductivity ratios $\widehat{X}_i$, $i = 1, \ldots, N_u$, i.e. equation

(4.1) becomes:

$$\mathbf{V}_m(\widetilde{X}_1,\ldots,\widetilde{X}_{N_u},\mathbf{r}_d,\mathbf{d}) = \mathbf{V}_m(\widehat{X}_1,\ldots,\widehat{X}_{N_u},\mathbf{r}_d,\mathbf{d}) + \sum_{i=1}^{N_u}(\widetilde{X}_i - \widehat{X}_i)\frac{\partial \mathbf{V}_m}{\partial X_i}\Big|_{X_i=\widehat{X}_i} \tag{6.10}$$

up to the first order.

When considering the five shell spherical head model for solving the EEG inverse problem with multiple uncertainties, three possibilities exist, see the discussion in 6.3.3. The first two possibilities require only two conductivity ratio uncertainties that is skull and CSF, skull and white matter; and the last possibility includes the three conductivity ratio uncertainties.

When considering the uncertainties of skull and CSF, the simulated potentials will contain the two derivative terms with respect to the conductivity ratios $X_{c,2}$ and $X_{c,3}$ defined in (6.2). And the cost function in this case, denoted by $\mathrm{mRCD}_{23}(\mathbf{r}_d)$ is given by:

$$\frac{\|\mathbf{V}_{\text{meas}} - \mathbf{V}_{\text{m}} - (\widetilde{X}_{c,2} - \widehat{X}_{c,2})\frac{\partial \mathbf{V}_{\text{m}}}{\partial X_{c,2}}|_{X_{c,2}=\widehat{X}_{c,2}} - (\widetilde{X}_{c,3} - \widehat{X}_{c,3})\frac{\partial \mathbf{V}_{\text{m}}}{\partial X_3}|_{X_{c,3}=\widehat{X}_{c,3}}\|}{\|\mathbf{V}_{\text{meas}}\|} \tag{6.11}$$

where $\mathbf{V}_{\text{m}}$ is given by equation (6.7) for the assumed conductivity ratios. For the skull and the white matter case, the cost function denoted by $\mathrm{mRCD}_{24}(\mathbf{r}_d)$ is

$$\frac{\|\mathbf{V}_{\text{meas}} - \mathbf{V}_{\text{m}} - (\widetilde{X}_{c,2} - \widehat{X}_{c,2})\frac{\partial \mathbf{V}_{\text{m}}}{\partial X_{c,2}}|_{X_{c,2}=\widehat{X}_{c,2}} - (\widetilde{X}_{c,4} - \widehat{X}_{c,4})\frac{\partial \mathbf{V}_{\text{m}}}{\partial X_{c,4}}|_{X_{c,4}=\widehat{X}_{c,4}}\|}{\|\mathbf{V}_{\text{meas}}\|} \tag{6.12}$$

Including the selection of the potentials in these relations as described in ***Step 3*** and ***5*** of the algorithm, the previous relations become respectively for $\mathrm{mRCD}^s_{23}(\mathbf{r}_d)$:

$$\frac{\|\Delta\mathbf{S} - (\widetilde{X}_{c,2} - \widehat{X}_{c,2})\frac{\partial \mathbf{S}_{\text{m}}}{\partial X_2}|_{X_{c,2}=\widehat{X}_{c,2}} - (\widetilde{X}_3 - \widehat{X}_3)\frac{\partial \mathbf{S}_{\text{m}}}{\partial X_{c,3}}|_{X_{c,3}=\widehat{X}_{c,3}}\|}{\|\mathbf{V}_{\text{meas}}\|} \tag{6.13}$$

and $\mathrm{mRCD}^s_{24}(\mathbf{r}_d)$:

$$\frac{\|\Delta\mathbf{S} - (\widetilde{X}_{c,2} - \widehat{X}_{c,2})\frac{\partial \mathbf{S}_{\text{m}}}{\partial X_{c,2}}|_{X_{c,2}=\widehat{X}_{c,2}} - (\widetilde{X}_{c,4} - \widehat{X}_{c,4})\frac{\partial \mathbf{S}_{\text{m}}}{\partial X_{c,4}}|_{X_{c,4}=\widehat{X}_{c,4}}\|}{\|\mathbf{V}_{\text{meas}}\|} \tag{6.14}$$

with

$$\Delta \mathbf{S} = \mathbf{S}_{\text{meas}} - \mathbf{S}_{\text{m}} \tag{6.15}$$

The neural dipole is determined by the minimization of the above mRCD cost function:

$$\mathbf{r}_d^* = \arg\min_{\mathbf{r}_d} \text{mRCD}(\mathbf{r}_d) \tag{6.16}$$

with given measured potentials.

Since the Taylor coefficients (6.9) are not known beforehand, we perform in each kth iteration of the mRCD scheme, a fitting procedure that fits the potential difference

$$\Delta \mathbf{V}^{(k)} = \mathbf{V}_{\text{meas}} - \mathbf{L}(X_1, X_2, \ldots, X_{N_u}, \mathbf{r}_d)\mathbf{L}^{\dagger}(X_1, X_2, \ldots, X_{N_u}, \mathbf{r}_d)\mathbf{V}_{\text{meas}} \tag{6.17}$$

to the sensitivities $\mathbf{W}_i^{(k)}$ given in (6.4). In the case of $N_u = 2$ uncertainties, this is a fitting in a plane and for $N_u > 2$ in a hyperplane.

At the opposite of the classical scheme of the RCD method, when using only one uncertainty in the inverse problem, the new approach introduces a selection procedure on two different sensitivity values (the first order derivatives). Several possibilities therefore exist for the selection of the potentials to solve the inverse problem with the goal to improve the accuracy.

6.4.4 Selection procedure for multiple uncertainties

Introducing multiple uncertainties in the cost function of the RCD method as in equation (6.8), needs some particular attention in the selecting process of the sensors during the minimization procedure. It is possible to set certain thresholds γ_i, $i = 1, \ldots, N_u$ for sensitivity values where a subset of potentials is formed and used in the inverse procedure. In this case, we impose the following condition:

$$\frac{\partial \mathbf{V}_{\text{m}}(\mathbf{r}_d^{(k)})}{\partial X_i}\Big|_{X_i = \widehat{X}_i} \leq \gamma_i \tag{6.18}$$

More specifically, two selection strategies are possible. The first strategy consists to apply the selection on the first derivative $\dfrac{\partial V}{\partial X_{c,2}}$ and to use the obtained indexes during the selection as the selected potentials of the second derivative $\dfrac{\partial V}{\partial X_{c,i}}$ $(i = 3, 4)$. It is important to use the same indexes for the two derivatives for all the inputs during the minimization procedure, otherwise this leads to

irregularity of the solution. Note here that during the minimization procedure, we impose for each derivative to be less or equal to the same threshold. This means that the subset of the derivative $\frac{\partial V}{\partial X_{c,i}}$ that is used in the cost function may contain data which is not necessarily minimally influence by the conductivity ratio. The second approach consists to perform the selection simultaneously on $\frac{\partial V}{\partial X_{c,2}}$ and $\frac{\partial V}{\partial X_{c,i}}$ and to compare the indexes. If the indexes are the same, this means that the data used are both minimally influenced by the conductivities $X_{c,2}$ and $X_{c,i}$ and can be used simultaneously in the procedure. This suggests that a very limited subset could be at the end necessary for the case of multiple uncertainties in the simulated potentials. From sensitivity analysis results, this second option is hard to achieve since it is difficult to obtain sensors that are the same time less sensitive to the three conductivity ratios. We will then, focus on the first approach which seems possible to realize.

6.5. Results and discussion

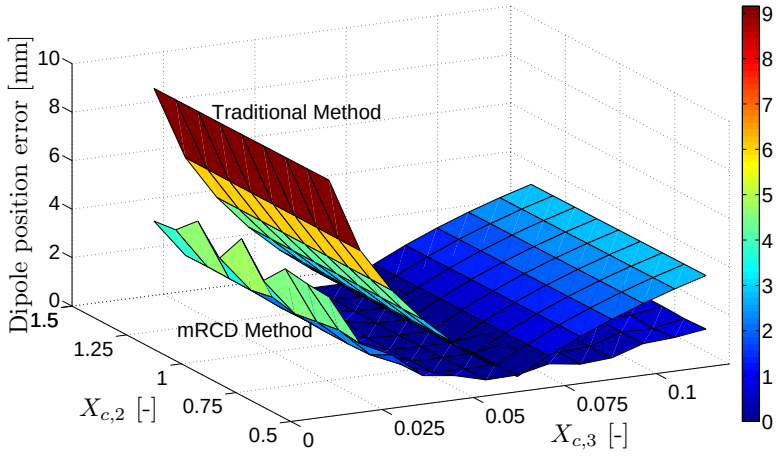

Figure 6.6: Results of the EEG inverse problem with uncertainties of skull and CSF with the RCD method for dipole $\mathbf{r}_d$=[52.5, 15.5, 7.7]mm with orientation $\mathbf{e}_x$.

In this section, results of the EEG inverse problem are presented when using the RCD methodology elaborated in section 6.4. We compare in a first stage the reduction in recovery errors when using the RCD method compared to the results of the traditional methodology. In figure 6.6 results of the traditional

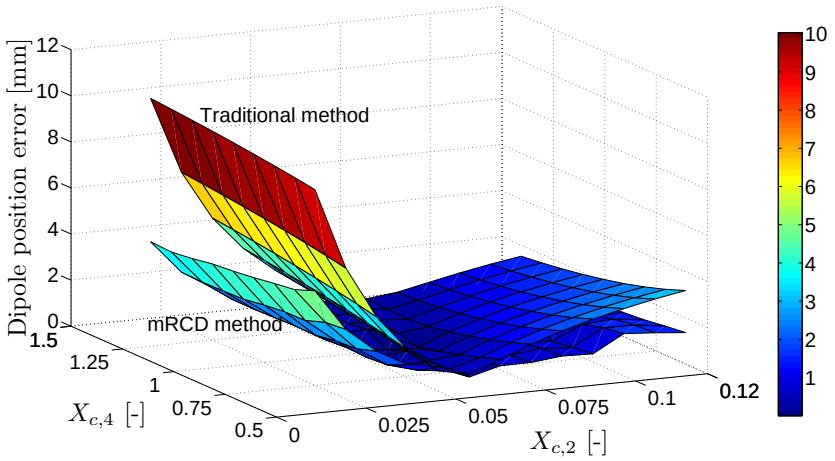

Figure 6.7: Results of the EEG inverse problem with uncertainties of the skull and the white matter with the RCD method for dipole $\mathbf{r}_d$=[52.5, 15.5, 7.7]mm with orientation $\mathbf{e}_x$.

method with the relative residual energy (RRE) as cost function (see section 3.2 in chapter 3) and the RCD method with cost function mRCD^s_{23} are displayed on the same figure. Figure 6.7 compares the traditional methodology with the RCD method (cost function mRCD^s_{24}). The same trend in reduction is observed. When considering respectively the uncertainties of skull and white matter as observed in figure 6.7 , an improvement of 0.5 to 6 mm was recorded in the reconstruction of the source, while this improvement was limited to 5 mm when the uncertainties of the skull and CSF were considered (see figure 6.6).

As observed in previous chapters with a three shell spherical head model, the skull layer largely influences the reconstruction of the source in a simple spherical head model. The new approach in this chapter shows that incorporating multiple uncertainties when using a five shell spherical head model leads to an improvement of the accuracy. We also compare the efficiency of the mRCD methodology compared to the RCD methodology that deals with a single uncertainty. We observe a marginal increase in accuracy meaning that reduction is mainly carried out for the most dominant uncertainty, i.e. uncertainty that has a high impact upon the forward model. This is in this case the conducivity ratio associated to the skull.

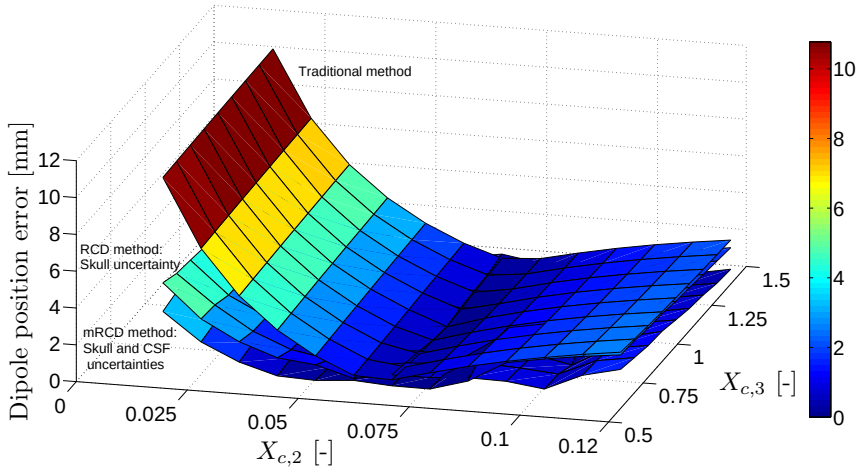

Figure 6.8: Results of the EEG inverse problem with uncertainties of the skull and the white matter with the single RCD method and the multiple RCD method for dipole $\mathbf{r}_d$=[52.5, 35.0, 7.0]mm with orientation $\mathbf{e}_x$.

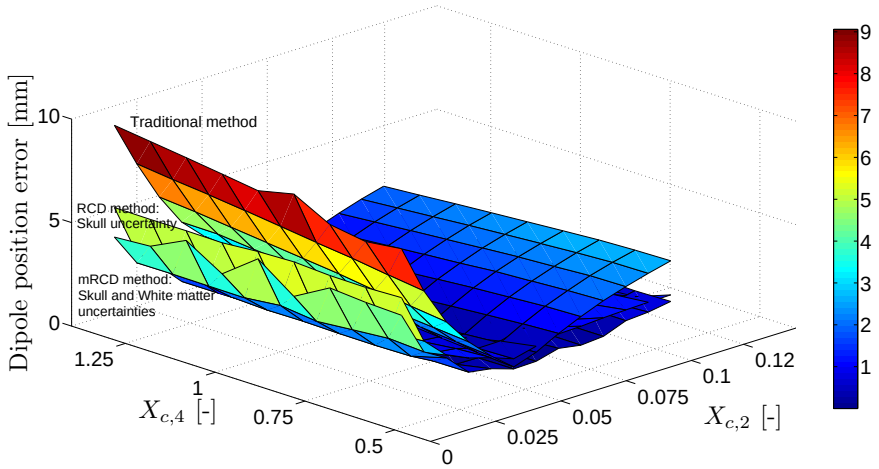

Figure 6.9: Results of the EEG inverse problem with uncertainties of the skull and the white matter with the single RCD method and the multiple RCD method for dipole $\mathbf{r}_d$=[61.6, 42.0, 10.5]mm with orientation $\mathbf{e}_x$.

6.6. Conclusions

In this chapter, we extended the RCD methodology to be applicable for multiple uncertainties, i.e. the mRCD method. A five layered spherical head model was used as forward model. We observed that the potential values do not

have the same sensitivity values to the conductivity ratios: the potentials values are less sensitive to a change of value in the conductivity ratio of the scalp and gray matter, and sensitive to the rest of the layers with a different order of magnitude. From the sensitivity analysis, one can confirm that the skull is the most sensitive layers when considering spherical head models in general. We also observed that the best results for the different combinations for multiple uncertainties, were obtained for low conductivity ratios as it was the case with a three shell spherical head model. We performed numerical experiments and showed a decrease in dipole position error when using the mRCD compared to the traditional methodology. We performed numerical experiments for the reduction of two uncertainties: the skull to grey matter and the CSF to grey matter ratios. We also performed reduction of two other uncertainties: the skull to grey matter and the white matter to grey matter ratios. We showed that the decrease in recovery errors is mainly achieved in the most dominant conductivity, i.e. the skull to grey matter conductivity ratio. We also showed that the mRCD is more optimal than the original RCD methodology that deals with a single uncertainty.

CHAPTER 7

General Conclusion and Future Work

7.1. Conclusions

In this thesis, techniques for the reduction of reconstruction errors in electromagnetic inverse problems were introduced. Indeed, noise in the measurements and uncertainties in the forward model give rise to errors in the reconstructed parameters when solving the inverse problem. A reduction technique was developed and applied onto electroencephalography (EEG) source analysis.

Electroencephalography (EEG) is the recording of the electrical activity arising from the neurons within the brain. The resulting signals of the electrical activity of the brain over a short period of time, are recorded by a set of electrodes placed at the surface of the head. The results of these measurements may be used to detect abnormalities related to electrical activity of the brain. Starting from Maxwell's equations in their quasi-static formulation and from a physical model of the head, the forward EEG problem predicts the measurements that would be obtained for a given electrical activity of the brain. In this thesis, the electrical activity of the brain is described by a configuration of current sources, i.e. electrical dipole sources, and the used head models are multi-layered concentric spherical head models. The so-called inverse EEG problem starts from measured EEG data and recovers the locations and orientations of the current sources. A loss in accuracy of the recovered neural sources may occur because of uncertainties in the forward model.

It has been shown that the EEG forward problem solution highly depends on the electrical conductivity values of the different tissues present in the head. In particular, for the three shell spherical head model, this is the case for the skull to soft tissue conductivity ratio. In practice, it is difficult to measure the real value of the conductivity ratio. In order to quantify this dependence, we defined and analyzed the sensitivity of the sensor to this conductivity ratio. It is possible using sensitivity analysis to determine which sensors are highly affected by the conductivity and those who are not when considering a dipole source in a specific region. In the numerical simulations carried out, it was observed that the sensitivity of the sensor potentials is characterized by the position and orientation of the dipole in the brain and the specified value of the conductivity ratio. Consequently, sensitivity analysis is thus a tool to determine the propagation of the uncertain conductivity onto the EEG forward problem. Therefore, it became important to study in the three shell spherical head model the effect of the skull to soft tissue conductivity ratio on the simulated potentials which need to be as accurate as possible, and to develop a strategy that improves the accuracy of the solution of the inverse problem.

Indeed, it is shown that the accuracy of the EEG inverse problem also highly depends on the conductivity ratio as observed from the simulations. We even observed that the influence of the conductivity ratio can exceed the influence due to measurement noise in some cases (when large discrepancy exists between assumed and actual conductivity ratio) when recovering the EEG inverse solution. In the case of the traditional source reconstruction methods, the influence of the conductivity ratio uncertainty on the EEG inverse problem solution is quite high and can be of the order of centimeters. Finally, results of the sensitivity analysis for all considered dipole positions have shown very high sensitivity values for low skull to soft tissue conductivity ratios.

As a next step we introduced a new approach which we called the 'Reduced Conductivity Dependence (RCD) method' for obtaining solutions for the inverse problem that are more accurate in the sense that the results are less degraded by the uncertain conductivity ratio. In order to obtain this improvement of the spatial accuracy of the EEG source localization, the fundamentals of the proposed method are the use of the sensitivity of the potentials at the various electrodes and the formulation of novel cost functions.

Indeed, we formulated the RCD cost function in such a way that, contrary to state of the art techniques, the sensitivity of the sensors to the uncertain skull to soft tissue conductivity ratio is included. Moreover, we proposed a selection procedure that removes the sensors that are highly influenced

by the uncertain conductivity ratio. In a first stage, the RCD method was developed for reconstructing a single electrical dipole where the forward model contains a single uncertainty, i.e. the skull to soft tissue conductivity ratio. Numerical experiments were performed for different active electrical dipoles and for different actual conductivity ratios, i.e. unknown conductivity ratio values that correspond with reality, and assumed conductivity ratios, i.e. conductivity ratio values that are used in the forward model for solving the inverse problem. The results show that a reduction in dipole localization errors is obtained to 60-80% in the case that no noise is available in the measured data sets. However, when the data sets contain noise, then the efficiency of the RCD method is only 20-60%, depending on the noise level in the data sets used for solving the inverse problem. The reason for the less efficiency in the noise case is because the fitting procedure, needed within the RCD method for approximating the Taylor coefficients, is not performing well when noise is available in the data sets.

We also investigated the use of the RCD method in the case of using a higher number of electrodes within the EEG cap. Contrary to the traditional method, a reduction in dipole localization errors is observed when increasing the number of electrodes within the EEG cap. We state that the RCD method has an important advantage compared to state of the art methods when the EEG cap contains dense sensing electrodes. This is due to the fact that a higher variety of sensors can be selected within the RCD method. Moreover, the fitting procedure within the RCD procedure works in a more accurate way. The developed RCD method is innovative in the sense that for a given configuration of electrodes, spatial resolution can be improved, not by increasing the number of electrodes as often suggested, but instead by making a selection of potentials less affected by the sensitivity. It was assumed that a high number of electrodes in an EEG cap does not increase the spatial resolution for the traditional approach. However, a larger number of electrodes together with the selection strategy increases sufficiently the spatial resolution in the EEG dipole localization. This is an important conclusion within this doctoral work.

A single current dipole model may be used to represent well-localized active neural sources for events like epileptic spikes or early stages of an epileptic seizure. Indeed, a simple and in many cases valid model of brain electrical activity assumes a focal source in a spherical shaped head. The single current dipole is then adequate to model the location in space, as well as the magnitude and orientation of current flow. However, several simultaneously active sources are better modeled by multiple dipoles, i.e. the electrical activity must be approximated by multiple dipoles to achieve a more realistic analysis study. For that reason we extended the RCD method to the robust recovery

of a limited number of multiple sources when using the Recursively Applied and Projected Multiple Signal Classification (RAP-MUSIC) algorithm. This comprises the second stage of this doctoral thesis.

We introduced the so-called RCD RAP-MUSIC methodology where the subspace correlation cost function is altered and where selection of electrodes is carried out in each iteration of the minimization procedure. Results of the numerical experiments showed that the sensitivity analysis remains an important factor for the improvement of the accuracy in the reconstruction of the multiple sources. The selection method provides to the combined RCD RAP-MUSIC method, data with relevant information for a better reconstruction of the source. A total difference of more than 15 millimeters was even recorded in the noise case, for high level of noise when using a total of 5 dipoles.

The new method has proved to be robust to noise at the opposite of the single dipole case when it has been observed that for high level of noise in the measurements, the RCD method solution converges towards the traditional solution. The simulations have also shown that the efficiency recorded when the measurements do not contain noise, can also be observed in the case of noise in the case of multiple dipoles. The developed RCD RAP-MUSIC method is useful for the localization of a limited number of dipoles in the brain with results displaying a good improvement of the spatial accuracy.

In reality, the uncertainty may concern multiple conductivities and were studied in a third stage. Improved forms of spherical head models have led to the design of four, five and multiple layers in spherical head models. These advanced forms of the spherical model consist of multiple number of spheres to represent layers of different tissues, like the scalp, the skull, the cerebro-spinal fluid layer, the gray and the white matter. The use of these five layers models has led to better forward model evaluations. The RCD methodology was extended so that it is applicable when the forward model contains multiple uncertainties.

Results from numerical experiments showed that when using spherical head models with multiple layers, the potential values do not have the same sensitivity values to the conductivity ratio to each layer. It was observed that the sensor potential values are less sensitive to a change of value in the conductivity ratio of the scalp to gray matter, while a higher sensitivity for the sensor potentials was observed for the other layers. From the sensitivity analysis, one can confirm that the skull conductivity corresponds with the highest sensor potential sensitivity when considering spherical head models

in general. We also observed that the best results for the different combinations for multiple uncertainties, were obtained for low conductivity ratios as it was the case with a three shell spherical head model.

The various sensitivities were included in the RCD cost function and the influence of two uncertainties was investigated. Results of the simulations show that incorporating two uncertainties in the cost function lead to a better reconstruction of the dipole parameters in comparison to the traditional methodology. Moreover, the results of the RCD method when including multiple uncertainties has a better functioning than the RCD method that was originally developed in the first stage where a single uncertainty can be incorporated.

7.2. Future research

It was observed during the computations that the minimization of the RCD cost function, even for a single dipole, does not always result into a global minimum. Such situation may lead to numerical instabilities. Some mathematical work (i.e. numerical analysis, optimization) needs to be done to improve the used minimization method or to provide a more stable minimization method. The multistart simplex technique can be an option to overcome the problem of local minima, often encountered during the selection of the sensors. Another possibility is to formulate the RCD methodology within a trust region framework so to stabilize the algorithm.

In the presented work, the RCD cost function only includes the first order derivatives of the sensor potentials to the uncertain conductivity ratio. More mathematical work should lead to a more elaborate framework in which one could decide up to what order of derivative is needed to be included in the RCD cost function in order to reduce the uncertainty propagation of the conductivity ratio. Here, we should focus not only on EEG inverse problems but also on other uncertain inverse problems.

Different subsets of sensors are used during the iterative procedure for solving the inverse problem where a fixed number of selected sensors is defined beforehand. We foresee that during the iterative procedure, it is possible that the selected information is not optimal for each iterative step. Indeed, it may happen that due to fixing the number of selected sensors for some steps important information is excluded or in the opposite case that irrelevant sensor information is included in the computation while not needed. Therefore, for each iteration an algorithm needs to be developed for determin-

ing the relevant contributions of the sensors according to criteria to be defined.

Other topics of future research are the following:
Clinical validation using real measured data: The RCD methodology was validated in this thesis using numerical experiments. In order to validate the RCD methodology in a more thorough way, EEG signals measured in a clinical setup upon several patients should be used as input to the inverse problem. These patients need to have suffered from epileptic seizures (at the time of the EEG measurements) and need to be rendered seizure free after surgery. Validation can be carried out by comparing the region indicated by the RCD methodology and the region that was surgically removed. Another possibility is to use data originating from depth electrodes that were invasively monitored and which pinpoints the epileptogenic zone. Comparison with the source location recovered using the RCD solution methodology can also be a validation strategy. When carrying out the above validation strategies, comparisions can be made with the source locations recovered using the traditional inverse methodology. Moreover, a realistic head model needs to be used and the sensor locations need to be accurately known so to eliminate as much as possible other sources of errors.

Conductivity uncertainty distribution: The model of conductivity ratio values used in this thesis is not stochastic, it is a uniform distribution resulting from values often found in the literature. Future work should be done with a stochastic distribution of the conductivity ratios.

Anisotropic conductivity and realistic head models: Results of the RCD method in this thesis were limited to isotropic conductivities and constitutes a relevant work towards improvement of EEG source analysis. Future work can consist in using the RCD in realistic head models where the potentials are calculated using numerical techniques. A first step was made in Appendix C. Investigations can be carried out in a first stage by using isotropic conductivities. Next, anisotropic conductivities based on diffusion tensor magnetic resonance images can be incorporated in the realistic head model where the uncertainty to the conductivity can be reduced in the inverse problem. Moreover, the RCD method can then be evaluated using clinical EEG data.

Selection for noise: A future work should investigate if the selection of sensors for solving the inverse problem could be extended by not only considering the sensitivity to the conductivity ratio but also to the sensitivity to stochastic noise. In that case the increase of the localization error due to the presence of noise in the measurements could be reduced by selecting the appropriate

sensors.

Validation of the new methodology: Initial results of the RCD method using a simple spherical head model have shown a decrease in the dipole position error. Improvement on dipole position was equally recorded on all the geometries used in this thesis, and these results are promising and a validation of the developed method for real data should be considered in the future. Using several sets of real measurements in the RCD method will surely give a real efficiency of the proposed methodology.

APPENDICES

APPENDIX A

EEG Electrode Coordinates

Several electrode configurations are used in this dissertation. The cartesian coordinates of the electrode configuration are obtained using the relation:

$$\begin{aligned} x &= \mathrm{R}\cos\theta\sin\phi \\ y &= \mathrm{R}\sin\theta\sin\phi \\ z &= \mathrm{R}\cos\phi \end{aligned} \tag{A.1}$$

where R =9.2 cm, which is the radius of the scalp. This relation is useful in the computation of the angle θ between the position of the dipole and the electrodes as described in the expression of the potential V, see (2.14), and the value of the sensitivity $\dfrac{\partial V}{\partial X}$.

It is important to notice that the inter-electrode distance is reduced for higher number of electrodes. In this thesis, we are using electrode configurations with 27, 56, 74, 112, 148 and 256 electrodes. In order to get a particular configuration of electrodes, one needs to change the value of `radius` (See 5^{th} line of the code). For example if `radius=40`, we have a configuration of `56 electrodes`. More configurations are built up on the variation of the value taken by `radius`.

As an example, figure A.1 shows the electrode configuration of 256 electrodes, as used in the computations of chapter 6.

```
% electrode position generator

% initialization
```

```
theta = (0:15:120) .*pi/180 ;
radiussphere=9.2;
radius=30;
%radius=8.52(261 electrodes), radius=8.6(257 electrodes),
% radius=15(148 electrodes), radius=30(74 electrodes)
%radius=40(56 electrodes), radius=35(64 electrodes)
distbetweenelectr = radius*pi/180*9.2;


% Number of electrodes
totallength = 2*pi*radiussphere.*sqrt(1-(cos(theta)).^2);
Nelectr = round(totallength./distbetweenelectr);

% Phi calculation

for k=1:length(theta);
    Angles.theta{k} = theta(k) ;
    if Nelectr(k)==0
        DeltaPhi(k) = 2*pi;
        Phi{k} = 0;
        Angles.phi{k} = Phi{k};
    else
        DeltaPhi(k) = 2*pi/Nelectr(k);
        Phi{k} = 0: DeltaPhi(k) : ((2*pi) - DeltaPhi(k));
        Angles.phi{k} = Phi{k};
    end
end

TotalNumberElectr=sum(Nelectr)+1
Angles

% Final Generation of Elpos

el=[];
for k=1:length(theta)
    for kk=1:length(Angles.phi{k})
        el = [el ; Angles.theta{k} Angles.phi{k}(kk)];
    end
end
```

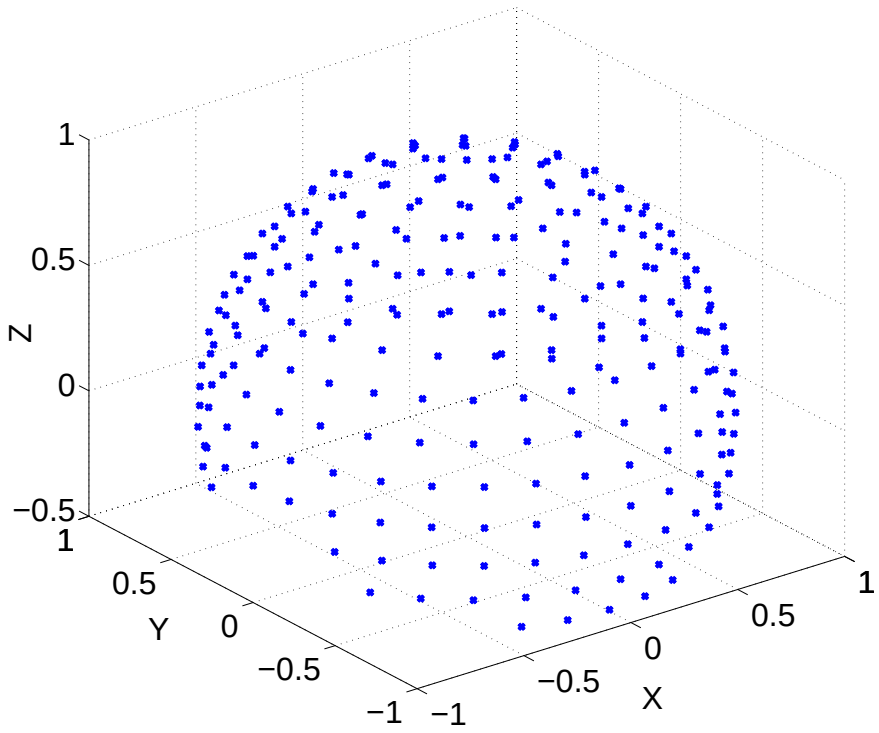

Figure A.1: Geometry of the head with EEG cap: 256 electrodes are used for computations in chapter 6. The EEG recording electrode positions are indicated by the small points.

APPENDIX B

Analytical computation of the Derivatives

In this appendix, we will construct the analytical expressions for the derivatives of the potentials to the conductivity ratio X and the the electrode position θ in the spherical head model. In the first part, we describe the first and second order derivatives of the potentials to the conductivity ratio X. Two approaches are used: first the direct computation of the derivatives starting from the analytical solution of Poisson's equation described in chapter 2 with

$$\mathbf{V}(X, \mathbf{r}_d, \mathbf{d}) = \mathbf{L}(X, \mathbf{r}_d)\mathbf{d} \tag{B.1}$$

and second, the use of the optimal dipole orientation in least squares sense that involves the measured signals $\mathbf{V}_{\text{meas}}$:

$$\mathbf{V}(X, \mathbf{r}_d) = \mathbf{L}(X, \mathbf{r}_d)\mathbf{L}(X, \mathbf{r}_d)^{\dagger}\mathbf{V}_{\text{meas}} \tag{B.2}$$

2.1. Computation of the first and second order derivatives

2.1.1 Computation of the first order derivative V'

The RCD method is mainly based on the sensitivity of the potentials. A direct differentiation of the potential distribution validated by a numerical method is given in this section. The potential distribution as the semi-analytical solution of the poisson equation (2.10) is :

$$\mathrm{V} = \frac{1}{4\pi\sigma_{soft}\mathrm{R}^2}\sum_{\mathrm{i}=1}^{\infty}\frac{X(2\mathrm{i}+1)^3}{\mathrm{g_i}(\mathrm{i}+1)\mathrm{i}}\mathrm{l}^{\mathrm{i}-1}[\mathrm{i}\mathrm{d_r}\mathrm{P_i}(\cos\theta) + \mathrm{d_t}\mathrm{P_i^1}(\cos\theta)] \tag{B.3}$$

where

$$g_i = [(i+1)X+i]\Big[\frac{iX}{i+1}+1\Big] + (1-X)\Big[(i+1)X+i\Big](f_1^{i_1} - f_2^{i_1}) - i(1-X)^2(f_1/f_2)^{i_1}$$

Defining $G(\theta) = [id_r P_i(\cos\theta) + d_t P_i^1(\cos\theta)]$ and $g_i = f_i(X)$, and taking into account that the infinite series in (B.3) is often truncated when we are computing the potential distribution on the spherical head model (only the first $N_{max} = 40$ terms are used), the previous relation becomes:

$$V = \frac{1}{4\pi\sigma_{soft}R^2}\sum_{i=1}^{N_{max}} \frac{X(2i+1)^3}{f_i(X)(i+1)i} l^{i-1} G(\theta) \tag{B.4}$$

Partial derivation of this new relation with respect to X only gives:

$$\frac{\partial V}{\partial X} = \frac{1}{4\pi\sigma_{soft}R^2}\sum_{i=1}^{N_{max}} \frac{\partial}{\partial X}\Big(\frac{X}{f_i(X)}\Big)\frac{(2i+1)^3}{(i+1)i} l^{i-1} G(\theta) \tag{B.5}$$

which becomes:

$$\frac{\partial V}{\partial X} = \frac{1}{4\pi\sigma_{soft}R^2}\sum_{i}^{N_{max}} \Big(\frac{f_i(X) - Xf'_i(X)}{f_i(X)^2}\Big)\frac{(2i+1)^3}{(i+1)i} b^{i-1} G(\theta) \tag{B.6}$$

where $f'_i(X)$ is given by the relation:

$$f'_i(X) = \frac{\partial f_i(X)}{\partial X} = (i+1)\Big[\frac{iX}{i+1}+1\Big] + \Big((i+1)X+i\Big)\Big[\frac{i}{i+1}\Big] \tag{B.7}$$

$$-[(i+1)X+i](f_1^{i_1} - f_2^{i_1}) + (1-X)(i+1)(f_1^{i_1} - f_2^{i_1}) + 2i(1-X)(f_1/f_2)^{i_1}$$

A more simple expression of f'_i is:

$$\frac{\partial f_i(X)}{\partial X} = \frac{(i+1)[iX+(i+1)] + i[(i+1)X+i]}{i+1} \tag{B.8}$$

$$+\Big[(1-X)(i+1) - [(i+1)X+i]\Big]\Big(f_1^{i_1} - f_2^{i_1}\Big) + 2i(1-X)(f_1/f_2)^{i_1}$$

Setting $H_i(X) = \Big(\frac{f_i(X) - Xf'_i(X)}{f_i(X)^2}\Big)$ with the inputs $f_i(X)$ and $f'_i(X)$ already known, the derivative of the potential to the conductivity ratio becomes:

$$\frac{\partial \mathrm{V}}{\partial X} = \frac{1}{4\pi\sigma_{soft}\mathrm{R}^2} \sum_{\mathrm{i}=1}^{N_{\max}} \mathrm{H_i(X)} \frac{(2\mathrm{i}+1)^3}{(\mathrm{i}+1)\mathrm{i}} l^{\mathrm{i}-1} \mathrm{G}(\theta) \tag{B.9}$$

2.1.2 Computation of the second order derivative V''

Using previous result i.e. (B.9), the second order derivative can be written as

$$\frac{\partial^2 \mathrm{V}}{\partial X^2} = \frac{1}{4\pi\sigma_{soft}\mathrm{R}^2} \sum_{\mathrm{i}}^{N_{\max}} \frac{\partial \mathrm{H_i(X)}}{\partial X} \frac{(2\mathrm{i}+1)^3}{(\mathrm{i}+1)\mathrm{i}} l^{\mathrm{i}-1} \mathrm{G}(\theta) \tag{B.10}$$

where

$$\frac{\partial \mathrm{H_i(X)}}{\partial X} = \frac{\mathrm{f'_i(X)f_i^2(X)} - [\mathrm{f'_i(X)} + X\mathrm{f''_i(X)}]\mathrm{f_i^2(X)} - 2\mathrm{f_i(X)f'_i}(X)[\mathrm{f_i(X)} - X\mathrm{f'_i(X)}]}{\mathrm{f_i^4(X)}}$$

which becomes after simplifications:

$$\frac{\partial \mathrm{H_i(X)}}{\partial X} = \frac{-[X\mathrm{f''_i(X)}]\mathrm{f_i(X)} - 2\mathrm{f'_i(X)}[\mathrm{f_i(X)} - X\mathrm{f'_i(X)}]}{\mathrm{f_i^3(X)}}$$

Using previous result as seen in (B.8) we can compute $\mathrm{f''_i(X)}$. So

$$\mathrm{f''(X)} = \frac{[\mathrm{i}(\mathrm{i}+1) + \mathrm{i}(\mathrm{i}+1)]}{(\mathrm{i}+1)} - [2(\mathrm{i}+1)]\left(\mathrm{f_1^{i_1}} - \mathrm{f_2^{i_1}}\right) - 2\mathrm{i}(\mathrm{f_1}/\mathrm{f_2})^{\mathrm{i_1}}$$

Gathering all the terms, a more simple expression becomes:

$$\mathrm{f''_i(X)} = 2\mathrm{i} - 2(\mathrm{i}+1)\left(\mathrm{f_1^{i_1}} - \mathrm{f_2^{i_1}}\right) - 2\mathrm{i}(\mathrm{f_1}/\mathrm{f_2})^{\mathrm{i_1}}$$

and finally,

$$\frac{\partial \mathrm{H_i(X)}}{\partial X} = \frac{-\left(2\mathrm{i} - 2(\mathrm{i}+1)\left(\mathrm{f_1^{i_1}} - \mathrm{f_2^{i_1}}\right) - 2\mathrm{i}(\mathrm{f_1}/\mathrm{f_2})^{\mathrm{i_1}}\right)X\mathrm{f_i(X)} - 2\mathrm{f'_i(X)}\left[\mathrm{f_i(X)} - X\mathrm{f'_i(X)}\right]}{\mathrm{f_i^3(X)}}$$

Where the inputs, $\mathrm{f_i(X)}$ and $\mathrm{f'_i(X)}$ are already given in the previous section.

2.2. Alternative computations of the derivatives

While implementing the RCD method, a new approach for computing the derivatives of the potentials to the conductivity ratio X, was introduced. This takes into account the optimal dipole $\mathbf{d}_{\mathrm{opt}}$.

2.2.1 Alternative first order derivative V′

As explained in chapter 2, the simulated potentials V_i, $i = 1, \ldots, N$ can be written as $\mathbf{V}(X, \mathbf{r}_d, \mathbf{d}) = \mathbf{L}(X, \mathbf{r}_d)\mathbf{d}$. It is also known that the dipole orientation can be approximated in a least squares sense using (3.3): $\mathbf{d}_{\text{opt}} = \mathbf{L}^{\dagger}(X, \mathbf{r}_d)\mathbf{V}_{\text{meas}}$. Taking this into account, the simulated potential becomes:

$$\mathbf{V}(X, \mathbf{r}_d, \mathbf{d}) = \mathbf{L}(X, \mathbf{r}_d)\mathbf{L}^{\dagger}(X, \mathbf{r}_d)\mathbf{V}_{\text{meas}} \tag{B.11}$$

So a simple derivation with respect to X gives:

$$\begin{aligned} \frac{\partial \mathbf{V}}{\partial X}(X, \mathbf{r}_d, \mathbf{d}) &= \frac{\partial \mathbf{L}}{\partial X}\mathbf{L}^{\dagger}(X, \mathbf{r}_d).\mathbf{V}_{\text{meas}} + \mathbf{L}(X, \mathbf{r}_d)\frac{\partial \mathbf{L}^{\dagger}}{\partial X}.\mathbf{V}_{\text{meas}} \\ &= \Big[\frac{\partial \mathbf{L}}{\partial X}\mathbf{L}^{\dagger}(X, \mathbf{r}_d) + \mathbf{L}(X, \mathbf{r}_d)\frac{\partial \mathbf{L}^{\dagger}}{\partial X}\Big].\mathbf{V}_{\text{meas}} \end{aligned} \tag{B.12}$$

Due to the fact that $\mathbf{L}^{\dagger}(X, \mathbf{r}_d) = \Big(\mathbf{L}^{\mathrm{T}}(X, \mathbf{r}_d)\mathbf{L}(X, \mathbf{r}_d)\Big)^{-1}.\mathbf{L}^{\mathrm{T}}(X, \mathbf{r}_d)$, equation (B.12) could be written as:

$$\begin{aligned} \frac{\partial \mathbf{V}}{\partial X}(X, \mathbf{r}_d, \mathbf{d}) &= \frac{\partial \mathbf{L}(X, \mathbf{r}_d)}{\partial X}\mathbf{L}^{\dagger}\mathbf{V}_{\text{meas}} + \mathbf{L}(X, \mathbf{r}_d)\frac{\partial (\mathbf{L}^{\mathrm{T}}\mathbf{L})^{-1}}{\partial X}\mathbf{L}^{\mathrm{T}}\mathbf{V}_{\text{meas}} \\ &+ \mathbf{L}(X, \mathbf{r}_d)(\mathbf{L}^{\mathrm{T}}\mathbf{L})^{-1}\frac{\partial \mathbf{L}^{\mathrm{T}}}{\partial X}\mathbf{V}_{\text{meas}} \end{aligned} \tag{B.13}$$

Note that $\mathbf{L}$, $\mathbf{L}^{\mathrm{T}}$ have a $\mathbf{r}_d$ and X dependence; but for simplicity of the notation, this will not be mentioned explicitly in the equations below.

Using the fact that the derivative of the inverse of a matrix $\mathbf{A}$ with respect to a variable t is given by $\frac{\partial \mathbf{A}^{-1}}{\partial \mathrm{t}} = -\mathbf{A}^{-1}\frac{\partial \mathbf{A}}{\partial \mathrm{t}}\mathbf{A}^{-1}$, the previous expression becomes:

$$\begin{aligned} \frac{\partial \mathbf{V}}{\partial X}(X, \mathbf{r}_d, \mathbf{d}) = \frac{\partial \mathbf{L}}{\partial X}\mathbf{L}^{\dagger}\mathbf{V}_{\text{meas}} - \mathbf{L}\Big[(\mathbf{L}^{\mathrm{T}}\mathbf{L})^{-1}\frac{\partial (\mathbf{L}^{\mathrm{T}}\mathbf{L})}{\partial X}(\mathbf{L}^{\mathrm{T}}\mathbf{L})^{-1}\mathbf{L}^{\mathrm{T}}\Big]\mathbf{V}_{\text{meas}} \\ +\mathbf{L}(\mathbf{L}^{\mathrm{T}}\mathbf{L})^{-1}\frac{\partial \mathbf{L}^{\mathrm{T}}}{\partial X}\mathbf{V}_{\text{meas}} \end{aligned}$$

And finally, we have:

$$\frac{\partial \mathbf{V}}{\partial X}(X, \mathbf{r}_d, \mathbf{d}) = \frac{\partial \mathbf{L}}{\partial X}\mathbf{L}^{\dagger}\mathbf{V}_{\text{meas}} - \mathbf{L}\Big[(\mathbf{L}^{\mathrm{T}}\mathbf{L})^{-1}\Big(\frac{\partial \mathbf{L}^{\mathrm{T}}}{\partial X}\mathbf{L} + \mathbf{L}^{\mathrm{T}}\frac{\partial \mathbf{L}}{\partial X}\Big)(\mathbf{L}^{\mathrm{T}}\mathbf{L})^{-1}\mathbf{L}^{\mathrm{T}}\Big]\mathbf{V}_{\text{meas}}$$

$$+ \mathbf{L}(\mathbf{L}^{\mathrm{T}}\mathbf{L})^{-1}\frac{\partial \mathbf{L}^{\mathrm{T}}}{\partial X}\mathbf{V}_{\mathrm{meas}} \tag{B.14}$$

2.2.2 Alternative second order derivative V''

Using the previous result, we can compute the second term of the derivative. Thus, from (B.11)

$$\begin{aligned}\frac{\partial^2 \mathbf{V}}{\partial X^2}(X, \mathbf{r}_d, \mathbf{d}) &= \frac{\partial}{\partial X}\Big[\frac{\partial \mathbf{V}}{\partial X}(X, \mathbf{r}_d, \mathbf{d})\Big] = \frac{\partial}{\partial X}\Big[\frac{\partial \mathbf{L}}{\partial X}\mathbf{L}^{\dagger} + \mathbf{L}\frac{\partial \mathbf{L}^{\dagger}}{\partial X}\Big].\mathbf{V}_{\mathrm{meas}} \\ &= \Big[\frac{\partial^2 \mathbf{L}}{\partial X^2}\mathbf{L}^{\dagger} + \frac{\partial \mathbf{L}}{\partial X}\frac{\partial \mathbf{L}^{\dagger}}{\partial X} + \frac{\partial \mathbf{L}}{\partial X}\frac{\partial \mathbf{L}^{\dagger}}{\partial X} + \mathbf{L}\frac{\partial^2 \mathbf{L}^{\dagger}}{\partial X^2}\Big]\mathbf{V}_{\mathrm{meas}}\end{aligned} \tag{B.15}$$

Gathering all the terms, we finally have:

$$\frac{\partial^2 \mathbf{V}}{\partial X^2}(X, \mathbf{r}_d, \mathbf{d}) = \underbrace{\frac{\partial^2 \mathbf{L}}{\partial X^2}\mathbf{L}^{\dagger}\mathbf{V}_{\mathrm{meas}}}_{1} + \underbrace{\mathbf{L}\frac{\partial^2 \mathbf{L}^{\dagger}}{\partial X^2}\mathbf{V}_{\mathrm{meas}}}_{2} + \underbrace{2\frac{\partial \mathbf{L}}{\partial X}\frac{\partial \mathbf{L}^{\dagger}}{\partial X}\mathbf{V}_{\mathrm{meas}}}_{3}$$

In order to get a full expression of the second order derivative, each term should be expressed entirely.

We already know that $\mathbf{L}^{\dagger} = \left(\mathbf{L}^{\mathrm{T}}\mathbf{L}\right)^{-1}.\mathbf{L}^{\mathrm{T}}$ and that

$$\begin{aligned}\frac{\partial \mathbf{L}^{\dagger}}{\partial X} &= \frac{\partial (\mathbf{L}^{\mathrm{T}}\mathbf{L})^{-1}}{\partial X}\mathbf{L}^{\mathrm{T}} + \left(\mathbf{L}^{\mathrm{T}}\mathbf{L}\right)^{-1}\frac{\partial \mathbf{L}^{\mathrm{T}}}{\partial X} \\ &= -\left(\mathbf{L}^{\mathrm{T}}\mathbf{L}\right)^{-1}\frac{\partial\left(\mathbf{L}^{\mathrm{T}}\mathbf{L}\right)}{\partial X}\left(\mathbf{L}^{\mathrm{T}}\mathbf{L}\right)^{-1}.\mathbf{L}^{\mathrm{T}} + \left(\mathbf{L}^{\mathrm{T}}\mathbf{L}\right)^{-1}\frac{\partial \mathbf{L}^{\mathrm{T}}}{\partial X}\end{aligned} \tag{B.16}$$

So the first (1) and the third (3) relation become respectively:

$$\underbrace{\frac{\partial^2 \mathbf{L}}{\partial X^2}\mathbf{L}^{\dagger}\mathbf{V}_{\mathrm{meas}}}_{1} = \frac{\partial^2 \mathbf{L}}{\partial X^2}\left(\mathbf{L}^{\mathrm{T}}\mathbf{L}\right)^{-1}.\mathbf{L}^{\mathrm{T}}\mathbf{V}_{\mathrm{meas}} \tag{B.17}$$

$$\underbrace{2\frac{\partial \mathbf{L}}{\partial X}\frac{\partial \mathbf{L}^{\dagger}}{\partial X}\mathbf{V}_{\mathrm{meas}}}_{3} = 2\frac{\partial \mathbf{L}}{\partial X}\Big[-(\mathbf{L}^{\mathrm{T}}\mathbf{L})^{-1}\frac{\partial (\mathbf{L}^{\mathrm{T}}\mathbf{L})}{\partial X}(\mathbf{L}^{\mathrm{T}}\mathbf{L})^{-1}.\mathbf{L}^{\mathrm{T}} + (\mathbf{L}^{\mathrm{T}}\mathbf{L})^{-1}\frac{\partial \mathbf{L}^{\mathrm{T}}}{\partial X}\Big]\mathbf{V}_{\mathrm{meas}} \tag{B.18}$$

For the second term, using relation (B.16) above we have

$$\underbrace{\mathbf{L}\frac{\partial^2 \mathbf{L}^{\dagger}}{\partial X^2}\mathbf{V}_{\text{meas}}}_{2} = \mathbf{L}\frac{\partial}{\partial X}\Big[\frac{\partial \mathbf{L}^{\dagger}}{\partial X}\Big]\mathbf{V}_{\text{meas}}$$

$$= \mathbf{L}\frac{\partial}{\partial X}\Big[-\Big(\mathbf{L}^{\mathrm{T}}\mathbf{L}\Big)^{-1}\frac{\partial\Big(\mathbf{L}^{\mathrm{T}}\mathbf{L}\Big)}{\partial X}\Big(\mathbf{L}^{\mathrm{T}}\mathbf{L}\Big)^{-1}\mathbf{L}^{\mathrm{T}} + (\mathbf{L}^{\mathrm{T}}\mathbf{L})^{-1}\frac{\partial \mathbf{L}^{\mathrm{T}}}{\partial X}\Big]\mathbf{V}_{\text{meas}} \tag{B.19}$$

which becomes:

$$= \mathbf{L}\frac{\partial}{\partial X}\Big[-\Big(\mathbf{L}^{\mathrm{T}}\mathbf{L}\Big)^{-1}[\frac{\partial \mathbf{L}^{\mathrm{T}}}{\partial X}\mathbf{L} + \mathbf{L}^{\mathrm{T}}\frac{\partial \mathbf{L}}{\partial X}]\Big(\mathbf{L}^{\mathrm{T}}\mathbf{L}\Big)^{-1}\mathbf{L}^{\mathrm{T}} + (\mathbf{L}^{\mathrm{T}}\mathbf{L})^{-1}\frac{\partial \mathbf{L}^{\mathrm{T}}}{\partial X}\Big]\mathbf{V}_{\text{meas}} \tag{B.20}$$

Differentiating the expression into large brackets, we have:

$$= -\mathbf{L}\frac{\partial\Big(\mathbf{L}^{\mathrm{T}}\mathbf{L}\Big)^{-1}}{\partial X}\Big[[\frac{\partial \mathbf{L}^{\mathrm{T}}}{\partial X}\mathbf{L} + \mathbf{L}^{\mathrm{T}}\frac{\partial \mathbf{L}}{\partial X}]\Big(\mathbf{L}^{\mathrm{T}}\mathbf{L}\Big)^{-1}\mathbf{L}^{\mathrm{T}}\Big]\mathbf{V}_{\text{meas}}$$

$$-\mathbf{L}\Big(\mathbf{L}^{\mathrm{T}}\mathbf{L}\Big)^{-1}\frac{\partial}{\partial X}\Big[[\frac{\partial \mathbf{L}^{\mathrm{T}}}{\partial X}\mathbf{L} + \mathbf{L}^{\mathrm{T}}\frac{\partial \mathbf{L}}{\partial X}]\Big(\mathbf{L}^{\mathrm{T}}\mathbf{L}\Big)^{-1}\mathbf{L}^{\mathrm{T}}\Big]\mathbf{V}_{\text{meas}}$$

$$+\mathbf{L}\frac{\partial}{\partial X}\Big[(\mathbf{L}^{\mathrm{T}}\mathbf{L})^{-1}\Big]\frac{\partial \mathbf{L}^{\mathrm{T}}}{\partial X}\mathbf{V}_{\text{meas}} + \mathbf{L}(\mathbf{L}^{\mathrm{T}}\mathbf{L})^{-1}\frac{\partial}{\partial X}\Big[\frac{\partial \mathbf{L}^{\mathrm{T}}}{\partial X}\Big]\mathbf{V}_{\text{meas}} \tag{B.21}$$

$$= \mathbf{L}(\mathbf{L}^{\mathrm{T}}\mathbf{L})^{-1}\frac{\partial\Big(\mathbf{L}^{\mathrm{T}}\mathbf{L}\Big)}{\partial X}(\mathbf{L}^{\mathrm{T}}\mathbf{L})^{-1}\Big[[\frac{\partial \mathbf{L}^{\mathrm{T}}}{\partial X}\mathbf{L} + \mathbf{L}^{\mathrm{T}}\frac{\partial \mathbf{L}}{\partial X}]\Big(\mathbf{L}^{\mathrm{T}}\mathbf{L}\Big)^{-1}\mathbf{L}^{\mathrm{T}}\Big]\mathbf{V}_{\text{meas}}$$

$$-\mathbf{L}\Big(\mathbf{L}^{\mathrm{T}}\mathbf{L}\Big)^{-1}\frac{\partial}{\partial X}\Big[[\frac{\partial \mathbf{L}^{\mathrm{T}}}{\partial X}\mathbf{L} + \mathbf{L}^{\mathrm{T}}\frac{\partial \mathbf{L}}{\partial X}]\Big(\mathbf{L}^{\mathrm{T}}\mathbf{L}\Big)^{-1}\mathbf{L}^{\mathrm{T}}\Big]\mathbf{V}_{\text{meas}}$$

$$+\mathbf{L}(\mathbf{L}^{\mathrm{T}}\mathbf{L})^{-1}\Big[\frac{\partial^2 \mathbf{L}^{\mathrm{T}}}{\partial X^2}\Big]\mathbf{V}_{\text{meas}} - \mathbf{L}(\mathbf{L}^{\mathrm{T}}\mathbf{L})^{-1}\frac{\partial}{\partial X}\Big[(\mathbf{L}^{\mathrm{T}}\mathbf{L})\Big](\mathbf{L}^{\mathrm{T}}\mathbf{L})^{-1}\frac{\partial \mathbf{L}^{\mathrm{T}}}{\partial X}\mathbf{V}_{\text{meas}} \tag{B.22}$$

$$= \mathbf{L}(\mathbf{L}^{\mathrm{T}}\mathbf{L})^{-1}\Big[\frac{\partial \mathbf{L}^{\mathrm{T}}}{\partial X}\mathbf{L} + \mathbf{L}^{\mathrm{T}}\frac{\partial \mathbf{L}}{\partial X}\Big](\mathbf{L}^{\mathrm{T}}\mathbf{L})^{-1}\Big[[\frac{\partial \mathbf{L}^{\mathrm{T}}}{\partial X}\mathbf{L} + \mathbf{L}^{\mathrm{T}}\frac{\partial \mathbf{L}}{\partial X}]\Big(\mathbf{L}^{\mathrm{T}}\mathbf{L}\Big)^{-1}\mathbf{L}^{\mathrm{T}}\Big]\mathbf{V}_{\text{meas}}$$

$$-\mathbf{L}\Big(\mathbf{L}^{\mathrm{T}}\mathbf{L}\Big)^{-1}\frac{\partial}{\partial X}\Big[[\frac{\partial \mathbf{L}^{\mathrm{T}}}{\partial X}\mathbf{L}+\mathbf{L}^{\mathrm{T}}\frac{\partial \mathbf{L}}{\partial X}]\Big]\Big(\mathbf{L}^{\mathrm{T}}\mathbf{L}\Big)^{-1}\mathbf{L}^{\mathrm{T}}\mathbf{V}_{\mathrm{meas}}$$

$$-\mathbf{L}\Big(\mathbf{L}^{\mathrm{T}}\mathbf{L}\Big)^{-1}\Big[[\frac{\partial \mathbf{L}^{\mathrm{T}}}{\partial X}\mathbf{L}+\mathbf{L}^{\mathrm{T}}\frac{\partial \mathbf{L}}{\partial X}]\Big]\Big[\frac{\partial\Big((\mathbf{L}^{\mathrm{T}}\mathbf{L})^{-1}\Big)}{\partial X}\mathbf{L}^{\mathrm{T}}+\Big(\mathbf{L}^{\mathrm{T}}\mathbf{L}\Big)^{-1}\frac{\partial \mathbf{L}^{\mathrm{T}}}{\partial X}\Big]\mathbf{V}_{\mathrm{meas}}$$

$$+\mathbf{L}(\mathbf{L}^{\mathrm{T}}\mathbf{L})^{-1}\frac{\partial^2 \mathbf{L}^{\mathrm{T}}}{\partial X^2}\mathbf{V}_{\mathrm{meas}}-\mathbf{L}(\mathbf{L}^{\mathrm{T}}\mathbf{L})^{-1}\frac{\partial}{\partial X}\Big[(\mathbf{L}^{\mathrm{T}}\mathbf{L})\Big](\mathbf{L}^{\mathrm{T}}\mathbf{L})^{-1}\frac{\partial \mathbf{L}^{\mathrm{T}}}{\partial X}\mathbf{V}_{\mathrm{meas}} \quad \text{(B.23)}$$

And by differentiating all the terms, we have:

$$=\mathbf{L}(\mathbf{L}^{\mathrm{T}}\mathbf{L})^{-1}\Big[\frac{\partial \mathbf{L}^{\mathrm{T}}}{\partial X}\mathbf{L}+\mathbf{L}^{\mathrm{T}}\frac{\partial \mathbf{L}}{\partial X}\Big](\mathbf{L}^{\mathrm{T}}\mathbf{L})^{-1}\Big[[\frac{\partial \mathbf{L}^{\mathrm{T}}}{\partial X}\mathbf{L}+\mathbf{L}^{\mathrm{T}}\frac{\partial \mathbf{L}}{\partial X}]\Big(\mathbf{L}^{\mathrm{T}}\mathbf{L}\Big)^{-1}\mathbf{L}^{\mathrm{T}}\Big]\mathbf{V}_{\mathrm{meas}}$$

$$-\mathbf{L}\Big(\mathbf{L}^{\mathrm{T}}\mathbf{L}\Big)^{-1}\Big[[\frac{\partial^2 \mathbf{L}^{\mathrm{T}}}{\partial X^2}\mathbf{L}+\mathbf{L}^{\mathrm{T}}\frac{\partial^2 \mathbf{L}}{\partial X^2}+2\frac{\partial \mathbf{L}^{\mathrm{T}}}{\partial X}\frac{\partial \mathbf{L}}{\partial X}]\Big]\Big(\mathbf{L}^{\mathrm{T}}\mathbf{L}\Big)^{-1}\mathbf{L}^{\mathrm{T}}\mathbf{V}_{\mathrm{meas}}$$

$$-\mathbf{L}\Big(\mathbf{L}^{\mathrm{T}}\mathbf{L}\Big)^{-1}\Big[[\frac{\partial \mathbf{L}^{\mathrm{T}}}{\partial X}\mathbf{L}+\mathbf{L}^{\mathrm{T}}\frac{\partial \mathbf{L}}{\partial X}]\Big]\cdot$$

$$\Big[-\Big((\mathbf{L}^{\mathrm{T}}\mathbf{L})^{-1}\Big)[\frac{\partial \mathbf{L}^{\mathrm{T}}}{\partial X}\mathbf{L}+\mathbf{L}^{\mathrm{T}}\frac{\partial \mathbf{L}}{\partial X}]\Big((\mathbf{L}^{\mathrm{T}}\mathbf{L})^{-1}\Big)\mathbf{L}^{\mathrm{T}}+\Big(\mathbf{L}^{\mathrm{T}}\mathbf{L}\Big)^{-1}\frac{\partial \mathbf{L}^{\mathrm{T}}}{\partial X}\Big]\mathbf{V}_{\mathrm{meas}}$$

$$+\mathbf{L}(\mathbf{L}^{\mathrm{T}}\mathbf{L})^{-1}\Big[\frac{\partial^2 \mathbf{L}^{\mathrm{T}}}{\partial X^2}\Big]\mathbf{V}_{\mathrm{meas}}-\mathbf{L}(\mathbf{L}^{\mathrm{T}}\mathbf{L})^{-1}\frac{\partial}{\partial X}\Big[(\mathbf{L}^{\mathrm{T}}\mathbf{L})\Big](\mathbf{L}^{\mathrm{T}}\mathbf{L})^{-1}\frac{\partial \mathbf{L}^{\mathrm{T}}}{\partial X}\mathbf{V}_{\mathrm{meas}} \quad \text{(B.24)}$$

So from what precedes, it follows that

$$\underbrace{\mathbf{L}\frac{\partial^2 \mathbf{L}^{\dagger}}{\partial X^2}\mathbf{V}_{\mathrm{meas}}}_{2}=$$

$$\mathbf{L}(\mathbf{L}^{\mathrm{T}}\mathbf{L})^{-1}\Big[\frac{\partial \mathbf{L}^{\mathrm{T}}}{\partial X}\mathbf{L}+\mathbf{L}^{\mathrm{T}}\frac{\partial \mathbf{L}}{\partial X}\Big](\mathbf{L}^{\mathrm{T}}\mathbf{L})^{-1}\Big[[\frac{\partial \mathbf{L}^{\mathrm{T}}}{\partial X}\mathbf{L}+\mathbf{L}^{\mathrm{T}}\frac{\partial \mathbf{L}}{\partial X}]\Big(\mathbf{L}^{\mathrm{T}}\mathbf{L}\Big)^{-1}\mathbf{L}^{\mathrm{T}}\Big]\mathbf{V}_{\mathrm{meas}}$$

$$-\mathbf{L}\Big(\mathbf{L}^{\mathrm{T}}\mathbf{L}\Big)^{-1}\Big[[\frac{\partial^2 \mathbf{L}^{\mathrm{T}}}{\partial X^2}\mathbf{L}+\mathbf{L}^{\mathrm{T}}\frac{\partial^2 \mathbf{L}}{\partial X^2}+2\frac{\partial \mathbf{L}^{\mathrm{T}}}{\partial X}\frac{\partial \mathbf{L}}{\partial X}]\Big]\Big(\mathbf{L}^{\mathrm{T}}\mathbf{L}\Big)^{-1}\mathbf{L}^{\mathrm{T}}\mathbf{V}_{\mathrm{meas}}$$

$$-\mathbf{L}\Big(\mathbf{L}^{\mathrm{T}}\mathbf{L}\Big)^{-1}\Big[[\frac{\partial \mathbf{L}^{\mathrm{T}}}{\partial X}\mathbf{L}+\mathbf{L}^{\mathrm{T}}\frac{\partial \mathbf{L}}{\partial X}]\Big]\cdot$$

$$\Big[-\Big((\mathbf{L}^{\mathrm{T}}\mathbf{L})^{-1}\Big)[\frac{\partial \mathbf{L}^{\mathrm{T}}}{\partial X}\mathbf{L}+\mathbf{L}^{\mathrm{T}}\frac{\partial \mathbf{L}}{\partial X}]\Big((\mathbf{L}^{\mathrm{T}}\mathbf{L})^{-1}\Big)\mathbf{L}^{\mathrm{T}}+\Big(\mathbf{L}^{\mathrm{T}}\mathbf{L}\Big)^{-1}\frac{\partial \mathbf{L}^{\mathrm{T}}}{\partial X}\Big]\mathbf{V}_{\mathrm{meas}}$$

$$+\mathbf{L}(\mathbf{L}^{\mathrm{T}}\mathbf{L})^{-1}\frac{\partial^2 \mathbf{L}^{\mathrm{T}}}{\partial X^2}\mathbf{V}_{\mathrm{meas}}-\mathbf{L}(\mathbf{L}^{\mathrm{T}}\mathbf{L})^{-1}\Big[\frac{\partial \mathbf{L}^{\mathrm{T}}}{\partial X}\mathbf{L}+\mathbf{L}^{\mathrm{T}}\frac{\partial \mathbf{L}}{\partial X}\Big](\mathbf{L}^{\mathrm{T}}\mathbf{L})^{-1}\frac{\partial \mathbf{L}^{\mathrm{T}}}{\partial X}\mathbf{V}_{\mathrm{meas}} \tag{B.25}$$

Gathering all the terms (1), (2) and (3) respectively we finally have

$$\frac{\partial^2 \mathbf{V}}{\partial X^2}(X,\mathbf{r}_d,\mathbf{d})=\frac{\partial^2 \mathbf{L}}{\partial X^2}\Big(\mathbf{L}^{\mathrm{T}}\mathbf{L}\Big)^{-1}.\mathbf{L}^{\mathrm{T}}\mathbf{V}_{\mathrm{meas}}$$

$$+\mathbf{L}(\mathbf{L}^{\mathrm{T}}\mathbf{L})^{-1}\Big[\frac{\partial \mathbf{L}^{\mathrm{T}}}{\partial X}\mathbf{L}+\mathbf{L}^{\mathrm{T}}\frac{\partial \mathbf{L}}{\partial X}\Big](\mathbf{L}^{\mathrm{T}}\mathbf{L})^{-1}\Big[[\frac{\partial \mathbf{L}^{\mathrm{T}}}{\partial X}\mathbf{L}+\mathbf{L}^{\mathrm{T}}\frac{\partial \mathbf{L}}{\partial X}]\Big(\mathbf{L}^{\mathrm{T}}\mathbf{L}\Big)^{-1}\mathbf{L}^{\mathrm{T}}\Big]\mathbf{V}_{\mathrm{meas}}$$

$$-\mathbf{L}\Big(\mathbf{L}^{\mathrm{T}}\mathbf{L}\Big)^{-1}\Big[[\frac{\partial^2 \mathbf{L}^{\mathrm{T}}}{\partial X^2}\mathbf{L}+\mathbf{L}^{\mathrm{T}}\frac{\partial^2 \mathbf{L}}{\partial X^2}+2\frac{\partial \mathbf{L}^{\mathrm{T}}}{\partial X}\frac{\partial \mathbf{L}}{\partial X}]\Big]\Big(\mathbf{L}^{\mathrm{T}}\mathbf{L}\Big)^{-1}\mathbf{L}^{\mathrm{T}}\mathbf{V}_{\mathrm{meas}}$$

$$-\mathbf{L}\Big(\mathbf{L}^{\mathrm{T}}\mathbf{L}\Big)^{-1}\Big[[\frac{\partial \mathbf{L}^{\mathrm{T}}}{\partial X}\mathbf{L}+\mathbf{L}^{\mathrm{T}}\frac{\partial \mathbf{L}}{\partial X}]\Big]\cdot$$

$$\Big[-\Big((\mathbf{L}^{\mathrm{T}}\mathbf{L})^{-1}\Big)[\frac{\partial \mathbf{L}^{\mathrm{T}}}{\partial X}\mathbf{L}+\mathbf{L}^{\mathrm{T}}\frac{\partial \mathbf{L}}{\partial X}]\Big((\mathbf{L}^{\mathrm{T}}\mathbf{L})^{-1}\Big)\mathbf{L}^{\mathrm{T}}+\Big(\mathbf{L}^{\mathrm{T}}\mathbf{L}\Big)^{-1}\frac{\partial \mathbf{L}^{\mathrm{T}}}{\partial X}\Big]\mathbf{V}_{\mathrm{meas}}$$

$$+\mathbf{L}(\mathbf{L}^{\mathrm{T}}\mathbf{L})^{-1}\frac{\partial^2 \mathbf{L}^{\mathrm{T}}}{\partial X^2}\mathbf{V}_{\mathrm{meas}}-\mathbf{L}(\mathbf{L}^{\mathrm{T}}\mathbf{L})^{-1}\Big[\frac{\partial \mathbf{L}^{\mathrm{T}}}{\partial X}\mathbf{L}+\mathbf{L}^{\mathrm{T}}\frac{\partial \mathbf{L}}{\partial X}\Big](\mathbf{L}^{\mathrm{T}}\mathbf{L})^{-1}\frac{\partial \mathbf{L}^{\mathrm{T}}}{\partial X}\mathbf{V}_{\mathrm{meas}}$$

$$+2\frac{\partial \mathbf{L}}{\partial X}\Big[-(\mathbf{L}^{\mathrm{T}}\mathbf{L})^{-1}[\frac{\partial \mathbf{L}^{\mathrm{T}}}{\partial X}\mathbf{L}+\mathbf{L}^{\mathrm{T}}\frac{\partial \mathbf{L}}{\partial X}](\mathbf{L}^{\mathrm{T}}\mathbf{L})^{-1}.\mathbf{L}^{\mathrm{T}}+(\mathbf{L}^{\mathrm{T}}\mathbf{L})^{-1}.\frac{\partial \mathbf{L}^{\mathrm{T}}}{\partial X}\Big]\mathbf{V}_{\mathrm{meas}} \quad \text{(B.26)}$$

APPENDIX C

RCD methodology using realistic head models

The Reduced Conductivity Dependence method was extensively applied onto a realistic head model where input to this work was provided by this doctoral work and which was submitted to [152].

3.1. Materials and Methods

We use in this study a realistic head model so to eliminate the geometrical modeling errors and we use EEG electrodes with accurate placement. Moreover, we assume that the number of sources is known. The used head model is patient-specific and is based on MR image data. The used head model in the presented simulation study consists of isotropic conductivities where we want to assess the influence of the absolute conductivity values on the recovered neural source locations. More correct simulations could be performed using a realistic head model with the incorporation of anisotropic conductivities. However, we focus here on providing a proof of concept of the presented SES procedure in a realistic head model with respect to the uncertain skull to soft tissue conductivity ratio.
In the following we outline the steps taken for constructing the forward model and then we present the inverse techniques for recovering the neural sources.

3.1.1 Forward realistic model

3.1.1.1 Volume conductor head model: registration and segmentation

In order to calculate the potentials at the electrodes due to a current dipole source, a volume conductor model is needed. The volume conductor model

describes the geometry and the different tissue types. Each tissue type is assigned a label, which is then used to assign a conductivity. In our study we used a realistic head model that was derived from segmented T1 weighted MRI images. The MRI images were obtained by a 3 Tesla MRI scanner (Siemens Trio, Erlangen, Germany) using a 3 dimensional MP RAGE sequence with a repetition time (TR) of 1550 ms and a echo time (TE) of 2.48 ms. The result was a $256 \times 256 \times 176$ matrix of isotropic voxels of $0.9\text{mm} \times 0.9\text{mm} \times 0.9\text{mm}$. To construct the brain compartment, SPM8 was used to segment the white matter, grey matter and cerebro-spinal fluid ([153]). This resulted in probability values for each voxel, indicating its probability of belonging to white matter, gray matter or cerebro-spinal fluid (CSF). The voxels are then assigned to the compartment for which the voxel had the highest probability. The skull compartment was constructed by a dilation operation of the brain compartment and was on average 6 mm thick. The scalp compartment was obtained by using opening, closing and hole filling operation the thresholded MR image. This way we could make a distinction between head and air. The skull and brain compartments were then added to the whole head model. Figure C.1 shows an axial, sagittal and coronal plane of the used volume conductor head model.

3.1.1.2 Finite difference method for the forward EEG problem

After defining the head model, the electrode positions have to be determined. We used a 10-10 standard electrode setup, consisting of 81 electrodes. The electrodes were projected on to the scalp.

The forward problem relates the electrode potentials to a dipole source in a specified geometry. This relation can be expressed by solving the Poisson equation:

$$\nabla \cdot (\sigma(x,y,z) \cdot \nabla \phi(x,y,z)) = I\delta(\mathbf{r} - \mathbf{r}_1) - I\delta(\mathbf{r} - \mathbf{r}_2) \tag{C.1}$$

with $\phi(x,y,z)$ the potential distribution inside the head model. $\sigma(x,y,z)$ denotes the conductivity value which is position ($\mathbf{r} = [x,y,z]$) dependent. $\mathbf{r}_1$, $\mathbf{r}_2$ are the location coordinates of the monopoles of the dipole: the current source and current sink, respectively. I is the amplitude of the dipole. The numerical method that is used here for solving (C.1), is based on the Finite Difference Method (FDM), elaborated in ([154, 155]). The method results in the solution of a large sparse linear system of equations which can be solved using the so-called successive overrelaxation method ([156]). Due to the fact that the computation time becomes too expensive when using successive overrelaxation for the solution of the forward problem, the reciprocity theorem is used ([157]). For an extensive validation and further details of the used isotropic

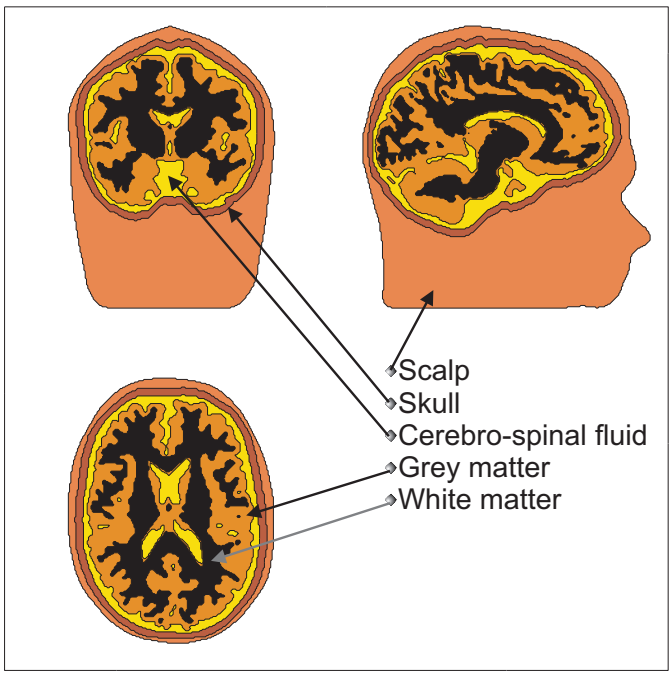

Figure C.1: The coronal, sagital and axial plane of the head model. The test dipoles were placed in each voxel of the gray and white matter. The different compartments are indicated: scalp, skull, cerebro-spinal fluid, gray matter and white matter.

forward model, see ([154]). Figure C.2 shows a schematic outline of the steps taken for generating the lead fields using the realistic head model.
The so-called lead field matrix $\mathbf{L} \in R^{q\times 3}$ links the dipole location, denoted by $\mathbf{r}_d$, with the EEG potentials $V_{m,i}$, $i = 1,\ldots,q$ at the given q electrode positions. We denote the EEG potentials by the q-dimensional vector $\mathbf{V}_m$ and is linear with the dipole orientation $\mathbf{d}$:

$$\mathbf{V}_m = \mathbf{L}(\mathbf{r}_d)\mathbf{d}. \tag{C.2}$$

3.1.1.3 Influence of conductivity on EEG forward problem

The lead fields $\mathbf{L}(\mathbf{r}_d)$ depend upon the skull to soft tissue conductivity ratio

$$\xi = \frac{\sigma_{skull}}{\sigma_{soft}} \tag{C.3}$$

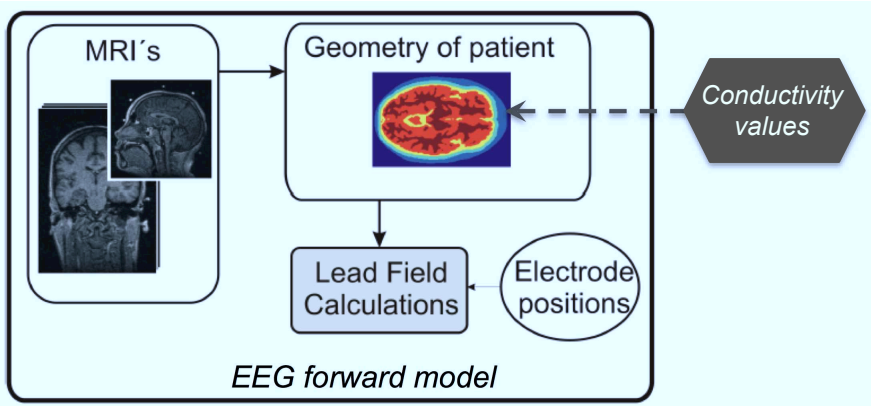

Figure C.2: Outline of the forward model: from Magnetic Resonance Images, the geometry of the head is deduced and for given conductivity values and electrode positions the lead field is computed.

since the computed potentials ϕ in the Poisson equation (C.1) depend upon $\sigma(x,y,z)$. We denote this dependence by $\mathbf{L}(\mathbf{r}_d,\xi)$, $\mathbf{V}_m(\mathbf{r}_d,\mathbf{d},\xi)$. We assume here the soft tissue to be the brain and the scalp tissue. The forward propagation of ξ to the potential values is shown in figure C.3 for a certain fixed dipole location and orientation. When assuming a conductivity ratio (e.g. $\widetilde{\xi} = 1/10$) which is significantly different from the actual conductivity ratio ($\xi^* = 1/50$) of the patient under study, then a large misfit in the EEG dipole localization can occur because of the propagation of ξ to $\mathbf{V}_m$.
In figure C.3 we can also observe that some potentials are very sensitive to ξ while other potentials are less sensitive. Indeed, when computing the sensitivity of the potentials to the conductivity ratio

$$\mathbf{S}(\mathbf{r}_d,\mathbf{d},\widetilde{\xi}) = \frac{\partial \mathbf{V}_m(\mathbf{r}_d,\mathbf{d},\xi)}{\partial \xi}\Big|_{\xi=\widetilde{\xi}} \tag{C.4}$$

for a fixed source position and orientation, then different S_i ($i = 1,\ldots,q$) values are found. The sensitivity of the potential at every electrode is depicted in figure C.4. Figure C.5 shows the absolute difference in computed potentials due to the use of different ξ. More elaborated studies of the influence of conductivity on the EEG forward potentials have been carried out by e.g. ([22,23]).

3.1.2 Traditional EEG inverse problem

The EEG inverse problem aims at recovering the neural source locations and orientations that correspond with a certain set of measured EEG potentials $\mathbf{V}_{meas}$. Several source localization approaches exist, depending on the as-

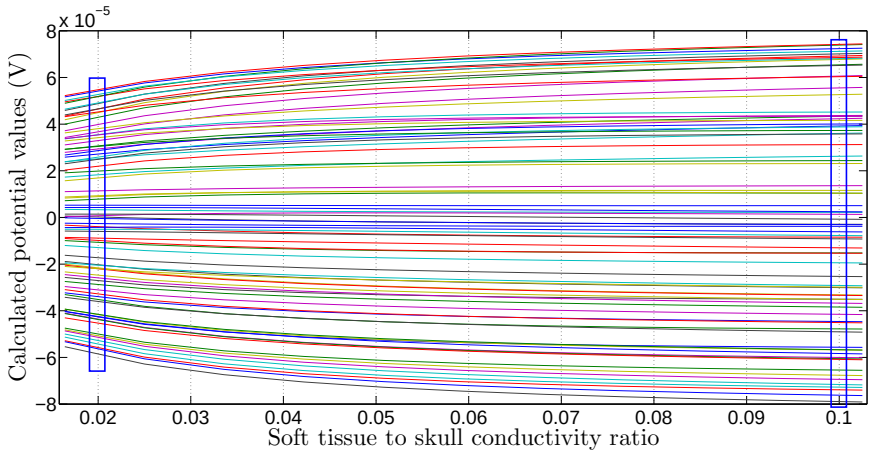

Figure C.3: Dependence of computed EEG potential values to ξ for a fixed position ($\mathbf{r}_d$ near the center of the brain) and orientation ($\mathbf{d} = [0.6, 0.6, 0.6]$) of dipole source.

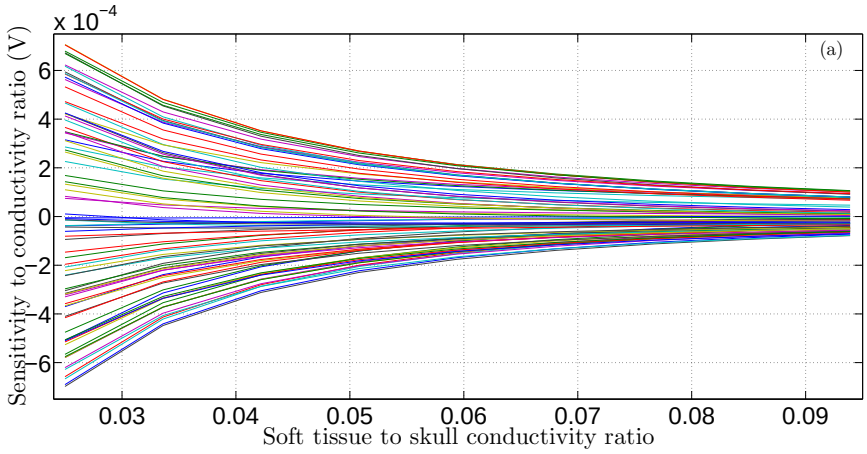

Figure C.4: Sensitivity of EEG potentials to ξ for a fixed position and orientation of dipole source at all electrodes. The dipole position is positioned near the center of the brain with orientation $\mathbf{d} = [0.6, 0.6, 0.6]$.

sumed source model: single dipole localization based on the minimization of a least squares cost function ([10]), limited number of multiple dipoles ($< q$) recovered using multiple signal classification algorithms ([12]), and distributed source models where a highly underdetermined system of linear equations needs to be solve ([158]). In this paper we use inverse problem formulations which are well-posed.

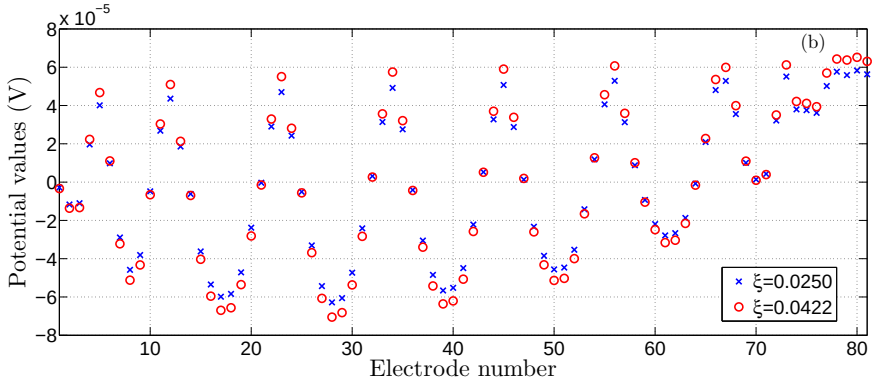

Figure C.5: Absolute values of EEG potentials for different ξ at all electrodes. The dipole position is positioned near the center of the brain with orientation $\mathbf{d} = [0.6, 0.6, 0.6]$.

The inverse problem for a single dipole is nonlinearly solved by iteratively minimizing a cost function $\mathcal{Y}$:

$$\mathbf{r}_d^* = \arg\min_{\mathbf{r}_d} \mathcal{Y}(\mathbf{r}_d) \tag{C.5}$$

which yields recovered dipole location $\mathbf{r}_d^*$. The orientation can be recovered by calculating $\mathbf{d}^* = \mathbf{L}(\mathbf{r}_d^*)^\dagger \mathbf{V}_{meas}$ with $\mathbf{L}^\dagger$ the pseudo inverse of the lead field matrix. $\mathcal{Y}$ is the following least squares cost function:

$$\mathcal{Y}(\mathbf{r}_d) = \frac{\|\mathbf{V}_{meas} - \mathbf{L}(\mathbf{r}_d)\mathbf{L}(\mathbf{r}_d)^\dagger \mathbf{V}_{meas}\|}{\|\mathbf{V}_{meas}\|} \tag{C.6}$$

with $||.||$ the L_2 norm. The dipole orientation is not included in $\mathcal{Y}$ by considering the optimal dipole orientation components $\mathbf{d}_{opt} = \mathbf{L}(\mathbf{r}_d)^\dagger \mathbf{V}_{meas}$. For solving (C.5) the widely-used Nelder-Mead simplex is used here as in ([112, 159]). The above inverse problem is formulated to solve the EEG inverse problem at a single time instant and can be extended (for multiple time instances) in a spatio-temporal way.

The solution of the EEG inverse problem for multiple dipoles (with number of dipoles less than the number of channel measurements) can be obtained using the Recursively Applied and Projected-MUltiple SIgnal Classification (RAP-MUSIC) methodology ([12]). We denote here the so-called spatio-temporal data matrix as

$$\mathbf{F}_m = [\mathbf{L}(\mathbf{r}_{d,1}), \ldots, \mathbf{L}(\mathbf{r}_{d,p})][\mathbf{d}_1^T, \ldots, \mathbf{d}_p^T]^T \tag{C.7}$$

for p dipoles (with locations $\mathbf{r}_{d,i}$, $i = 1,\ldots,p$). The $3 \times n$-matrix $\mathbf{d}_i$ ($i = 1,\ldots,p$) represents the time course of the ith dipole moment. n is the number of samples registered by the EEG. The following cost function needs to be maximized for each dipole:

$$\mathbf{r}^*_{d,k} = \arg\max_{\mathbf{r}_d}(subcorr(\Pi^{\perp}_{\mathbf{A}_{k-1}}\mathbf{L}(\mathbf{r}_d), \Pi^{\perp}_{\mathbf{A}_{k-1}}\Phi_{sig})_1) \tag{C.8}$$

with $\Pi^{\perp}_{\mathbf{A}_{k-1}} = (\mathbf{I} - \mathbf{A}_{k-1}\mathbf{A}^{\dagger}_{k-1})$ the projection matrix constructed by $\mathbf{A}_{k-1}$, a matrix containing in each column the topographies of the already found $k-1$ sources ([12]). Φ_{sig} is the signal subspace of the spatio-temporal measurement matrix.

The propagation of the uncertain brain tissue conductivity values onto the inverse solutions can be quantified e.g. using Monte Carlo simulations ([28]), stochastic Cramér Rao Bound technique ([27]), polynomial chaos decomposition ([160]). We can theoretically express this propagation to the inverse solution by redefining (C.5):

$$\mathbf{r}^*_d(\xi) = \arg\min_{\mathbf{r}_d} \mathcal{Y}(\mathbf{r}_d, \xi) \tag{C.9}$$

where the cost function depends on ξ because $\mathbf{L}(\mathbf{r}_d, \xi)$. The corresponding propagation to the dipole orientation can be determined by $\mathbf{d}^* = \mathbf{L}(\mathbf{r}^*_d(\xi), \xi)^{\dagger}\mathbf{V}_{meas}$. For the case of recovering a limited number of dipoles, (C.9) can be iteratively used:

$$\mathbf{r}^*_{d,k}(\xi) = \arg\min_{\mathbf{r}_d} \mathcal{Y}_k(\mathbf{r}_d, \xi) \tag{C.10}$$

$$\mathcal{Y}_k(\mathbf{r}_d, \xi) = -subcorr(\Pi^{\perp}_{\mathbf{A}_{k-1}}\mathbf{L}(\mathbf{r}_d, \xi), \Pi^{\perp}_{\mathbf{A}_{k-1}}\Phi_{sig})_1 \tag{C.11}$$

for the recovery of the $k = 1,\ldots,p$ dipoles.

3.1.3 Subspace Electrode Selection methodology

The aim of the SES methodology is to reduce the propagation of the uncertain ξ values to the inverse solutions, i.e. bringing the recovered $\mathbf{r}^*_d(\widetilde{\xi})$ with assumed conductivity ratio $\widetilde{\xi}$ closer to the actual dipole location $\mathbf{r}^*_d$ for a patient with actual conductivity ratio ξ^* and EEG measurements $\mathbf{V}_{meas}$. The SES methodology is based on two major ideas: (i) redefinition of the traditional cost function, (ii) selection of potentials in each iteration of the minimization procedure.

3.1.3.1 Redefinition of the traditional cost functions

In the ideal case (no noise, no electrode mislocations, correct geometry and isotropic conductivities) we can theoretically state that the measured potentials equal the simulated potentials for the actual conductivity ratio ξ^* at the actual dipole position and orientation $\{\mathbf{r}_{d,act}, \mathbf{d}_{act}\}$:

$$\begin{aligned} \mathbf{V}_{meas} &\equiv \mathbf{V}_m(\mathbf{r}_{d,act}, \mathbf{d}_{act}, \xi^*) && \text{(C.12)} \\ &\equiv \mathbf{L}(\mathbf{r}_{d,act}, \xi^*)\mathbf{d}_{act} && \text{(C.13)} \\ &\equiv \mathbf{L}(\mathbf{r}_{d,act}, \xi^*)\mathbf{L}(\mathbf{r}_{d,act}, \xi^*)^{\dagger}\mathbf{V}_{meas} && \text{(C.14)} \end{aligned}$$

When using however an assumed conductivity ratio $\widetilde{\xi} \neq \xi^*$, then a dipole location $\mathbf{r}_d^* \neq \mathbf{r}_{d,act}$ corresponds with the measurement vector:

$$\mathbf{V}_{meas} \simeq \mathbf{V}_m(\mathbf{r}_d^*, \mathbf{d}^*, \widetilde{\xi}) \tag{C.15}$$

where $\simeq$ is a symbolic notation for the closest $\mathbf{V}_m$ to $\mathbf{V}_{meas}$, meaning that $\|\mathbf{V}_{meas} - \mathbf{V}_m(\mathbf{r}_d^*, \mathbf{d}^*, \widetilde{\xi})\|$ is minimal for $\mathbf{r}_d^*$.

The term on the right in (C.12) can be written as a first order expansion (up to order $\mathcal{O}(\|\xi^* - \widetilde{\xi}\|^2)$):

$$\mathbf{V}_{meas} = \mathbf{V}_m(\mathbf{r}_{d,act}, \mathbf{d}_{act}, \widetilde{\xi}) + (\xi^* - \widetilde{\xi})\frac{\partial \mathbf{V}_m(\mathbf{r}_{d,act}, \mathbf{d}_{act}, \xi)}{\partial \xi}\Big|_{\xi=\widetilde{\xi}} \tag{C.16}$$

where the second right hand side term depends on the propagation of the uncertainty to the forward problem, see equation (C.4). If one uses a certain assumed conductivity ratio $\widetilde{\xi}$, then (C.16) would be a sufficient forward model, but the Taylor coefficient ξ^* is however unknown.
The Taylor coefficient $\alpha = \xi^* - \widetilde{\xi}$ can be approximated by fitting the data set $\mathbf{Y} = \mathbf{V}_{meas} - \mathbf{V}_m(\mathbf{r}_{d,act}, \mathbf{d}_{act}, \widetilde{\xi})$ with $\mathbf{S} = \frac{\partial \mathbf{V}_m(\mathbf{r}_{d,act}, \mathbf{d}_{act}, \xi)}{\partial \xi}\Big|_{\xi=\widetilde{\xi}}$. But since in the iterative minimization, $\mathbf{r}_d \neq \mathbf{r}_{d,act}$, this fitting is not linear so that errors are made with respect to α but when $\mathbf{r}_d$ approaches $\mathbf{d}_{act}$ this Taylor coefficient is better determined. Figure C.6 illustrates equation (C.16) with potential values for actual $\xi^* = 0.0422$ and potential values using the linear model with assumed $\widetilde{\xi} = 0.025$. The Taylor coefficient was determined using the above mentioned fitting procedure. We can observe a closer approximation of the actual potentials when comparing this with the potentials $\mathbf{V}_m(\mathbf{r}_{d,act}, \mathbf{d}_{act}, \widetilde{\xi})$ in figure C.5.
It is also possible to write (C.12) as a second order expansion:

$$\begin{aligned} \mathbf{V}_{meas} \;=\; & \mathbf{V}_m(\mathbf{r}_{d,act}, \mathbf{d}_{act}, \widetilde{\xi}) + (\xi^* - \widetilde{\xi})\frac{\partial \mathbf{V}_m(\mathbf{r}_{d,act}, \mathbf{d}_{act}, \xi)}{\partial \xi}\Big|_{\xi=\widetilde{\xi}} \\ & + \frac{(\xi^* - \widetilde{\xi})^2}{2}\frac{\partial^2 \mathbf{V}_m(\mathbf{r}_{d,act}, \mathbf{d}_{act}, \xi)}{\partial^2 \xi}\Big|_{\xi=\widetilde{\xi}} \end{aligned} \tag{C.17}$$

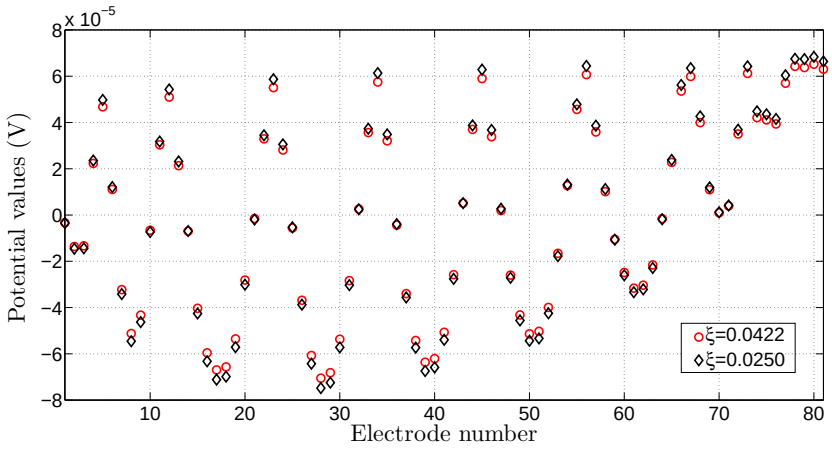

Figure C.6: computed EEG potentials for $\xi = 0.0422$ using $\mathbf{L}(\mathbf{r}_d, \xi)\mathbf{d}$ and computed potentials using linear model (C.16) for assumed conductivity ratio $\tilde{\xi} = 0.0250$.

α can here be determined by performing the following:

$$\alpha^* = \arg\min_{\alpha} \|\mathbf{Y} - \alpha\mathbf{S} - \alpha^2\mathbf{H}\| \tag{C.18}$$

with $\mathbf{H} = \frac{1}{2}\frac{\partial^2 \mathbf{V}_m(\mathbf{r}_{d,act}, \mathbf{d}_{act}, \xi)}{\partial^2 \xi}\Big|_{\xi=\tilde{\xi}}$.

A different fitting procedure needs to be performed when a limited number of multiple dipoles need to be recovered. Indeed, the cost function (C.11) has no longer an m-dimensional measurement vector as input but an $m \times r$ dimensional signal subspace matrix with r the number of topographies in the signal subspace. A different sensitivity than (C.4) needs to be defined. We consider in the spatio-temporal case the use of the principal vector $\mathbf{U}$ that is associated with the principal angle of the subspace correlation function. This principal vector can be computed following ([145]) and depends in the l-th iteration of the minimization procedure (C.10) of the k-th dipole upon Φ_{sig} and the conductivity dependent $\mathbf{L}(\mathbf{r}_d, \xi)$. Therefore, the following sensitivity to conductivity ratio is computed in each iteration:

$$\mathbf{S}_{sub} = \frac{\partial \mathbf{U}}{\partial \xi}\Big|_{\tilde{\xi}} \tag{C.19}$$

and can be approximated by finite differentiation. α is now approximated by fitting $\mathbf{U}$ with $\mathbf{S}_{sub}$.

Using the above, we are able to adapt the traditional cost functions for single dipole localization (C.6) and for multiple dipole localization (C.11): $\mathcal{Y} \rightarrow \mathcal{Y}^{SES}$.

The following basic operation needs to be performed in these traditional cost functions:

$$\mathbf{L}(\mathbf{r}_d, \widetilde{\xi}) \rightarrow \mathbf{L}(\mathbf{r}_d, \widetilde{\xi}) + \alpha\mathbf{T} \tag{C.20}$$

for the first order case with the above mentioned fitting procedures. $\mathbf{T}$ is the sensitivity of the lead field matrix to ξ, similar to $\mathbf{S}$: $T_{ij} = \frac{\partial L_{ij}}{\partial \xi}$. Cost function (C.6) becomes:

$$\mathcal{Y}^{SES}(\mathbf{r}_d, \xi) = \frac{\|\mathbf{V}_{meas} - (\mathbf{L}(\mathbf{r}_d, \xi) + \alpha\mathbf{T})(\mathbf{L}(\mathbf{r}_d, \xi) + \alpha\mathbf{T})^{\dagger}\mathbf{V}_{meas}\|}{\|\mathbf{V}_{meas}\|} \tag{C.21}$$

and (C.11) becomes:

$$\mathcal{Y}_k^{SES}(\mathbf{r}_d, \xi) = -subcorr(\Pi^{\perp}_{\mathbf{A}_{k-1}}\mathbf{L}(\mathbf{r}_d, \xi) + \alpha\mathbf{T}, \Pi^{\perp}_{\mathbf{A}_{k-1}}\Phi_{sig})_1 \tag{C.22}$$

3.1.3.2 Selection of Electrodes

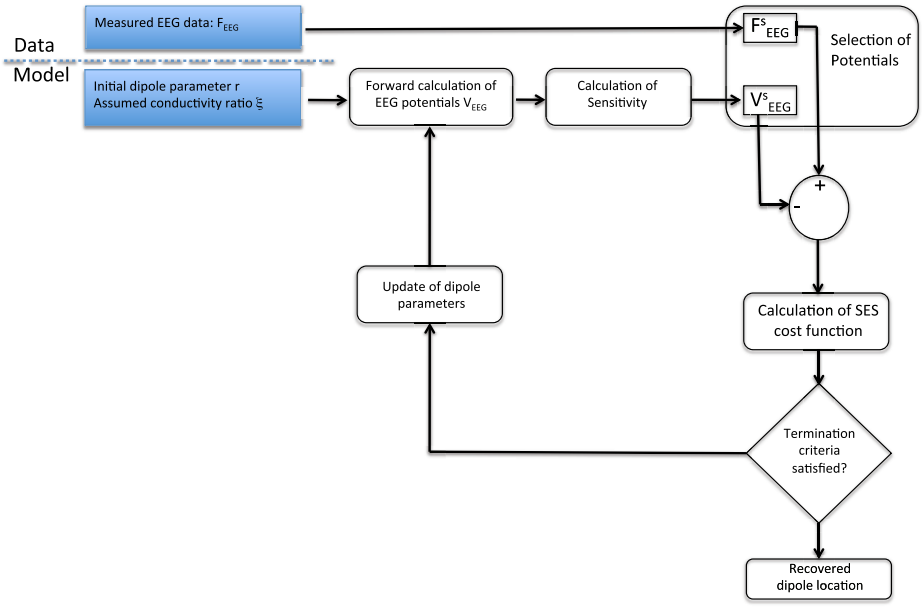

Figure C.7: Schematic overview of the iterative SES methodology.

During the minimization (C.9) or (C.10), iterates $\mathbf{r}_d^{(l)}$ are evaluated in the forward model and due to the uncertain conductivity values, the minimization path is affected by the uncertainty. Therefore, we select in the l-th iteration those potentials with lowest sensitivity to conductivity. Potentials with highest sensitivity are eliminated in that iteration since they carry information that

is affected by the uncertain conductivity. There are two possibilities to select the potentials: either select the potentials on the basis of a threshold: $S_i < \epsilon$ with ϵ a predefined threshold value or select each time a fixed limited number of potentials. At each evaluation of the forward model, the following selection operation is carried out upon the data sets:

$$\mathbf{V}_{meas} \in R^m \rightarrow \mathbf{V}^S_{meas} \in R^s \tag{C.23}$$
$$\Phi_{sig} \in R^{m\times r} \rightarrow \Phi^S_{sig} \in R^{s\times r} \tag{C.24}$$
$$\mathbf{V}_m \in R^m \rightarrow \mathbf{V}^S_m \in R^s \tag{C.25}$$
$$\mathbf{L} \in R^{m\times 3} \rightarrow \mathbf{L}^S \in R^{s\times 3} \tag{C.26}$$
$$\mathbf{T} \in R^{m\times 3} \rightarrow \mathbf{T}^S \in R^{s\times 3} \tag{C.27}$$

with $s < q$ the number of selected electrodes out of the total of q electrodes. Since the sensitivity is taken into account in the cost function, selection is also carried out on the sensitivity matrices. Taking the operations (C.23) and (C.20) into account, the SES cost functions $\mathcal{Y}^{SES}(\mathbf{r}_d, \xi)$ in (C.21), (C.22) become:

$$\frac{\|\mathbf{V}^S_{meas} - (\mathbf{L}^S(\mathbf{r}_d,\xi) + \alpha\mathbf{T}^S)(\mathbf{L}^S(\mathbf{r}_d,\xi) + \alpha\mathbf{T}^S)^\dagger \mathbf{V}^S_{meas}\|}{\|\mathbf{V}^S_{meas}\|} \tag{C.28}$$

and

$$-\,subcorr(\Pi^\perp_{\mathbf{A}_{k-1}}\mathbf{L}^S(\mathbf{r}_d,\xi) + \alpha\mathbf{T}^S, \Pi^\perp_{\mathbf{A}_{k-1}}\Phi^S_{sig})_1 \tag{C.29}$$

respectively. The above can be extended to a second order SES cost function.
Figure C.7 outlines the SES methodology: in a first stage the potentials and sensitivities are computed. In a second stage, selection is carried out on the computed and measured EEG data set with the internal fitting procedure. Thirdly, using this data set, the SES cost function (C.28) and (C.29) is computed leading to an update of the dipole parameters. The update can be carried out using a given minimization procedure. Here, the Nelder-Mead simplex method is used.

3.2. Results and Discussion

3.2.1 Single dipole localization

3.2.1.1 No noise case

In order to investigate the influence of assuming a wrong conductivity, we first solve the forward problem using actual dipole specifications $\mathbf{r}_{d,act}, \mathbf{d}_{act}$ for a certain actual conductivity ratio ξ^*. Starting from these potentials $\mathbf{V}_m(\mathbf{r}_{d,act}, \mathbf{d}_{act}, \xi^*)$ (without adding noise), we solve the inverse problem using

a forward model with assumed conductivity ratio $\widetilde{\xi}$. We evaluate the dipole position error using the Euclidean distance between the original dipole location $\mathbf{r}_{d,act}$ and the estimated dipole location $\mathbf{r}_d^*$: $\|\mathbf{r}_d^* - \mathbf{r}_{d,act}\|$. Since we are using a numerical realistic head model, the lead field are not a continuous function of ξ but need to be computed for different discrete conductivity ratio values. The sensitivity $\mathbf{S}$ and second order term $\mathbf{H}$ are approximated using finite differentiation of these lead fields to the conductivity ratio. Lead field matrices were computed for the following values of ξ: $0.0164 + n\,0.0086$ for $n = 0, \ldots, 8$. In this way, we cover the interval $1/60$ until $1/10$. The values in this interval are usually used as possible values for the conductivity ratio.

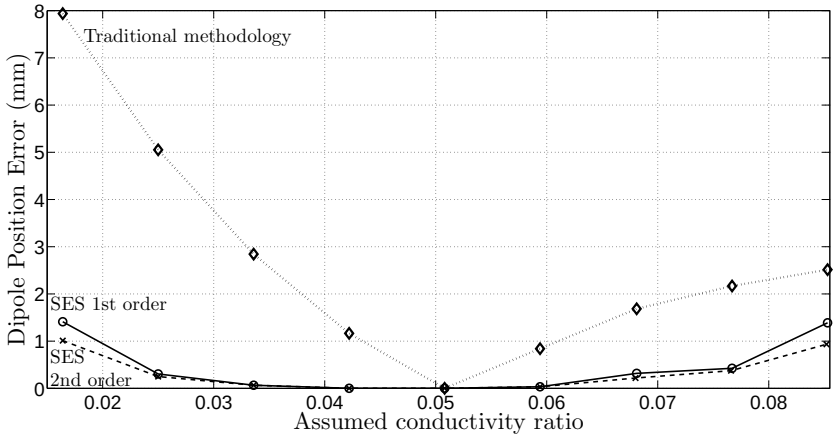

Figure C.8: Dipole position error of a single dipole when using traditional method and selection methodology ($s = 20$) of the first and second order. The dipole is located in the hippocampus.

Figure C.8 shows the single dipole localization error where the actual conductivity ratio is assumed to be around $\xi^* = 1/20$. We observe from this figure that the SES methodology decreases the dipole position error. Indeed, when assuming a conductivity value $\widetilde{\xi} = 1/60$, then the error is decreased from 8 mm to 1.5 mm when using the first order SES methodology. The dipole position error is even more decreased when using the second order SES, especially for assumed conductivity ratios far from the actual conductivity ratio. This can be explained by the fact that the validity region of the linear first order model is smaller than the second order model. Figure C.9 shows the fit of the data to the constant α for the second order case when using (C.18). The number of selected electrodes in the performed simulation studies in this paper is $s = 20$ out of the total of $q = 81$ electrodes.

In a next stage, we investigated the global efficiency of the methodology. We placed in each voxel of the grey matter a certain dipole and computed its cor-

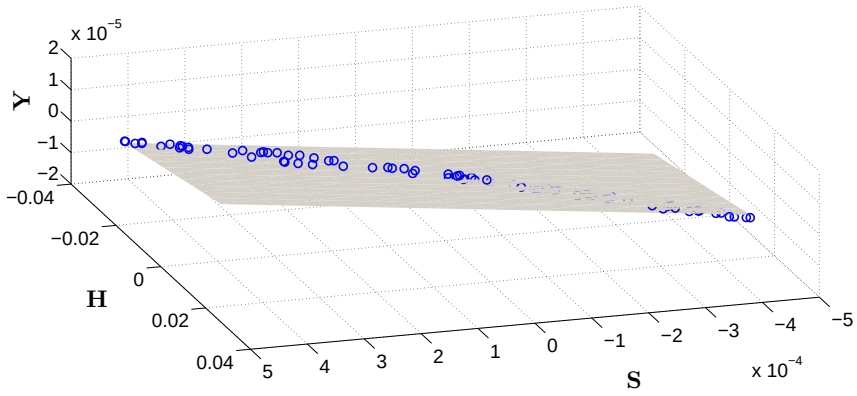

Figure C.9: Determining α in the plane: $\mathbf{Y} \approx \alpha\mathbf{S} + \alpha^2\mathbf{H}$ using (C.18).

responding EEG potential for $\xi^* = 1/20$. The inverse problem was then solved using an assumed conductivity ratio of $\widetilde{\xi} = 1/40$. The dipole position errors in the axial plane are shown in figures C.10, C.11, C.12 for dipoles oriented in the x, y and z direction respectively. We observe an overall decrease in dipole position error where errors of up to 1 cm are decreased to less than 4 mm. Figures C.10, C.11, C.12 illustrate the corresponding dipole orientation errors. The angle between the vector components of the original dipole $\mathbf{d}_{act}$ and estimated dipole orientation $\mathbf{d}^*$ is computed using the cosine rule:

$$\angle(\mathbf{d}^*, \mathbf{d}_{act}) = \arccos\left(\frac{\mathbf{d}^*\mathbf{d}_{act}}{\|\mathbf{d}^*\| \, \|\mathbf{d}_{act}\|}\right) \tag{C.30}$$

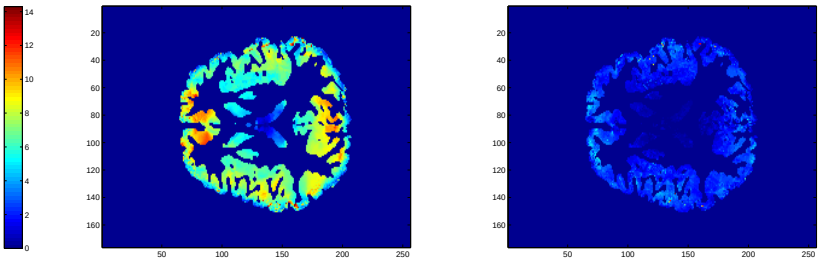

Figure C.10: Dipole position errors (mm) of dipoles oriented in the x-direction when using traditional method (left) and when using Subspace Electrode Selection (right).

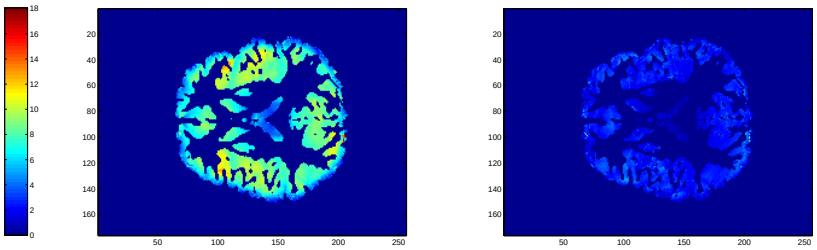

Figure C.11: Dipole position errors (mm) of dipoles oriented in the y-direction when using traditional method (left) and when using Subspace Electrode Selection (right).

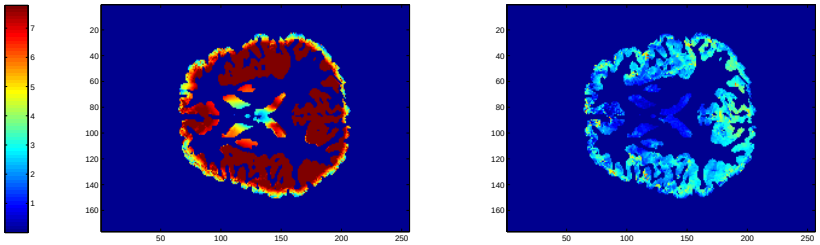

Figure C.12: Dipole position errors (mm) of dipoles oriented in the z-direction when using traditional method (left) and when using Subspace Electrode Selection (right).

3.2.1.2 Noise case

Contrary to the previous simulation study, we added noise $\mathbf{n}$ to the previously computed potentials: $\mathbf{V}_m(\mathbf{r}_{d,act}, \mathbf{d}_{act}, \xi^*) + \mathbf{n}$. The noise is white Gaussian with a certain standard deviation σ_n. The noise level in the data set is determined by $\frac{\sigma_n}{V_{m,RMS}}$ with $V_{m,RMS}$ the root mean square value of the no noise simulated potentials $\mathbf{V}_m(\mathbf{r}_{d,act}, \mathbf{d}_{act}, \xi^*)$. In order to determine in an average way the influence of noise at a certain noise level, the inverse problem is solved 50 times with random noise added to the potentials.

Figure C.13 shows the average dipole position error for various noise levels when using the traditional methodology and when using the SES methodology with fitting procedure based on $\mathbf{S}$ and $\mathbf{Y}$, as mentioned in section 3.1.3.1. It is clear that the advantage of SES is counteracted by the noise. The reason for the bad noise robustness of this procedure is because the residual of the fitting becomes very high when noise is available in the measurements, i.e. the cost function is no longer correct. For very high noise levels, the SES methodology

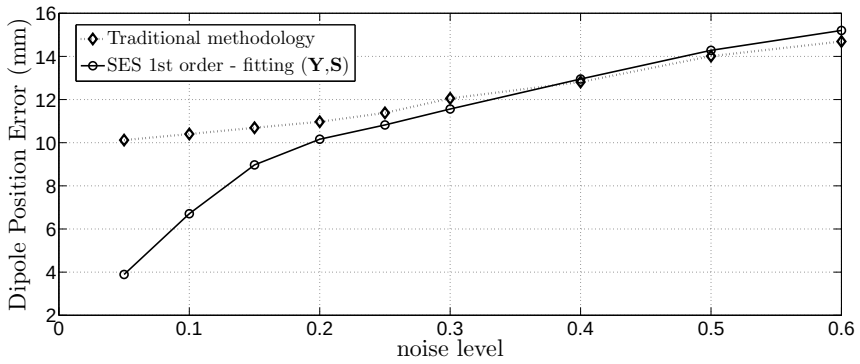

Figure C.13: Dipole Position Error using traditional methodology and SES methodology to the first and second order with incorporation of noise in simulation study. The fitting procedure in SES consists in fitting the data sets **Y** to **S**. The used data sets were generated for actual conductivity ratio $\xi^* = 1/20$ and the inverse problem is solved for each data point 50 times using a forward model with assumed conductivity ratio $\widetilde{\xi} = 1/60$.

is even worse than the traditional methodology. Therefore, we used instead the fitting procedure based on the principal vector of the subspace correlation function:

$$subcorr(\mathbf{L}(\mathbf{r}_d, \xi), \mathbf{V}_{meas})_1 \tag{C.31}$$

A more accurate fit was performed since the principal vector is much less affected by the noise than the absolute values of the computed potentials. Indeed, figure C.14 shows the average dipole position error when using the traditional cost function and when using the SES methodology with fitting of data sets **U** and $\mathbf{S}_{sub}$. We can observe that the SES of second order has little advantage compared to the SES first order when noise is included in the measurements. This result shows that it is possible to use the SES methodology in the realistic noise case, provided that a correct internal fitting procedure is used that is based on the principal vectors of the lead field and measured EEG potentials.

3.2.2 Multiple dipole localization

We also investigated the errors made by a limited number of multiple dipoles. For given p test dipoles, which are simultaneously active, with certain positions $\mathbf{r}_{d,act,k}$ and time varying dipole orientations $\mathbf{d}_{act,k}$ ($k = 1, \ldots, p$), the forward problem was solved for the actual conductivity ratio in the realistic head model, yielding a spatio-temporal EEG potential set. We assumed the time courses of the multiple dipoles as epileptic spikes or as sinusoidal time

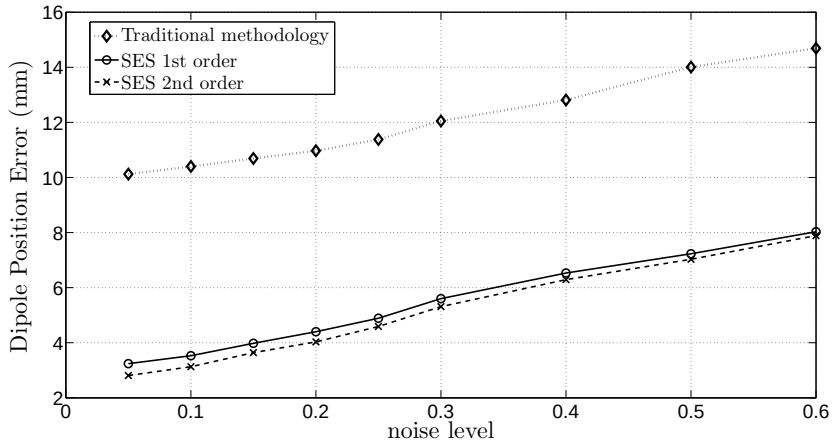

Figure C.14: Dipole Position Error using traditional methodology and SES methodology to the first and second order with incorporation of noise in simulation study. The fitting procedure in SES uses data sets $\mathbf{S}_{sub}$ and $\mathbf{U}$. The used data sets were generated for actual conductivity ratio $\xi^* = 1/20$ and the inverse problem is solved for each data point 50 times using a forward model with assumed conductivity ratio $\widetilde{\xi} = 1/60$.

courses (with frequency 10, 12 or 15 Hz). n = 200 time steps were considered, which corresponds with 1s of EEG data. The inverse problem is then solved using a certain assumed conductivity ratio value.

Figures C.15 and C.16 show the errors made when recovering two dipoles using the traditional, SES first order and SES second order. We observe again a decrease in dipole position error and the advantage of using the second order versus the first order is relatively negligible. The results for resolving more than 2 dipoles are shown in table C.1 for clarity. We depict here the percentual decrease in dipole position error which is computed as $100\frac{E_{Trad}-E_{SES}}{E_{Trad}}$ with E_{Trad} the average dipole position errors of the p used dipoles. E_{SES} is computed in the same way. The added noise set is again white Gaussian noise.

From this table we can observe that the decrease in error is smaller for a larger number of dipoles but remains stable. The reason for this stability is because the RAP-MUSIC based SES methodology uses in each maximization of the RAP-MUSIC cost function the whole set of electrodes where selection is then carried upon. The noise robustness of the methodology is shown in the third column where the percentual decrease stays stable. The inverse problem was solved starting from 20 noisy data sets with same noise level of 0.2.

Table C.1: Dipole position error with the number of dipoles p varying from 2 till 5. The percentual decrease in dipole position error of the used first order SES compared to the traditional methodology is depicted in the case of no noise and noise of level 0.2 in the data set.

p	% decrease (no noise)	% decrease (0.2 noise level)
2	68.49	63.32
3	64.28	59.63
4	61.30	57.10
5	62.51	55.98

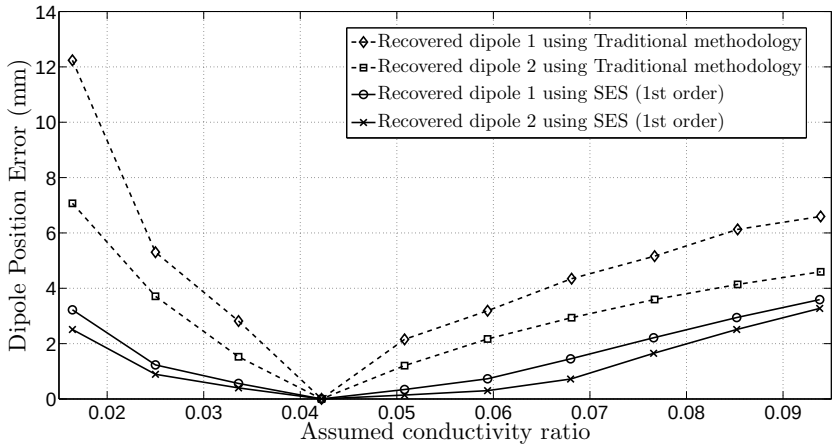

Figure C.15: Dipole Position Errors for two dipoles using traditional RAP-MUSIC algorithm and using the first order SES methodology.

3.2.3 Cost function surface and minimization path

Due to the use of the SES cost functions (C.28), (C.29) the landscape is different than the traditional cost functions. Figure C.17 and C.18 show the cost function surface of the traditional least squares cost function and of the SES cost function surface respectively. This measured EEG potentials $\mathbf{V}_m(\mathbf{r}_{d,act}, \mathbf{d}_{act}, \xi^*)$ were generated for dipole location $\mathbf{r}_{d,act} = [68, 118, 130]$, dipole orientation $\mathbf{d}_{act} = [0.5, 0.4, 0.7]$ with actual conductivity ratio $\xi^* = 1/20$. The traditional cost function $\mathcal{Y}(\mathbf{r}_d, \widetilde{\xi})$ and the first order SES cost function $\mathcal{Y}^{SES}(\mathbf{r}_d, \widetilde{\xi})$ were computed for every voxel in the neighborhood of $\mathbf{r}_{d,act}$ with assumed $\widetilde{\xi} = 1/40$. When comparing these figures, we can observe that the landscape of the cost function is altered. Moreover, the minimum of the cost function is located in the SES case closer to the actual dipole location.

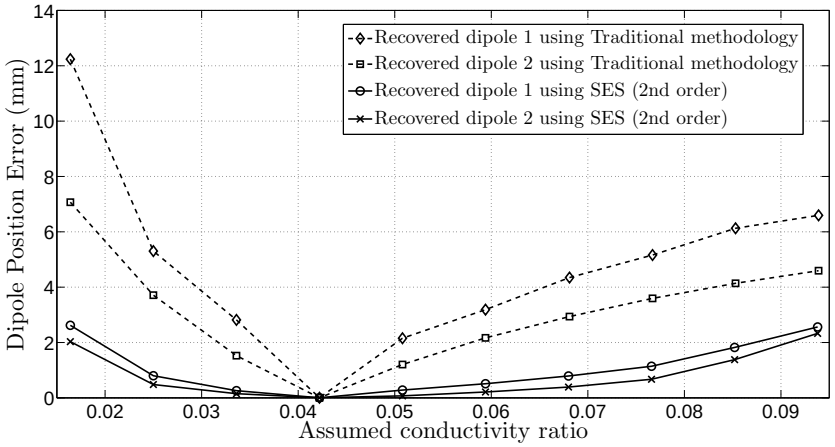

Figure C.16: Dipole Position Errors for two dipoles using traditional RAP-MUSIC algorithm and using the second order SES methodology.

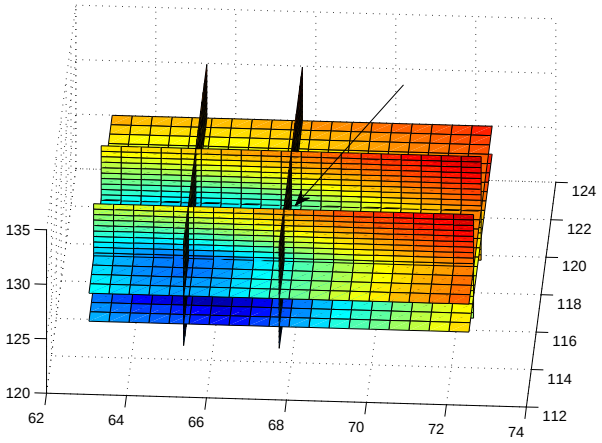

Figure C.17: Traditional RRE cost function surface near actual dipole $\mathbf{r}_{d,act} = [68, 118, 130]$ (arrow) with EEG sample generated by actual $\xi^* = 1/20$ and solved using assumed $\widetilde{\xi} = 1/40$.

Moreover, figure C.19 shows the path of the iterates $\mathbf{r}_d^{(l)}$ during the minimization of the traditional and SES cost function. SES follows a certain minimum path of uncertainty, i.e. the iterates are least affected by the uncertainty. A video shows the dynamic behavior of the selection procedure during that minimization, i.e. the operations (C.23)-(C.27) that affect the minimization of the

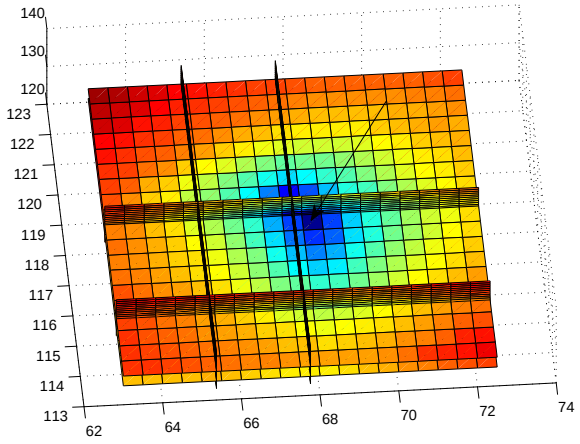

Figure C.18: SES cost function surface near actual dipole $\mathbf{r}_{d,act} = [68, 118, 130]$ (arrow) with EEG sample generated by actual $\xi^* = 1/20$ and solved using assumed $\tilde{\xi} = 1/40$.

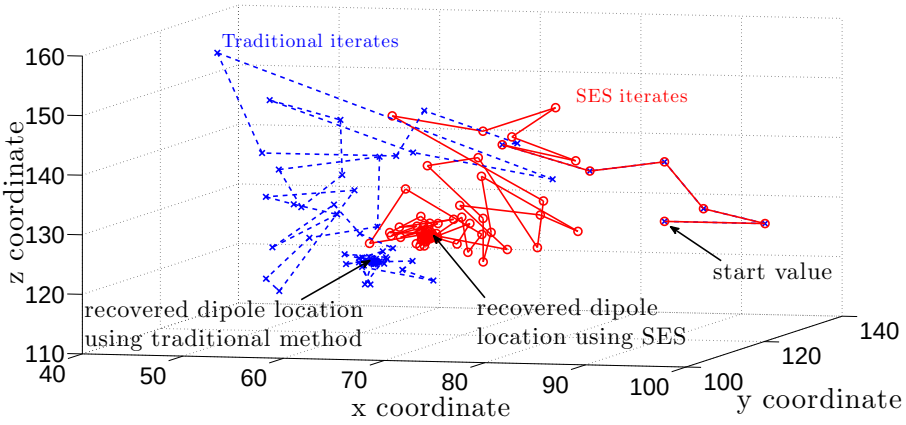

Figure C.19: Path followed by the minimization procedure when minimization the traditional and SES cost function.

SES cost function. The positions of dipoles herein are scaled to the electrode positions.

3.2.4 Drawbacks of SES

The major drawback of the proposed methodology is that the minimization is highly sensitive upon the start value of the dipole. A minimization procedure with multiple start values is needed. The SES cost function contains many local minima and further theoretical work is needed for stabilizing this minimization. A possible means is the use of trust region methodologies. A second drawback of the SES methodology is that it is much more time demanding compared to the traditional approach. The needed computational time for the minimization procedure is on average approximately 44% larger. This is due to the internal fitting procedure and the calculation of the sensitivities in each iteration. For the second order SES, the time is even more time demanding. Thirdly, the SES procedure needs more memory because the sensitivity calculations are based on the finite differentiation of lead fields that are computed for different conductivity ratios in the neighborhood of the assumed conductivity ratio.

3.3. Conclusion

When solving the EEG inverse problem, a cost function needs to be minimized. For EEG dipole source reconstruction this is the widely used traditional least squares cost function of the measured EEG potentials versus the computed EEG potentials. Because the computed EEG potentials are sensitive to the conductivity values, a propagation of the uncertain conductivity values occurs towards the recovered source estimates. In this paper, we introduced the Subspace Electrode Selection (SES) methodology for the reduction of the propagation of the uncertain conductivity values to the inverse solutions. SES uses the following basic operations: (a) redefinition of the cost function with inclusion of the sensitivity of the forward model to the uncertain conductivity ratio and (b) the selection of electrodes that are least affected by the conductivity ratio. The results show that the method enhances the source localization depending on the position of the dipoles, noise in measurements and the deviation of the assumed conductivity ratio value to the actual conductivity ratio. Special care is needed with respect to the internal fitting procedure within the redefined cost function, but fitting the principal vector to their sensitivities of the subspace correlation function of the measured EEG potentials and the lead field matrix.

Further research can be concentrated on decreasing the propagation of multiple uncertainties in EEG dipole analysis and on incorporating other uncertainties such as electrode misplacements, geometrical and source modeling errors. However, the uncertainty of the conductivity has the largest impact onto EEG source analysis. More correct research can be done when incorpo-

rating anisotropic conductivities in the head model with uncertain absolute conductivity values. The methodology has the potential to be applied onto other imaging modalities where the measurements need to be interpreted with a numerical model where uncertainties are included. The presented method can be valuable for brain research where as accurate as possible neural source specifications need to be recovered starting from EEG.

Bibliography

[1] T. Kringsa, H. Keith, B. Chiappaa, N. Cuffinc, I. Jeffrey, Cochiusa, S. Connollya, and G. Rees Cosgroveb, "Accuracy of eeg dipole source localization using implanted sources in the human brain," *Clinical Neurophysiology Elsevier*, vol. 110, no. 1, pp. 106–114, Jan. 1999.

[2] I. Carette, A. Dewaele, A. Van Dycke, and et al., "Invasive video-eeg monitoring at the reference center for refractory epilepsy at ghent university hospital," *European Journal of Neurology*, vol. 14, p. 82, 2007.

[3] M. Pugliatti, E. Beghi, L. Forsgren, M. Ekman, and P. Sobocki, "Estimating the cost of epilepsy in europe: A review with economic modeling," *Epilepsia*, vol. 48, no. 12, pp. 2224–2233, 2007.

[4] P. Boon, M. D'Have, P. Van Walleghem, G. Michielsen, K. Vonck, J. Caemaert, and J. De Reuck, "Direct medical costs of refractory epilepsy incurred by three different treatment modalities: a prospective assessment," *Epilepsia*, vol. 43, no. 1, pp. 96–102, 2002.

[5] L. Geddes and L. Baker, "The specific resistance of biological material-a compendium of data for the biomedical engineer and physiologist," *Medical and Biological Engineering*, vol. 5, pp. 271–293, 1967.

[6] D. Guttiérrez, A. Nehorai, and C. Muravchik, "Estimating brain conductivities and dipole source signals with eeg arrays," *IEEE Transactions on Biomedical Engineering*, vol. 51, no. 12, pp. 2113–2122, 2004.

[7] S. Laureys, S. Goldman, and P. Peigneux, *Brain Imaging*. John Wiley Ltd, 2002.

[8] O. Ryynänen, J. Hyttinen, and J. Malmivuo, "Effect of skull resistivity and measurement noise on the spatial resolution of eeg," *IJBEM*, vol. 7, no. 1, pp. 1–4, 2005.

[9] M. Bernd, W. Graf, and M. Beer, "Safety assessment of structures in view of fuzzy randomness," *Computers and Structures*, vol. 81, pp. 1567–1582, 2003.

[10] J. De Munck, B. Van Dijk, and H. Spekreijse, "Mathematical dipoles are adequate to describe realistic generators of human brain activity," *IEEE Transactions on Biomedical Engineering*, vol. 35, pp. 960–965, 1988.

[11] S. Baillet, J. C. Mosher, and R. M. Leahy, "Electromagnetic brain mapping," pp. 14–30, 2001.

[12] R. Mosher, J.C.and Leahy, "Source localization using recursively applied and projected (rap) music," *IEEE Trans. Sign. Proc*, vol. 37, pp. 332–340, 1999.

[13] B. E. Knosche, T. and, H. Jagers, and M. Peters, "Determining the number of independent sources of the eeg: A simulation study on information criteria," *Brain Topogr*, vol. 11, pp. 111–124, 1998.

[14] B. X and H. B, "Estimation of number of independent brain electric sources from the scalp eegs," *IEEE Trans Biomed Eng*, vol. 53, pp. 1883–1892, 2006.

[15] B. Vanrumste, G. Van Hoey, R. Van de Walle, M. Have, I. Lemahieu, and P. Boon, "The performance of the spherical head model compared to the realistic head model

in dipole localization with noisy eeg," *Medical Engineering and Physics*, vol. 24, no. 6, pp. 403–408, 2002.

[16] P. H. Laarne, M. L. Tenhunen-Eskelinen, J. K. Hyttinen, and H. J. Eskola, "Effect of eeg electrode density on dipole localization accuracy using two realistically shaped skull resistivity models," *Brain Topography*, vol. 12, no. 4, pp. 249–254, 2000.

[17] J. Sijbers, B. Vanrumste, G. Van Hoey, P. Boon, and M. Verhoye, "Automatic localization of eeg electrode markers within 3d mr data," *Magnetic Resonance Imaging*, vol. 18, pp. 485–488, 2000.

[18] R. Pohlmeier, H. Buchner, G. Knoll, A. Rienacker, R. Beckmann, and J. Pesch, "The influence of skull-conductivity misspecification on inverse source localization in realistically shaped finite element models," *Brain Topography*, vol. 9, no.3, pp. 157–162, 1997.

[19] J. Haueisen, D. Tuch, C. Ramon, P. Schimpf, V. Wedeen, J. George, and J. Belliveau, "The influence of brain tissue anisotropy on human eeg and meg," *NeuroImage*, vol. 15, pp. 159–166, 2002.

[20] C. Wolters, A. Anwander, X. Tricoche, D. Weinstein, M. Koch, and R. MacLeod, "Influence of tissue conductivity anisotropy on eeg/meg field and return current computation in a realistic head model: a simulation and visualization study using high-resolution finite element modeling," *NeuroImage*, vol. 30, no.3, pp. 813–826, 2006.

[21] H. Hallez, B. Vanrumste, P. Van Hese, S. Delputte, and I. Lemahieu, "Dipole estimation errors due to differences in modeling anisotropic conductivities in realistic head models for eeg source analysis," *Physics in Medicine and Biology*, vol. 53, no.7, pp. 1877–1894, 2008.

[22] J. Haueisen, C. Ramon, M. Eiselt, H. Brauer, and H. Nowak, "Influence of tissue resistivities on neuromagnetic fields and electric potentials studied with a finite element model of the head," *IEEE Trans. Biomed. Eng*, vol. 44, pp. 727–735, 1997.

[23] P. Laarne, P. Kauppinen, J. Hyttinen, J. Malmivuo, and H. Eskola, "Effects of tissue resistivities on electroencephalogram sensitivity distribution," *Med. & Biol. Eng. & Comput.*, vol. 37, no.5, pp. 555–559, 1999.

[24] N. Gencer and C. Acar, "Sensitivity of eeg and meg measurements to tissue conductivity," *Physics in Medicine and Biology*, vol. 49, no.5, pp. 701–717, 2004.

[25] S. Vallaghe and M. Clerc, "A global sensitivity analysis of three- and four-layer eeg conductivity models," *IEEE Trans Biomed Eng.*, vol. 56, no. 4, pp. 988–995, 2009.

[26] B. Vanrumste, G. Van Hoey, R. Van de Walle, M. Have, I. Lemahieu, and P. Boon, "Dipole location errors in electroencephalogram source analysis due to volume conductor model errors," *Medical Biological Engineering and Computing*, vol. 38, pp. 528–534, 2000.

[27] S. Plis, J. George, S. Jun, D. Ranken, P. Volegov, and D. Schmidt, "Probabilistic forward model for electroencephalography source analysis," *Physics in Medicine and Biology*, vol. 52, no.17, pp. 5309–5327, 2007.

[28] H. Chen, F.and Hallez and S. Staelens, "Influence of skull conductivity perturbations on eeg dipole source analysis," *Med. Phys.*, vol. 37, no. 8, pp. 4475–4484, 2010.

[29] L. Geddes and L. Baker, "The specific resistance of biological materiala compendium of data for the biomedical engineer and physiologist," *Medical and Biological Engineering*, vol. 5, no.3, pp. 271–293, 1967.

[30] T. Oostendorp, J. Delbeke, and D. Stegeman, "The conductivity of the human skull: results of in vivo and in vitro measurements," *IEEE Transactions on Biomedical Engineering*, vol. 47, no.11, pp. 1487–1492, 2000.

[31] S. I. Gonçalves, J. C. de Munck, J. P. A. Verbunt, F. Bijma, R. M. Heethaar, and F. Lopes da Silva, "In vivo measurement of the brain and skull resistivities using an eit-based method and realistic models for the head," *IEEE Transactions on Biomedical Engineering*, vol. 50, no.6, pp. 754–767, 2003.

[32] R. Hoekema, G. Wieneke, F. Leijten, C. van Veelen, P. van Rijen, G. Huiskamp, J. Ansems, and A. van Huffelen, "Measurement of the conductivity of the skull, temporarily removed during epilepsy surgery," *Brain Topogr*, vol. 16, no.1, pp. 29–38, 2003.

[33] Y. Lai, W. van Drongelen, L. Ding, K. E. Hecox, V. L. Towle, D. M. Frim, and B. He, "Estimation of in vivo human brain-to-skull conductiv- ity ratio from simultaneous extra- and intra-cranial electrical potential recordings.," *Clinical Neurophysiology*, vol. 116, no.2, pp. 456–465, 2005.

[34] C. Gabriel, "Dielectric properties of biological tissue: variation with age," *Bioelectromagnetics*, vol. Suppl 7, pp. S12–S18, 2005.

[35] P. L. Nunez, *Electric field of the brain*. London: Oxford University Press, 1981.

[36] E. Niedermeyer and F. H. Lopes da Silva, *Electroencephalography: Basic principles, clinical applications and related fields*. Lippincott, Williams & Wilkins, Philadelphia., .1993 3rd edition.

[37] D. Zumsteg and H. Gregor Wieser, "Presurgical evaluation: Current role of invasive eeg," *Epilepsia*, vol. 41. (Suppl. 3), pp. S55–S60, 2000.

[38] P. Boon, K. Vonck, V. De Herdt, P. Claeys, D. Van Roost, L. Goossens, E. Achten, G. Vingerhoets, E. Thiery, I. Goethals, M. Van Zandijcke, M. Goethals, and J. Caemaert, "Tertiary epilepsy care in belgium: The practice at ghent university hospital reference centre for refractory epilepsy," *Epilepsia*, vol. 46, suppl.6, p. 318, 2005.

[39] J. Haueisen, C. Ramon, H. Brauer, and H. Nowak, "The influence of local tissue conductivity changes on the magnetoencephalogram and the electroencephalogram," *Biomedical Techniques*, vol. 45, pp. 211–214, 2000.

[40] R. Van Uitert, C. Johnson, and L. Zhukov, "Influence of head tissue conductivity in forward and inverse magnetoencephalographic simulations using realistic head models," *IEEE Transactions on Biomedical Engineering*, vol. 51, no. 12, pp. 2129–2137, 2004.

[41] S. Baillet, J. C. Mosher, and R. M. Leahy, "Electromagnetic brain mapping," *IEEE Signal Processing Magazine*, vol. 18, No. 6, pp. 14–30, Nov. 2001.

[42] P. Nunez, *Localization of brain activity with electroencephalography Advances in Neurology, Magnetoencephalography*, vol. 54 ed S Sato. (New York: Raven Press), 1990.

[43] G. Demoment, "Image reconstruction and restoration: Overview of common estimation structures and problems," *IEEE Transaction on Acoustics, Speech, and Signal Processing*, vol. 37, no 12, 1989.

[44] G. Huiskamp, "Interindividual variability of skull conductivity: an eeg-meg analysis," *International Journal of Bioelectromagnetism*, vol. 10, no. 1, pp. 25–30, 2008.

[45] S. Ueno and N. Iriguchi, "Impedance magnetic resonance imaging: amethod for imaging of impedance distributions based on magnetic resonance imaging," *J. Appl. Phys.*, vol. 83, pp. 6450–6452, 1998.

[46] J. Haueisen, D. S. Tuch, C. Ramon, P. H. Schimpf, V. J. Wedeen, J. S. George, and J. W. Belliveau, "The influence of brain tissue anisotropy on human eeg and meg," *Neuroimage*, vol. 15, pp. 159–166, 2002.

[47] T. Ferree, K. Eriksen, and D. Tucker, "Regional head tissue conductivity estimation for improved eeg analysis," *Physics in Medicine and Biology*, vol. 47, no.12, pp. 1584–1592, 2000.

[48] T. Oostendorp, J. Delbeke, and D. Stegeman, "The conductivity of the human skull: Results of in vivo and in vitro measurements," *IEEE Transactions on Biomedical Engineering*, vol. 47, no.11, pp. 1487–1492, 2000.

[49] S. Gonc, J. De Munck, J. Verbunt, R. M. Heethaar, and F. Lopes da Silva, "In vivo measurement of the brain and skull resistivities using an eit based method and the combined analysis of sef/sep data.," *IEEE Transactions on Biomedical Engineering*, vol. 50, no. 9, pp. 1124–1128, 2003.

[50] S. Vallaghe, M. Clerc, and J. Badier, "In vivo conductivity estimation using somatosensory evoked potentials and cortical constraint on the source," in *Proceedings of ISBI 2007*, (Arlington, USA), pp. 1036–1039, 2007.

[51] K. Boone, D. Barber, and B. Brown, "Review imaging with electricity: report of the european concerted action on impedance tomography," *J. Med. Eng. Technol*, vol. 21, pp. 201–232, 1997.

[52] L. Borcea, "Electrical impedance tomography," *Inverse Problems*, vol. 18, pp. R99–R136, 2002.

[53] G. M. Clerc, J. Adde, T. Kybic, Papadopoulo, and J. Badier., "In vivo conductivity estimation with symmetric boundary elements.," *International Journal of Bioelectromagnetism, In Jaakko Malmivuo, editor*, vol. 7, pp. 307–310, 2005.

[54] H. Hans, *Incorporation of anisotropic conductivities in EEG source analysis*. PhD thesis, Ghent University, 2009.

[55] W. Lee, Z. Liu, B. Mueller, K. Lim, and B. He, "Influence of white matter anisotropic conductivity on eeg source localization: comparison to fmri in human primary visual cortex," *Clin Neurophysiol*, vol. 120, no.12, pp. 2071–2081, Dec. 2009.

[56] G. Crevecoeur, *Numerical Methods for low frequency electromagnetic optimization and inverse problems using multi-level techniques (PHD thesis)*. University of Ghent, 2009.

[57] H. Jasper, "The ten-twenty electrode system of the international federation," *Electroencephalogr Clin Neurophysiol*, vol. 10, pp. 371–375, 1958.

[58] G. Chatrian, E. Lettich, and P. Nelson, "Ten percent electrode system for topographic studies of spontaneous and evoked eeg activity," *American Journal of Electroencephalography and Technologies*, vol. 25, pp. 83–92, 1985.

[59] G. Klem, H. Luders, H. Jasper, and C. Elger, "The ten-twenty electrode system of the international federation," *Electroencephalography Clinical Neurophysiology*, vol. Supplement 52, pp. 3–6, 1999.

[60] M. Nuwer, "Recording electrode site nomenclature," *Journal of Clinical Neurophysiology*, vol. 4, pp. 121–133, 1987.

[61] J. Malmivuo and R. Plonsey, *Bioelectromagnetism: Principles and Applications of Bioelectric and Biomagnetic Fields p.258*. Oxford University Press, USA; 1 edition, July 27, 1995.

[62] R. Oostenveld and R. Praamstra, "The five percent electrode system for high-resolution eeg and erp measurements," *Clin Neurophysiol*, vol. 112, pp. 713–719, 2001.

[63] A. Gevins, P. Brickett, B. Costales, J. Le, and B. Reutter, "Beyond topographic mapping: toward functional-anatomical imaging with 124-channel eeg and 3-d mris," *Brain Topology*, vol. 3, pp. 53–64, 1990.

[64] O. R. M. Ryynanen, J. A. K. Hyttinen, and J. Malmivuo, "Effect of measurement noise and electrode density on the spatial resolution of cortical potential distribution with different resistivity values for the skull," *IEEE Transactions on Biomedical Engineering*, vol. 53 no. 9, pp. 1851–1858, 2006.

[65] D. Rubio and M. I. Troparevsky, "The eeg forward problem: theoretical and numerical aspects," *Latin American applied research [online].*, vol. 36, no.2, pp. 87–92, 2006.

[66] F. Vatta, F. Meneghini, F. Esposito, S. Mininel, and F. Di Salle, "Realistic and spherical head modeling for eeg forward problem solution: a comparative cortex-based analysis," *Computational Intelligence and Neuroscience. Special issue on processing of brain signals by using hemodynamic and neuroelectromagnetic modalities*, vol. 2010, pp. 1–11, 2010.

[67] G. Marin, C. Guerin, S. Baillet, L. Garnero, and G. Meunier, "Influence of skull anisotropy for the forward and inverse problem in eeg: Simulation studies using fem on realistic head models," *Human Brain Mapping*, vol. 6, pp. 250–269, 1998.

[68] Matti, Hämäläinen, R. Hari, J. Risto, Ilmoniemi, J. Knuutila, Olli, and V. Lounasmaa, "Magnetoencephalography-theory, instrumentation and applications to noninvasive studies of the working human brain. review of modern physics," *Review of modern physics*, vol. 65(2), pp. 413–497, April 1993.

[69] M. Hamalainen, R. Hari, R. J.Ilmoniemi, J. Knuutila, and v. Olli Lounasmaa, "Magnetoencephalography-theory, instrumentation, and application to non-invasive studies of the working human brain," *Review of Modern Physics*, vol. 65 no.2, pp. 413–497, 1993 .

[70] R. Plonsey and D. B. Heppner, "Considerations of quasistationarity in electrophysiological systems.," *Bulletin of Mathematical Biophysics*, vol. 29, no. 4, pp. 657–664, 1967.

[71] B. Vanrumste, G. Van Hoey, R. Van de Walle, M. R. P. D'Hav, I. A. Lemahieu, and P. A. J. M. Boon, "The validation of the finite difference method and reciprocity for solving the inverse problem in eeg dipole source analysis," *Brain Topography*, vol. 14, no.2, pp. 83–92, 2001.

[72] W. David and C. R. Johnson, "Effects of geometric uncertainty on the inverse eeg problem," in *Computational, Experimental, and Numerical Methods for Solving Ill-Posed Inverse Imaging Problems: Medical and Nonmedical Applications*, pp. 138–145, SPIE, 1997.

[73] D. A. Brody, F. H. Terry, and R. E. Ideker, "Eccentric dipole in a spherical medium: Generalized expression for surface potentials," *IEEE Trans. Biomed. Eng.*, vol. 20, pp. 141–143, 1973.

[74] D. Yao, "Electric potential produced by a dipole in a homogeneous conducting sphere," *IEEE Trans Biomed Eng*, vol. 47, pp. 964–966, 2000.

[75] M. Hämälainen and J. Sarvas, "Realistic conductivity geometry model of the human head for interpretation of neuromagnetic data," *IEEE Trans. Biomed. Eng.*, vol. 36, pp. 165–171., 1989.

[76] J. Mosher, P. Lewis, and R. Leahy, "Multiple dipole modeling and localization from spatiotemporal megdata," *IEEE Transactions on Biomedical Engineering*, vol. 39, no.6, pp. 541–557, 1992.

[77] Z. Zhang, "A fast method to compute surface potentials generated by dipoles within multilayer anisotropic spheres," *Physics in Medecine and Biology.*, vol. 40, no.1, pp. 335–349, 1995.

[78] J. De Munck and M. J. Peters, "A fast method to compute the potential in the multisphere," *IEEE transactions on Biomedical engineering*, vol. 40, pp. 1166–1174, 1993.

[79] B. N. Cuffin and D. Cohen, "Magnetic fields of a dipole in special volume conductor shapes," *IEEE Trans. Biomed. Eng.*, vol. BME-24, pp. 372–381, 1977.

[80] B. N. Cuffin, "Eccentric spheres models of the head," *IEEE Trans. Biomed. Eng.*, vol. 38, pp. 871–878, 1991.

[81] B. N. Cuffin, "Effects of head shapes on eegs and megs," *IEEE Trans. Biomed. Eng.*, vol. 37, pp. 15–22, 1990.

[82] B. N. Cuffin, "Eeg localization accuracy improvements using realistically shaped head models," *IEEE Transactions on Biomedical Engineering*, vol. 43 no. 3, pp. 299–303, 1996.

[83] N. Chauveau, X. Franceries, B. Doyon, B. Rigaud, J. Morucci, and P. Celsis, "Effects of skull thickness, anisotropy, and inhomogeneity on forward eeg/erp computations using a spherical three-dimensional resistor mesh model," *Human Brain Mapping*, vol. 21, pp. 86–97, 2004.

[84] G. Huiskamp, M. Dijk Vroeijenstijn, R. . van Dijk, G. Wieneke, and A. Huffelen, "The need for correct realistic geometry in the inverse eeg problem," *IEEE Transactions on Biomedical Engineering*, vol. 46, no. 11, pp. 1281–1287, 1999.

[85] G. Marin, C. Guerin, S. Baillet, L. Garnero, and G. Meunier, "Influence of skull anisotropy for the forward and inverse problems in eeg: simulation studies using fem on realistic head models," *Human Brain Mapping*, vol. 6, pp. 250–269, 1998 .

[86] H. Hallez, B. Vanrumste, P. Van Hese, Y. D'Asseler, I. Lemahieu, and R. Van de Walle, "A finite difference method with reprocity used in incorporate anisotropy in electroencephalogram dipole source localization," *Physics in Medecine and Biology*, vol. 50:, pp. 3787–3806, 2005.

[87] H. I. Saleheen and T. N. Kwong, "New finite difference formulations for general inhomogeneous anisotropic bioelectric problems," *IEEE Transcations on Biomedical Engineering*, vol. 44, no. 9, pp. 800–809, 1997.

[88] V. Etienne, E. Chaljub, J. Virieux, and N. Glinsky, "An hp-adaptive discontinuous galerkin finite-element method for 3-d elastic wave modelling," *Geophysical Journal International*, vol. 183, pp. 941–962, 2010.

[89] R. T. FENNER, "The boundary integral equation (boundary element) method in engineering stress analysis," *The Journal of Strain Analysis for Engineering Design*, vol. 18, no. 4, pp. 199–205, 1983.

[90] S. J., "Basic mathematical and electromagnetic concepts of the biomagnetic inverse problem," *Physics in Medicine and Biology*, vol. 32, pp. 11–22, 1987.

[91] E. Olivi, M. Yvinec, M. Clerc, and T. Papadopoulo, "Quantitative comparisons of forward problems in meeg," *INRIA Research Report*, vol. 3, no. 6364, pp. 4–5, 2007.

[92] M. I. Troparevsky and D. Rubio, "On the weak solutions of the forward problem in eeg," *Journal of Applied Mathematics*, vol. 12, pp. 647–656, 2003 .

[93] A. El Badia, T., and Ha-Duong, "An inverse source problem in potential analysis," *IOP, Inverse Problems*, vol. 16, pp. 651–663, 2000.

[94] C. Wolters and J. C. de Munck, "Volume conduction," *Scholarpedia*, vol. 2, no.3, p. 1738, 2007.

[95] J. Ary, S. Klein, and D. Fender, "Location of sources of evoked scalp potentials: corrections for skull and scalp thicknesses.," *IEEE Transactions on Biomedical Engineering*, vol. 6, pp. 447–452., 1981.

[96] J. Haueisen, C. Ramon, H. Brauer, and H. Nowak, "The influence of local conductivity changes on meg and eeg," *Biomed. Tech*, vol. 45 no. 7-8, pp. 211–214, 2000.

[97] S. Knakea, E. Halgren, H. Shiraishi, K. Hara, H. Hamer, P. Grant, V. Carr, D. Foxe, S. Camposano, E. Busa, T. Witzel, M. Hämäläinen, S. Ahlfors, E. Bromfield, P. Black, B. Bourgeois, A. Cole, G. Cosgrove, B. Dworetzky, J. Madsen, P. Larsson, D. Schomer, E. Thiele, A. Dale, B. Rosen, and S. Stufflebeam, "The value of multichannel meg and eeg in the presurgical evaluation of 70 epilepsy patients," *Epilepsy Research*, vol. 69, pp. 80–86, 2006.

[98] S. Baillet and L. Garnero, "A bayesian approach to introducing anatomo-functional priors in the eeg/meg inverse problem," *IEEE Transactions on Biomedical Engineering*, vol. 44, No 5, pp. 374–385, May 1997.

[99] R. Schmidt, "Multiple emitter location and signal parameter estimation," *IEEE Trans Antennas Propagat*, vol. AP-34, pp. 276–280, 1986.

[100] P. S. Mosher, J. C.and Lewis and R. M. Leahy, "Multiple dipole modeling and localization from spatio-temporal meg data," *Transactions on Biomedical Engineering*, vol. 39, No 6, pp. 541–553, 1992.

[101] R. Pascual Marqui, "Review for solving the eeg inverse problem," *IJBEM*, vol. 1, no.1, pp. 75–86, 1999.

[102] C. Michel, M. Murray, G. Lantz, S. Gonzalez, L. Spinelli, and R. Grave de Peralta, "Eeg source imaging.," *Clinical Neurophysiology*, vol. 115, pp. 2195–2222, 2004.

[103] K. Sekihara and N. S. Hild, K.E. and, "A novel adaptive beamformer for meg source reconstruction effective when large background brain activities exist," *IEEE Trans Biomed Eng*, vol. 53, no. 9, pp. 1755–1764, 2006.

[104] I. F. Gorodnitsky, J. S. George, and D. R. Bhaskar *Electroencephalography and clinical Neurophysiology*, vol. 95, pp. 231–251, 1995.

[105] R. Pascual-Marqui, C. M. Michel, and D. Lehmann, "Low resolution electromagnetic tomography: a new method for localizing electrical activity in the brain," *International Journal of Psychophysiology*, vol. 18, pp. 49–65, 1994.

[106] N. J. Trujillo-Barreto, E. Aubert-Vzquez, and P. A. Valds-Sosa, "Bayesian model averaging in eeg/meg imaging," *Neuroimage*, vol. 21, no. 4, pp. 1300–1319, Apr. 2004.

[107] U. Wagner, S. Gais, H. Haider, R. Verleger, and J. Born, "Sleep inspires insight," *Nature*, vol. 427, pp. 352–355, 2004.

[108] J. De Munck, V. D. B.W., and H. Spekkreijse, "Mathematical dipoles are edequate to describe realistic generators of human brain activity," *IEEE Transactions on Biomedical Engineering*, vol. 35, pp. 960–965, 1988.

[109] J. C. Mosher, R. M. Leahy, and P. S. Lewis, "Eeg and meg: forward solutions for inverse methods," *IEEE Trans. Biomed. Eng*, vol. 46, pp. 245–249, 1999.

[110] J. Mosher and R. Leahy, "Source localization using recursively applied and projected (rap) music," *IEEE Trans Biomed Eng*, vol. 39, pp. 332–340, 1999.

[111] G. Crevecoeur, H. Hallez, P. Van Hese, Y. D'Asseler, L. Dupré, and R. Van de Walle, "A hybrid algorithm for solving the eeg inverse problem from spatio-temporal eeg data," *Med. Biol. Engin. Comput*, vol. 46, pp. 767–777,, 2008.

[112] M. Huang, C. Aine, S. Supek, E. Best, D. Ranken, and E. Flynn, "Multi-start downhill simplex method for spatio-temporal source localization in magnetoencephalography," *IEEE Trans Biomed Engin*, vol. 45, pp. 716–723, 1998.

[113] E. Menninghaus, B. Lutkenhoner, and S. Gonzalez Andino, "Localization of a dipolar source in a skull phantom: Realistic versus spherical model," *IEEE Trans. Biomed. Engn*, vol. 25, pp. 986–989, 1994.

[114] M. S. Hämäläinen and R. J. Ilmoniemi, "Interpreting magnetic fields of the brain: minimum norm estimates," *Medical and Biological Engineering and Computing*, vol. 32, no.1, pp. 35–42, 1994.

[115] J. Wang, S. Williamson, and L. Kaufman, "Magnetic source images determined by a lead-field analysis: the unique minimum-norm least-squares estimation," *IEEE Transactions on Biomedical Engineering*, vol. 39, no. 7, pp. 665–675, 1992.

[116] R. Grave de Peralta, S. Gonzalez, G. Lantz, C. Michel, and T. Landis, "Noninvasive localization of electromagnetic epileptic activity. i method descriptions and simulations.," *Brain Topography*, vol. 14, pp. 131–137, 2001.

[117] M. Schmid, C.and Polito, "A structured probabilistic model for recognition," *Computer Vision and Pattern Recognition*, vol. 2, pp. 485–490, 1999.

[118] S. Baillet and L. Garnero, "A bayesian approach to introducing anatomo-functional priors in the eeg/meg inverse problem," *IEEE Trans. Biomed. Eng*, vol. 44, pp. 374–385, 1997.

[119] L. Gavit, S. Baillet, J. Mangin, J. Pescatore, and L. Garnero, "A multiresolution framework to meg/eeg source imaging," *IEEE Transactions on Biomedical Engineering*, vol. 48, no. 10, pp. 1080–1087, 2001.

[120] R. Menendez, S. G. Andino, G. Lantz, C. M. Michel, and T. Landis, "Noninvasive localization of electromagnetic epileptic activity. i. method descriptions and simulations," *Brain Topography*, vol. 14, no. 2, pp. 131–137, 2001.

[121] D. McNay, E. Michielssen, R. Rogers, S. Taylor, M. Akhtari, and W. Sutherling, "Multiple source localization using genetic algorithms," *Journal of Neuroscience Methods*, vol. 64, no. 2, pp. 163–172, 1996.

[122] A. Lomax and R. Snieder, "Identifying sets of acceptable solutions to non-linear, geophysical inverse problems which have complicated misfit functions," *Non linear Processes in Geophysics*, vol. 2, pp. 222–227, 1995.

[123] R. Sclabassi, M. Sonmez, and M. Sun, "Eeg source localization: a neural network approach," *Neurol Res*, vol. 23, no. 5, pp. 457–464, July 2001.

[124] R. Grech, T. Cassar, J. o. Muscat, K. P. Camilleri, S. G Fabri, M. Zervakis, P. Xanthopoulos, V. Sakkalis, and B. Vanrumste, "Review on solving the inverse problem in eeg source analysis," *Journal of NeuroEngineering and Rehabilitation*, vol. 5, no.25, pp. 1–33, 2008.

[125] K. Uutela, M. Hamalainen, and R. Salmelin, "Global optimization in the localization of neuromagnetic sources," *IEEE Transactions on Biomedical Engineering*, vol. 45, no.6, pp. 716–723, 1998.

[126] W. Press, S. Teukolsky, W. Vetterling, and B. Flannery, *Numerical recipes in C.* Cambridge University Press, 1995.

[127] C. Ramon, P. Schimpf, and J. Haueisen, "Influence of the head models eeg simulation and inverse source localization," *Biomedical Engineering Online*, vol. 5, pp. 1–13, 2006.

[128] S. Ahokas, J. Malmivuo, and P. Kauppinen, "Development of low noise active electrode for high-resolution eeg," in *IFMBE Proceedings*, pp. 876–879, 2009.

[129] O. Hannu, P. Peitsa, O. Juuso, V. Antti, and T. Leena, "Eeg noise cancellation by a subspace method based on wavelet decomposition," *International medical journal of experimental and clinical research*, vol. 8, no. 11, pp. MT199–MT204, 2002.

[130] S. Fitzgibbon, D. Powers, K. Pope, and C. Clark, "Removal of eeg noise and artifact using blind source separation.," *Journal of Clinical Neurophysiology*, vol. 24, no. 3, pp. 232–234, 2007.

[131] R. M. Leahy, J. C. Mosher, M. E. Spencer, M. X. Huang, and J. D. Lewine, "A study of dipole localization accuracy for meg and eeg using a human skull phantom," *Electroenceph. Clin. Neurophysiol.*, vol. 107, pp. 159–73., 1998.

[132] T. J. C. Faes, H. Van der Meij, R. Heethaar, Mand, and J. C. De Munck, "The resistivity of human tissue (100 hz10 mhz): a meta-analysis of review studies.," *Physiol. Meas.*, vol. 20, pp. R1–R10., 1999.

[133] S. I. Gonçalves, J. C. de Munck, P. A. V. Jeroen, F. Bijma, R. M. Heethaar, and d. S. Fernando Lopes, "In vivo measurement of the brain and skull resistivities using an eit-based method and realistic models for the head," *IEEE Transactions On Biomedical Engineering*, vol. 50, no. 6, pp. 754–767, 2003.

[134] S. Plis, J. George, S. C. Jun, D. M. Ranken, P. L. Volegov, and D. M. Schmidt, "Probabilistic forward model for electroencephalography source analysis," *Physics In Medicine And Biology*, vol. 52, pp. 5309–5327, 2007.

[135] G. Van Hoey, B. Vanrumste, M. D'Have, R. Van de Walle, I. Lemahieu, and P. Boon, "The influence of measurement noise and electrode mislocalization on eeg dipole source localization," *Med Biol Eng Comput*, vol. 38, no. 3, pp. 287–296, 2000.

[136] W. H. Lee, Z. Liua, B. A. Muellerb, K. Limb, and H. Bin, "Influence of white matter anisotropic conductivity on eeg source localization: Comparison to fmri in human primary visual cortex," *Clinical Neurophysiology*, vol. 120, Issue 12, pp. 2071–2081, Dec. 2009.

[137] G. Van Hoey, *Detectie en bronlokalisatie van epileptische hersenactiviteit met behulp van EEG-signalen*. PhD thesis, Ghent University, 2000.

[138] L. Ding, G. A. Worrell, T. D. Lagerlund, and H. Bin, "3d source localization of interictal spikes in epilepsy patients with mri lesions," *Phys. Med. Biol*, vol. 51, pp. 4047–4062, 2006.

[139] J. Ebersole, "Noninvasive localization of epileptogenic foci by eeg source modeling," *Epilepsia*, vol. 41, suppl. 3, pp. S24–S33, 2000.

[140] P. L. Nunez, "The brain's magnetic field some effects of multiple sources on locahzatmn methods," *Electroencephalogr. Chn Neurophystol*, vol. 63, pp. 75–82, 1986.

[141] D. Khosla, M. Singh, and M. Don, "Spatio-termporal eeg source localization using simulated annealing," *IEEE Transactions on Biomedical Engineering*, vol. 44, pp. 1075–1091, 1997.

[142] J. Mosher, P. S. Lewis, and R. M. Leahy, "Multiple dipole modeling and localization from spatio-temporal meg data," *IEEE Transactions on Biomedical Engineering*, vol. 39, no.6, pp. 541–553, 1992.

[143] B. J. Roth, D. Ko, I. R. von Albertini-Carletti, D. Scaffidi, and S. Sato, "Dipole localization in patients with epilepsy using the realistically shaped head model," *Electroencephalogr. Clin. Neurophysiol.*, vol. 102, pp. 159–166, 1997.

[144] J. C. Mosher and R. M. Leahy, "Recursive music: a framework for eeg andmeg source localization," *IEEE Trans.Signal Process*, vol. 45, pp. 1342–1354, 1998.

[145] G. Golub and C. Loan, *Matrix computations*. Baltimore, Maryland, Johns Hopkins, 3rd edition p.604, 1996.

[146] R. Uitert, D. Weinstein, and C. Johnson, "Can a spherical model substitute for a realistic head model in forward and inverse meg simulations ?," in *In Proc. 13th Int.Conf. on Biomagnetism*, pp. 798–800.

[147] J. C. deMunck and M. J. Peters, "A fast method to compute the potential in the multisphere model," *IEEE Trans. Biomed. Eng.*, vol. 40, pp. 1166–1174, 1993.

[148] C. Ramon, P. Schimpf, and J. Haueisen, "Effect of model complexity on eeg source localizations," *Neurology and Clinical Neurophysiology*, vol. 81, pp. 1–5, 2004.

[149] K. Wendel, N. Narra, M. Hannula, P. Kauppinen, and J. Malmivuo, "The influence of csf on eeg sensitivity distributions of multilayered head models," *IEEE Transactions on Biomedical Engineering*, vol. 55, no. 4,, pp. 1454–1456, 2008.

[150] C. Ramon, P. H. Schimpf, and J. Haueisen, "Influence of head models on eeg simulations and inverse source localizations," *Biomedical Engineering OnLine*, vol. 5, no. 10, pp. 1–13, 2006.

[151] C. H. Wolters, A. Anwander, X. Tricoche, S. Lew, and C. R. Johnson, "Influence of local and remote white matter conductivity anisotropy for a thalamic source on eeg/meg field and return current computation," *IJBEM*, vol. 7, no. 1, pp. 1–4, 2005.

[152] G. Crevecoeur, L. Dupré, H. Hallez, V. Montes, and S. Staelens, "Subspace electrode selection methodology for the reduction of the propagation of uncertain conductivity values in eeg dipole localization: A simulation study using a patient-specific head model," *Physics in Medicine and Biology*, submitted, 2011.

[153] K. Friston, J. Ashburner, S. Kiebel, T. Nichols, and W. Penny, *Statistical Parametric Mapping: The Analysis of Functional Brain Images*. New York: Academic Press, Nov 2006.

[154] B. Vanrumste, G. Van Hoey, R. Van de Walle, M. Have, I. Lemahieu, and P. Boon, "The validation of the finite difference and reciprocity for solving the inverse problem in eeg dipole source analysis," *Brain Topography*, vol. 14, no. 2, pp. 83–92, 2001.

[155] H. Hallez, B. Vanrumste, P. Van Hese, Y. D'Asseler, I. Lemahieu, and V. de Walle R., "A finite difference method with reciprocity used to incorporate anisotropy in electroencephalogram dipole source localization," *Phys. Med. Biol.*, vol. 50, no. 16, pp. 3787–3806, 2005.

[156] R. Barrett, M. Berry, T. Chan, J. Demmel, J. Donato, V. Dongarra Eijkhout, R. Pozo, C. Romine, and H. der Vorst, *Templates for the Solution of Linear Systems: Building Blocks for Iterative Methods*. Philadelphia PA: SIAM, 2nd edition ed., 1994.

[157] S. Rush and D. Driscoll, "Eeg electrode sensitivity-an application of reciprocity," *IEEE Trans. Biomed.*, vol. 16, pp. 15–22, 1969.

[158] R. Pascual-Marqui, "Review of methods for solving the eeg inverse problem.," *International journal of bioelectromagnetism*, vol. 1, pp. 75–86, 1999.

[159] G. Crevecoeur, H. Hallez, P. Van Hese, Y. DAsseler, L. Dupré, and R. Van de Walle, "A hybrid algorithm for solving the eeg inverse problem from spatio-temporal eeg data," *Med. Biol. Engin. & Comput*, vol. 46, pp. 767–777, 2008.

[160] R. Gaignaire, G. Crevecoeur, L. Dupré, R. Sabariego, P. Dular, and C. Geuzaine, "Stochastic uncertainty quantification of the conductivity in eeg source analysis by using polynomial chaos decomposition.," *IEEE Trans. Magn.*, vol. 46, no. 8, pp. 3457–3460, 2010.